

UNIVERSITY OF RIJEKA  
FACULTY OF ENGINEERING

Damjan Banić

**A SHEAR DEFORMABLE BEAM MODEL FOR  
STABILITY ANALYSIS OF COMPOSITE  
FRAMES**

DOCTORAL DISSERTATION

Rijeka, 2023.

UNIVERSITY OF RIJEKA  
FACULTY OF ENGINEERING

Damjan Banić

**A SHEAR DEFORMABLE BEAM MODEL FOR  
STABILITY ANALYSIS OF COMPOSITE  
FRAMES**

DOCTORAL DISSERTATION

Thesis Supervisors: Prof. Goran Turkalj, PhD  
Prof. Domagoj Lanc, PhD

Rijeka, 2023.

SVEUČILIŠTE U RIJECI  
TEHNIČKI FAKULTET

Damjan Banić

**GREĐNI MODEL S UKLJUČENIM UTJECAJEM  
POSMIČNIH DEFORMACIJA ZA ANALIZU  
STABILNOSTI KOMPOZITNIH OKVIRNIH  
KONSTRUKCIJA**

DOKTORSKI RAD

Mentori: prof. dr. sc. Goran Turkalj  
prof. dr. sc. Domagoj Lanc

Rijeka, 2023.

Thesis supervisors: Prof. Goran Turkalj, PhD, University of Rijeka, Faculty of Engineering  
Prof. Domagoj Lanc, PhD, University of Rijeka, Faculty of Engineering

The doctoral thesis was defended on \_\_\_\_\_ 2023. at the Faculty of Engineering University of Rijeka, before the committee consisting of:

1. Prof. Josip Brnić, PhD, Profesor emeritus, University of Rijeka, Faculty of Engineering
2. Prof. Zdenko Tonković, PhD, University of Zagreb, Faculty of Mechanical Engineering and Naval Architecture
3. Prof. Nicholas Fantuzzi, PhD, University of Bologna, Department of Civil, Chemical, Environmental and Materials Engineering

# Acknowledgments

---

Dear Mom and Dad, thank you. Thank you also to Nikola, Marija, Ivan, and Vjeko, and to all of your families. And lastly, thank you the most to my dear wife Marija and to dear God.

# Abstract

---

This doctoral dissertation focuses on addressing the issue of non-linear stability in frame structures composed of thin-walled composite beam elements. A numerical approach is presented to tackle this challenge, involving the development of an original 1D finite element model. The research delves into several key aspects. Firstly, the dissertation introduces the research problem and scientific motivation, outlining the main objectives and purpose of the study. It also provides a brief overview of previous studies on the buckling of thin-walled composite beams.

The study delves into composite materials, with a particular emphasis on fiber-reinforced composites. It explores the macro mechanics of single-layer composites, specifically those with arbitrarily oriented layers under plane stress and plane deformation states.

The research also focuses on the fundamentals of mechanics for thin-walled composite beam supports, considering the influence of shear deformations. Assumptions underlying the proposed model are discussed, and the displacement field of the thin-walled cross-section is defined, taking into account both linear and nonlinear components. The internal force resultants of the cross-section are analyzed, particularly for cross-sections containing cross-ply laminates and angle-ply laminates. The dissertation also describes the procedure for calculating cross-section properties. Also, a computer program CCSC for calculation of composite cross-section properties has been developed.

A finite element formulation is presented to analyze the stability of the frame structures. The model is designed to perform both linearized and nonlinear stability analysis. Beam finite element consists of 14 degrees of freedom and employs the principle of virtual work to derive the elastic and geometric stiffness matrices. Nonlinear analysis is conducted using an incremental-iterative procedure based on the generalized displacement control method. The updated Lagrangian formulation is utilized to solve the equilibrium equations.

The dissertation includes the development of the computer program THINWALL V18. Variety of examples are analyzed to validate the numerical model, considering different cross-sections composed of symmetric and balanced composites, as well as various boundary conditions and different frame structures.

Lastly, the research concludes with a discussion of the contributions and scientific achievements. It also outlines potential directions for future research and suggests improvements in the

field of buckling of thin-walled composite beams, particularly with regard to the inclusion of shear deformations.

Overall, this doctoral dissertation provides a comprehensive numerical approach to assess the non-linear stability of frame structures composed of thin-walled composite beam elements. By enhancing the understanding and optimization of such structures, this research contributes to the advancement of structural engineering in the field of composite materials.

**Keywords:** thin-walled composite cross-section, laminates, shear deformations, shear coupling effects, beam model, buckling analysis

# Sažetak

---

Ovaj doktorski rad bavi se pitanjem nelinearne stabilnosti okvirnih konstrukcija sastavljenih od tankostijenih kompozitnih grednih nosača. Predstavljen je numerički pristup za rješavanje ovog problema, uključujući razvoj izvornog 1D modela pomoću metode konačnih elemenata. Istraživanje se bavi s nekoliko ključnih aspekata. Prvo, doktorski rad uvodi problem istraživanja i motivaciju, ocrtavajući glavne ciljeve i svrhu istraživanja. Također daje pregled prethodnih istraživanja o izvicanju tankostijenih kompozitnih grednih konstrukcija.

Istraživanje se bavi kompozitnim materijalima, s posebnim naglaskom na kompozite ojačane vlaknima (*fiber reinforced composites*). Istražuje makromehaniku jednoslojnih kompozita, posebno onih s proizvoljno orijentiranim slojevima pod ravninskim stanjem naprezanja i ravninskim stanjem deformacije.

Istraživanje je također usredotočeno na osnove mehanike tankostijenih kompozitnih grednih nosača s utjecajem posmičnih deformacija. Raspravljaju se pretpostavke na kojima se temelji predloženi model i definira polje pomaka tankostjenog poprečnog presjeka, uzimajući u obzir linearne i nelinearne komponente. Analizirane su rezultante unutarnjih sila poprečnog presjeka, posebno za poprečne presjeke koji sadrže takozvane *cross-ply* laminate i *angle-ply* laminate. U doktorskom radu je opisan postupak proračuna karakteristika poprečnog presjeka. Također je razvijen program CCSC za izračun karakteristika kompozitnog poprečnog presjeka.

Prikazana je konačno elementna formulacija za analizu stabilnosti okvirnih konstrukcija. Model je dizajniran za izvođenje linearizirane i nelinearne analize stabilnosti. Gredni konačni element sastoji se od 14 stupnjeva slobode i koristi princip virtualnih radova za izvođenje elastične i geometrijske matrice krutosti. Nelinearna analiza provodi se primjenom inkrementalno-iterativnog postupka koji se temelji na takozvanoj *generalised displacement control* metodi. Za rješavanje ravnotežnih jednadžbi koristi se *Updated Lagrangian* formulacija.

Doktorski rad uključuje izradu računalnog programa THINWALL V18. Analizirani su različiti primjeri za validaciju numeričkog modela, uzimajući u obzir različite poprečne presjeke sastavljene od takozvanih *symmetric* i *balanced* kompozita, kao i različite rubne uvjete i različite tipove okvirnih konstrukcija.

Na kraju, istraživanje završava raspravom o doprinosima i znanstvenim dostignućima. Također ocrtava potencijalne pravce budućih istraživanja i predlaže poboljšanja u području izvicanja tankostijenih kompozitnih grednih konstrukcija, s naglaskom na uključivanje posmičnih



deformacija.

Općenito, ova doktorska disertacija nudi sveobuhvatan numerički pristup procjeni nelinearne stabilnosti okvirnih konstrukcija sastavljenih od tankostijenih kompozitnih grednih elemenata. Poboljšanjem razumijevanja i optimizacije takvih konstrukcija, ovo istraživanje pridonosi napretku konstrukcijskog inženjerstva u području kompozitnih materijala.

**Ključne riječi:** tankostjeni kompozitni presjek, laminati, posmične deformacije, interakcije posmičnih defomacija, gredni model, analiza izvijanja

# TABLE OF CONTENTS

---

<b>Acknowledgments</b>	<b>v</b>
<b>Abstract</b>	<b>vi</b>
<b>Sažetak</b>	<b>viii</b>
<b>1 INTRODUCTION</b>	<b>1</b>
1.1 Motivation .....	1
1.2 Analysis of the previous research.....	2
1.3 Purpose, Objectives and Contributions of the Research .....	5
1.4 The structure of the doctoral thesis .....	6
<b>2 MECHANICS OF COMPOSITE MATERIALS</b>	<b>9</b>
2.1 Macromechanical behavior of a lamina .....	10
2.1.1 <i>Stress-strain relations for anisotropic materials</i> .....	10
2.1.2 <i>Stress-strain relations for orthotropic materials</i> .....	11
2.2 Plane stress in an orthotropic material .....	12
2.3 Plane stress for a lamina of an arbitrary orientation.....	13
<b>3 COMPOSITE THIN-WALLED BEAM</b>	<b>17</b>
3.1 Basic assumptions .....	17
3.2 Kinematics of the beam.....	19
3.3 Deformations and strain tensor.....	20
3.4 Stress resultants-strain components relations for a cross-ply laminate.....	23
3.5 Stress resultants-strain components relations for a angle ply laminate.....	33
3.6 Cross-section properties .....	38
<b>4 FINITE ELEMENT FORMULATION</b>	<b>53</b>
4.1 Thin-walled beam finite element.....	53
4.2 Virtual work principle .....	55
4.3 <i>Updated Lagrangian</i> (UL) formulation .....	62
4.4 Hermite shape functions .....	66
4.5 Finite element equation .....	73

<b>5</b>	<b>COMPUTER PROGRAMS CCSC AND THINWALL V18</b>	<b>75</b>
5.1	CCSC program description .....	75
5.2	THINWALL V18 brief program description .....	78
5.3	Numerical examples .....	81
5.3.1	<i>Example 1</i> .....	82
5.3.2	<i>Example 2</i> .....	89
5.3.3	<i>Example 3</i> .....	91
5.3.4	<i>Example 4</i> .....	93
5.3.5	<i>Example 5</i> .....	96
5.3.6	<i>Example 6</i> .....	98
5.3.7	<i>Example 7</i> .....	101
5.3.8	<i>Example 8</i> .....	103
5.3.9	<i>Example 9</i> .....	107
5.3.10	<i>Example 10</i> .....	111
<b>6</b>	<b>CONCLUSION</b>	<b>117</b>
	<b>Bibliography</b>	<b>119</b>
	<b>List of symbols and abbreviations</b>	<b>124</b>
	List of symbols.....	124
	List of abbreviations .....	129
	<b>List of figures</b>	<b>130</b>
	<b>List of tables</b>	<b>133</b>
	<b>Curriculum vitae</b>	<b>134</b>
	<b>List of published works</b>	<b>135</b>

# 1 INTRODUCTION

---

The introductory section of the doctoral thesis will present general information about the conducted research, including scientific motivation, an overview of existing research, contributions and the purpose of the study, as well as the organization of the doctoral work.

## 1.1 Motivation

The motivation for researching load-bearing composite structures is multifaceted. Firstly, load-bearing composite structures have great potential for achieving optimal solutions in terms of weight, load capacity, functionality, construction costs, energy efficiency, and resistance to chemical processes. The use of composite materials allows designers to achieve higher load-bearing capacity with reduced weight, which can result in material and energy savings in construction.

Secondly, load-bearing composite structures exhibit a more complex response to external loading compared to conventional structures. Slender beam elements with thin-walled cross-sections have an increased tendency to lose stability of deformation and experience buckling. Instability in beam structures can manifest in the form of pure flexural, pure torsional, flexural-torsional, or lateral deformation. All these deformation forms represent global instability or buckling modes. Thin-walled frames are also susceptible to local instability modes where significant cross-sectional distortion occurs due to the loss of stability in the initial cross-sectional shape. This can lead to structural collapse even before the occurrence of global instability. Therefore, in the optimal design of structures, special attention needs to be paid to accurately determining the limit state of deformation modes, namely buckling strength. Analytical solutions are only available for simpler cases, necessitating the development and application of numerical solutions.

Thirdly, traditional Euler-Bernoulli assumptions fail to accurately account for the actual deformation of the cross-section. First-order and higher-order shear deformation theories have been developed to address the limitations of traditional analyses based on the Euler-Bernoulli assumption. These theories incorporate the effects of shear deformation in the analysis of beam structures, resulting in more accurate predictions of deformations and structural responses.

## 1.2 Analysis of the previous research

Load-bearing composite structures generally contain slender beam structural elements of thin-walled cross-section. The response of such optimized structures to external loading is much more complex compared to traditional structures, with an increased tendency to lose stability and experience buckling [9,10,14–16,44,45,48,59].

The occurrence of instability in beam structures can manifest in various deformation forms, including pure flexural, pure torsional, torsional-flexural, or lateral deformation. These deformation forms are known as global instability forms or global buckling forms. Thin-walled frames are also susceptible to local instability forms, where significant distortion of the cross-section occurs, leading to structural collapse even before the global instability form occurs [9,10,14,16,48,59].

Therefore, in the optimal design of composite structures, it is crucial to determine the limit state of stability, specifically the buckling strength, for different deformation forms. While analytical solutions are available for simpler cases [22,32,53,54,61,62], the development and application of numerical solutions become a necessity for more complex scenarios [9,10,14–16,44,45,48,59].

The introduction of composites in structural design further complicates the process but offers the potential for achieving optimal solutions in terms of weight, load-bearing capacity, functionality, construction cost, energy efficiency, and resistance to chemical processes [6,36–41,75]. However, shear deformations have a significant impact on the transverse displacements, natural vibration frequencies, and critical buckling loads of composite structures. Traditional analyses based on the Euler-Bernoulli assumption can lead to significant errors when shear deformations are not properly accounted for [17,18,24,53].

To address these challenges, researchers have presented geometric nonlinear analyses of composite beam structures considering shear deformations [7,8,44,45,48,59,66,70–73,9,10,14–16,30,31,43]. Some studies also include bending-torsion coupling effects, particularly for asymmetric cross-sections where the principal bending and shear axes do not coincide [50].

In recent studies [66], composite frames with semi-rigid connections were investigated using a geometrically nonlinear beam model that accounts for shear deformation effects. Previous research considered unidirectional orthotropic composite structures and included shear deformation coupling effects in the virtual elastic strain energy while neglecting them in the force-strain relationships. However, in the present study, shear coupling effects due to the non-

symmetry of the cross-section are introduced even in the force-strain relationships, allowing for the modeling of cross-sections made of symmetric and balanced laminates. Improved shear-deformable beam formulations, considering bending-torsion coupling effects, are utilized [7,8,30,31,43,66].

In the context of the updated Lagrangian (UL) formulation [34,65], nonlinear displacement fields of the cross-section are used to obtain the element geometric stiffness. This approach includes second-order displacement terms to account for large rotation effects. By considering semi-tangential descriptions of internal bending and torsion moments, equilibrium conditions at the frame joint are preserved, allowing for any spatial orientation of the beam members with respect to the joint [33,74].

To mitigate the shear-locking effect [52], interdependent shape functions for deflection, slope, twist rotations, and warping parameters are employed within the finite element procedure. The incremental-iteration algorithm is defined using the generalized displacement control method [74]. The nodal orientations are updated based on the semitangential rotation transformation rule, ensuring the accurate representation of internal bending and torsion moments [4,64,67].

Furthermore, the deformability of the cross-section is a crucial consideration in the analysis of composite beam structures. Traditional Euler-Bernoulli assumptions fail to accurately account for the actual deformation of the cross-section. To address the limitations of traditional analyses based on the Euler-Bernoulli assumption, first-order and higher-order shear deformation theories have been developed.

The first-order shear deformation theory considers the shear deformation effects by including a shear correction factor in the transverse displacement field. This theory accounts for the non-uniform distribution of transverse shear stresses through the thickness of the beam. By considering the shear deformation effects, more accurate results can be obtained for composite beam structures [17,18,24,53].

However, in certain cases, the first-order shear deformation theory may not capture all the important deformation modes accurately, especially for thick beams or structures with pronounced shear effects. In such cases, higher-order shear deformation theories are utilized [19,27,28,47,49,51,55].

Higher-order shear deformation theories introduce additional displacement variables to account for higher-order terms in the deformation field. These theories provide more accurate predictions for the transverse shear stresses and displacements throughout the thickness of the

beam. The additional variables can capture the effects of transverse shear deformation more effectively, resulting in improved accuracy for analyzing composite structures.

The use of higher-order shear deformation theories in conjunction with geometric nonlinear analyses allows for a more comprehensive understanding of the behavior of composite beam structures. These theories enable the consideration of complex deformation modes, such as bending-torsion coupling effects and non-symmetry of cross-sections, resulting in more accurate predictions of stability and buckling behavior.

Overall, the incorporation of first-order and higher-order shear deformation theories in the analysis of composite beam structures enhances the accuracy of the results and provides valuable insights for the optimal design of load-bearing composite structures [7,8,44,45,48,59,66,9,10,14–16,30,31,43].

Furthermore, the deformability of the cross-section plays a significant role in the analysis of composite beam structures. Traditional analyses based on Euler-Bernoulli assumptions assume that the cross-section remains undeformed during bending. However, in reality, the cross-section undergoes deformation, especially for slender beam elements with thin-walled cross-sections.

To accurately capture the behavior of composite structures, it is essential to consider the deformability of the cross-section. This involves analyzing both the global and local effects of cross-sectional distortion. Local instability forms can occur when the initial cross-sectional shape becomes unstable, leading to significant distortion of the cross-section and potential collapse before the occurrence of global instability forms [9,10,14,16,48,59].

In recent studies, various theories have been developed to analyze the deformability of the cross-section in composite beam structures. One such theory is the General Beam Theory (GBT), which incorporates the deformability of the cross-section by expressing the displacement field using specific forms of cross-sectional deformation. GBT models assume certain deformation modes of the cross-section and express the displacement field based on these modes, providing a more accurate representation of the actual behavior of the structure [26,56–59].

Another approach is the Constrained Finite Strip Method (cFSM), which also considers the deformability of the cross-section. cFSM models the cross-section as a set of interconnected strips, allowing for the analysis of both local and global effects of buckling and deformation. This method provides a computationally efficient approach to capture the deformability of the cross-section and predict the behavior of composite beam structures [1,2].

By considering the deformability of the cross-section, these theories enable more accurate analyses of both local and global effects, such as bending, torsion, and buckling. They provide valuable insights into the stability and overall performance of composite beam structures, allowing for more precise optimization of their design parameters.

In summary, accounting for the deformability of the cross-section is crucial for accurately predicting the behavior of composite beam structures. The utilization of theories like GBT and cFSM allows for a more comprehensive analysis of both local and global effects, leading to improved design and optimization strategies for load-bearing composite structures.

### **1.3 Purpose, Objectives and Contributions of the Research**

The purpose of this research is to develop a numerical algorithm for the stability analysis of composite frame structures, taking into account the limitations of traditional analyses based on the Euler-Bernoulli assumption. Traditional Euler-Bernoulli assumptions fail to accurately account for the actual deformation of the cross-section. Therefore, the goal of this study is to overcome these limitations by incorporating first-order shear deformation theory.

The numerical algorithm, based on the beam finite element, will encompass the material non-homogeneity of the cross-section, as well as geometric nonlinearity in terms of including large displacements and rotations of the structural elements. The development of this algorithm is motivated by the need to accurately capture the complex response of load-bearing composite structures, which often contain slender beam elements with thin-walled cross-sections. These structures exhibit a higher tendency to lose stability and experience buckling phenomena.

To accurately determine the stability limit of deformation forms, particularly buckling strength, numerical solutions become a necessity. Analytical solutions are only available for simpler cases, while more complex scenarios require the development and application of numerical methods. This research aims to provide such numerical solutions for composite frame structures.

The algorithm will utilize an updated Lagrangian incremental formulation, allowing for the consideration of large rotations and displacements. It will also incorporate a 2D numerical model to determine the geometric characteristics of the cross-section. The effects of shear deformations, including the bending-torsion coupling effects, will be included in the beam model.

By developing these numerical models and algorithms, this research intends to contribute to the field of engineering practice by providing a reliable tool for describing the geometrically



nonlinear response of composite beam structures in frame structures. The results of this study will enhance the understanding of the behavior of composite structures under external loading and facilitate the optimal design of such structures.

#### **1.4 The structure of the doctoral thesis**

The structure of the doctoral dissertation is organized into chapters, each covering a specific part of the research.

The first chapter introduces the research problem and scientific motivation. It outlines the main objectives and purpose of the research, as well as provides a brief overview of previous studies in the field of buckling of thin-walled composite beams.

The second chapter presents composite materials, with a particular emphasis on fiber reinforced composite materials. It discusses the macro mechanics of single-layer composites, especially related to arbitrarily oriented layers under plane stress and plane deformation states.

The third chapter presents the fundamentals of mechanics for thin-walled composite beam supports, considering the influence of shear deformations. It states the assumptions on which the presented model is based. The displacement field of the thin-walled cross-section is defined, dividing it into linear and nonlinear components, along with the corresponding strain tensor. The internal force resultants of the cross-section are shown, specifically for cross-sections containing cross-ply laminates and angle-ply laminates. The procedure for calculating cross-section properties is described.

In the fourth chapter, the finite element formulation of the analyzed problem is presented. The proposed model is designed for both linearized and nonlinear stability analysis. Linearized analysis is suitable for quickly checking critical loads and the corresponding deformation shape of the structure, while nonlinear analysis tracks the response of deformation with respect to the applied load. The final model has 14 degrees of freedom. The elastic and geometric stiffness matrices are derived using the principle of virtual work. Nonlinear analysis is based on an incremental-iterative procedure, using the generalized displacement method developed by the candidate's mentor. The updated Lagrangian formulation is used to solve the equilibrium equations.

The fifth chapter describes the computer programs CCSC and THINWALL V18. Along with the program's schematic flow, a brief description of all subprograms is provided. Ten examples

are analyzed to validate the numerical model. The considered results show two different models: one including shear deformations and one excluding shear deformations. Various cross-sections, composed of different symmetric and balanced composites, are examined. Different boundary conditions and types of beam support structures are also considered.

The last chapter presents the conclusions of the conducted research, discussing the contributions of the dissertation and the scientific achievements. Ideas and directions for future research and potential improvements in the field of buckling of thin-walled composite beams with the inclusion of shear deformations are presented.



## 2 MECHANICS OF COMPOSITE MATERIALS

---

Composite materials are a class of materials made by combining two or more different constituents with different physical or chemical properties. These components, known as the matrix and reinforcement, work together to create a material with improved mechanical, thermal, or electrical properties that exceed those of the individual components alone.

The matrix material in a composite serves as a binder that holds the reinforcement in place and transfers loads between the reinforcing elements. It can be a polymer, a metal, a ceramic material, or even a combination of these materials. The choice of matrix depends on the specific application requirements and the desired properties of the composite.

The reinforcement phase provides strength and stiffness to the composite. It is typically in the form of fibers, particles or flakes. Common reinforcing materials include carbon fibers, glass fibers, aramid fibers and nanoparticles. The selection of reinforcement depends on factors such as desired strength, stiffness and resistance to environmental influences.

The combination of matrix and reinforcement in a composite results in synergistic properties that cannot be achieved with either component alone. Composites feature a high strength-to-weight ratio, excellent fatigue resistance, corrosion resistance, and tailored electrical and thermal conductivity. They are used in aerospace, automotive, construction, sports equipment and many other industries [21,23,29,68].

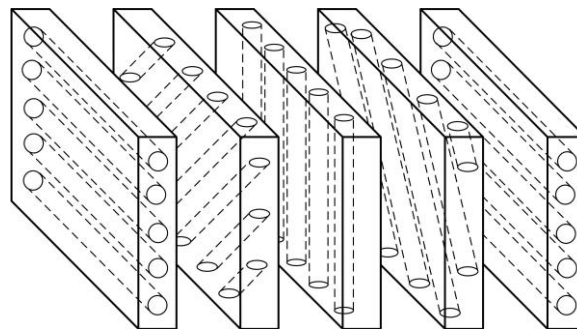


*Fig. 2.1 Unbonded view of fiber-reinforced composite laminate*

Four commonly accepted types of composite materials are:

- fibrous composite materials that consist of fibers in a matrix
- particulate composite materials that are composed of particles in a matrix
- laminated composite materials that consist of layers of various materials
- combinations of some or all of the first three types

This thesis focuses on the utilization of fiber-reinforced composite laminates in thin-walled beams, delving into their widespread application in engineering practice and the underlying

mechanical theory. The fundamental terminology associated with these laminates, include laminae or plies, represent flat configurations of unidirectional or woven fibers embedded in a matrix. Additionally, the concept of a laminate, a bonded stack of laminae exhibiting different orientations of the main material directions, as shown in Fig. 2.1 [29], is discussed in detail.

## 2.1 Macromechanical behavior of a lamina

Macromechanics of single-layer composites involves the study of the overall mechanical behavior and properties of composite materials at the macroscopic scale. It focuses on understanding how the arrangement, orientation, and mechanical properties of the constituent materials affect the mechanical response of the composite as a whole.

An important aspect of macromechanics is the analysis of the effective properties of single-layer composites. Effective properties describe the overall behavior of the composite based on the properties of its constituent materials and their arrangement. These properties include stiffness, strength, and thermal expansion. The orientation, volume fraction, and mechanical properties of the reinforcing phase significantly affect the effective properties.

Another important aspect of macromechanics is understanding the stress and strain distribution within the composite layer. Load transfer between the matrix and the reinforcing phases is critical to achieving the desired mechanical properties. The arrangement and orientation of the reinforcing phase plays an important role in determining the stress distribution and load carrying capacity of the composite.

### 2.1.1 Stress-strain relations for anisotropic materials

The stresses in an elementary volume will first be defined in order to establish stress-strain relations for anisotropic materials. The generalized Hooke's law relating stresses to strains can be written in contracted notation as follows:

$$\sigma_i = C_{ij} \varepsilon_j \quad i, j = 1, \dots, 6 \quad (2.1)$$

where  $\sigma_i$  are the stress components shown in Fig. 2.2,  $\varepsilon_j$  are the strain components and  $C_{ij}$  is the stiffness matrix. It should be noted that:

$$\tau_{12} = \tau_{21}, \quad \tau_{13} = \tau_{31}, \quad \tau_{23} = \tau_{32}, \quad C_{ij} = C_{ji} \quad (2.2)$$

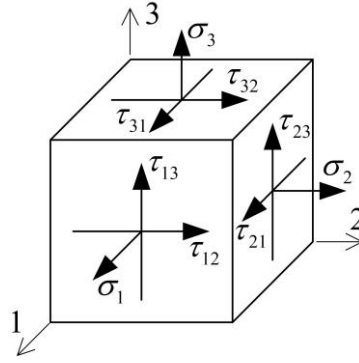


Fig. 2.2 Stresses in an elemental volume

Then the stress-strain relations in matrix form for anisotropic material can be written as:

$$\begin{Bmatrix} \sigma_1 \\ \sigma_2 \\ \sigma_3 \\ \tau_{23} \\ \tau_{31} \\ \tau_{12} \end{Bmatrix} = \begin{bmatrix} C_{11} & C_{12} & C_{13} & C_{14} & C_{15} & C_{16} \\ C_{12} & C_{22} & C_{23} & C_{24} & C_{25} & C_{26} \\ C_{13} & C_{23} & C_{33} & C_{34} & C_{35} & C_{36} \\ C_{14} & C_{24} & C_{34} & C_{44} & C_{45} & C_{46} \\ C_{15} & C_{25} & C_{35} & C_{45} & C_{55} & C_{56} \\ C_{16} & C_{26} & C_{36} & C_{46} & C_{56} & C_{66} \end{bmatrix} \begin{Bmatrix} \varepsilon_1 \\ \varepsilon_2 \\ \varepsilon_3 \\ \gamma_{23} \\ \gamma_{31} \\ \gamma_{12} \end{Bmatrix} \quad (2.3)$$

If the reverse relations are to be expressed compliance matrix  $S_{ij}$  is used:

$$\begin{Bmatrix} \varepsilon_1 \\ \varepsilon_2 \\ \varepsilon_3 \\ \gamma_{23} \\ \gamma_{31} \\ \gamma_{12} \end{Bmatrix} = \begin{bmatrix} S_{11} & S_{12} & S_{13} & S_{14} & S_{15} & S_{16} \\ S_{12} & S_{22} & S_{23} & S_{24} & S_{25} & S_{26} \\ S_{13} & S_{23} & S_{33} & S_{34} & S_{35} & S_{36} \\ S_{14} & S_{24} & S_{34} & S_{44} & S_{45} & S_{46} \\ S_{15} & S_{25} & S_{35} & S_{45} & S_{55} & S_{56} \\ S_{16} & S_{26} & S_{36} & S_{46} & S_{56} & S_{66} \end{bmatrix} \begin{Bmatrix} \sigma_1 \\ \sigma_2 \\ \sigma_3 \\ \tau_{23} \\ \tau_{31} \\ \tau_{12} \end{Bmatrix} \quad (2.4)$$

### 2.1.2 Stress-strain relations for orthotropic materials

If the material has the two orthogonal planes of material property symmetry, then that material is called orthotropic material. The stress-strain relations for orthotropic material can be written in stiffness matrix form as follows:

$$\begin{Bmatrix} \sigma_1 \\ \sigma_2 \\ \sigma_3 \\ \tau_{23} \\ \tau_{31} \\ \tau_{12} \end{Bmatrix} = \begin{bmatrix} C_{11} & C_{12} & C_{13} & 0 & 0 & 0 \\ C_{12} & C_{22} & C_{23} & 0 & 0 & 0 \\ C_{13} & C_{23} & C_{33} & 0 & 0 & 0 \\ 0 & 0 & 0 & C_{44} & 0 & 0 \\ 0 & 0 & 0 & 0 & C_{55} & 0 \\ 0 & 0 & 0 & 0 & 0 & C_{66} \end{bmatrix} \begin{Bmatrix} \varepsilon_1 \\ \varepsilon_2 \\ \varepsilon_3 \\ \gamma_{23} \\ \gamma_{31} \\ \gamma_{12} \end{Bmatrix} \quad (2.5)$$

While the stain-stress relations are written in compliance matrix form as:

$$\begin{Bmatrix} \varepsilon_1 \\ \varepsilon_2 \\ \varepsilon_3 \\ \gamma_{23} \\ \gamma_{31} \\ \gamma_{12} \end{Bmatrix} = \begin{bmatrix} S_{11} & S_{12} & S_{13} & 0 & 0 & 0 \\ S_{12} & S_{22} & S_{23} & 0 & 0 & 0 \\ S_{13} & S_{23} & S_{33} & 0 & 0 & 0 \\ 0 & 0 & 0 & S_{44} & 0 & 0 \\ 0 & 0 & 0 & 0 & S_{55} & 0 \\ 0 & 0 & 0 & 0 & 0 & S_{66} \end{bmatrix} \begin{Bmatrix} \sigma_1 \\ \sigma_2 \\ \sigma_3 \\ \tau_{23} \\ \tau_{31} \\ \tau_{12} \end{Bmatrix} \quad (2.6)$$

The compliance matrix components in orthotropic material can be expressed over engineering constants as follows:

$$\begin{aligned} S_{11} &= \frac{1}{E_1}, & S_{22} &= \frac{1}{E_2}, & S_{33} &= \frac{1}{E_3}, & S_{44} &= \frac{1}{G_{23}}, & S_{55} &= \frac{1}{G_{31}}, & S_{66} &= \frac{1}{G_{12}}, \\ S_{12} &= -\frac{\nu_{12}}{E_1} = -\frac{\nu_{21}}{E_2}, & S_{13} &= -\frac{\nu_{13}}{E_1} = -\frac{\nu_{31}}{E_3}, & S_{23} &= -\frac{\nu_{23}}{E_2} = -\frac{\nu_{32}}{E_3} \end{aligned} \quad (2.7)$$

where  $E$ ,  $G$  and  $\nu$  are elastic modulus, shear modulus and Poisson's ratio respectively. The Stiffness matrix components can be expressed over compliance matrix components for the orthotropic material as follows:

$$\begin{aligned} C_{11} &= \frac{S_{22}S_{33} - S_{23}^2}{S}, & C_{22} &= \frac{S_{33}S_{11} - S_{13}^2}{S}, & C_{33} &= \frac{S_{11}S_{22} - S_{12}^2}{S}, \\ C_{12} &= \frac{S_{13}S_{23} - S_{12}S_{33}}{S}, & C_{13} &= \frac{S_{12}S_{23} - S_{13}S_{22}}{S}, & C_{23} &= \frac{S_{12}S_{13} - S_{23}S_{11}}{S}, \\ C_{44} &= \frac{1}{S_{44}}, & C_{55} &= \frac{1}{S_{55}}, & C_{66} &= \frac{1}{S_{66}}, \end{aligned} \quad (2.8)$$

where:

$$S = S_{11}S_{22}S_{33} - S_{11}S_{23}^2 - S_{22}S_{13}^2 - S_{33}S_{12}^2 + 2S_{12}S_{23}S_{13} \quad (2.9)$$

## 2.2 Plane stress in an orthotropic material

For unidirectionally reinforced lamina in the 1-2 plane as shown in Fig. 2.3, a plane stress state is defined by setting:

$$\sigma_3 = 0, \quad \tau_{23} = 0, \quad \tau_{31} = 0 \quad (2.10)$$

which is very practical assumption when dealing with thin plates with two orthogonal planes of material property symmetry.

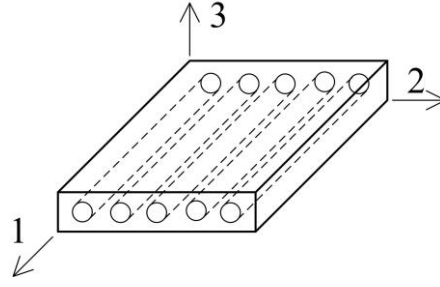


Fig. 2.3 Unidirectionally reinforced lamina

Then the strain-stress relations from Eq. (2.6) reduce to:

$$\begin{Bmatrix} \varepsilon_1 \\ \varepsilon_2 \\ \gamma_{12} \end{Bmatrix} = \begin{bmatrix} S_{11} & S_{12} & 0 \\ S_{12} & S_{22} & 0 \\ 0 & 0 & S_{66} \end{bmatrix} \begin{Bmatrix} \sigma_1 \\ \sigma_2 \\ \tau_{12} \end{Bmatrix} \quad (2.11)$$

The stress-strain relations can be expressed in similar manner from Eq. (2.5) as:

$$\begin{Bmatrix} \sigma_1 \\ \sigma_2 \\ \tau_{12} \end{Bmatrix} = \begin{bmatrix} Q_{11} & Q_{12} & 0 \\ Q_{12} & Q_{22} & 0 \\ 0 & 0 & Q_{66} \end{bmatrix} \begin{Bmatrix} \varepsilon_1 \\ \varepsilon_2 \\ \gamma_{12} \end{Bmatrix} = \mathbf{Q} \begin{Bmatrix} \varepsilon_1 \\ \varepsilon_2 \\ \gamma_{12} \end{Bmatrix} \quad (2.12)$$

where the  $Q_{ij}$  are so-called reduced stiffnesses [29] for a plane stress state in 1-2 plane. They can be determined as follows:

$$Q_{ij} = C_{ij} - \frac{C_{i3}C_{j3}}{C_{33}} \quad i, j = 1, 2, 6 \quad (2.13)$$

and by the use of Eqs. (2.7), (2.8) and (2.9) following is obtained:

$$Q_{11} = \frac{E_1}{1 - \nu_{12}\nu_{21}}, \quad Q_{22} = \frac{E_2}{1 - \nu_{12}\nu_{21}}, \quad Q_{12} = \frac{\nu_{12}E_2}{1 - \nu_{12}\nu_{21}} = \frac{\nu_{21}E_1}{1 - \nu_{12}\nu_{21}}, \quad Q_{66} = G_{12} \quad (2.14)$$

where it should be noted that:

$$\frac{\nu_{12}}{E_1} = \frac{\nu_{21}}{E_2} \quad (2.15)$$

### 2.3 Plane stress for a lamina of an arbitrary orientation

Although in previous section stresses and strains were defined in principal material coordinates for an orthotropic material (1-2). However, by combining a laminate with different laminae angles as shown in Fig. 2.1, it can happen that the principal direction of orthotropy of particular laminae do not coincide with coordinate directions of laminate as shown in Fig. 2.4.



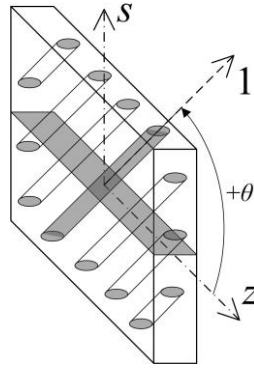


Fig. 2.4 Lamina of an arbitrary orientation

It can be recalled from elementary mechanics that relation between principal and arbitrary strains for plane stress condition is:

$$\begin{bmatrix} \varepsilon_1 & \gamma_{12}/2 \\ \gamma_{12}/2 & \varepsilon_2 \end{bmatrix} = \begin{bmatrix} \cos \theta & \sin \theta \\ -\sin \theta & \cos \theta \end{bmatrix} \begin{bmatrix} \varepsilon_z & \gamma_{zs}/2 \\ \gamma_{zs}/2 & \varepsilon_s \end{bmatrix} \begin{bmatrix} \cos \theta & -\sin \theta \\ \sin \theta & \cos \theta \end{bmatrix} \quad (2.16)$$

which leads to:

$$\begin{Bmatrix} \varepsilon_1 \\ \varepsilon_2 \\ \gamma_{12} \end{Bmatrix} = \mathbf{T}_\varepsilon \begin{Bmatrix} \varepsilon_z \\ \varepsilon_s \\ \gamma_{zs} \end{Bmatrix} \quad (2.17)$$

where:

$$\mathbf{T}_\varepsilon = \begin{bmatrix} \cos^2 \theta & \sin^2 \theta & (\sin 2\theta)/2 \\ \sin^2 \theta & \cos^2 \theta & -(\sin 2\theta)/2 \\ -\sin 2\theta & \sin 2\theta & \cos 2\theta \end{bmatrix} \quad (2.18)$$

Similarly the relation between principal and arbitrary stresses for plane stress condition is:

$$\begin{bmatrix} \sigma_1 & \tau_{12} \\ \tau_{12} & \sigma_2 \end{bmatrix} = \begin{bmatrix} \cos \theta & \sin \theta \\ -\sin \theta & \cos \theta \end{bmatrix} \begin{bmatrix} \sigma_z & \tau_{zs} \\ \tau_{zs} & \sigma_s \end{bmatrix} \begin{bmatrix} \cos \theta & -\sin \theta \\ \sin \theta & \cos \theta \end{bmatrix} \quad (2.19)$$

which leads to:

$$\begin{Bmatrix} \sigma_1 \\ \sigma_2 \\ \tau_{12} \end{Bmatrix} = \begin{bmatrix} \cos^2 \theta & \sin^2 \theta & \sin 2\theta \\ \sin^2 \theta & \cos^2 \theta & -\sin 2\theta \\ -(\sin 2\theta)/2 & (\sin 2\theta)/2 & \cos 2\theta \end{bmatrix} \begin{Bmatrix} \sigma_z \\ \sigma_s \\ \tau_{zs} \end{Bmatrix} \quad (2.20)$$

To obtain relation for laminate coordinate directions (z-s) inverse expression is required:

$$\begin{Bmatrix} \sigma_z \\ \sigma_s \\ \tau_{zs} \end{Bmatrix} = \mathbf{T}_\sigma \begin{Bmatrix} \sigma_1 \\ \sigma_2 \\ \tau_{12} \end{Bmatrix} \quad (2.21)$$

where:

$$\mathbf{T}_\sigma = \begin{bmatrix} \cos^2 \theta & \sin^2 \theta & -\sin 2\theta \\ \sin^2 \theta & \cos^2 \theta & \sin 2\theta \\ (\sin 2\theta)/2 & -(\sin 2\theta)/2 & \cos 2\theta \end{bmatrix} \quad (2.22)$$

If now relation between stresses and strains from Eq. (2.12) is expanded with Eqs. (2.17) and (2.21) following is obtained:

$$\begin{Bmatrix} \sigma_z \\ \sigma_s \\ \tau_{zs} \end{Bmatrix} = \mathbf{T}_\sigma \mathbf{Q} \mathbf{T}_\varepsilon \begin{Bmatrix} \varepsilon_z \\ \varepsilon_s \\ \gamma_{zs} \end{Bmatrix} \quad (2.23)$$

which leads to:

$$\begin{Bmatrix} \sigma_z \\ \sigma_s \\ \tau_{zs} \end{Bmatrix} = \hat{\mathbf{Q}} \begin{Bmatrix} \varepsilon_z \\ \varepsilon_s \\ \gamma_{zs} \end{Bmatrix} \quad (2.24)$$

where  $\hat{\mathbf{Q}}$  are transformed reduced stiffnesses [29]:

$$\hat{\mathbf{Q}} = \mathbf{T}_\sigma \mathbf{Q} \mathbf{T}_\varepsilon = \begin{bmatrix} \hat{Q}_{11} & \hat{Q}_{12} & \hat{Q}_{16} \\ \hat{Q}_{12} & \hat{Q}_{22} & \hat{Q}_{26} \\ \hat{Q}_{16} & \hat{Q}_{26} & \hat{Q}_{66} \end{bmatrix} \quad (2.25)$$

Matrix elements in Eq. (2.25) are given with the following expressions:

$$\begin{aligned} \hat{Q}_{11} &= Q_{11} \cos^4 \theta + Q_{22} \sin^4 \theta + \left( Q_{66} + \frac{1}{2} Q_{12} \right) \sin^2 2\theta \\ \hat{Q}_{22} &= Q_{22} \cos^4 \theta + Q_{11} \sin^4 \theta + \left( Q_{66} + \frac{1}{2} Q_{12} \right) \sin^2 2\theta \\ \hat{Q}_{66} &= \frac{1}{4} (Q_{11} + Q_{22} - 2Q_{12}) \sin^2 2\theta + Q_{66} \cos^2 2\theta \end{aligned} \quad (2.26)$$

$$\hat{Q}_{12} = Q_{12} + \frac{1}{4} (Q_{11} + Q_{22} - 4Q_{66} - 2Q_{12}) \sin^2 2\theta$$

$$\hat{Q}_{16} = \frac{1}{4} (Q_{11} - Q_{22}) \sin 2\theta + \frac{1}{8} (Q_{11} + Q_{22} - 4Q_{66} - 2Q_{12}) \sin 4\theta$$

$$\hat{Q}_{26} = \frac{1}{4} (Q_{11} - Q_{22}) \sin 2\theta - \frac{1}{8} (Q_{11} + Q_{22} - 4Q_{66} - 2Q_{12}) \sin 4\theta$$

Since in this thesis a beam model is considered, there are two simplification cases that are further studied. In the first case it will be considered that  $\varepsilon_s = 0$  which can be achieved by

restraining the cross-section with some sort of boundary conditions. First case consideration leads to following relation:

$$\begin{Bmatrix} \sigma_z \\ \tau_{zs} \end{Bmatrix} = \begin{bmatrix} \widehat{Q}_{11} & \widehat{Q}_{16} \\ \widehat{Q}_{16} & \widehat{Q}_{66} \end{bmatrix} \begin{Bmatrix} \varepsilon_z \\ \gamma_{zs} \end{Bmatrix} \quad (2.27)$$

A more natural approach when considering a beam model, since it is not advisable nor practical to load a beam along the contour coordinate of the cross-section, is to consider that  $\sigma_s = 0$ . This is second case which will be elaborated in more detail:

$$\begin{Bmatrix} \sigma_z \\ 0 \\ \tau_{zs} \end{Bmatrix} = \begin{bmatrix} \widehat{Q}_{11} & \widehat{Q}_{12} & \widehat{Q}_{16} \\ \widehat{Q}_{12} & \widehat{Q}_{22} & \widehat{Q}_{26} \\ \widehat{Q}_{16} & \widehat{Q}_{26} & \widehat{Q}_{66} \end{bmatrix} \begin{Bmatrix} \varepsilon_z \\ \varepsilon_s \\ \gamma_{zs} \end{Bmatrix} \quad (2.28)$$

The expression from Eq. (2.28) can be condensed by replacing  $\varepsilon_s$  with a following expression:

$$\varepsilon_s = -\frac{\widehat{Q}_{12}}{\widehat{Q}_{22}} \varepsilon_z - \frac{\widehat{Q}_{26}}{\widehat{Q}_{22}} \gamma_{zs} \quad (2.29)$$

leading to following:

$$\begin{Bmatrix} \sigma_z \\ \tau_{zs} \end{Bmatrix} = \begin{bmatrix} \bar{Q}_{11} & \bar{Q}_{16} \\ \bar{Q}_{16} & \bar{Q}_{66} \end{bmatrix} \begin{Bmatrix} \varepsilon_z \\ \gamma_{zs} \end{Bmatrix} \quad (2.30)$$

where:

$$\bar{Q}_{11} = \widehat{Q}_{11} - \frac{\widehat{Q}_{12}^2}{\widehat{Q}_{22}}, \quad \bar{Q}_{66} = \widehat{Q}_{66} - \frac{\widehat{Q}_{26}^2}{\widehat{Q}_{22}}, \quad \bar{Q}_{16} = \widehat{Q}_{16} - \frac{\widehat{Q}_{12}\widehat{Q}_{26}}{\widehat{Q}_{22}} \quad (2.31)$$

As this is more natural approach when dealing with the beam model, the relation from Eq. (2.30) will be the primary constitutive relation used in this thesis, opposed to relation from Eq. (2.27), and for the  $k$ -th ply of the laminate the constitutive equation will be written in the following form:

$$\begin{Bmatrix} \sigma_{zk} \\ \tau_{zsk} \end{Bmatrix} = \begin{bmatrix} \bar{Q}_{11k} & \bar{Q}_{16k} \\ \bar{Q}_{16k} & \bar{Q}_{66k} \end{bmatrix} \begin{Bmatrix} e_z \\ e_{zs} \end{Bmatrix} \quad (2.32)$$

# 3 COMPOSITE THIN-WALLED BEAM

---

## 3.1 Basic assumptions

A beam is generally a deformable body in which the length of the beam is significantly greater than the dimensions of its cross-section. The cross-section itself can be either solid or thin-walled. A thin-walled beam is characterized by one dimension of the cross section (wall thickness) being much smaller than the others. Thin-walled beams can be further classified as open, closed, or combined based on the shape of their cross-section. In terms of the symmetry of the cross-section, three categories of thin-walled beams are distinguished: asymmetric, uniaxially symmetric and biaxially symmetric. In asymmetric cross sections, the center of gravity and the shear center do not coincide. In uniaxially symmetric cross sections, the shear center is located in the axis of symmetry, while in biaxially symmetric cross sections, the shear center is located in the center of the center of gravity.

The shear center is the point in the cross section at which the sum of the moments of all internal shear forces in bending must equal zero. It has been established that the shear center coincides with the torsion center [25]. The torsion center, on the other hand, is the point around which the cross-section rotates during twisting or torsion. Torsion can also occur in combination with bending or flexure. In the case of non-circular cross-sections, the cross-section experiences warping during torsion, resulting in axial displacements at different points within the cross-section [3]. These axial displacements occur due to the rotation of longitudinal phases and their sliding caused by shear or tangential stresses. When axial movements are unconstrained, all cross-sections can freely deform, resulting in primary tangential stresses. This scenario is known as clean, free, uniform, or St. Venant's torsion, where torsion occurs without bending [11].

However, if these movements are restricted in certain cross sections or if the torsional moment is changed along the beam, the cross sections cannot deform uniformly. As a result, the distances between individual points of the same fiber change, leading to the development of normal stresses. These normal stresses vary along the beam and across the height of the cross-section, giving rise to secondary tangential stresses. This type of torsion is referred to as non-uniform or Vlasov torsion, or torsion with restrained warping [5,12,13,46,60].

In beams with solid cross-sections, the impact of secondary tangential stresses can be disre-

garded due to their negligible warping. Similarly, in thin-walled beams with closed cross-sections, the considerable torsional rigidity swiftly dampens normal stresses resulting from limited warping. As a result, secondary tangential stresses can only locally reach higher magnitudes.

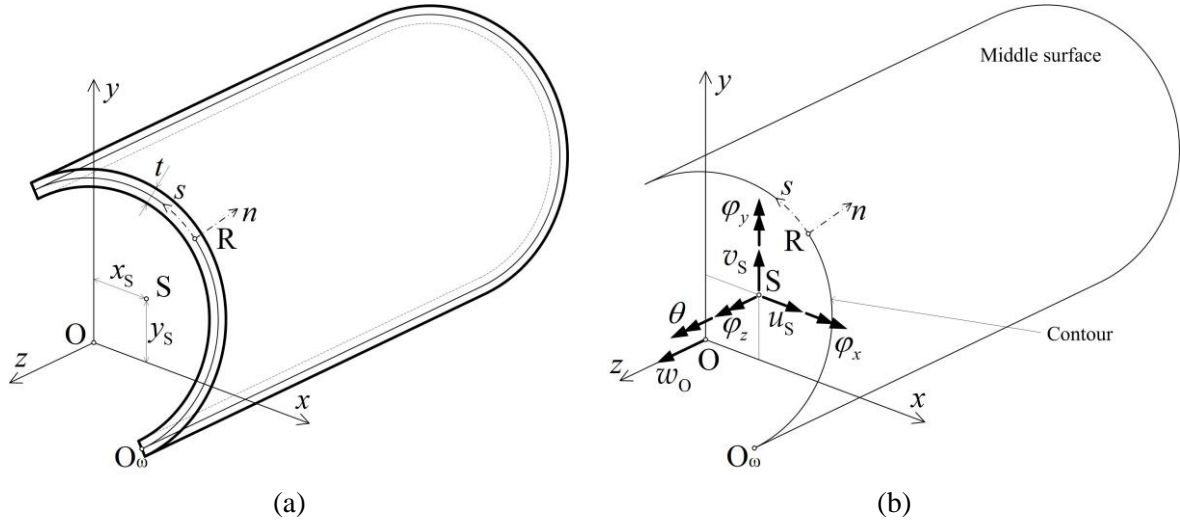


Fig. 3.1 Thin-walled beam with open cross-section: (a) full geometry, (b) middle surface with rigid-body displacements

In this thesis, the large deformation of a straight beam with an arbitrary open thin-walled composite cross-section is considered, as depicted in Fig. 3.1. A Cartesian coordinate system is chosen, where the  $x$ - and  $y$ -axes are aligned with the principal inertial axes of the cross-section, and the longitudinal  $z$ -axis is made to pass through the centroid  $O$  of each cross-section. The position coordinates  $x_s$  and  $y_s$  define the shear center  $S$  of the cross-section. The positions of the principal axes, centroid, and shear center are determined by material weighting.

The displacements of the cross-section are defined as follows: the rigid-body translations of the cross-section are denoted as  $w_O$ ,  $u_S$ , and  $v_S$ , while the rigid-body rotations of the cross-section are represented by  $\varphi_z$ ,  $\varphi_x$ , and  $\varphi_y$ , respectively. Additionally, the warping parameter  $\theta$  is taken into account. It should be noted that all displacement components are defined with respect to the shear center, except for the axial displacement  $w_O$ , which is defined with respect to the centroid. The cross-section is characterized by the contour coordinate  $s$  and the thickness coordinate  $n$ . The starting point of the contour coordinate  $s$ , referred to as the sector null point, is denoted as  $O_\omega$ . The contour coordinate pertains to the mid-surface of the beam.

The theory presented in this thesis is based on several assumptions:

- the projection of the contour in the  $(x, y)$  plane remains unchanged during the deformation process and behaves as a rigid body
- shear deformation caused by St. Venant's warping in the mid-surface is neglected
- shear deformations along the countur line are not equal to zero

- translations and rotations are allowed to be large, but strains are treated as small
- each ply in the composite laminate is assumed to be a thin, homogeneous and orthotropic plate with uniform material properties within the ply
- the plies are assumed to be perfectly bonded together, with no interfacial slippage or separation
- plane stress state in the ply
- the constitutive behavior of each ply is assumed to follow linear elastic principles, where stress is linearly related to strain
- the laminate is assumed to maintain a constant curvature during deformation, meaning that the individual plies remain flat and do not undergo large deformations
- the beam model will be defined for the symmetrical and balanced laminates

### 3.2 Kinematics of the beam

To accurately determine the deformations occurring under load in a thin-walled beam, a precise displacement field must be defined. Considering the beam model in this thesis, which takes into account large rotations, both linear and nonlinear displacement terms need to be included. The displacements are defined as functions of the longitudinal axis  $z$ :

$$\begin{aligned} w_o = w_o(z), \quad u_s = u_s(z), \quad v_s = v_s(z), \quad \varphi_z = \varphi_z(z), \\ \varphi_x = \varphi_x(z), \quad \varphi_y = \varphi_y(z), \quad \theta = \theta(z) \end{aligned} \quad (3.1)$$

while due to the shear deformations, rigid-body rotations are not perpendicular to the longitudinal axis  $z$ :

$$\varphi_x \neq -dv_s/dz, \quad \varphi_y \neq du_s/dz, \quad \theta \neq -d\varphi_z/dz \quad (3.2)$$

The linear displacement terms are given by the following expression, where  $\Omega$  represents the principal warping function:

$$\begin{aligned} w &= w_o + y \varphi_x - x \varphi_y + \Omega \theta \\ u &= u_s - (y - y_s) \varphi_z \\ v &= v_s + (x - x_s) \varphi_z \end{aligned} \quad (3.3)$$

To account for the large rotations, a nonlinear displacement field is necessary, resulting in the following expression:

$$W = w + \tilde{w}, \quad U = u + \tilde{u}, \quad V = v + \tilde{v} \quad (3.4)$$

where:

$$\begin{aligned}\tilde{w} &= \left[ \varphi_z \varphi_x (x - x_s) + \varphi_z \varphi_y (y - y_s) \right] / 2 \\ \tilde{u} &= \left[ \varphi_z^2 x_s + \varphi_x \varphi_y y - (\varphi_z^2 + \varphi_y^2) x \right] / 2 \\ \tilde{v} &= \left[ \varphi_z^2 y_s + \varphi_x \varphi_y x - (\varphi_z^2 + \varphi_x^2) y \right] / 2\end{aligned}\quad (3.5)$$

Due to the deformation of the thin-walled beam, the reference point R is displaced to the position of the reference point after deformation, denoted as R', as depicted in Fig. 3.2.

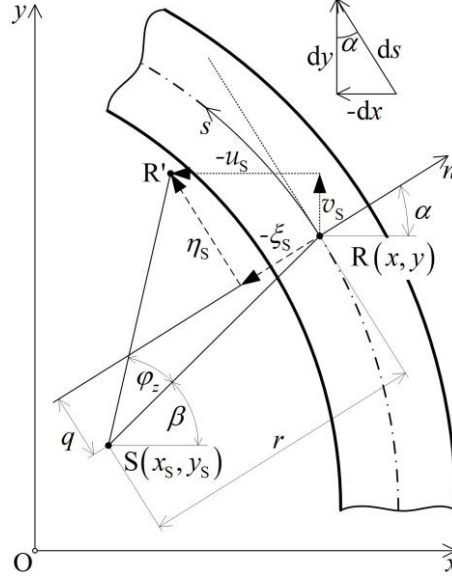


Fig. 3.2 Rigid-body displacements of a thin-walled cross-section

Then the displacement in the countour  $s$  direction can be expressed as:

$$\eta_s = v_s \cos \alpha - u_s \sin \alpha + \varphi_z r \quad (3.6)$$

where:

$$\sin \alpha = -dx/ds \quad \cos \alpha = dy/ds \quad r = d\Omega/ds \quad (3.7)$$

By substituting Eq. (3.7) into Eq. (3.6), the following expression is obtained:

$$\eta_s = v_s \frac{dy}{ds} + u_s \frac{dx}{ds} + \varphi_z \frac{d\Omega}{ds} \quad (3.8)$$

### 3.3 Deformations and strain tensor

Since it has been assumed that shear deformations along the contour line are not equal to zero ( $e_{zs} \neq 0$ ), the contour deformations will be expressed as follows:

$$e_{zs} (n=0) = \frac{\partial w}{\partial s} + \frac{\partial \eta_s}{\partial z} = \frac{dy}{ds} \varphi_x - \frac{dx}{ds} \varphi_y + \frac{d\Omega}{ds} \theta + \frac{dv_s}{dz} \frac{dy}{ds} + \frac{du_s}{dz} \frac{dx}{ds} + \frac{d\varphi_z}{dz} \frac{d\Omega}{ds} \quad (3.9)$$

which leads to:

$$e_{zs}(n=0) = \left( \frac{du_s}{dz} - \varphi_y \right) \frac{dx}{ds} + \left( \frac{dv_s}{dz} + \varphi_x \right) \frac{dy}{ds} + \left( \frac{d\varphi_z}{dz} + \theta \right) \frac{d\Omega}{ds} \quad (3.10)$$

Then the components due to the shear deformability in the main axis sytem  $(x, y)$  are:

$$e_{zx}^{SD} = du_s/dz - \varphi_y, \quad e_{zy}^{SD} = dv_s/dz + \varphi_x, \quad \theta^{SD} = d\varphi_z/dz + \theta \quad (3.11)$$

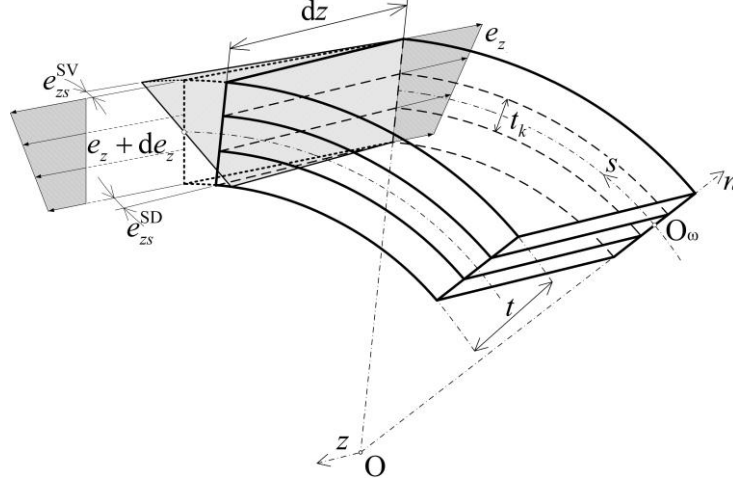


Fig. 3.3 Deformation of the composite thin-walled beam cut off

As assumed, shear deformation strains along the contour line  $s$  ( $e_{zs}^{SD}$ ) are constant along the thickness of the cross-section wall, which can be seen in Fig. 3.3. Although for contour line total shear strains are equal to shear deformation strains  $e_{zs}(n=0) = e_{zs}^{SD}$ , since the St. Venant strains are assumed zero for the contour line, as can be seen in Fig. 3.3. To obtain total shear strains, shear deformation strains and St. Venant strains need to be combined:

$$e_{zs} = e_{zs}^{SV} + e_{zs}^{SD} \quad (3.12)$$

To define St. Venant strains, the stress function  $\Psi$ , refined for the composite cross-section, will be used as defined by some authors [20,50]:

$$\Psi = -\bar{Q}_{66k} \theta (t^2/4 - n^2) \quad (3.13)$$

Function  $\Psi$  is stress based function, and St. Venant stresses can be obtained from it as follows:

$$\tau_{zs}^{SV} = -\partial\Psi/\partial n = 2\bar{Q}_{66k} \theta n \quad (3.14)$$

If the constitutive relation from the Eq. (2.32) is considered, and by ignoring the coupling term  $\bar{Q}_{16k}$  the following relation for the St. Venant strains can be obtained as follows:

$$e_{zs}^{SV} = 2\theta n \quad (3.15)$$



The presented model utilizes the Green-Lagrange strain tensor in order to account for the large rotations:

$$\varepsilon_{ij} = \frac{1}{2} \left[ (u_i + \tilde{u}_i)_{,j} + (u_j + \tilde{u}_j)_{,i} + (u_k + \tilde{u}_k)_{,i} (u_k + \tilde{u}_k)_{,j} \right] \approx e_{ij} + \eta_{ij} + \tilde{e}_{ij} \quad i, j, k = 1, 2, 3 \quad (3.16)$$

where:

$$e_{ij} = \frac{1}{2} (u_{i,j} + u_{j,i}), \quad \eta_{ij} = \frac{1}{2} (u_{k,i} u_{k,j}), \quad \tilde{e}_{ij} = \frac{1}{2} (\tilde{u}_{i,j} + \tilde{u}_{j,i}) \quad (3.17)$$

According to the first assumption from chapter 3.1, the following is valid:

$$\varepsilon_{11} = \varepsilon_x = 0, \quad \varepsilon_{22} = \varepsilon_y = 0, \quad 2\varepsilon_{12} = \gamma_{xy} = 0 \quad (3.18)$$

In Eq. (3.17)  $e_{ij}$  is a Cauchy strain tensor for which non zero components can be expressed as:

$$\begin{aligned} e_z &= \frac{\partial w}{\partial z} = \frac{dw_o}{dz} + y \frac{d\varphi_x}{dz} - x \frac{d\varphi_y}{dz} + \Omega \frac{d\theta}{dz} \\ e_{zs} &= e_{zx}^{SD} \frac{dx}{ds} + e_{zy}^{SD} \frac{dy}{ds} + \theta^{SD} \frac{d\Omega}{ds} + 2\theta n \end{aligned} \quad (3.19)$$

and components of shear strains in global reference system can be expressed as:

$$\begin{aligned} e_{zx} &= e_{zs} \frac{dx}{ds} = e_{zx}^{SD} \frac{dx}{ds} \frac{dx}{ds} + e_{zy}^{SD} \frac{dy}{ds} \frac{dx}{ds} + \theta^{SD} \frac{d\Omega}{ds} \frac{dx}{ds} + 2\theta n \frac{dx}{ds} \\ e_{zy} &= e_{zs} \frac{dy}{ds} = e_{zx}^{SD} \frac{dx}{ds} \frac{dy}{ds} + e_{zy}^{SD} \frac{dy}{ds} \frac{dy}{ds} + \theta^{SD} \frac{d\Omega}{ds} \frac{dy}{ds} + 2\theta n \frac{dy}{ds} \end{aligned} \quad (3.20)$$

From Eq. (3.17) the components of the  $\eta_{ij}$  tensor can be expressed as:

$$\begin{aligned} \eta_{33} = \eta_z &= \frac{1}{2} \left[ \left( \frac{\partial w}{\partial z} \right)^2 + \left( \frac{\partial u}{\partial z} \right)^2 + \left( \frac{\partial v}{\partial z} \right)^2 \right] = \frac{1}{2} \left\{ \left( \frac{dw_o}{dz} + y \frac{d\varphi_x}{dz} - x \frac{d\varphi_y}{dz} + \Omega \frac{d\theta}{dz} \right)^2 \right. \\ &\quad \left. + \left[ \frac{du_s}{dz} - (y - y_s) \frac{d\varphi_z}{dz} \right]^2 + \left[ \frac{dv_s}{dz} + (x - x_s) \frac{d\varphi_z}{dz} \right]^2 \right\} \\ 2\eta_{31} = \eta_{zx} &= \frac{\partial w}{\partial z} \frac{\partial w}{\partial x} + \frac{\partial u}{\partial z} \frac{\partial u}{\partial x} + \frac{\partial v}{\partial z} \frac{\partial v}{\partial x} \\ &= \left( \frac{dw_o}{dz} + y \frac{d\varphi_x}{dz} - x \frac{d\varphi_y}{dz} + \Omega \frac{d\theta}{dz} \right) \left( -\varphi_y + \frac{\partial \Omega}{\partial x} \theta \right) + \left[ \frac{dv_s}{dz} + (x - x_s) \frac{d\varphi_z}{dz} \right] \varphi_z \\ 2\eta_{32} = \eta_{zy} &= \frac{\partial w}{\partial z} \frac{\partial w}{\partial y} + \frac{\partial u}{\partial z} \frac{\partial u}{\partial y} + \frac{\partial v}{\partial z} \frac{\partial v}{\partial y} \\ &= \left( \frac{dw_o}{dz} + y \frac{d\varphi_x}{dz} - x \frac{d\varphi_y}{dz} + \Omega \frac{d\theta}{dz} \right) \left( \varphi_x + \frac{\partial \Omega}{\partial y} \theta \right) - \left[ \frac{du_s}{dz} - (y - y_s) \frac{d\varphi_z}{dz} \right] \varphi_z \end{aligned} \quad (3.21)$$

From Eq. (3.17) the components of the  $\tilde{e}_{ij}$  tensor can be expressed as:

$$\begin{aligned} \tilde{e}_{33} = \tilde{e}_z &= \frac{\partial \tilde{w}}{\partial z} = \frac{1}{2} \left[ (x-x_s) \left( \varphi_x \frac{d\varphi_z}{dz} + \varphi_z \frac{d\varphi_x}{dz} \right) + (y-y_s) \left( \varphi_y \frac{d\varphi_z}{dz} + \varphi_z \frac{d\varphi_y}{dz} \right) \right] \\ 2\tilde{e}_{31} = \tilde{e}_{zx} &= \frac{\partial \tilde{w}}{\partial x} + \frac{\partial \tilde{u}}{\partial z} = \frac{1}{2} \left[ \varphi_z \varphi_x - 2x\varphi_y \frac{d\varphi_y}{dz} - 2(x-x_s)\varphi_z \frac{d\varphi_z}{dz} + y \left( \varphi_x \frac{d\varphi_y}{dz} + \varphi_y \frac{d\varphi_x}{dz} \right) \right] \\ 2\tilde{e}_{32} = \tilde{e}_{zy} &= \frac{\partial \tilde{w}}{\partial y} + \frac{\partial \tilde{v}}{\partial z} = \frac{1}{2} \left[ \varphi_z \varphi_y - 2y\varphi_x \frac{d\varphi_x}{dz} - 2(y-y_s)\varphi_z \frac{d\varphi_z}{dz} + x \left( \varphi_x \frac{d\varphi_y}{dz} + \varphi_y \frac{d\varphi_x}{dz} \right) \right] \end{aligned} \quad (3.22)$$

### 3.4 Stress resultants-strain components relations for a cross-ply laminate

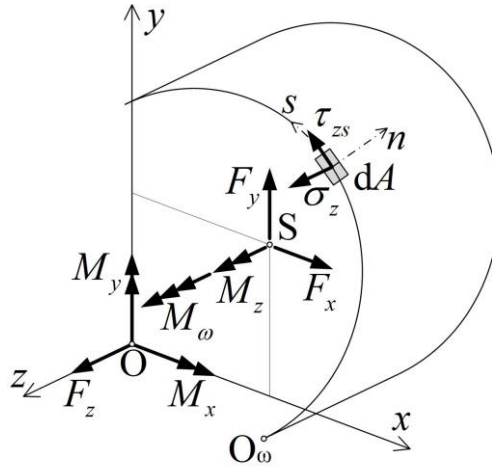


Fig. 3.4 Stress resultants of the cross-section

In the case of a cross-ply laminate, the constitutive equation for a single ply can be simplified from Eq. (2.32) to:

$$\begin{Bmatrix} \sigma_{zk} \\ \tau_{zsk} \end{Bmatrix} = \begin{bmatrix} \bar{Q}_{11k} & 0 \\ 0 & \bar{Q}_{66k} \end{bmatrix} \begin{Bmatrix} e_z \\ e_{zs} \end{Bmatrix} \quad (3.23)$$

Since  $\sigma_x = \sigma_y = \tau_{xy} = 0$ , the stress resultants can be defined as follows:

$$\begin{aligned} F_z &= \int_A \sigma_z dA, \quad F_x = \int_A \tau_{zx} dA, \quad F_y = \int_A \tau_{zy} dA, \quad M_x = \int_A \sigma_z y dA, \\ M_y &= -\int_A \sigma_z x dA, \quad M_\omega = \int_A \sigma_z \Omega dA, \quad M_z = T_{SV} + T_\omega + T_\sigma, \quad T_{SV} = -2 \int_A \Psi dA, \\ T_\omega &= \int_A \tau_{zs} r dA = \int_A \tau_{zs} \frac{d\Omega}{ds} dA, \quad T_\sigma = \bar{K} \frac{d\varphi}{dz}, \quad \bar{K} = \int_A \sigma_z \left[ (x-x_s)^2 + (y-y_s)^2 \right] dA \end{aligned} \quad (3.24)$$

In Eq. (3.24), the variables are defined as follows:  $F_z$  represents the axial force applied at the

centroid, while  $F_x$  and  $F_y$  denote the shear forces acting at the shear center in the  $x$  and  $y$  directions, respectively.  $M_z$  corresponds to the total torque with respect to the shear center, which is a combination of the Saint Venant torque  $T_{SV}$ , the warping torque  $T_\omega$ , and an additional torsional moment attributed to the Wagner's effect  $T_\sigma$ .  $M_x$  and  $M_y$  represent the bending moments around the  $x$  and  $y$  axes, respectively. Furthermore,  $M_\omega$  signifies the bimoment, and  $\bar{K}$  denotes the Wagner's coefficient.

In order to develop the beam theory for composite materials, which is similar to the beam theory for homogeneous materials, the concept of the reference moduli will be introduced. These moduli can be chosen arbitrarily, but in this study, we will calculate them using the following formula:

$$\bar{Q}_{11R} = \frac{1}{A} \int_{s-t/2}^{t/2} \int \bar{Q}_{11k} \, dn \, ds, \quad \bar{Q}_{66R} = \frac{1}{A} \int_{s-t/2}^{t/2} \int \bar{Q}_{66k} \, dn \, ds, \quad \bar{Q}_{16R} = \frac{1}{A} \int_{s-t/2}^{t/2} \int \bar{Q}_{16k} \, dn \, ds \quad (3.25)$$

Here, the cross-section surface is represented by  $A$ . By this principle, the classical cross-section properties can be weighted with these reference moduli to obtain the so-called modulus-weighted cross-section properties. It is worth noting that the reference moduli are constant for the entire cross-section, and therefore, they can be extracted from the surface integrals.

From Eq. (3.24) the expressions for the shear forces and twisting moment due to restrained warping, follow as:

$$\begin{aligned} F_x &= \int_A \tau_{zx} \, dA = \int_A \bar{Q}_{66k} \, e_{zx} \, dA \\ &= \bar{Q}_{66R} \int_s^N \sum_{k=1}^{n_k} \int_{n_{k-1}}^{n_k} \frac{\bar{Q}_{66k}}{\bar{Q}_{66R}} \left[ e_{zx}^{SD} \left( \frac{dx}{ds} \right)^2 + e_{zy}^{SD} \frac{dy}{ds} \frac{dx}{ds} + \theta^{SD} \frac{d\Omega}{ds} \frac{dx}{ds} + 2\theta n \frac{dx}{ds} \right] dn \, ds \\ F_y &= \int_A \tau_{zy} \, dA = \int_A \bar{Q}_{66k} \, e_{zy} \, dA \\ &= \bar{Q}_{66R} \int_s^N \sum_{k=1}^{n_k} \int_{n_{k-1}}^{n_k} \frac{\bar{Q}_{66k}}{\bar{Q}_{66R}} \left[ e_{zx}^{SD} \frac{dx}{ds} \frac{dy}{ds} + e_{zy}^{SD} \left( \frac{dy}{ds} \right)^2 + \theta^{SD} \frac{d\Omega}{ds} \frac{dy}{ds} + 2\theta n \frac{dy}{ds} \right] dn \, ds \\ T_\omega &= \int_A \tau_{zs} \frac{d\Omega}{ds} \, dA \\ &= \bar{Q}_{66R} \int_s^N \sum_{k=1}^{n_k} \int_{n_{k-1}}^{n_k} \frac{\bar{Q}_{66k}}{\bar{Q}_{66R}} \left( e_{zx}^{SD} \frac{dx}{ds} \frac{d\Omega}{ds} + e_{zy}^{SD} \frac{dy}{ds} \frac{d\Omega}{ds} + \theta^{SD} \left( \frac{d\Omega}{ds} \right)^2 + 2\theta n \frac{d\Omega}{ds} \right) dn \, ds \end{aligned} \quad (3.26)$$

where  $N$  represents the number of plies in the cross-section branch,  $n_k$  and  $n_{k-1}$  represent the thickness coordinate of the  $k$ -th ply, which will be described in one of the following subchapters.

Alternatively, if the matrix form without considering the impact of the St. Venant part (which

becomes zero when integrated over the thickness of the cross-section branch) is considered, the following form is obtained:

$$\begin{Bmatrix} F_x \\ F_y \\ T_\omega \end{Bmatrix} = \bar{Q}_{66R} \begin{bmatrix} A_x & A_{xy} & A_{x\omega} \\ A_{xy} & A_y & A_{y\omega} \\ A_{x\omega} & A_{y\omega} & A_\omega \end{bmatrix} \begin{Bmatrix} e_{zx}^{SD} \\ e_{zy}^{SD} \\ \theta^{SD} \end{Bmatrix} \quad (3.27)$$

where:

$$\begin{aligned} A_x &= \int_s \sum_{k=1}^N \int_{n_{k-1}}^{n_k} \frac{\bar{Q}_{66k}}{\bar{Q}_{66R}} \left( \frac{dx}{ds} \right)^2 dn ds, & A_y &= \int_s \sum_{k=1}^N \int_{n_{k-1}}^{n_k} \frac{\bar{Q}_{66k}}{\bar{Q}_{66R}} \left( \frac{dy}{ds} \right)^2 dn ds, \\ A_\omega &= \int_s \sum_{k=1}^N \int_{n_{k-1}}^{n_k} \frac{\bar{Q}_{66k}}{\bar{Q}_{66R}} \left( \frac{d\Omega}{ds} \right)^2 dn ds, & A_{xy} &= \int_s \sum_{k=1}^N \int_{n_{k-1}}^{n_k} \frac{\bar{Q}_{66k}}{\bar{Q}_{66R}} \frac{dx}{ds} \frac{dy}{ds} dn ds, \\ A_{x\omega} &= \int_s \sum_{k=1}^N \int_{n_{k-1}}^{n_k} \frac{\bar{Q}_{66k}}{\bar{Q}_{66R}} \frac{dx}{ds} \frac{d\Omega}{ds} dn ds, & A_{y\omega} &= \int_s \sum_{k=1}^N \int_{n_{k-1}}^{n_k} \frac{\bar{Q}_{66k}}{\bar{Q}_{66R}} \frac{dy}{ds} \frac{d\Omega}{ds} dn ds \end{aligned} \quad (3.28)$$

Further on, if the virtual elastic strain energy due to work of the shear stress resultants in the contour direction from Eq. (3.27) by the use of Eq. (3.19) and (3.23) is expressed, following is obtained:

$$\begin{aligned} \delta U_E^{SD} &= \int_0^l \int_s \sum_{k=1}^N \left( \int_{n_{k-1}}^{n_k} \tau_{zs}^{SD} \delta e_{zs}^{SD} dn \right) ds dz = \int_0^l \int_s \sum_{k=1}^N \left( \int_{n_{k-1}}^{n_k} \bar{Q}_{66k} e_{zs}^{SD} \delta e_{zs}^{SD} dn \right) ds dz \\ &= \int_0^l \bar{Q}_{66R} \int_s \sum_{k=1}^N \left[ \int_{n_{k-1}}^{n_k} \frac{\bar{Q}_{66k}}{\bar{Q}_{66R}} \left( e_{zx}^{SD} \frac{dx}{ds} + e_{zy}^{SD} \frac{dy}{ds} + \theta^{SD} \frac{d\Omega}{ds} \right) \right. \\ &\quad \left. \delta \left( e_{zx}^{SD} \frac{dx}{ds} + e_{zy}^{SD} \frac{dy}{ds} + \theta^{SD} \frac{d\Omega}{ds} \right) dn \right] ds dz \end{aligned} \quad (3.29)$$

$$\begin{aligned} \delta U_E^{SD} &= \int_0^l \bar{Q}_{66R} \left( A_x e_{zx}^{SD} \delta e_{zx}^{SD} + A_{xy} e_{zx}^{SD} \delta e_{zy}^{SD} + A_{x\omega} e_{zx}^{SD} \delta \theta^{SD} \right. \\ &\quad \left. + A_{xy} e_{zy}^{SD} \delta e_{zx}^{SD} + A_y e_{zy}^{SD} \delta e_{zy}^{SD} + A_{y\omega} e_{zy}^{SD} \delta \theta^{SD} \right. \\ &\quad \left. + A_{x\omega} \theta^{SD} \delta e_{zx}^{SD} + A_{y\omega} \theta^{SD} \delta e_{zy}^{SD} + A_\omega \theta^{SD} \delta \theta^{SD} \right) dz \end{aligned}$$

The shear stress resultants – shear strains relation from the Eq. (3.27) is easily connected to the form of the Eq. (3.29).

In order to demonstrate the need for a different approach, the virtual elastic strain energy for the homogeneous rectangle cross-section shown in Fig. 3.5 will be calculated. There is only one layer and the following is valid:

$$\bar{Q}_{66R} = \bar{Q}_{66k} = \bar{Q}_{66}, \quad dx/ds = -\sin(-90^\circ) = 1, \quad dy/ds = \cos(-90^\circ) = 0, \quad r = d\Omega/ds = 0 \quad (3.30)$$

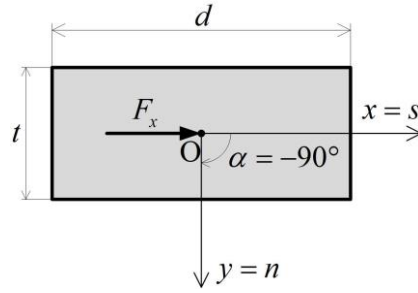


Fig. 3.5 Cross-section example

Then the constants from Eq. (3.28) can be calculated as:

$$A_x = \int_{-\frac{d}{2}}^{\frac{d}{2}} \int_{-\frac{t}{2}}^{\frac{t}{2}} \left( \frac{dx}{ds} \right)^2 dn ds = d t = A \quad (3.31)$$

$$A_y = A_{xy} = A_\omega = A_{x\omega} = A_{y\omega} = 0$$

From Eq. (3.31), the virtual elastic strain energy follows as:

$$\delta U_E^{SD} = \int_0^l A \bar{Q}_{66} e_{zx}^{SD} \delta e_{zx}^{SD} dz \quad (3.32)$$

and if the relation from the Eq. (3.27) is introduced:

$$\delta U_E^{SD} = \int_0^l \frac{F_x \delta F_x}{A \bar{Q}_{66}} dz \quad (3.33)$$

Since Eq. (3.33) assumes a uniform shear strain distribution along the contour line, and consequently a uniform shear stress distribution, it does not include the shear correction factor 6/5 for a rectangular cross-section. Thus, a more comprehensive approach is required to calculate the virtual elastic strain energy resulting from Vlasov's theory, which for a homogeneous cross-section gives a parabolic shear stress distribution [30,31,43,69], i.e.

$$\tau_{zs}^{SD} = \frac{F_y S_{x1}}{I_x t} + \frac{F_x S_{y1}}{I_y t} + \frac{T_\omega S_{\omega 1}}{I_\omega t} \quad (3.34)$$

where  $S_{x1}$ ,  $S_{y1}$  and  $S_{\omega 1}$  are the first area and sectorial moment for the part of the cross-section cut off, respectively.  $I_x$ ,  $I_y$  and  $I_\omega$  are the second area moments and the warping constant, respectively.

To derive the expression for the shear stress in the composite cross-section, the normal stress resultants for the composite cross-section need to be defined. By using Eqs. (3.19), (3.23) and (3.24), the axial force, the bending moments and the bimoment can be expressed as:

$$\begin{aligned}
 F_z &= \int \sum_{s=1}^N \int_{n_{k-1}}^{n_k} \bar{Q}_{11k} e_z dn ds = \bar{Q}_{11R} \int \sum_{s=1}^N \int_{n_{k-1}}^{n_k} \frac{\bar{Q}_{11k}}{\bar{Q}_{11R}} e_z dn ds \\
 &= \bar{Q}_{11R} \int \sum_{s=1}^N \int_{n_{k-1}}^{n_k} \frac{\bar{Q}_{11k}}{\bar{Q}_{11R}} \left( \frac{dw_o}{dz} + y \frac{d\varphi_x}{dz} - x \frac{d\varphi_y}{dz} + \Omega \frac{d\theta}{dz} \right) dn ds \\
 &= \bar{Q}_{11R} \left( A^* \frac{dw_o}{dz} + S_x^* \frac{d\varphi_x}{dz} - S_y^* \frac{d\varphi_y}{dz} + S_\omega^* \frac{d\theta}{dz} \right) \\
 M_x &= \int \sum_{s=1}^N \int_{n_{k-1}}^{n_k} \bar{Q}_{11k} e_z y dn ds = \bar{Q}_{11R} \int \sum_{s=1}^N \int_{n_{k-1}}^{n_k} \frac{\bar{Q}_{11k}}{\bar{Q}_{11R}} e_z y dn ds \\
 &= \bar{Q}_{11R} \int \sum_{s=1}^N \int_{n_{k-1}}^{n_k} \frac{\bar{Q}_{11k}}{\bar{Q}_{11R}} \left( y \frac{dw_o}{dz} + y^2 \frac{d\varphi_x}{dz} - xy \frac{d\varphi_y}{dz} + y \Omega \frac{d\theta}{dz} \right) dn ds \\
 &= \bar{Q}_{11R} \left( S_x^* \frac{dw_o}{dz} + I_x^* \frac{d\varphi_x}{dz} - I_{xy}^* \frac{d\varphi_y}{dz} + I_{y\omega}^* \frac{d\theta}{dz} \right) \\
 M_y &= - \int \sum_{s=1}^N \int_{n_{k-1}}^{n_k} \bar{Q}_{11k} e_z x dn ds = - \bar{Q}_{11R} \int \sum_{s=1}^N \int_{n_{k-1}}^{n_k} \frac{\bar{Q}_{11k}}{\bar{Q}_{11R}} e_z x dn ds \\
 &= \bar{Q}_{11R} \int \sum_{s=1}^N \int_{n_{k-1}}^{n_k} \frac{\bar{Q}_{11k}}{\bar{Q}_{11R}} \left( -x \frac{dw_o}{dz} - xy \frac{d\varphi_x}{dz} + x^2 \frac{d\varphi_y}{dz} - x \Omega \frac{d\theta}{dz} \right) dn ds \\
 &= \bar{Q}_{11R} \left( -S_y^* \frac{dw_o}{dz} - I_{xy}^* \frac{d\varphi_x}{dz} + I_y^* \frac{d\varphi_y}{dz} - I_{x\omega}^* \frac{d\theta}{dz} \right) \\
 M_\omega &= \int \sum_{s=1}^N \int_{n_{k-1}}^{n_k} \bar{Q}_{11k} e_z \Omega dn ds = \bar{Q}_{11R} \int \sum_{s=1}^N \int_{n_{k-1}}^{n_k} \frac{\bar{Q}_{11k}}{\bar{Q}_{11R}} e_z \Omega dn ds \\
 &= \bar{Q}_{11R} \int \sum_{s=1}^N \int_{n_{k-1}}^{n_k} \frac{\bar{Q}_{11k}}{\bar{Q}_{11R}} \left( \Omega \frac{dw_o}{dz} + y \Omega \frac{d\varphi_x}{dz} - x \Omega \frac{d\varphi_y}{dz} + \Omega^2 \frac{d\theta}{dz} \right) dn ds \\
 &= \bar{Q}_{11R} \left( S_\omega^* \frac{dw_o}{dz} + I_{y\omega}^* \frac{d\varphi_x}{dz} - I_{x\omega}^* \frac{d\varphi_y}{dz} + I_\omega^* \frac{d\theta}{dz} \right)
 \end{aligned} \tag{3.35}$$

where  $A^*$  is the modulus-weighted cross-sectional area.  $S_x^*$  and  $S_y^*$  are the modulus-weighted first area moments,  $S_\omega^*$  is the modulus-weighted first sectorial moment.  $I_x^*$ ,  $I_y^*$  and  $I_{xy}^*$  are the modulus-weighted second area moments,  $I_{x\omega}^*$  and  $I_{y\omega}^*$  are the modulus-weighted second sectorial moments,  $I_\omega^*$  is the modulus-weighted warping constant. Furthermore, in the above equations  $dw_o/dz$ ,  $d\varphi_x/dz$ ,  $d\varphi_y/dz$  and  $d\theta/dz$  should be recognised as the generalised deformations, respectively.

When the  $x$ - and  $y$ -axes are the principal ones, and if the warping function is defined for the

principal pole and the principal origin, the following is valid:

$$S_x^* = S_y^* = I_{xy}^* = S_\omega^* = I_{x\omega}^* = I_{y\omega}^* = 0 \quad (3.36)$$

In such a case, the generalised deformations from Eq. (3.35) can be rewritten as:

$$\frac{dw_O}{dz} = \frac{F_z}{\bar{Q}_{11R} A^*}, \quad \frac{d\varphi_x}{dz} = \frac{M_x}{\bar{Q}_{11R} I_x^*}, \quad \frac{d\varphi_y}{dz} = \frac{M_y}{\bar{Q}_{11R} I_y^*}, \quad \frac{d\theta}{dz} = \frac{M_\omega}{\bar{Q}_{11R} I_\omega^*} \quad (3.37)$$

and the reference normal stress can be expressed as:

$$\sigma_{zR} = \bar{Q}_{11R} e_z = \frac{F_z}{A^*} + \frac{M_x}{I_x^*} y - \frac{M_y}{I_y^*} x + \frac{M_\omega}{I_\omega^*} \Omega \quad (3.38)$$

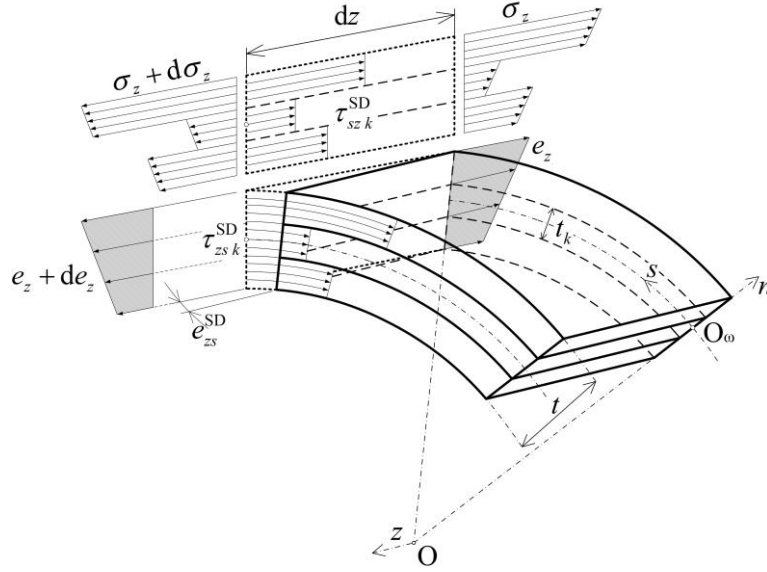


Fig. 3.6 Stresses and strains of the composite thin-walled beam cut off

According to Fig. 3.6 and Eq. (3.23), the reference shear stress  $\tau_{zsR}^{SD}(s, z)$  over the thickness  $t$  is:

$$\sum_{k=1}^N \tau_{zsR}^{SD} t_k = \sum_{k=1}^N \tau_{zsR}^{SD} t_k = \bar{Q}_{66R} e_{zs}^{SD} \sum_{k=1}^N \left[ \frac{\bar{Q}_{66k}}{\bar{Q}_{66R}} (n_k - n_{k-1}) \right] = \tau_{zsR}^{SD} \hat{A}_{66} \quad (3.39)$$

where:

$$\tau_{zsR}^{SD} = \bar{Q}_{66R} e_{zs}^{SD}, \quad \hat{A}_{66} = \sum_{k=1}^N \left[ \frac{\bar{Q}_{66k}}{\bar{Q}_{66R}} (n_k - n_{k-1}) \right] \quad (3.40)$$

Since the boundary condition at a free edge of the cross-section is

$$\tau_{zsR}^{SD}(0, z) = 0 \quad (3.41)$$

the equilibrium condition in the  $z$ -direction for the part of the cross-section cut off at  $s$ , Fig. 3.6, yields:

$$\int_0^s \left( \sum_{k=1}^N \int_{n_{k-1}}^{n_k} d\sigma_{zR} \frac{\bar{Q}_{11k}}{\bar{Q}_{11R}} dn \right) ds = \tau_{zsR}^{SD} \hat{A}_{66} dz \quad (3.42)$$

After introducing Eq. (3.38), it follows:

$$\int_0^s \left[ \sum_{k=1}^N \int_{n_{k-1}}^{n_k} \frac{\bar{Q}_{11k}}{\bar{Q}_{11R}} \left( \frac{dF_z}{A^*} + \frac{dM_x}{I_x^*} y - \frac{dM_y}{I_y^*} x + \frac{dM_\omega}{I_\omega^*} \Omega \right) dn \right] ds = \tau_{zsR}^{SD} \hat{A}_{66} dz \quad (3.43)$$

i.e.

$$\frac{dF_z}{dz} \frac{A_1^*}{A^*} + \frac{dM_x}{dz} \frac{S_{x1}^*}{I_x^*} - \frac{dM_y}{dz} \frac{S_{y1}^*}{I_y^*} + \frac{dM_\omega}{dz} \frac{S_{\omega 1}^*}{I_\omega^*} = \tau_{zsR}^{SD} \hat{A}_{66} \quad (3.44)$$

Since the following equilibrium conditions are valid:

$$\frac{dF_z}{dz} = 0; \quad \frac{dM_x}{dz} = F_y; \quad \frac{dM_y}{dz} = -F_x; \quad \frac{dM_\omega}{dz} = T_\omega \quad (3.45)$$

the reference shear stress  $\tau_{zsR}^{SD}$  from Eq. (3.43) can be expressed as:

$$\tau_{zsR}^{SD} = \frac{F_y S_{x1}^*}{I_x^* \hat{A}_{66}} + \frac{F_x S_{y1}^*}{I_y^* \hat{A}_{66}} + \frac{T_\omega S_{\omega 1}^*}{I_\omega^* \hat{A}_{66}} \quad (3.46)$$

It should be noted that, respectively,  $S_{x1}^*$ ,  $S_{y1}^*$  and  $S_{\omega 1}^*$  are the modulus-weighted first area and sectorial moments for the part of the cross-section cut off at  $s$ .

By utilizing Eqs. (3.23), (3.40) and (3.46), the virtual elastic strain energy of the beam shown in Fig. 3.1, resulting from the shear deformability, can be expressed as follows:

$$\begin{aligned} \delta U_E^{SD} &= \int_0^l \int_s \sum_{k=1}^N \left( \int_{n_{k-1}}^{n_k} \tau_{zs}^{SD} \delta e_{zs}^{SD} dn \right) ds dz = \int_0^l \int_s \sum_{k=1}^N \left( \int_{n_{k-1}}^{n_k} \bar{Q}_{66k} e_{zs}^{SD} \delta e_{zs}^{SD} dn \right) ds dz \\ &= \int_0^l \frac{1}{\bar{Q}_{66R}} \int_s \sum_{k=1}^N \left( \int_{n_{k-1}}^{n_k} \frac{\bar{Q}_{66k}}{\bar{Q}_{66R}} \tau_{zsR}^{SD} \delta \tau_{zsR}^{SD} dn \right) ds dz \end{aligned} \quad (3.47)$$

i.e.

$$\begin{aligned} \delta U_E^{SD} &= \int_0^l \frac{1}{\bar{Q}_{66R}} \left[ \frac{k_x}{A^*} F_x \delta F_x + \frac{k_{xy}}{A^*} F_x \delta F_y + \frac{k_{x\omega}}{\sqrt{A^* I_t^*}} F_x \delta T_\omega \right. \\ &\quad \left. + \frac{k_{xy}}{A^*} F_y \delta F_x + \frac{k_y}{A^*} F_y \delta F_y + \frac{k_{y\omega}}{\sqrt{A^* I_t^*}} F_y \delta T_\omega \right. \\ &\quad \left. + \frac{k_{x\omega}}{\sqrt{A^* I_t^*}} T_\omega \delta F_x + \frac{k_{y\omega}}{\sqrt{A^* I_t^*}} T_\omega \delta F_y + \frac{k_\omega}{I_t^*} T_\omega \delta T_\omega \right] dz \end{aligned} \quad (3.48)$$



where, respectively,  $k_x$ ,  $k_y$ ,  $k_\omega$ ,  $k_{xy}$ ,  $k_{x\omega}$  and  $k_{y\omega}$  are the shear correction factors defined as:

$$\begin{aligned}
 k_x &= \frac{A^*}{(I_y^*)^2 \widehat{A}_{66s}} \int (S_{y1}^*)^2 ds, & k_y &= \frac{A^*}{(I_x^*)^2 \widehat{A}_{66s}} \int (S_{x1}^*)^2 ds \\
 k_{xy} &= \frac{A^*}{I_x^* I_y^* \widehat{A}_{66s}} \int S_{x1}^* S_{y1}^* ds, & k_\omega &= \frac{I_t^*}{(I_\omega^*)^2 \widehat{A}_{66s}} \int (S_{\omega 1}^*)^2 ds \\
 k_{x\omega} &= \frac{\sqrt{A^* I_t^*}}{I_y^* I_\omega^* \widehat{A}_{66s}} \int S_{y1}^* S_{\omega 1}^* ds, & k_{y\omega} &= \frac{\sqrt{A^* I_t^*}}{I_x^* I_\omega^* \widehat{A}_{66s}} \int S_{x1}^* S_{\omega 1}^* ds
 \end{aligned} \tag{3.49}$$

Similar to Eq. (3.29), the relationship between shear strain and shear stress resultants can be readily derived from Eq. (3.48):

$$\begin{Bmatrix} e_{zx}^{SD} \\ e_{zy}^{SD} \\ \theta^{SD} \end{Bmatrix} = \frac{1}{\bar{Q}_{66R}} \begin{bmatrix} \frac{k_x}{A^*} & \frac{k_{xy}}{A^*} & \frac{k_{x\omega}}{\sqrt{A^* I_t^*}} \\ \frac{k_{xy}}{A^*} & \frac{k_y}{A^*} & \frac{k_{y\omega}}{\sqrt{A^* I_t^*}} \\ \frac{k_{x\omega}}{\sqrt{A^* I_t^*}} & \frac{k_{y\omega}}{\sqrt{A^* I_t^*}} & \frac{k_\omega}{I_t^*} \end{bmatrix} \begin{Bmatrix} F_x \\ F_y \\ T_\omega \end{Bmatrix} \tag{3.50}$$

If the shear stress resultants are expressed in terms of shear strains, the inverse relationship is obtained:

$$\begin{Bmatrix} F_x \\ F_y \\ T_\omega \end{Bmatrix} = \bar{Q}_{66R} \begin{bmatrix} \frac{A^*}{K_x} & \frac{A^*}{K_{xy}} & \frac{\sqrt{A^* I_t^*}}{K_{x\omega}} \\ \frac{A^*}{K_{xy}} & \frac{A^*}{K_y} & \frac{\sqrt{A^* I_t^*}}{K_{y\omega}} \\ \frac{\sqrt{A^* I_t^*}}{K_{x\omega}} & \frac{\sqrt{A^* I_t^*}}{K_{y\omega}} & \frac{I_t^*}{K_\omega} \end{bmatrix} \begin{Bmatrix} e_{zx}^{SD} \\ e_{zy}^{SD} \\ \theta^{SD} \end{Bmatrix} \tag{3.51}$$

where:

$$\begin{bmatrix} \frac{A^*}{K_x} & \frac{A^*}{K_{xy}} & \frac{\sqrt{A^* I_t^*}}{K_{x\omega}} \\ \frac{A^*}{K_{xy}} & \frac{A^*}{K_y} & \frac{\sqrt{A^* I_t^*}}{K_{y\omega}} \\ \frac{\sqrt{A^* I_t^*}}{K_{x\omega}} & \frac{\sqrt{A^* I_t^*}}{K_{y\omega}} & \frac{I_t^*}{K_\omega} \end{bmatrix} = \begin{bmatrix} \frac{k_x}{A^*} & \frac{k_{xy}}{A^*} & \frac{k_{x\omega}}{\sqrt{A^* I_t^*}} \\ \frac{k_{xy}}{A^*} & \frac{k_y}{A^*} & \frac{k_{y\omega}}{\sqrt{A^* I_t^*}} \\ \frac{k_{x\omega}}{\sqrt{A^* I_t^*}} & \frac{k_{y\omega}}{\sqrt{A^* I_t^*}} & \frac{k_\omega}{I_t^*} \end{bmatrix}^{-1} \quad (3.52)$$

To check if this approach solves the exact virtual elastic strain energy for the cross-section from Fig. 3.5, first some constants need to be defined:

$$\bar{Q}_{66R} = \bar{Q}_{66k} = \bar{Q}_{66}, \quad A^* = A, \quad \hat{A}_{66} = t, \quad I_x^* = I_x = \frac{dt^3}{12}, \quad I_y^* = I_y = \frac{td^3}{12} \quad (3.53)$$

also, although not true, for the sake of simplicity it will be considered that:

$$S_x^* = S_x = S_\omega^* = S_\omega = 0 \quad (3.54)$$

Now the first area moment for the  $y$  axis need to be defined as the function of the  $x$  coordinate:

$$S_y^*(x) = S_y(x) = \int_A x dA = t \int_{-d/2}^{d/2} x dx = t \frac{x^2}{2} + C \quad (3.55)$$

and if the condition that first area moment for the free edge is zero is introduced, the constant  $C$  is obtained as:

$$S_y\left(-\frac{d}{2}\right) = S_y\left(\frac{d}{2}\right) = 0 = t \frac{\left(-\frac{d}{2}\right)^2}{2} + C \quad (3.56)$$

$$C = -\frac{d^2 t}{8}$$

Now the shear correction factors from Eq. (3.49) can be calculated as follows:

$$k_x = \frac{A}{t^2 d^6} \int_{-d/2}^{d/2} [S_y(x)]^2 dx = \frac{144}{t^2 d^5} \int_{-d/2}^{d/2} \left( t \frac{x^2}{2} - \frac{d^2 t}{8} \right)^2 dx \quad (3.57)$$

$$k_x = \frac{144}{t^2 d^5} \int_{-d/2}^{d/2} \left( t^2 \frac{x^4}{4} - \frac{x^2 d^2 t^2}{8} + \frac{d^4 t^2}{64} \right) dx = \frac{144}{t^2 d^5} \left( t^2 \frac{x^5}{20} - \frac{x^3 d^2 t^2}{24} + \frac{d^4 t^2 x}{64} \right) \Big|_{-d/2}^{d/2}$$

$$k_x = \frac{144}{t^2 d^5} \left[ \frac{t^2}{20} \left( \frac{d^5}{32} - \frac{-d^5}{32} \right) - \frac{d^2 t^2}{24} \left( \frac{d^3}{8} - \frac{-d^3}{8} \right) + \frac{d^4 t^2}{64} \left( \frac{d}{2} - \frac{-d}{2} \right) \right]$$

$$k_x = \frac{144}{t^2 d^5} \left[ \frac{t^2 d^5}{320} - \frac{t^2 d^5}{96} + \frac{t^2 d^5}{64} \right] = \frac{144(3-10+15)}{960} = \frac{1152}{960} = \frac{6}{5}$$

$$k_y = k_{xy} = k_\omega = k_{x\omega} = k_{y\omega} = 0$$

and from there, the virtual elastic strain energy follow from Eq. (3.48) as:

$$\delta U_E^{SD} = \int_0^l k_x \frac{F_x \delta F_x}{A \bar{Q}_{66}} dz = \int_0^l \frac{6}{5} \frac{F_x \delta F_x}{A \bar{Q}_{66}} dz \quad (3.58)$$

Upon comparing the virtual elastic strain energy expressions from Eq. (3.33) and (3.58), it is evident that the former, which does not accurately account for shear stresses, exhibits a difference of 20% when compared to the latter.

Furthermore, the St. Venant torsional moment can be defined by using Eq. (3.24), and by utilizing Eqs. (3.13) and (3.23), the following expression is obtained:

$$T_{SV} = -2 \int \sum_{s=1}^N \int_{n_{k-1}}^{n_k} \Psi dn ds = -\bar{Q}_{66R} \theta I_t^* \quad (3.59)$$

where torsional constant is calculated in the following way:

$$I_t^* = -2 \int \sum_{s=1}^N \int_{n_{k-1}}^{n_k} \frac{\bar{Q}_{66k}}{\bar{Q}_{66R}} \left( \frac{t^2}{4} - n^2 \right) dn ds \quad (3.60)$$

As a secondary effect arising from the warping of the cross-section, an additional torsional moment occurs due to normal stresses. This phenomenon is referred to as the Wagner's effect, and it gives rise to what is known as pure torsional buckling in the thin-walled beams. However, in the case of solid cross-section beams, the Wagner's effect is commonly neglected. The value of this secondary torsional moment can be expressed as follows:

$$T_\sigma = \bar{K} \frac{d\varphi}{dz} \quad (3.61)$$

By utilizing Eqs. (3.23) and (3.24), the Wagner's coefficient can be expressed as follows:

$$\bar{K} = \int \sum_{s=1}^N \int_{n_{k-1}}^{n_k} \bar{Q}_{11k} e_z \left[ (x-x_s)^2 + (y-y_s)^2 \right] dn ds \quad (3.62)$$

and if the Eq. (3.38) is introduced the following is obtained:

$$\bar{K} = \int \sum_{s=1}^N \int_{n_{k-1}}^{n_k} \frac{\bar{Q}_{11k}}{\bar{Q}_{11R}} \sigma_{zR} \left[ (x-x_s)^2 + (y-y_s)^2 \right] dn ds \quad (3.63)$$

$$= F_z \alpha_z + M_x \alpha_x + M_y \alpha_y + M_\omega \alpha_\omega$$

where:

$$\begin{aligned}
 \alpha_z &= \frac{I_x^* + I_y^*}{A^*} + x_s^2 + y_s^2, \\
 \alpha_x &= \frac{1}{I_x^*} \int \sum_{s=1}^N \int_{n_{k-1}}^{n_k} \frac{\bar{Q}_{11k}}{\bar{Q}_{11R}} (x^2 y + y^3) dn ds - 2y_s, \\
 \alpha_y &= -\frac{1}{I_y^*} \int \sum_{s=1}^N \int_{n_{k-1}}^{n_k} \frac{\bar{Q}_{11k}}{\bar{Q}_{11R}} (x^3 + xy^2) dn ds + 2x_s, \\
 \alpha_\omega &= \frac{1}{I_\omega^*} \int \sum_{s=1}^N \int_{n_{k-1}}^{n_k} \frac{\bar{Q}_{11k}}{\bar{Q}_{11R}} (x^2 + y^2) \Omega dn ds
 \end{aligned} \tag{3.64}$$

### 3.5 Stress resultants-strain components relations for a angle ply laminate

By considering only the coupling between the normal stress resultants and the St. Venant torsional moment, the axial force, bending moments, and bimoment can be expressed by using Eqs. (2.32), (3.19) and (3.24) as follows:

$$\begin{aligned}
 F_z &= \int \sum_{s=1}^N \int_{n_{k-1}}^{n_k} (\bar{Q}_{11k} e_z + \bar{Q}_{16k} e_{zs}^{SV}) dn ds \\
 &= \bar{Q}_{11R} \left( A^* \frac{dw_0}{dz} + S_x^* \frac{d\varphi_x}{dz} - S_y^* \frac{d\varphi_y}{dz} + S_\omega^* \frac{d\theta}{dz} \right) + 2\bar{Q}_{16R} E_{15} \theta \\
 M_x &= \int \sum_{s=1}^N \int_{n_{k-1}}^{n_k} (\bar{Q}_{11k} e_z y + \bar{Q}_{16k} e_{zs}^{SV} y) dn ds \\
 &= \bar{Q}_{11R} \left( S_x^* \frac{dw_0}{dz} + I_x^* \frac{d\varphi_x}{dz} - I_{xy}^* \frac{d\varphi_y}{dz} + I_{y\omega}^* \frac{d\theta}{dz} \right) + 2\bar{Q}_{16R} E_{25} \theta \\
 M_y &= -\int \sum_{s=1}^N \int_{n_{k-1}}^{n_k} (\bar{Q}_{11k} e_z x + \bar{Q}_{16k} e_{zs}^{SV} x) dn ds \\
 &= \bar{Q}_{11R} \left( -S_y^* \frac{dw_0}{dz} - I_{xy}^* \frac{d\varphi_x}{dz} + I_y^* \frac{d\varphi_y}{dz} - I_{x\omega}^* \frac{d\theta}{dz} \right) - 2\bar{Q}_{16R} E_{35} \theta \\
 M_\omega &= \int \sum_{s=1}^N \int_{n_{k-1}}^{n_k} (\bar{Q}_{11k} e_z \Omega + \bar{Q}_{16k} e_{zs}^{SV} \Omega) dn ds \\
 &= \bar{Q}_{11R} \left( S_\omega^* \frac{dw_0}{dz} + I_{y\omega}^* \frac{d\varphi_x}{dz} - I_{x\omega}^* \frac{d\varphi_y}{dz} + I_\omega^* \frac{d\theta}{dz} \right) + 2\bar{Q}_{16R} E_{45} \theta
 \end{aligned} \tag{3.65}$$

$$\begin{aligned}
 T_{SV} &= \int \sum_{s=1}^N \int_{n_{k-1}}^{n_k} (2\Psi + \bar{Q}_{16k} e_z n) dn ds \\
 &= -\bar{Q}_{66R} \theta I_t^* + \bar{Q}_{16R} E_{15} \frac{dw_o}{dz} + \bar{Q}_{16R} E_{25} \frac{d\varphi_x}{dz} - \bar{Q}_{16R} E_{35} \frac{d\varphi_y}{dz} + \bar{Q}_{16R} E_{45} \frac{d\theta}{dz}
 \end{aligned}$$

where:

$$\begin{aligned}
 E_{15} &= \int \sum_{s=1}^N \int_{n_{k-1}}^{n_k} \frac{\bar{Q}_{16k}}{\bar{Q}_{16R}} n dn ds, & E_{25} &= \int \sum_{s=1}^N \int_{n_{k-1}}^{n_k} \frac{\bar{Q}_{16k}}{\bar{Q}_{16R}} n y dn ds \\
 E_{35} &= \int \sum_{s=1}^N \int_{n_{k-1}}^{n_k} \frac{\bar{Q}_{16k}}{\bar{Q}_{16R}} n x dn ds, & E_{45} &= \int \sum_{s=1}^N \int_{n_{k-1}}^{n_k} \frac{\bar{Q}_{16k}}{\bar{Q}_{16R}} n \Omega dn ds
 \end{aligned} \tag{3.66}$$

This relation between normal stress resultants and strains will be categorized as Euler-Bernouli (EB) relation, which in matrix form will have the following expression:

$$\begin{Bmatrix} F_z \\ M_x \\ M_y \\ M_\omega \\ T_{SV} \end{Bmatrix} = \mathbf{Q}^{EB} \begin{Bmatrix} dw_o/dz \\ d\varphi_x/dz \\ d\varphi_y/dz \\ d\theta/dz \\ 2\theta \end{Bmatrix}, \quad \mathbf{Q}^{EB} = \begin{bmatrix} \bar{Q}_{11R} A^* & 0 & 0 & 0 & \bar{Q}_{16R} E_{15} \\ 0 & \bar{Q}_{11R} I_x^* & 0 & 0 & \bar{Q}_{16R} E_{25} \\ 0 & 0 & \bar{Q}_{11R} I_y^* & 0 & -\bar{Q}_{16R} E_{35} \\ 0 & 0 & 0 & \bar{Q}_{11R} I_\omega^* & \bar{Q}_{16R} E_{45} \\ \bar{Q}_{16R} E_{15} & \bar{Q}_{16R} E_{25} & -\bar{Q}_{16R} E_{35} & \bar{Q}_{16R} E_{45} & -\frac{1}{2} \bar{Q}_{66R} I_t^* \end{bmatrix} \tag{3.67}$$

The relation between shear stress resultants and shear strain from Eq. (3.51) will be categorized as shear deformable (SD) relation, which in matrix form will be written as:

$$\begin{Bmatrix} F_x \\ F_y \\ T_\omega \end{Bmatrix} = \mathbf{Q}^{SD} \begin{Bmatrix} e_{zx}^{SD} \\ e_{zy}^{SD} \\ \theta^{SD} \end{Bmatrix}, \quad \mathbf{Q}^{SD} = \bar{Q}_{66R} \begin{bmatrix} \frac{A^*}{K_x} & \frac{A^*}{K_{xy}} & \frac{\sqrt{A^* I_t^*}}{K_{x\omega}} \\ \frac{A^*}{K_{xy}} & \frac{A^*}{K_y} & \frac{\sqrt{A^* I_t^*}}{K_{y\omega}} \\ \frac{\sqrt{A^* I_t^*}}{K_{x\omega}} & \frac{\sqrt{A^* I_t^*}}{K_{y\omega}} & \frac{I_t^*}{K_\omega} \end{bmatrix} \tag{3.68}$$

To obtain the couplings between the EB and SD stress resultants and strains, the virtual elastic energy principle will be employed, by using Eq. (2.32), similar to procedure used to obtain Eq. (3.50):

$$\begin{aligned}
 \delta U_E^{CO} &= \int_0^l \int \sum_{s=1}^N \left[ \int_{n_{k-1}}^{n_k} (\bar{Q}_{16k} e_{zs}^{SD} \delta e_z + \bar{Q}_{16k} e_z \delta e_{zs}^{SD}) dn \right] ds dz = \delta U_E^{COL} + \delta U_E^{COR} \\
 \delta U_E^{COL} &= \int_0^l \int \sum_{s=1}^N \left( \int_{n_{k-1}}^{n_k} \bar{Q}_{16k} e_{zs}^{SD} \delta e_z dn \right) ds dz = \int_0^l \int \sum_{s=1}^N \left[ \int_{n_{k-1}}^{n_k} \left( \bar{Q}_{16R} \frac{\bar{Q}_{16k}}{\bar{Q}_{16R}} \frac{\tau_{zsR}^{SD}}{\bar{Q}_{66R}} \delta \frac{\sigma_{zR}}{\bar{Q}_{11R}} \right) dn \right] ds dz
 \end{aligned} \tag{3.69}$$

$$\delta U_E^{\text{COL}} = \int_0^l \frac{\bar{Q}_{16R}}{\bar{Q}_{11R} \bar{Q}_{66R}} \int \sum_{s=1}^N \left[ \int_{n_{k-1}}^{n_k} \left( \frac{\bar{Q}_{16k}}{\bar{Q}_{16R}} \tau_{zsR}^{\text{SD}} \delta \sigma_{zR} \right) dn \right] ds dz$$

By introducing the Eq. (3.38) and (3.46) following is obtained:

$$\begin{aligned} \delta U_E^{\text{COL}} &= \int_0^l \frac{\bar{Q}_{16R}}{\bar{Q}_{11R} \bar{Q}_{66R}} \int \sum_{s=1}^N \left[ \int_{n_{k-1}}^{n_k} \left( \frac{\bar{Q}_{16k}}{\bar{Q}_{16R}} \tau_{zsR}^{\text{SD}} \delta \sigma_{zR} \right) dn \right] ds dz \\ &= \int_0^l \frac{\bar{Q}_{16R}}{\bar{Q}_{11R} \bar{Q}_{66R}} \left( \frac{k_{61}}{A^*} F_x \delta F_z + \frac{k_{71}}{A^*} F_y \delta F_z + \frac{k_{81}}{\sqrt{A^* I_t^*}} T_\omega \delta F_z \right. \\ &\quad + \frac{k_{62}}{\sqrt{A^* I_t^*}} F_x \delta M_x + \frac{k_{72}}{\sqrt{A^* I_t^*}} F_y \delta M_x + \frac{k_{82}}{I_x^*} T_\omega \delta M_x \\ &\quad - \frac{k_{63}}{\sqrt{A^* I_t^*}} F_x \delta M_y - \frac{k_{73}}{\sqrt{A^* I_t^*}} F_y \delta M_y - \frac{k_{83}}{I_y^*} T_\omega \delta M_y \\ &\quad \left. + \frac{k_{64}}{I_y^*} F_x \delta M_\omega + \frac{k_{74}}{I_x^*} F_y \delta M_\omega + \frac{k_{84}}{\sqrt{A^* I_t^*}} T_\omega \delta M_\omega \right) dz \end{aligned} \quad (3.70)$$

where:

$$\begin{aligned} k_{61} &= \frac{1}{I_y^* \widehat{A}_{66s}} \int S_{y1}^* \sum_{k=1}^N \left( \int_{n_{k-1}}^{n_k} \frac{\bar{Q}_{16k}}{\bar{Q}_{16R}} dn \right) ds, & k_{62} &= \frac{\sqrt{A^* I_t^*}}{I_x^* I_y^* \widehat{A}_{66s}} \int S_{y1}^* \sum_{k=1}^N \left( \int_{n_{k-1}}^{n_k} \frac{\bar{Q}_{16k}}{\bar{Q}_{16R}} y dn \right) ds, \\ k_{63} &= \frac{\sqrt{A^* I_t^*}}{(I_y^*)^2 \widehat{A}_{66s}} \int S_{y1}^* \sum_{k=1}^N \left( \int_{n_{k-1}}^{n_k} \frac{\bar{Q}_{16k}}{\bar{Q}_{16R}} x dn \right) ds, & k_{64} &= \frac{1}{I_\omega^* \widehat{A}_{66s}} \int S_{y1}^* \sum_{k=1}^N \left( \int_{n_{k-1}}^{n_k} \frac{\bar{Q}_{16k}}{\bar{Q}_{16R}} \Omega dn \right) ds, \\ k_{71} &= \frac{1}{I_x^* \widehat{A}_{66s}} \int S_{x1}^* \sum_{k=1}^N \left( \int_{n_{k-1}}^{n_k} \frac{\bar{Q}_{16k}}{\bar{Q}_{16R}} dn \right) ds, & k_{72} &= \frac{\sqrt{A^* I_t^*}}{(I_x^*)^2 \widehat{A}_{66s}} \int S_{x1}^* \sum_{k=1}^N \left( \int_{n_{k-1}}^{n_k} \frac{\bar{Q}_{16k}}{\bar{Q}_{16R}} y dn \right) ds, \\ k_{73} &= \frac{\sqrt{A^* I_t^*}}{I_x^* I_y^* \widehat{A}_{66s}} \int S_{x1}^* \sum_{k=1}^N \left( \int_{n_{k-1}}^{n_k} \frac{\bar{Q}_{16k}}{\bar{Q}_{16R}} x dn \right) ds, & k_{74} &= \frac{1}{I_\omega^* \widehat{A}_{66s}} \int S_{x1}^* \sum_{k=1}^N \left( \int_{n_{k-1}}^{n_k} \frac{\bar{Q}_{16k}}{\bar{Q}_{16R}} \Omega dn \right) ds, \\ k_{81} &= \frac{\sqrt{A^* I_t^*}}{A^* I_\omega^* \widehat{A}_{66s}} \int S_{\omega 1}^* \sum_{k=1}^N \left( \int_{n_{k-1}}^{n_k} \frac{\bar{Q}_{16k}}{\bar{Q}_{16R}} dn \right) ds, & k_{82} &= \frac{1}{I_\omega^* \widehat{A}_{66s}} \int S_{\omega 1}^* \sum_{k=1}^N \left( \int_{n_{k-1}}^{n_k} \frac{\bar{Q}_{16k}}{\bar{Q}_{16R}} y dn \right) ds, \\ k_{83} &= \frac{1}{I_\omega^* \widehat{A}_{66s}} \int S_{\omega 1}^* \sum_{k=1}^N \left( \int_{n_{k-1}}^{n_k} \frac{\bar{Q}_{16k}}{\bar{Q}_{16R}} x dn \right) ds, & k_{84} &= \frac{\sqrt{A^* I_t^*}}{(I_\omega^*)^2 \widehat{A}_{66s}} \int S_{\omega 1}^* \sum_{k=1}^N \left( \int_{n_{k-1}}^{n_k} \frac{\bar{Q}_{16k}}{\bar{Q}_{16R}} \Omega dn \right) ds, \end{aligned} \quad (3.71)$$

By utilizing Eqs. (3.37), (3.51), (3.65) and (3.70), the following expression can be derived:

$$\begin{aligned}
 \delta U_E^{\text{COL}} = \int_0^l \bar{Q}_{16R} \left[ \left( \frac{A^*}{K_{61}} e_{zx}^{\text{SD}} + \frac{A^*}{K_{71}} e_{zy}^{\text{SD}} + \frac{\sqrt{A^* I_t^*}}{K_{81}} \theta^{\text{SD}} \right) \delta \frac{dw_0}{dz} \right. \\
 + \left( \frac{\sqrt{A^* I_t^*}}{K_{62}} e_{zx}^{\text{SD}} + \frac{\sqrt{A^* I_t^*}}{K_{72}} e_{zy}^{\text{SD}} + \frac{I_t^*}{K_{82}} \theta^{\text{SD}} \right) \delta \frac{d\varphi_x}{dz} \\
 + \left( -\frac{\sqrt{A^* I_t^*}}{K_{63}} e_{zx}^{\text{SD}} - \frac{\sqrt{A^* I_t^*}}{K_{73}} e_{zy}^{\text{SD}} - \frac{I_t^*}{K_{83}} \theta^{\text{SD}} \right) \delta \frac{d\varphi_y}{dz} \\
 \left. + \left( \frac{I_\omega^*}{\sqrt{I_t^*} K_{64}} e_{zx}^{\text{SD}} + \frac{I_\omega^*}{\sqrt{I_t^*} K_{74}} e_{zy}^{\text{SD}} + \frac{I_\omega^*}{\sqrt{A^*} K_{84}} \theta^{\text{SD}} \right) \delta \frac{d\theta}{dz} \right] dz
 \end{aligned} \tag{3.72}$$

where:

$$\begin{aligned}
 \frac{1}{K_{61}} &= \left( \frac{k_{61}}{K_x} + \frac{k_{71}}{K_{xy}} + \frac{k_{81}}{K_{x\omega}} \right), & \frac{1}{K_{62}} &= \left( \frac{I_x^* k_{62}}{I_t^* K_x} + \frac{I_x^* k_{72}}{I_t^* K_{xy}} + \frac{k_{82}}{K_{x\omega}} \right) \\
 \frac{1}{K_{63}} &= \left( \frac{I_y^* k_{63}}{I_t^* K_x} + \frac{I_y^* k_{73}}{I_t^* K_{xy}} + \frac{k_{83}}{K_{x\omega}} \right), & \frac{1}{K_{64}} &= \left( \frac{k_{64} \sqrt{I_t^*} A^*}{K_x I_y^*} + \frac{k_{74} \sqrt{I_t^*} A^*}{K_{xy} I_x^*} + \frac{k_{84}}{K_{x\omega}} \right) \\
 \frac{1}{K_{71}} &= \left( \frac{k_{61}}{K_{xy}} + \frac{k_{71}}{K_y} + \frac{k_{81}}{K_{y\omega}} \right), & \frac{1}{K_{72}} &= \left( \frac{I_x^* k_{62}}{I_t^* K_{xy}} + \frac{I_x^* k_{72}}{I_t^* K_y} + \frac{k_{82}}{K_{y\omega}} \right) \\
 \frac{1}{K_{73}} &= \left( \frac{I_y^* k_{63}}{I_t^* K_{xy}} + \frac{I_y^* k_{73}}{I_t^* K_y} + \frac{k_{83}}{K_{y\omega}} \right), & \frac{1}{K_{74}} &= \left( \frac{k_{64} \sqrt{I_t^*} A^*}{K_{xy} I_y^*} + \frac{k_{74} \sqrt{I_t^*} A^*}{K_y I_x^*} + \frac{k_{84}}{K_{y\omega}} \right) \\
 \frac{1}{K_{81}} &= \left( \frac{k_{61}}{K_{x\omega}} + \frac{k_{71}}{K_{y\omega}} + \frac{k_{81}}{K_\omega} \right), & \frac{1}{K_{82}} &= \left( \frac{I_x^* k_{62}}{I_t^* K_{x\omega}} + \frac{I_x^* k_{72}}{I_t^* K_{y\omega}} + \frac{k_{82}}{K_\omega} \right) \\
 \frac{1}{K_{83}} &= \left( \frac{I_y^* k_{63}}{I_t^* K_{x\omega}} + \frac{I_y^* k_{73}}{I_t^* K_{y\omega}} + \frac{k_{83}}{K_\omega} \right), & \frac{1}{K_{84}} &= \left( \frac{k_{64} \sqrt{I_t^*} A^*}{K_{x\omega} I_y^*} + \frac{k_{74} \sqrt{I_t^*} A^*}{K_{y\omega} I_x^*} + \frac{k_{84}}{K_\omega} \right)
 \end{aligned} \tag{3.73}$$

It can analogously be derived that:

$$\begin{aligned}
 \delta U_E^{\text{COR}} = \int_0^l \bar{Q}_{16R} \left[ \frac{dw_0}{dz} \left( \frac{A^*}{K_{61}} \delta e_{zx}^{\text{SD}} + \frac{A^*}{K_{71}} \delta e_{zy}^{\text{SD}} + \frac{\sqrt{A^* I_t^*}}{K_{81}} \delta \theta^{\text{SD}} \right) \right. \\
 + \frac{d\varphi_x}{dz} \left( \frac{\sqrt{A^* I_t^*}}{K_{62}} \delta e_{zx}^{\text{SD}} + \frac{\sqrt{A^* I_t^*}}{K_{72}} \delta e_{zy}^{\text{SD}} + \frac{I_t^*}{K_{82}} \delta \theta^{\text{SD}} \right) \\
 + \frac{d\varphi_y}{dz} \left( -\frac{\sqrt{A^* I_t^*}}{K_{63}} \delta e_{zx}^{\text{SD}} - \frac{\sqrt{A^* I_t^*}}{K_{73}} \delta e_{zy}^{\text{SD}} - \frac{I_t^*}{K_{83}} \delta \theta^{\text{SD}} \right) \\
 \left. + \frac{d\theta}{dz} \left( \frac{I_\omega^*}{\sqrt{I_t^*} K_{64}} \delta e_{zx}^{\text{SD}} + \frac{I_\omega^*}{\sqrt{I_t^*} K_{74}} \delta e_{zy}^{\text{SD}} + \frac{I_\omega^*}{\sqrt{A^*} K_{84}} \delta \theta^{\text{SD}} \right) \right] dz
 \end{aligned} \tag{3.74}$$

The terms from Eqs. (3.72) and (3.74) will be categorised as coupling relations (CO), which will form the coupling matrix  $\mathbf{Q}^{\text{CO}}$  as:

$$\mathbf{Q}^{\text{CO}} = \bar{Q}_{16R} \begin{bmatrix} \frac{A^*}{K_{61}} & \frac{A^*}{K_{71}} & \frac{\sqrt{A^* I_t^*}}{K_{81}} \\ \frac{\sqrt{A^* I_t^*}}{K_{62}} & \frac{\sqrt{A^* I_t^*}}{K_{72}} & \frac{I_t^*}{K_{82}} \\ -\frac{\sqrt{A^* I_t^*}}{K_{63}} & -\frac{\sqrt{A^* I_t^*}}{K_{73}} & -\frac{I_t^*}{K_{83}} \\ \frac{I_\omega^*}{\sqrt{I_t^*} K_{64}} & \frac{I_\omega^*}{\sqrt{I_t^*} K_{74}} & \frac{I_\omega^*}{\sqrt{A^*} K_{84}} \\ 0 & 0 & 0 \end{bmatrix} \tag{3.75}$$

In the context of the Eq. (3.75), a row of zeros is appended since the coupling between shear forces, warping torque, and St. Venant torque is not taken into account. Consequently, the relations between stress resultants and strains can be expressed in the block matrix form as follows:

$$\begin{Bmatrix} F_z \\ M_x \\ M_y \\ M_\omega \\ T_{\text{SV}} \\ F_x \\ F_y \\ T_\omega \end{Bmatrix} = \begin{bmatrix} \mathbf{Q}^{\text{EB}} & \mathbf{Q}^{\text{CO}} \\ (\mathbf{Q}^{\text{CO}})^T & \mathbf{Q}^{\text{SD}} \end{bmatrix} \begin{Bmatrix} dw_0/dz \\ d\varphi_x/dz \\ d\varphi_y/dz \\ d\theta/dz \\ 2\theta \\ e_{zx}^{\text{SD}} \\ e_{zy}^{\text{SD}} \\ \theta^{\text{SD}} \end{Bmatrix} \tag{3.76}$$



### 3.6 Cross-section properties

An arbitrary open thin-walled cross-section is considered, as shown in Fig. 3.7. The cross-section is divided into multiple rectangles, with each rectangle composed of orthotropic plies arranged in a symmetric and balanced laminate. In the figure,  $\hat{x}$  and  $\hat{y}$  represent the reference axes,  $\tilde{x}$  and  $\tilde{y}$  correspond to the centroid axes, and  $x$  and  $y$  represent the principal axes. The origin of the contour coordinate  $s$  is denoted by  $O_\omega$ , and  $R1$  signifies the number of rectangles present in the cross-section.

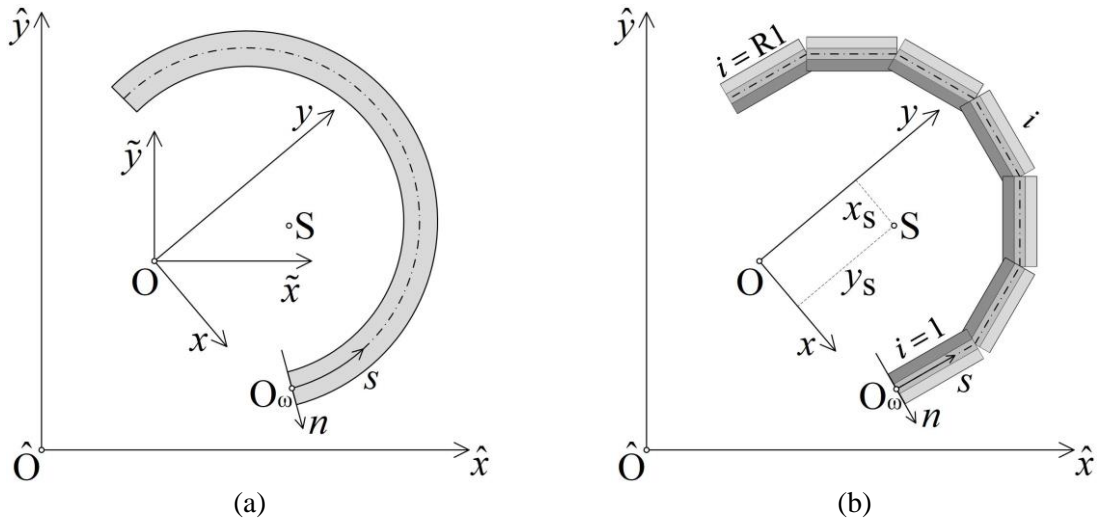


Fig. 3.7 Open thin-walled composite cross-section: (a) real geometry, (b) approximated geometry

In Fig. 3.8, the geometry of the  $i$ -th rectangle is depicted.  $N$  represents the number of plies, while  $R2$  indicates the number of divisions within the  $i$ -th rectangle. The variables  $s$  and  $n$  represent the contour and thickness coordinates, respectively.  $A$  signifies the position of an arbitrary point located at the  $j, k$  position within the rectangle, while  $R$  represents the position of the reference point situated on the centerline at the  $j - 1$  position.

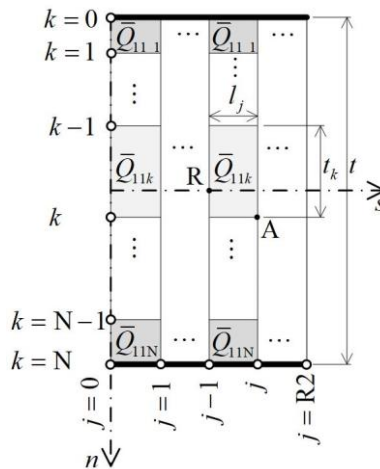


Fig. 3.8 Geometry of  $N$ -layered  $i$ -th rectangle

The laminate that constitutes the rectangle depicted in Fig. 3.8 will be denoted as  $[\theta_1/\dots/\theta_k/\dots/\theta_N]$ . Here,  $\theta_1$ ,  $\theta_k$ , and  $\theta_N$  represent the fiber angle direction (as shown in Fig. 2.4) for the first,  $k$ -th, and  $N$ -th ply, respectively. In this thesis, only balanced and symmetric laminates are considered, and as a result, the following notation is employed to describe a symmetric laminate:  $[\theta_1/\dots/\theta_{N/2}]_S$ .

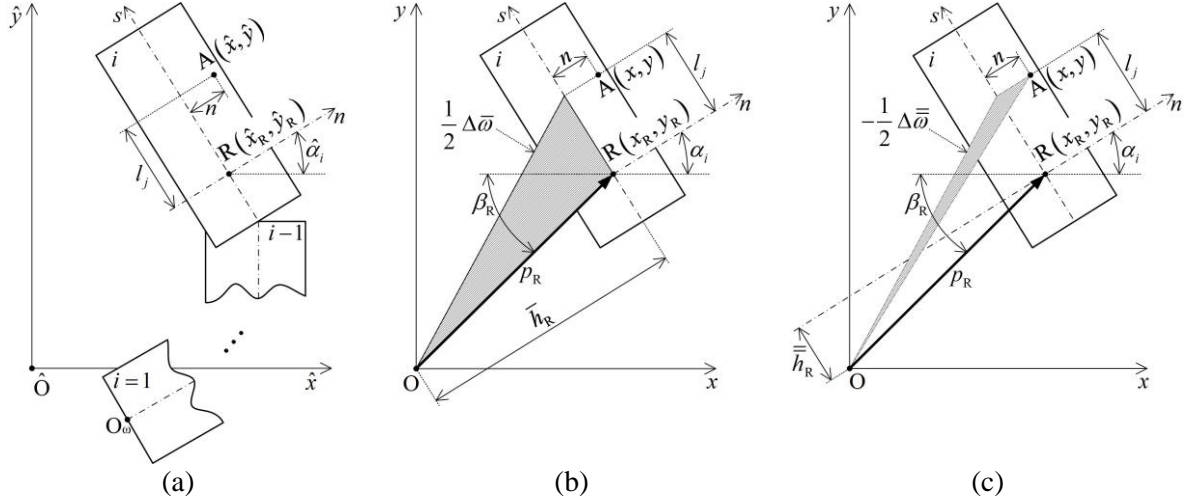


Fig. 3.9 Arbitrary rectangle geometry: (a) general coordinates, (b) contour warping function, (c) thickness warping function

According to Fig. 3.9 (a), the transformation from the local coordinate system  $(s, n)$  of each rectangle to the system of reference axes  $(\hat{x}, \hat{y})$  of the cross-section can be expressed as:

$$\begin{aligned}\hat{x} &= \hat{x}_R - l_j \sin \hat{\alpha}_i + n \cos \hat{\alpha}_i \\ \hat{y} &= \hat{y}_R + l_j \cos \hat{\alpha}_i + n \sin \hat{\alpha}_i\end{aligned}\quad (3.77)$$

To determine the principal axes of the cross-section, the position of the centroid needs to be calculated using a well-known formula from applied mechanics [25]:

$$\hat{x}_0 = \frac{\hat{S}_y^*}{A^*}, \quad \hat{y}_0 = \frac{\hat{S}_x^*}{A^*}\quad (3.78)$$

where  $A^*$ ,  $\hat{S}_x^*$  and  $\hat{S}_y^*$  are the modulus-weighted cross-section area and the modulus-weighted first area moments defined for the reference axes respectively. This properties can be calculated by the use of Eq. (3.77) in the following way:

$$A^* = \int_{s=-l/2}^{l/2} \int_{n=0}^{l_j} \frac{\bar{Q}_{11k}}{\bar{Q}_{11R}} dn ds = \sum_{i=1}^{R1} \sum_{j=1}^{R2} \left[ \int_0^{l_j} \sum_{k=1}^N \left( \int_{n_{k-1}}^{n_k} \frac{\bar{Q}_{11k}}{\bar{Q}_{11R}} dn \right) dl_j \right] = \sum_{i=1}^{R1} \sum_{j=1}^{R2} l_j \hat{A}_{11}\quad (3.79)$$

$$\begin{aligned}
 \hat{S}_x^* &= \int \int_{s-t/2}^{t/2} \hat{y} \frac{\bar{Q}_{11k}}{\bar{Q}_{11R}} dn ds = \sum_{i=1}^{R1} \sum_{j=1}^{R2} \left[ \int_0^{l_j} \sum_{k=1}^N \left( \int_{n_{k-1}}^{n_k} \hat{y} \frac{\bar{Q}_{11k}}{\bar{Q}_{11R}} dn \right) dl_j \right] \\
 &= \sum_{i=1}^{R1} \sum_{j=1}^{R2} \frac{l_j}{2} \left[ \hat{A}_{11} (2 \hat{y}_R + l_j \cos \hat{\alpha}_i) + 2 \hat{B}_{11} \sin \hat{\alpha}_i \right] \\
 \hat{S}_y^* &= \int \int_{s-t/2}^{t/2} \hat{x} \frac{\bar{Q}_{11k}}{\bar{Q}_{11R}} dn ds = \sum_{i=1}^{R1} \sum_{j=1}^{R2} \left[ \int_0^{l_j} \sum_{k=1}^N \left( \int_{n_{k-1}}^{n_k} \hat{x} \frac{\bar{Q}_{11k}}{\bar{Q}_{11R}} dn \right) dl_j \right] \\
 &= \sum_{i=1}^{R1} \sum_{j=1}^{R2} \frac{l_j}{2} \left[ \hat{A}_{11} (2 \hat{x}_R - l_j \sin \hat{\alpha}_i) + 2 \hat{B}_{11} \cos \hat{\alpha}_i \right]
 \end{aligned}$$

where:

$$\hat{A}_{11} = \sum_{k=1}^N \left[ \frac{\bar{Q}_{11k}}{\bar{Q}_{11R}} (n_k - n_{k-1}) \right], \quad \hat{B}_{11} = \frac{1}{2} \sum_{k=1}^N \left[ \frac{\bar{Q}_{11k}}{\bar{Q}_{11R}} (n_k^2 - n_{k-1}^2) \right] \quad (3.80)$$

After the properties from Eq. (3.79) are calculated, and position of the centroid is defined by the use of Eq. (3.78), whole cross-section is moved to the centroid ( $\tilde{x}$ ,  $\tilde{y}$ ):

$$\begin{aligned}
 \tilde{x} &= \hat{x} - \hat{x}_O \\
 \tilde{y} &= \hat{y} - \hat{y}_O
 \end{aligned} \quad (3.81)$$

It is also worth noting that the Eq. (3.77) have the same form for the centroid axes ( $\tilde{x}$ ,  $\tilde{y}$ ):

$$\begin{aligned}
 \tilde{x} &= \tilde{x}_R - l_j \sin \hat{\alpha}_i + n \cos \hat{\alpha}_i \\
 \tilde{y} &= \tilde{y}_R + l_j \cos \hat{\alpha}_i + n \sin \hat{\alpha}_i
 \end{aligned} \quad (3.82)$$

Since the cross-section has not been rotated, the slope of the rectangle  $\hat{\alpha}_i$  remains unchanged. In order to find the principal axes, the well-known formula can be used [25]:

$$\tan 2\chi = \frac{2\tilde{I}_{xy}^*}{\tilde{I}_y^* - \tilde{I}_x^*} \quad (3.83)$$

where  $\tilde{I}_x^*$ ,  $\tilde{I}_y^*$ ,  $\tilde{I}_{xy}^*$  are the modulus-weighted second area moments defined for the centroid axes. This properties can be calculated in the same manner as Eq. (3.79):

$$\begin{aligned}
 \tilde{I}_x^* &= \int \int_{s-t/2}^{t/2} \tilde{y}^2 \frac{\bar{Q}_{11k}}{\bar{Q}_{11R}} dn ds = \sum_{i=1}^{R1} \sum_{j=1}^{R2} \left[ \int_0^{l_j} \sum_{k=1}^N \left( \int_{n_{k-1}}^{n_k} \tilde{y}^2 \frac{\bar{Q}_{11k}}{\bar{Q}_{11R}} dn \right) dl_j \right] \\
 &= \sum_{i=1}^{R1} \sum_{j=1}^{R2} \frac{l_j}{12} \left\{ \hat{A}_{11} \left[ 3(2\tilde{y}_R + l_j \cos \hat{\alpha}_i)^2 + l_j^2 \cos^2 \hat{\alpha}_i \right] \right. \\
 &\quad \left. + 6\hat{B}_{11} (4\tilde{y}_R \sin \hat{\alpha}_i + l_j \sin 2\hat{\alpha}_i) + 12\hat{D}_{11} \sin^2 \hat{\alpha}_i \right\}
 \end{aligned} \quad (3.84)$$

$$\begin{aligned}
 \tilde{I}_y^* &= \int \int_{s=-l/2}^{l/2} \tilde{x}^2 \frac{\bar{Q}_{11k}}{\bar{Q}_{11R}} dn ds = \sum_{i=1}^{R1} \sum_{j=1}^{R2} \left[ \int_0^{l_j} \sum_{k=1}^N \left( \int_{n_{k-1}}^{n_k} \tilde{x}^2 \frac{\bar{Q}_{11k}}{\bar{Q}_{11R}} dn \right) dl_j \right] \\
 &= \sum_{i=1}^{R1} \sum_{j=1}^{R2} \frac{l_j}{12} \left\{ \hat{A}_{11} \left[ 3(2\tilde{x}_R - l_j \sin \hat{\alpha}_i)^2 + l_j^2 \sin^2 \hat{\alpha}_i \right] \right. \\
 &\quad \left. + 6\hat{B}_{11} (4\tilde{x}_R \cos \hat{\alpha}_i - l_j \sin 2\hat{\alpha}_i) + 12\hat{D}_{11} \cos^2 \hat{\alpha}_i \right\} \\
 \tilde{I}_{xy}^* &= \int \int_{s=-l/2}^{l/2} \tilde{x}\tilde{y} \frac{\bar{Q}_{11k}}{\bar{Q}_{11R}} dn ds = \sum_{i=1}^{R1} \sum_{j=1}^{R2} \left[ \int_0^{l_j} \sum_{k=1}^N \left( \int_{n_{k-1}}^{n_k} \tilde{x}\tilde{y} \frac{\bar{Q}_{11k}}{\bar{Q}_{11R}} dn \right) dl_j \right] \\
 &= \sum_{i=1}^{R1} \sum_{j=1}^{R2} \frac{l_j}{6} \left[ \hat{A}_{11} (6\tilde{x}_R \tilde{y}_R + 3l_j \tilde{K}_1 - l_j^2 \sin 2\hat{\alpha}_i) \right. \\
 &\quad \left. + \hat{B}_{11} (3l_j \cos 2\hat{\alpha}_i + 6\tilde{K}_2) + 3\hat{D}_{11} \sin 2\hat{\alpha}_i \right]
 \end{aligned}$$

where:

$$\hat{D}_{11} = \frac{1}{3} \sum_{k=1}^N \left[ \frac{\bar{Q}_{11k}}{\bar{Q}_{11R}} (n_k^3 - n_{k-1}^3) \right], \quad \tilde{K}_1 = \tilde{x}_R \cos \hat{\alpha}_i - \tilde{y}_R \sin \hat{\alpha}_i, \quad \tilde{K}_2 = \tilde{x}_R \sin \hat{\alpha}_i + \tilde{y}_R \cos \hat{\alpha}_i \quad (3.85)$$

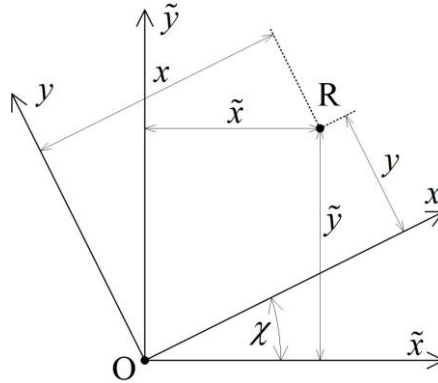


Fig. 3.10 Node transformation

In order to calculate the cross-section properties with respect to the principal axes, the entire cross-section needs to be rotated to align with the principal axes. To achieve this, all the nodes of the cross-section must be rotated using a transformation following from Fig. 3.10:

$$\begin{aligned}
 x &= \tilde{x} \cos \chi + \tilde{y} \sin \chi \\
 y &= -\tilde{x} \sin \chi + \tilde{y} \cos \chi
 \end{aligned}
 \quad \text{or} \quad
 \begin{Bmatrix} x \\ y \end{Bmatrix} = \begin{bmatrix} \cos \chi & \sin \chi \\ -\sin \chi & \cos \chi \end{bmatrix} \begin{Bmatrix} \tilde{x} \\ \tilde{y} \end{Bmatrix} \quad (3.86)$$

Using the procedure outlined in Eq. (3.86), the cross-section has been rotated by an angle  $\chi$  in the counterclockwise direction to align with the main axes. Consequently, the slopes of each rectangle need to be adjusted by the same amount. The changes can be expressed as follows:

$$\alpha_i = \hat{\alpha}_i - \chi \quad (3.87)$$

Same as Eqs. (3.77) and (3.82), the transformation from the local coordinate system  $(s, n)$  of each rectangle to the system of main axes  $(x, y)$  of the cross-section can be expressed as

$$\begin{aligned} x &= x_R - l_j \sin \alpha_i + n \cos \alpha_i \\ y &= y_R + l_j \cos \alpha_i + n \sin \alpha_i \end{aligned} \quad (3.88)$$

For the recalibration of the cross-section properties in the system of main axes, certain properties that were already determined and used for the determination of the main axes need to be recalculated. This can be achieved by applying the well-known parallel axis theorem [25]:

$$I_x^* = \tilde{I}_x^* - \hat{y}_O^2 A^*, \quad I_y^* = \tilde{I}_y^* - \hat{x}_O^2 A^*, \quad I_{xy}^* = \tilde{I}_{xy}^* - \hat{x}_O \hat{y}_O A^* \quad (3.89)$$

or by repeating the same process as in Eq. (3.84) for the main axes:

$$\begin{aligned} I_x^* &= \int \int_{s=-t/2}^{t/2} y^2 \frac{\bar{Q}_{11k}}{\bar{Q}_{11R}} dn ds = \sum_{i=1}^{R1} \sum_{j=1}^{R2} \left[ \int_0^{l_j} \sum_{k=1}^N \left( \int_{n_{k-1}}^{n_k} y^2 \frac{\bar{Q}_{11k}}{\bar{Q}_{11R}} dn \right) dl_j \right] \\ &= \sum_{i=1}^{R1} \sum_{j=1}^{R2} \frac{l_j}{12} \left\{ \hat{A}_{11} \left[ 3(2y_R + l_j \cos \alpha_i)^2 + l_j^2 \cos^2 \alpha_i \right] \right. \\ &\quad \left. + 6\hat{B}_{11} (4y_R \sin \alpha_i + l_j \sin 2\alpha_i) + 12\hat{D}_{11} \sin^2 \alpha_i \right\} \\ I_y^* &= \int \int_{s=-t/2}^{t/2} x^2 \frac{\bar{Q}_{11k}}{\bar{Q}_{11R}} dn ds = \sum_{i=1}^{R1} \sum_{j=1}^{R2} \left[ \int_0^{l_j} \sum_{k=1}^N \left( \int_{n_{k-1}}^{n_k} x^2 \frac{\bar{Q}_{11k}}{\bar{Q}_{11R}} dn \right) dl_j \right] \\ &= \sum_{i=1}^{R1} \sum_{j=1}^{R2} \frac{l_j}{12} \left\{ \hat{A}_{11} \left[ 3(2x_R - l_j \sin \alpha_i)^2 + l_j^2 \sin^2 \alpha_i \right] \right. \\ &\quad \left. + 6\hat{B}_{11} (4x_R \cos \alpha_i - l_j \sin 2\alpha_i) + 12\hat{D}_{11} \cos^2 \alpha_i \right\} \\ I_{xy}^* &= \int \int_{s=-t/2}^{t/2} xy \frac{\bar{Q}_{11k}}{\bar{Q}_{11R}} dn ds = \sum_{i=1}^{R1} \sum_{j=1}^{R2} \left[ \int_0^{l_j} \sum_{k=1}^N \left( \int_{n_{k-1}}^{n_k} xy \frac{\bar{Q}_{11k}}{\bar{Q}_{11R}} dn \right) dl_j \right] \\ &= \sum_{i=1}^{R1} \sum_{j=1}^{R2} \frac{l_j}{6} \left[ \hat{A}_{11} (6x_R y_R + 3l_j K_1 - l_j^2 \sin 2\alpha_i) \right. \\ &\quad \left. + \hat{B}_{11} (3l_j \cos 2\alpha_i + 6K_2) + 3\hat{D}_{11} \sin 2\alpha_i \right] \end{aligned} \quad (3.90)$$

where:

$$K_1 = x_R \cos \alpha_i - y_R \sin \alpha_i, \quad K_2 = x_R \sin \alpha_i + y_R \cos \alpha_i \quad (3.91)$$

To determine the position of the shear center and the sectorial cross-section properties, it is necessary to define the warping function. According to the Fig. 3.9 (b), the change of the contour warping is:

$$\Delta \bar{\omega} = \bar{h}_R l_j, \quad \bar{h}_R = x_R \cos \alpha_i + y_R \sin \alpha_i \quad (3.92)$$

while, according to the Fig. 3.9 (c), the change of the thickness warping is:

$$\Delta \bar{\bar{\omega}} = -\left(\bar{\bar{h}}_R + l_j\right)n, \quad \bar{\bar{h}}_R = y_R \cos \alpha_i - x_R \sin \alpha_i \quad (3.93)$$

Finally if the Eqs. (3.92) and (3.93) are combined and added to the warping of the reference point, the warping of an arbitrary point A on the cross-section rectangle can be calculated by the general definition of the warping function as:

$$\omega = \omega_R + \Delta \bar{\omega} + \Delta \bar{\bar{\omega}} = \omega_R + \bar{h}_R l_j - \bar{\bar{h}}_R n - l_j n \quad (3.94)$$

It should be noted that the warping of the reference point  $\omega_R$  is still unknown, and the pole of the warping function, as defined in Eq. (3.94), is assumed to be located at the centroid of the cross-section, as depicted in Fig. 3.9 (b) and Fig. 3.9 (c). The determination of the warping of the cross-section will be initiated from the origin of the contour coordinate  $O_\omega$ , assuming zero warping ( $\omega_R = 0$ ) for this starting point. Subsequently, the warping for any arbitrarily chosen point adjacent to the starting point can be calculated, and it will be utilized as a reference for the next arbitrarily chosen point. Through this process, the warping for the entire cross-section can be defined, with the origin chosen at  $O_\omega$  and the pole selected at the centroid of the cross-section.

To determine the position of the shear center relative to the centroid of the cross-section, a simple formula from applied mechanics will be employed [25]:

$$x_S = \frac{I_{y\omega}^*}{I_x^*}, \quad y_S = -\frac{I_{x\omega}^*}{I_y^*} \quad (3.95)$$

where the  $I_{x\omega}^*$  and  $I_{y\omega}^*$  are the modulus-weighted second sectorial moments of the cross-section calculated as follows:

$$\begin{aligned} I_{x\omega}^* &= \int \int_{s=-t/2}^{t/2} x\omega \frac{\bar{Q}_{11k}}{\bar{Q}_{11R}} dn ds = \sum_{i=1}^{R1} \sum_{j=1}^{R2} \left[ \int_0^{l_j} \sum_{k=1}^N \left( \int_{n_{k-1}}^{n_k} x\omega \frac{\bar{Q}_{11k}}{\bar{Q}_{11R}} dn \right) dl_j \right] \\ &= \sum_{i=1}^{R1} \sum_{j=1}^{R2} \frac{l_j}{6} \left\{ \hat{A}_{11} \left[ 6x_R \omega_R + 3l_j (x_R \bar{h}_R - \omega_R \sin \alpha_i) - 2l_j^2 \bar{h}_R \sin \alpha_i \right] \right. \\ &\quad \left. + \hat{B}_{11} \left[ 6\omega_R \cos \alpha_i - 6x_R \bar{\bar{h}}_R + 3l_j (\bar{\bar{h}}_R \cos \alpha_i + \bar{\bar{h}}_R \sin \alpha_i - x_R) + 2l_j^2 \sin \alpha_i \right] \right. \\ &\quad \left. - 3\hat{D}_{11} \cos \alpha_i (2\bar{\bar{h}}_R + l_j) \right\} \end{aligned} \quad (3.96)$$

$$\begin{aligned}
 I_{y\omega}^* &= \int \int_{s=-t/2}^{t/2} y\omega \frac{\bar{Q}_{11k}}{\bar{Q}_{11R}} dn ds = \sum_{i=1}^{R1} \sum_{j=1}^{R2} \left[ \int_0^{l_j} \sum_{k=1}^N \left( \int_{n_{k-1}}^{n_k} y\omega \frac{\bar{Q}_{11k}}{\bar{Q}_{11R}} dn \right) dl_j \right] \\
 &= \sum_{i=1}^{R1} \sum_{j=1}^{R2} \frac{l_j}{6} \left\{ \hat{A}_{11} \left[ 6y_R \omega_R + 3l_j (y_R \bar{h}_R + \omega_R \cos \alpha_i) + 2l_j^2 \bar{h}_R \cos \alpha_i \right] \right. \\
 &\quad \left. + \hat{B}_{11} \left[ 6\omega_R \sin \alpha_i - 6y_R \bar{h}_R + 3l_j (\bar{h}_R \sin \alpha_i - \bar{h}_R \cos \alpha_i - y_R) \right] - 2l_j^2 \cos \alpha_i \right\} \\
 &\quad - 3\hat{D}_{11} \sin \alpha_i (2\bar{h}_R + l_j) \left. \right\}
 \end{aligned}$$

From there, the principal warping function  $\Omega$  can be defined for the cross-section, or in other words, the warping for the pole placed in the shear center with respect to the principal origin of the contour coordinate, as follows [50]:

$$\begin{aligned}
 \Omega &= \omega + y_S x - x_S y - S_\omega^*/A^* = \Omega_R + r l_j - q n - l_j n \\
 r &= (x_R - x_S) \cos \alpha_i + (y_R - y_S) \sin \alpha_i, \quad q = (y_R - y_S) \cos \alpha_i - (x_R - x_S) \sin \alpha_i \\
 \Omega_R &= \omega_R + y_S x_R - x_S y_R - S_\omega^*/A^*
 \end{aligned} \tag{3.97}$$

where  $S_\omega^*$  is the modulus-weighted first sectorial moment of the cross-section calculated in the following way:

$$\begin{aligned}
 S_\omega^* &= \int \int_{s=-t/2}^{t/2} \omega \frac{\bar{Q}_{11k}}{\bar{Q}_{11R}} dn ds = \sum_{i=1}^{R1} \sum_{j=1}^{R2} \left[ \int_0^{l_j} \sum_{k=1}^N \left( \int_{n_{k-1}}^{n_k} \omega \frac{\bar{Q}_{11k}}{\bar{Q}_{11R}} dn \right) dl_j \right] = \\
 &= \sum_{i=1}^{R1} \sum_{j=1}^{R2} \frac{l_j}{2} \left[ \hat{A}_{11} (2\omega_R + l_j \bar{h}_R) - \hat{B}_{11} (2\bar{h}_R + l_j) \right]
 \end{aligned} \tag{3.98}$$

With the principal warping  $\Omega$  defined for the cross-section, modulus-weighted warping constant can be calculated as follows:

$$\begin{aligned}
 I_\omega^* &= \int \int_{s=-t/2}^{t/2} \Omega^2 \frac{\bar{Q}_{11k}}{\bar{Q}_{11R}} dn ds = \sum_{i=1}^{R1} \sum_{j=1}^{R2} \left[ \int_0^{l_j} \sum_{k=1}^N \left( \int_{n_{k-1}}^{n_k} \Omega^2 \frac{\bar{Q}_{11k}}{\bar{Q}_{11R}} dn \right) dl_j \right] \\
 &= \sum_{i=1}^{R1} \sum_{j=1}^{R2} l_j \left[ \hat{A}_{11} K_3^2 - 2\hat{B}_{11} K_3 K_4 + \hat{D}_{11} K_4^2 + \frac{l_j^2}{12} (\hat{A}_{11} r^2 - 2\hat{B}_{11} r + \hat{D}_{11}) \right]
 \end{aligned} \tag{3.99}$$

where:

$$K_3 = \Omega_R + \frac{1}{2} l_j r, \quad K_4 = q + \frac{1}{2} l_j \tag{3.100}$$

The modulus-weighted torsional constant from Eq. (3.60) can be calculated in the following way:

$$\begin{aligned}
 I_t^* &= 2 \int_{s=-l/2}^{l/2} \int_{n_{k-1}}^{n_k} \frac{\bar{Q}_{66k}}{\bar{Q}_{66R}} \left( \frac{t^2}{4} - n^2 \right) dn ds = \sum_{i=1}^{R1} \sum_{j=1}^{R2} \left\{ \int_0^{l_j} \sum_{k=1}^N \left[ \int_{n_{k-1}}^{n_k} \frac{\bar{Q}_{66k}}{\bar{Q}_{66R}} \left( \frac{t^2}{2} - 2n^2 \right) dn \right] dl_j \right\} \\
 &= \sum_{i=1}^{R1} \sum_{j=1}^{R2} \frac{l_j}{2} (t^2 \hat{A}_{66} - 4 \hat{D}_{66})
 \end{aligned} \tag{3.101}$$

where:

$$\hat{A}_{66} = \sum_{k=1}^N \left[ \frac{\bar{Q}_{66k}}{\bar{Q}_{66R}} (n_k - n_{k-1}) \right], \quad \hat{D}_{66} = \frac{1}{3} \sum_{k=1}^N \left[ \frac{\bar{Q}_{66k}}{\bar{Q}_{66R}} (n_k^3 - n_{k-1}^3) \right] \tag{3.102}$$

The integrals used in the wagner's coefficients from Eq. (3.64) can be calculated in the following way:

$$\begin{aligned}
 \int_s \sum_{k=1}^N \int_{n_{k-1}}^{n_k} \frac{\bar{Q}_{11k}}{\bar{Q}_{11R}} (x^2 y + y^3) dn ds &= \sum_{i=1}^{R1} \sum_{j=1}^{R2} \left\{ \int_0^{l_j} \sum_{k=1}^N \left[ \int_{n_{k-1}}^{n_k} \frac{\bar{Q}_{11k}}{\bar{Q}_{11R}} (x^2 y + y^3) dn \right] dl_j \right\} = \\
 &= \sum_{i=1}^{R1} \sum_{j=1}^{R2} \frac{l_j}{12} \left\{ 12 \hat{E}_{11} \sin \alpha_i + 6 \hat{D}_{11} \left[ 4 y_R + l_j \cos \alpha_i - 2 (y_R \cos 2\alpha_i - x_R \sin 2\alpha_i) \right] \right. \\
 &+ 4 \hat{B}_{11} \left[ \sin \alpha_i (l_j^2 + 3 x_R^2 + 9 y_R^2) + 6 x_R y_R \cos \alpha_i + 3 l_j (x_R \cos 2\alpha_i + y_R \sin 2\alpha_i) \right] \\
 &+ \hat{A}_{11} \left[ (l_j^2 + 2 x_R^2 + 6 y_R^2) (2 y_R + 3 l_j \cos \alpha_i) + 2 y_R (2 x_R - 3 l_j) (2 x_R - l_j) \right. \\
 &\left. \left. + 4 l_j x_R y_R (4 - 3 \sin \alpha_i) + 4 l_j^2 (y_R \cos 2\alpha_i - x_R \sin 2\alpha_i) \right] \right\}
 \end{aligned} \tag{3.103}$$

$$\begin{aligned}
 \int_s \sum_{k=1}^N \int_{n_{k-1}}^{n_k} \frac{\bar{Q}_{11k}}{\bar{Q}_{11R}} (x^3 + x y^2) dn ds &= \sum_{i=1}^{R1} \sum_{j=1}^{R2} \left\{ \int_0^{l_j} \sum_{k=1}^N \left[ \int_{n_{k-1}}^{n_k} \frac{\bar{Q}_{11k}}{\bar{Q}_{11R}} (x^3 + x y^2) dn \right] dl_j \right\} = \\
 &= \sum_{i=1}^{R1} \sum_{j=1}^{R2} \frac{l_j}{12} \left\{ 12 \hat{E}_{11} \cos \alpha_i + 6 \hat{D}_{11} \left[ 4 x_R - l_j \sin \alpha_i + 2 (x_R \cos 2\alpha_i + y_R \sin 2\alpha_i) \right] \right. \\
 &+ 4 \hat{B}_{11} \left[ \cos \alpha_i (l_j^2 + 9 x_R^2 + 3 y_R^2) + 6 x_R y_R \sin \alpha_i + 3 l_j (y_R \cos 2\alpha_i - x_R \sin 2\alpha_i) \right] \\
 &+ \hat{A}_{11} \left[ (l_j^2 + 6 x_R^2 + 2 y_R^2) (2 x_R - 3 l_j \sin \alpha_i) + 2 x_R (2 y_R - 3 l_j) (2 y_R - l_j) \right. \\
 &\left. \left. + 4 l_j x_R y_R (4 + 3 \cos \alpha_i) - 4 l_j^2 (x_R \cos 2\alpha_i + y_R \sin 2\alpha_i) \right] \right\}
 \end{aligned}$$



$$\begin{aligned}
 \int \sum_{s=1}^N \int_{n_{k-1}}^{n_k} \frac{\bar{Q}_{11k}}{\bar{Q}_{11R}} (x^2 + y^2) \Omega \, dn \, ds &= \sum_{i=1}^{R1} \sum_{j=1}^{R2} \left\{ \int_0^{l_j} \sum_{k=1}^N \left[ \int_{n_{k-1}}^{n_k} \frac{\bar{Q}_{11k}}{\bar{Q}_{11R}} (x^2 + y^2) \Omega \, dn \right] dl_j \right\} = \\
 &= \sum_{i=1}^{R1} \sum_{j=1}^{R2} \frac{l_j}{12} \left\{ -12\hat{E}_{11} K_4 + 12\hat{D}_{11} \left[ K_3 - 2K_4 (x_R \cos \alpha_i + y_R \sin \alpha_i) \right] \right. \\
 &+ 4\hat{A}_{11} \left[ l_j^2 K_3 + r l_j^3 + 3K_3 (x_R^2 + y_R^2) + l_j (4K_3 - \Omega_R) (y_R \cos \alpha_i - x_R \sin \alpha_i) \right] \\
 &+ \hat{B}_{11} \left[ 4l_j (4K_4 - q) (x_R \sin \alpha_i - y_R \cos \alpha_i) + 24K_3 (x_R \cos \alpha_i + y_R \sin \alpha_i) \right. \\
 &\quad \left. \left. - 4K_4 l_j^2 - l_j^3 - 12K_4 (x_R^2 + y_R^2) \right] \right\}
 \end{aligned}$$

where:

$$\hat{E}_{11} = \frac{1}{4} \sum_{k=1}^N \left[ \frac{\bar{Q}_{11k}}{\bar{Q}_{11R}} (n_k^4 - n_{k-1}^4) \right] \quad (3.104)$$

Now, the calculation of the shear correction factors from the Eq. (3.49) will be carried out. In order to evaluate the integrals in Eq. (3.49), it is necessary to define the modulus-weighted first area moments and first sectorial moment as functions of the contour coordinate  $s$ :

$$\begin{aligned}
 S_{x1}^* &= \int \int_{s=-t/2}^{t/2} y \frac{\bar{Q}_{11k}}{\bar{Q}_{11R}} \, dn \, ds \\
 &= \sum_{i=1}^{i-1} \sum_{j=1}^{R2} \left[ \int_0^{l_j} \sum_{k=1}^N \left( \int_{n_{k-1}}^{n_k} y \frac{\bar{Q}_{11k}}{\bar{Q}_{11R}} \, dn \right) dl_j \right] + \sum_{i,j=1}^j \left[ \int_0^{l_j} \sum_{k=1}^N \left( \int_{n_{k-1}}^{n_k} y \frac{\bar{Q}_{11k}}{\bar{Q}_{11R}} \, dn \right) dl_j \right] \\
 &= \hat{A}_{11} \frac{2l_j y_R + l_j^2 \cos \alpha_i}{2} + l_j \hat{B}_{11} \sin \alpha_i + S_{x0}^*
 \end{aligned} \quad (3.105)$$

$$\begin{aligned}
 S_{y1}^* &= \int \int_{s=-t/2}^{t/2} x \frac{\bar{Q}_{11k}}{\bar{Q}_{11R}} \, dn \, ds \\
 &= \sum_{i=1}^{i-1} \sum_{j=1}^{R2} \left[ \int_0^{l_j} \sum_{k=1}^N \left( \int_{n_{k-1}}^{n_k} x \frac{\bar{Q}_{11k}}{\bar{Q}_{11R}} \, dn \right) dl_j \right] + \sum_{i,j=1}^j \left[ \int_0^{l_j} \sum_{k=1}^N \left( \int_{n_{k-1}}^{n_k} x \frac{\bar{Q}_{11k}}{\bar{Q}_{11R}} \, dn \right) dl_j \right] \\
 &= \hat{A}_{11} \frac{2l_j x_R - l_j^2 \sin \alpha_i}{2} + l_j \hat{B}_{11} \cos \alpha_i + S_{y0}^*
 \end{aligned}$$

$$\begin{aligned}
 S_{\omega 1}^* &= \int_{s=-l/2}^{l/2} \int_{\Omega} \frac{\bar{Q}_{11k}}{\bar{Q}_{11R}} \, dn \, ds \\
 &= \sum_{i=1}^{i-1} \sum_{j=1}^{R2} \left[ \int_0^{l_j} \sum_{k=1}^N \left( \int_{n_{k-1}}^{n_k} \Omega \frac{\bar{Q}_{11k}}{\bar{Q}_{11R}} \, dn \right) dl_j \right] + \sum_{i,j=1}^j \left[ \int_0^{l_j} \sum_{k=1}^N \left( \int_{n_{k-1}}^{n_k} \Omega \frac{\bar{Q}_{11k}}{\bar{Q}_{11R}} \, dn \right) dl_j \right] \\
 &= \hat{A}_{11} \frac{2l_j \Omega_R + l_j^2 r}{2} - \hat{B}_{11} \frac{2l_j q + l_j^2}{2} + S_{\omega 0}^*
 \end{aligned}$$

where:

$$\begin{aligned}
 S_{x0}^* &= \sum_{i=1}^{i-1} \sum_{j=1}^{R2} \left( \hat{A}_{11} \frac{2l_j y_R + l_j^2 \cos \alpha_i}{2} + l_j \hat{B}_{11} \sin \alpha_i \right) \\
 &\quad + \sum_{i,j=1}^{j-1} \left( \hat{A}_{11} \frac{2l_j y_R + l_j^2 \cos \alpha_i}{2} + l_j \hat{B}_{11} \sin \alpha_i \right) \\
 S_{y0}^* &= \sum_{i=1}^{i-1} \sum_{j=1}^{R2} \left( \hat{A}_{11} \frac{2l_j x_R - l_j^2 \sin \alpha_i}{2} + l_j \hat{B}_{11} \cos \alpha_i \right) \\
 &\quad + \sum_{i,j=1}^{j-1} \left( \hat{A}_{11} \frac{2l_j x_R - l_j^2 \sin \alpha_i}{2} + l_j \hat{B}_{11} \cos \alpha_i \right) \\
 S_{\omega 0}^* &= \sum_{i=1}^{i-1} \sum_{j=1}^{R2} \left( \hat{A}_{11} \frac{2l_j \Omega_R + l_j^2 r}{2} - \hat{B}_{11} \frac{2l_j q + l_j^2}{2} \right) \\
 &\quad + \sum_{i,j=1}^{j-1} \left( \hat{A}_{11} \frac{2l_j \Omega_R + l_j^2 r}{2} - \hat{B}_{11} \frac{2l_j q + l_j^2}{2} \right)
 \end{aligned} \tag{3.106}$$

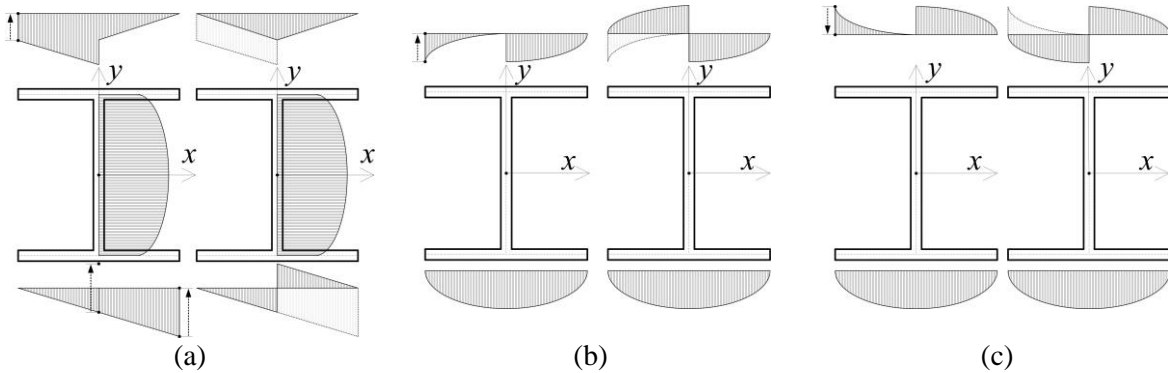


Fig. 3.11 Various distributions over the cross-section contour (left: distribution without correction, right: distribution with correction): (a)  $S_x^*$ , (b)  $S_y^*$ , (c)  $S_{\omega}^*$

Once the modulus-weighted first area moments and the modulus-weighted first sectorial moment are defined as functions of a contour coordinate,  $s$ , they must be calculated along the entire contour of the cross-section to obtain the distribution of these properties across the cross-section's contour. However, for cross-sections with more than two branches that have free ends

(such as the I profile), a correction procedure is necessary. This procedure ensures that the distribution of the entire cross-section branch, which is non-zero at the free end, is adjusted to satisfy the required condition, as illustrated in Fig. 3.11. After this procedure is finished, the integrals in the Eq. (3.49) can be calculated in the following way:

$$\begin{aligned}
 \int_s (S_{x1}^*)^2 ds &= \sum_{i=1}^{R1} \sum_{j=1}^{R2} \left[ \int_0^{l_j} (S_{x1}^*)^2 dl_j \right] = \sum_{i=1}^{R1} \sum_{j=1}^{R2} \frac{l_j}{60} \left[ 20l_j^2 \widehat{B}_{11}^2 \sin^2 \alpha_i + 60(S_{x0}^*)^2 \right. \\
 &+ l_j^2 \widehat{A}_{11}^2 (20y_R^2 + 3l_j^2 \cos^2 \alpha_i + 15l_j y_R \cos \alpha_i) + 60l_j \widehat{B}_{11} S_{x0}^* \sin \alpha_i \\
 &\left. + 5l_j^2 \widehat{A}_{11} \widehat{B}_{11} \sin \alpha_i (8y_R + 3l_j \cos \alpha_i) + 20l_j \widehat{A}_{11} S_{y0}^* (3y_R + l_j \cos \alpha_i) \right] \\
 \int_s (S_{y1}^*)^2 ds &= \sum_{i=1}^{R1} \sum_{j=1}^{R2} \left[ \int_0^{l_j} (S_{y1}^*)^2 dl_j \right] = \sum_{i=1}^{R1} \sum_{j=1}^{R2} \frac{l_j}{60} \left[ 20l_j^2 \widehat{B}_{11}^2 \cos^2 \alpha_i + 60(S_{y0}^*)^2 \right. \\
 &+ l_j^2 \widehat{A}_{11}^2 (20x_R^2 + 3l_j^2 \sin^2 \alpha_i - 15l_j x_R \sin \alpha_i) + 60l_j \widehat{B}_{11} S_{y0}^* \cos \alpha_i \\
 &\left. + 5l_j^2 \widehat{A}_{11} \widehat{B}_{11} \cos \alpha_i (8x_R - 3l_j \sin \alpha_i) + 20l_j \widehat{A}_{11} S_{y0}^* (3x_R - l_j \sin \alpha_i) \right] \\
 \int_s (S_{\omega 1}^*)^2 ds &= \sum_{i=1}^{R1} \sum_{j=1}^{R2} \left[ \int_0^{l_j} (S_{\omega 1}^*)^2 dl_j \right] = \sum_{i=1}^{R1} \sum_{j=1}^{R2} \frac{l_j}{240} \left\{ l_j^2 \widehat{A}_{11}^2 \left[ 3(\Omega_R + 4K_3)^2 + 5\Omega_R^2 \right] \right. \\
 &+ 40l_j S_{\omega 0}^* \left[ \widehat{A}_{11} (6K_3 - l_j r) - \widehat{B}_{11} (6K_4 - l_j) \right] + l_j^2 \widehat{B}_{11}^2 \left[ 3(q + 4K_4)^2 + 5q^2 \right] \\
 &\left. - 4l_j^2 \widehat{A}_{11} \widehat{B}_{11} \left[ (5K_3 - l_j r)(8K_4 - l_j) + 3l_j K_4 r \right] + 240(S_{\omega 0}^*)^2 \right\} \tag{3.107} \\
 \int_s S_{x1}^* S_{y1}^* ds &= \sum_{i=1}^{R1} \sum_{j=1}^{R2} \left[ \int_0^{l_j} S_{x1}^* S_{y1}^* dl_j \right] = \sum_{i=1}^{R1} \sum_{j=1}^{R2} \frac{l_j}{120} \left\{ 60l_j^2 \widehat{B}_{11} (S_{y0}^* \sin \alpha_i + S_{x0}^* \cos \alpha_i) \right. \\
 &+ l_j^2 \widehat{A}_{11}^2 (40x_R y_R + 15l_j K_1 - 3l_j^2 \sin 2\alpha_i) + 5l_j^2 \widehat{A}_{11} \widehat{B}_{11} (8K_2 + 3l_j \cos 2\alpha_i) \\
 &+ 20l_j^2 \widehat{A}_{11} \left[ S_{x0}^* (3x_R - l_j \sin \alpha_i) + S_{y0}^* (3y_R + l_j \cos \alpha_i) \right] + 20l_j^2 \widehat{B}_{11}^2 \sin 2\alpha_i \\
 &\left. + 120S_{x0}^* S_{y0}^* \right\}
 \end{aligned}$$

$$\begin{aligned}
 \int_s S_{x1}^* S_{\omega 1}^* ds &= \sum_{i=1}^{R1} \sum_{j=1}^{R2} \left[ \int_0^{l_j} S_{x1}^* S_{\omega 1}^* dl_j \right] = \sum_{i=1}^{R1} \sum_{j=1}^{R2} \frac{l_j}{120} \left\{ 120 S_{x0}^* S_{\omega 0}^* \right. \\
 &+ 20 l_j \widehat{B}_{11} \left[ 3 S_{\omega 0}^* \sin \alpha_i - S_{x0}^* (2 K_4 + q) \right] - 5 l_j^2 \widehat{B}_{11}^2 \sin \alpha_i (8 K_4 - l_j) \\
 &+ l_j^2 \widehat{A}_{11}^2 \left[ 5 y_R (8 K_3 - l_j r) + 3 l_j \cos \alpha_i (4 K_3 + \Omega_R) \right] \\
 &+ l_j^2 \widehat{A}_{11} \widehat{B}_{11} \left[ 5 \sin \alpha_i (8 K_3 - l_j r) - 5 y_R (8 K_4 - l_j) - 3 l_j \cos \alpha_i (4 K_4 + q) \right] \\
 &\left. + 20 l_j \widehat{A}_{11} \left[ S_{\omega 0}^* (3 y_R + l_j \cos \alpha_i) + S_{x0}^* (2 K_3 + \Omega_R) \right] \right\} \\
 \int_s S_{y1}^* S_{\omega 1}^* ds &= \sum_{i=1}^{R1} \sum_{j=1}^{R2} \left[ \int_0^{l_j} S_{y1}^* S_{\omega 1}^* dl_j \right] = \sum_{i=1}^{R1} \sum_{j=1}^{R2} \frac{l_j}{120} \left\{ 120 S_{y0}^* S_{\omega 0}^* \right. \\
 &+ 20 l_j \widehat{B}_{11} \left[ 3 S_{\omega 0}^* \cos \alpha_i - S_{y0}^* (2 K_4 + q) \right] - 5 l_j^2 \widehat{B}_{11}^2 \cos \alpha_i (8 K_4 - l_j) \\
 &+ l_j^2 \widehat{A}_{11}^2 \left[ 5 x_R (8 K_3 - l_j r) - 3 l_j \sin \alpha_i (4 K_3 + \Omega_R) \right] \\
 &+ l_j^2 \widehat{A}_{11} \widehat{B}_{11} \left[ 5 \cos \alpha_i (8 K_3 - l_j r) - 5 x_R (8 K_4 - l_j) + 3 l_j \sin \alpha_i (4 K_4 + q) \right] \\
 &\left. + 20 l_j \widehat{A}_{11} \left[ S_{\omega 0}^* (3 x_R - l_j \sin \alpha_i) + S_{y0}^* (2 K_3 + \Omega_R) \right] \right\}
 \end{aligned}$$

The integrals in the Eq. (3.66) can be calculated in the following way:

$$\begin{aligned}
 E_{15} &= \int_s \sum_{k=1}^N \int_{n_{k-1}}^{n_k} \frac{\bar{Q}_{16k}}{\bar{Q}_{16R}} n dn ds = \sum_{i=1}^{R1} \sum_{j=1}^{R2} \left[ \int_0^{l_j} \sum_{k=1}^N \left( \int_{n_{k-1}}^{n_k} \frac{\bar{Q}_{16k}}{\bar{Q}_{16R}} n dn \right) dl_j \right] = \sum_{i=1}^{R1} \sum_{j=1}^{R2} l_j \widehat{B}_{16} \\
 E_{25} &= \int_s \sum_{k=1}^N \int_{n_{k-1}}^{n_k} \frac{\bar{Q}_{16k}}{\bar{Q}_{16R}} n y dn ds = \sum_{i=1}^{R1} \sum_{j=1}^{R2} \left\{ \int_0^{l_j} \sum_{k=1}^N \left[ \int_{n_{k-1}}^{n_k} \frac{\bar{Q}_{16k}}{\bar{Q}_{16R}} n y dn \right] dl_j \right\} \\
 &= \sum_{i=1}^{R1} \sum_{j=1}^{R2} \frac{l_j}{2} (2 \widehat{B}_{16} y_R + l_j \widehat{B}_{16} \cos \alpha_i + 2 \widehat{D}_{16} \sin \alpha_i) \\
 E_{35} &= \int_s \sum_{k=1}^N \int_{n_{k-1}}^{n_k} \frac{\bar{Q}_{16k}}{\bar{Q}_{16R}} n x dn ds = \sum_{i=1}^{R1} \sum_{j=1}^{R2} \left\{ \int_0^{l_j} \sum_{k=1}^N \left[ \int_{n_{k-1}}^{n_k} \frac{\bar{Q}_{16k}}{\bar{Q}_{16R}} n x dn \right] dl_j \right\} \\
 &= \sum_{i=1}^{R1} \sum_{j=1}^{R2} \frac{l_j}{2} (2 \widehat{B}_{16} x_R - l_j \widehat{B}_{16} \sin \alpha_i + 2 \widehat{D}_{16} \cos \alpha_i) \\
 E_{45} &= \int_s \sum_{k=1}^N \int_{n_{k-1}}^{n_k} \frac{\bar{Q}_{16k}}{\bar{Q}_{16R}} n \Omega dn ds = \sum_{i=1}^{R1} \sum_{j=1}^{R2} \left\{ \int_0^{l_j} \sum_{k=1}^N \left[ \int_{n_{k-1}}^{n_k} \frac{\bar{Q}_{16k}}{\bar{Q}_{16R}} n \Omega dn \right] dl_j \right\} \\
 &= \sum_{i=1}^{R1} \sum_{j=1}^{R2} l_j (K_3 \widehat{B}_{16} - K_4 \widehat{D}_{16})
 \end{aligned} \tag{3.108}$$

where:

$$\widehat{\mathbf{B}}_{16} = \frac{1}{2} \sum_{k=1}^N \left[ \frac{\bar{Q}_{16k}}{\bar{Q}_{16R}} (n_k^2 - n_{k-1}^2) \right], \quad \widehat{\mathbf{D}}_{16} = \frac{1}{3} \sum_{k=1}^N \left[ \frac{\bar{Q}_{16k}}{\bar{Q}_{16R}} (n_k^3 - n_{k-1}^3) \right] \quad (3.109)$$

Lastly the integrals from the Eq (3.71) can be calculated as follows:

$$\begin{aligned} & \int_s S_{y1}^* \sum_{k=1}^N \left( \int_{n_{k-1}}^{n_k} \frac{\bar{Q}_{16k}}{\bar{Q}_{16R}} dn \right) ds = \\ & = \sum_{i=1}^{R1} \sum_{j=1}^{R2} \frac{l_j \widehat{\mathbf{A}}_{16}}{6} \left[ l_j \widehat{\mathbf{A}}_{11} (3x_R - l_j \sin \alpha_i) + 3\widehat{\mathbf{B}}_{11} l_j \cos \alpha_i + 6S_{y0}^* \right] \\ \\ & \int_s S_{y1}^* \sum_{k=1}^N \left( \int_{n_{k-1}}^{n_k} \frac{\bar{Q}_{16k}}{\bar{Q}_{16R}} y dn \right) ds = \sum_{i=1}^{R1} \sum_{j=1}^{R2} \frac{l_j}{48} \left\{ 24S_{y0}^* \left[ \widehat{\mathbf{A}}_{16} (2y_R + l_j \cos \alpha_i) + 2\widehat{\mathbf{B}}_{16} \sin \alpha_i \right] \right. \\ & + 4l_j \widehat{\mathbf{A}}_{11} \widehat{\mathbf{B}}_{16} \left[ l_j (\cos 2\alpha_i - 1) + 6x_R \sin \alpha_i \right] + 8l_j \widehat{\mathbf{A}}_{16} \widehat{\mathbf{B}}_{11} \left[ l_j (1 + \cos 2\alpha_i) + 3y_R \cos \alpha_i \right] \\ & \left. + l_j \widehat{\mathbf{A}}_{11} \widehat{\mathbf{A}}_{16} \left[ 8l_j (2x_R \cos \alpha_i - y_R \sin \alpha_i) - 3l_j^2 \sin 2\alpha_i + 24x_R y_R \right] + 12l_j \widehat{\mathbf{B}}_{11} \widehat{\mathbf{B}}_{16} \sin 2\alpha_i \right\} \\ \\ & \int_s S_{y1}^* \sum_{k=1}^N \left( \int_{n_{k-1}}^{n_k} \frac{\bar{Q}_{16k}}{\bar{Q}_{16R}} x dn \right) ds = \sum_{i=1}^{R1} \sum_{j=1}^{R2} -\frac{l_j}{48} \left\{ 24S_{y0}^* \left[ \widehat{\mathbf{A}}_{16} (l_j \sin \alpha_i - 2x_R) - 2\widehat{\mathbf{B}}_{16} \cos \alpha_i \right] \right. \\ & + 4l_j \widehat{\mathbf{A}}_{11} \widehat{\mathbf{B}}_{16} (6x_R \cos \alpha_i + l_j \sin 2\alpha_i) + 8l_j \widehat{\mathbf{A}}_{16} \widehat{\mathbf{B}}_{11} (3x_R \cos \alpha_i + l_j \sin 2\alpha_i) \\ & \left. + 3l_j \widehat{\mathbf{A}}_{11} \widehat{\mathbf{A}}_{16} \left[ l_j^2 (\cos 2\alpha_i - 1) + 8x_R (l_j \sin \alpha_i - x_R) \right] - 12l_j \widehat{\mathbf{B}}_{11} \widehat{\mathbf{B}}_{16} (1 + \cos 2\alpha_i) \right\} \quad (3.110) \\ \\ & \int_s S_{y1}^* \sum_{k=1}^N \left( \int_{n_{k-1}}^{n_k} \frac{\bar{Q}_{16k}}{\bar{Q}_{16R}} \Omega dn \right) ds = \sum_{i=1}^{R1} \sum_{j=1}^{R2} \frac{l_j}{24} \left\{ 24S_{y0}^* (\widehat{\mathbf{A}}_{16} K_3 - \widehat{\mathbf{B}}_{16} K_4) \right. \\ & + l_j \widehat{\mathbf{A}}_{11} \widehat{\mathbf{A}}_{16} \left[ 4K_3 (3x_R - l_j \sin \alpha_i) + l_j r (2x_R - l_j \sin \alpha_i) \right] \\ & + l_j \widehat{\mathbf{A}}_{11} \widehat{\mathbf{B}}_{16} \left[ 4K_4 (l_j \sin \alpha_i - 3x_R) + l_j (l_j \sin \alpha_i - 2x_R) \right] \\ & \left. + 2l_j \widehat{\mathbf{A}}_{16} \widehat{\mathbf{B}}_{11} \cos \alpha_i (6K_3 + l_j r) + 4l_j \widehat{\mathbf{B}}_{11} \widehat{\mathbf{B}}_{16} \cos \alpha_i (q - 4K_4) \right\} \\ \\ & \int_s S_{x1}^* \sum_{k=1}^N \left( \int_{n_{k-1}}^{n_k} \frac{\bar{Q}_{16k}}{\bar{Q}_{16R}} dn \right) ds = \\ & = \sum_{i=1}^{R1} \sum_{j=1}^{R2} \frac{l_j \widehat{\mathbf{A}}_{16}}{6} \left[ l_j \widehat{\mathbf{A}}_{11} (3y_R + l_j \cos \alpha_i) + 3\widehat{\mathbf{B}}_{11} l_j \sin \alpha_i + 6S_{x0}^* \right] \end{aligned}$$

$$\begin{aligned}
 \int_s S_{x1}^* \sum_{k=1}^N \left( \int_{n_{k-1}}^{n_k} \frac{\bar{Q}_{16k}}{\bar{Q}_{16R}} y \, dn \right) ds &= \sum_{i=1}^{R1} \sum_{j=1}^{R2} \frac{l_j}{24} \left[ 3\hat{A}_{11}\hat{A}_{16}l_j^2 \cos \alpha_i (4y_R + l_j \cos \alpha_i) \right. \\
 &+ 12l_j\hat{A}_{16}S_{x0}^* \cos \alpha_i + 2l_j^2 (2\hat{A}_{16}\hat{B}_{11} + \hat{A}_{11}\hat{B}_{16}) \sin 2\alpha_i \\
 &\left. + 12(\hat{A}_{16}y_R + \hat{B}_{16} \sin \alpha_i)(2S_{x0}^* + \hat{A}_{11}l_j y_R + \hat{B}_{11}l_j \sin \alpha_i) \right] \\
 \int_s S_{x1}^* \sum_{k=1}^N \left( \int_{n_{k-1}}^{n_k} \frac{\bar{Q}_{16k}}{\bar{Q}_{16R}} x \, dn \right) ds &= \sum_{i=1}^{R1} \sum_{j=1}^{R2} \frac{l_j}{48} \left\{ 24S_{x0}^* \left[ \hat{A}_{16} (2x_R - l_j \sin \alpha_i) + 2\hat{B}_{16} \cos \alpha_i \right] \right. \\
 &+ l_j\hat{A}_{11}\hat{A}_{16} \left[ 8l_j (x_R \cos \alpha_i - 2y_R \sin \alpha_i) + 24x_R y_R - 3l_j^2 \sin 2\alpha_i \right] + 12l_j\hat{B}_{11}\hat{B}_{16} \sin 2\alpha_i \\
 &\left. + 8l_j\hat{A}_{16}\hat{B}_{11} \left[ 3x_R \sin \alpha_i + l_j (\cos 2\alpha_i - 3) \right] + 4l_j\hat{A}_{11}\hat{B}_{16} \left[ l_j (1 + \cos 2\alpha_i) + 6y_R \cos \alpha_i \right] \right\} \\
 \int_s S_{x1}^* \sum_{k=1}^N \left( \int_{n_{k-1}}^{n_k} \frac{\bar{Q}_{16k}}{\bar{Q}_{16R}} \Omega \, dn \right) ds &= \sum_{i=1}^{R1} \sum_{j=1}^{R2} -\frac{l_j}{24} \left\{ 24S_{x0}^* (\hat{B}_{16}K_4 - \hat{A}_{16}K_3) \right. \\
 &- l_j\hat{A}_{11}\hat{A}_{16} \left[ 4K_3 (l_j \cos \alpha_i + 3y_R) + l_j r (l_j \cos \alpha_i + 2y_R) \right] \\
 &+ l_j\hat{A}_{11}\hat{B}_{16} \left[ 4K_4 (l_j \cos \alpha_i + 3y_R) + l_j (l_j \cos \alpha_i + 2y_R) \right] \\
 &\left. + 2l_j\hat{B}_{11}\hat{B}_{16} \sin \alpha_i (6K_4 + l_j) - 2l_j\hat{A}_{16}\hat{B}_{11} \sin \alpha_i [6K_3 + l_j r] \right\} \\
 \int_s S_{\omega 1}^* \sum_{k=1}^N \left( \int_{n_{k-1}}^{n_k} \frac{\bar{Q}_{16k}}{\bar{Q}_{16R}} \, dn \right) ds &= \\
 &= \sum_{i=1}^{R1} \sum_{j=1}^{R2} \frac{l_j \hat{A}_{16}}{6} \left[ l_j \hat{A}_{11} (2K_3 + \Omega_R) - l_j \hat{B}_{11} (2K_4 + q) + 6S_{\omega 0}^* \right] \\
 \int_s S_{\omega 1}^* \sum_{k=1}^N \left( \int_{n_{k-1}}^{n_k} \frac{\bar{Q}_{16k}}{\bar{Q}_{16R}} y \, dn \right) ds &= \\
 \sum_{i=1}^{R1} \sum_{j=1}^{R2} \frac{l_j}{24} \left\{ l_j \hat{A}_{16} \cos \alpha_i \left[ l_j \hat{A}_{11} (8K_3 - rl_j) - l_j \hat{B}_{11} (8K_4 - l_j) + 12S_{\omega 0}^* \right] \right. \\
 &\left. - 4(\hat{A}_{16}y_R + \hat{B}_{16} \sin \alpha_i) \left[ l_j \hat{B}_{11} (2K_4 + q) - l_j \hat{A}_{11} (2K_3 + \Omega_R) - 6S_{\omega 0}^* \right] \right\} \\
 \int_s S_{\omega 1}^* \sum_{k=1}^N \left( \int_{n_{k-1}}^{n_k} \frac{\bar{Q}_{16k}}{\bar{Q}_{16R}} x \, dn \right) ds &= \\
 \sum_{i=1}^{R1} \sum_{j=1}^{R2} \frac{l_j}{24} \left\{ l_j \hat{A}_{16} \sin \alpha_i \left[ l_j \hat{B}_{11} (8K_4 - l_j) - l_j \hat{A}_{11} (8K_3 - rl_j) - 12S_{\omega 0}^* \right] \right. \\
 &\left. + 4(\hat{A}_{16}x_R + \hat{B}_{16} \cos \alpha_i) \left[ l_j \hat{A}_{11} (2K_3 + \Omega_R) - l_j \hat{B}_{11} (2K_4 + q) + 6S_{\omega 0}^* \right] \right\}
 \end{aligned}$$

$$\int_s S_{\omega 1}^* \sum_{k=1}^N \left( \int_{n_{k-1}}^{n_k} \frac{\bar{Q}_{16k}}{\bar{Q}_{16R}} \Omega dn \right) ds = \sum_{i=1}^{R1} \sum_{j=1}^{R2} \frac{l_j^2}{12} \left[ l_j (K_3 - K_4 r) (\hat{A}_{16} \hat{B}_{11} - \hat{B}_{16} \hat{A}_{11}) \right. \\ \left. + 6 (K_3 \hat{A}_{16} - K_4 \hat{B}_{16}) (K_3 \hat{A}_{11} - K_4 \hat{B}_{11} + 2S_{\omega 0}^*) \right]$$

where:

$$\hat{A}_{16} = \sum_{k=1}^N \left[ \frac{\bar{Q}_{16k}}{\bar{Q}_{16R}} (n_k - n_{k-1}) \right] \quad (3.111)$$

It is important to note that for a symmetric laminate, the values of  $\hat{B}_{11}$ ,  $\hat{B}_{66}$  and  $\hat{B}_{16}$  are equal to zero. Additionally, in the case of a balanced laminate, the value of  $\hat{A}_{16}$  should also be equal to zero.

## 4 FINITE ELEMENT FORMULATION

---

The finite element method (FEM) is a widely used numerical technique in engineering practice due to its versatility, accuracy, and efficiency in analyzing complex structures and systems. It provides a systematic approach to discretize a continuous problem into a finite number of smaller elements, allowing engineers to simulate and understand the behavior of real-world systems. One of the key advantages of FEM is its ability to handle a wide range of engineering problems, including structural analysis, fluid dynamics, heat transfer, electromagnetic fields, and more. By dividing a complex geometry into smaller, simpler elements, FEM can accurately capture the local variations in properties and behavior, enabling engineers to model and predict the response of the system under different loading and boundary conditions.

Furthermore, FEM provides a flexible framework for incorporating material nonlinearity, geometric nonlinearities, and various physical phenomena. It allows engineers to simulate and analyze the behavior of structures under extreme conditions, such as large deformations, non-linear material behavior, and contact interactions. This capability is particularly valuable in designing structures that need to withstand complex loading scenarios or to optimize the performance of systems under different constraints. Another advantage of FEM is its efficiency in terms of computational resources. By discretizing the problem domain into smaller elements, FEM reduces the complexity of the equations and allows for efficient solution techniques. The system of equations can be solved using matrix algebra and numerical methods, enabling engineers to obtain accurate results within reasonable computational time.

### 4.1 Thin-walled beam finite element

A thin-walled beam finite element is a specialized element used in finite element analysis to model slender structures with thin walls, such as beams, trusses, and frames. This type of element is designed to accurately capture the bending and torsional behavior of thin-walled structures while considering the geometric and material properties of the cross-section. The element discretizes the beam into smaller segments and approximates the displacement field along the beam using interpolation functions. The stiffness matrix of the thin-walled beam element is formulated based on the presented governing equations, incorporating the geometry, material properties, and interpolation functions.



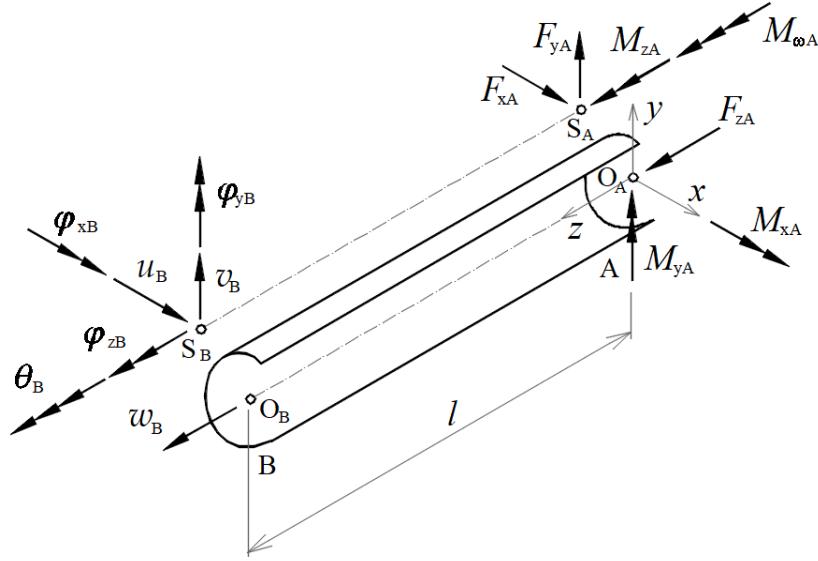


Fig. 4.1 Thin-walled beam finite element: nodal displacements and nodal forces

The Fig. 4.1 depicts a thin-walled beam finite element defined in a local coordinate system. The nodes of the finite element are marked as A and B. The  $z$ -axis represents the longitudinal axis of the finite element, passing through the centroids of all cross-sections. The  $x$  and  $y$  axes correspond to the principal central axes of inertia. O and S denote the material-weighted centroid and the material-weighted shear center of the cross-section at the nodes. The finite element has a total of 14 degrees of freedom, i.e., 7 nodal displacement components and 7 nodal force components at each node.

The vector of nodal displacements, as shown in Fig. 4.1, is given by:

$$\mathbf{u}^e = \begin{Bmatrix} \mathbf{u}_A^e \\ \mathbf{u}_B^e \end{Bmatrix}; \quad (\mathbf{u}_i^e)^T = \{w_i \quad u_i \quad v_i \quad \varphi_{zi} \quad \varphi_{xi} \quad \varphi_{yi} \quad \theta_i\}, \quad i = A, B \quad (4.1)$$

and the vector of nodal forces is represented as follows:

$$\mathbf{f}^e = \begin{Bmatrix} \mathbf{f}_A^e \\ \mathbf{f}_B^e \end{Bmatrix}; \quad (\mathbf{f}_i^e)^T = \{F_{zi} \quad F_{xi} \quad F_{yi} \quad M_{zi} \quad M_{xi} \quad M_{yi} \quad M_{\omega i}\}, \quad i = A, B \quad (4.2)$$

In Eqs. (4.1) and (4.2), the superscript "e" denotes the  $e$ -th finite element. It is important to note that the axial displacement  $w$ , as well as the axial force  $F_z$  and the bending moments  $M_x$  and  $M_y$ , are defined relative to the material-weighted centroid of the cross-section. On the other hand, all other displacements and nodal forces are defined with respect to the material-weighted shear center.

## 4.2 Virtual work principle

The principle of virtual work, which, in the absence of volume forces, is expressed as follows, will be applied to determine the equilibrium equations of a buckled thin-walled beam element:

$$\delta U = \delta W \rightarrow \int_V {}^t S_{ij} \delta {}^t \varepsilon_{ij} dV = \int_{A_\sigma} {}^t t_i \delta ({}^t u_i + {}^t \tilde{u}_i) dA_\sigma \quad i, j = 1, 2, 3 \quad (4.3)$$

where,  $\delta U$  is the virtual elastic strain energy,  $\delta W$  is the virtual work of external forces,  $S_{ij}$  represents the second Piola-Kirchhoff stress tensor,  $\varepsilon_{ij}$  represents the Green-Lagrange strain tensor,  $t_i$  denotes surface forces,  $u_i$  and  $\tilde{u}_i$  represents both linear and nonlinear displacement components, respectively, and the symbol  $\delta$  denotes virtual values. The superscript  $t$  indicates that the quantities refer to total values. By neglecting initial displacements and deformations prior to buckling, the following is obtained:

$${}^t S_{ij} = {}^0 S_{ij} + S_{ij}, \quad {}^t \varepsilon_{ij} = \varepsilon_{ij}, \quad {}^t t_i = {}^0 t_i + t_i, \quad {}^t u_i + {}^t \tilde{u}_i = u_i + \tilde{u}_i \quad (4.4)$$

where, the upper left index 0 on  $S_{ij}$  and  $t_i$  indicates that they refer to their starting or initial values, specifically to the values of internal and external forces in the case of undeformed beam. Quantities without the upper left index represent incremental values. By combining the Eqs. (3.16), (4.3), and (4.4) the following is obtained:

$$\int_V ({}^0 S_{ij} + S_{ij}) \delta (e_{ij} + \eta_{ij} + \tilde{e}_{ij}) dV = \int_{A_\sigma} ({}^0 t_i + t_i) \delta (u_i + \tilde{u}_i) dA_\sigma \quad (4.5)$$

and by ignoring the higher-order terms:

$$\int_V (S_{ij} \delta e_{ij} + {}^0 S_{ij} \delta e_{ij} + {}^0 S_{ij} \delta \eta_{ij} + {}^0 S_{ij} \delta \tilde{e}_{ij}) dV = \int_{A_\sigma} ({}^0 t_i \delta u_i + {}^0 t_i \delta \tilde{u}_i + t_i \delta u_i) dA_\sigma \quad (4.6)$$

Furthermore, assuming that the initial internal and external forces form a balanced system of forces, i.e.

$$\int_V {}^0 S_{ij} \delta e_{ij} dV = \int_{A_\sigma} {}^0 t_i \delta u_i dA_\sigma \quad (4.7)$$

By subtracting Eq. (4.7) from (4.6), the following is obtained:

$$\int_V S_{ij} \delta e_{ij} dV + \int_V {}^0 S_{ij} \delta \eta_{ij} dV + \int_V {}^0 S_{ij} \delta \tilde{e}_{ij} dV - \int_{A_\sigma} {}^0 t_i \delta \tilde{u}_i dA_\sigma = \int_{A_\sigma} t_i \delta u_i dA_\sigma \quad (4.8)$$

The linearized principle of virtual work is represented by Eq. (4.8), wherein the first integral corresponds to the virtual elastic strain energy of internal forces. The second integral accounts

for the standard geometric potential stemming from initial internal forces, while the third and fourth integrals represent the geometric potential arising from both initial internal and external forces, considering the effects of large rotations. Lastly, the fifth integral signifies the virtual work conducted by external forces. Alternatively, Eq. (4.8) can be written as:

$$\delta U_E + \delta U_G - \delta W = \delta \Pi = 0 \quad (4.9)$$

where:

$$\begin{aligned} \delta U_E &= \int_V S_{ij} \delta e_{ij} dV \\ \delta U_G &= \int_V {}^0 S_{ij} \delta \eta_{ij} dV + \int_V {}^0 S_{ij} \delta \tilde{e}_{ij} dV - \int_{A_\sigma} {}^0 t_i \delta \tilde{u}_i dA_\sigma \\ \delta W &= \int_{A_\sigma} t_i \delta u_i dA_\sigma \end{aligned} \quad (4.10)$$

where  $\Pi$  represents the total potential. The virtual elastic strain energy can be subdivided as follows:

$$\delta U_E = \delta U_E^{EB} + \delta U_E^{SD} + \delta U_E^{COL} + \delta U_E^{COR} \quad (4.11)$$

Where first term represents the virtual elastic strain energy arising from EB stress resultants given by Eq. (3.67), second term represents the virtual elastic strain energy arising from SD stress resultants and is given by Eq. (3.48), while the last two terms represent the virtual elastic strain energy arising due to coupling between EB and SD stress resultants and they are defined by Eqs. (3.72) and (3.74). The virtual elastic strain energy due to EB stress resultants can be calculated in the following way by applying the constitutive relation from Eq. (2.32):

$$\begin{aligned} \delta U_E^{EB} &= \int_0^l \int_s^N \sum_{k=1}^N \left[ \int_{n_{k-1}}^{n_k} (\sigma_{zk} \delta e_z + \tau_{zsk}^{SV} \delta e_{zs}^{SV}) dn \right] ds dz \\ &= \int_0^l \int_s^N \sum_{k=1}^N \left[ \int_{n_{k-1}}^{n_k} (\bar{Q}_{11k} e_z \delta e_z + \bar{Q}_{66k} e_{zs}^{SV} \delta e_{zs}^{SV} + \bar{Q}_{16k} e_{zs}^{SV} \delta e_z + \bar{Q}_{16k} e_z \delta e_{zs}^{SV}) dn \right] ds dz \\ &= \delta U_{E1}^{EB} + \delta U_{E2}^{EB} + \delta U_{E3}^{EB} \end{aligned} \quad (4.12)$$

The first term from Eq. (4.12) represents the virtual elastic strain energy arising from normal stress resultants, and is expanded by Eq. (3.19) as follows:

$$\begin{aligned}
 \delta U_{E1}^{EB} &= \int_0^l \bar{Q}_{11R} \int_s \sum_{k=1}^N \left[ \int_{n_{k-1}}^{n_k} \frac{\bar{Q}_{11k}}{\bar{Q}_{11R}} e_z \delta e_z dn \right] ds dz \\
 &= \int_0^l \bar{Q}_{11R} \left( A^* \frac{dw_o}{dz} \delta \frac{dw_o}{dz} + I_x^* \frac{d\varphi_x}{dz} \delta \frac{d\varphi_x}{dz} + I_y^* \frac{d\varphi_y}{dz} \delta \frac{d\varphi_y}{dz} + I_\omega^* \frac{d\theta}{dz} \delta \frac{d\theta}{dz} \right) dz
 \end{aligned} \tag{4.13}$$

The second term from Eq. (4.12) represents the virtual elastic strain energy arising from St. Venant stress resultants, and it can be expanded in the following way:

$$\delta U_{E2}^{EB} = \int_0^l \bar{Q}_{66R} \int_s \sum_{k=1}^N \left[ \int_{n_{k-1}}^{n_k} \frac{\bar{Q}_{66k}}{\bar{Q}_{66R}} e_{zs}^{SV} \delta e_{zs}^{SV} dn \right] ds dz = \int_0^l \bar{Q}_{66R} I_t^* \theta \delta \theta dz \tag{4.14}$$

The last term in Eq. (4.12) is due to the couplings between normal and St. Venant stress resultants and it can be extracted from Eq. (3.65) as:

$$\begin{aligned}
 \delta U_{E3}^{EB} &= \int_0^l \bar{Q}_{16R} \int_s \sum_{k=1}^N \left[ \int_{n_{k-1}}^{n_k} \frac{\bar{Q}_{16k}}{\bar{Q}_{16R}} (e_{zs}^{SV} \delta e_z + e_z \delta e_{zs}^{SV}) dn \right] ds dz \\
 &= 2 \int_0^l \bar{Q}_{16R} \left[ E_{15} \left( \theta \delta \frac{dw_o}{dz} + \frac{dw_o}{dz} \delta \theta \right) + E_{25} \left( \theta \delta \frac{d\varphi_x}{dz} + \frac{d\varphi_x}{dz} \delta \theta \right) \right. \\
 &\quad \left. - E_{35} \left( \theta \delta \frac{d\varphi_y}{dz} + \frac{d\varphi_y}{dz} \delta \theta \right) + E_{45} \left( \theta \delta \frac{d\theta}{dz} + \frac{d\theta}{dz} \delta \theta \right) \right] dz
 \end{aligned} \tag{4.15}$$

If the Eqs. (4.13), (4.14) and (4.15) are combined together, the expression for the virtual elastic strain energy arising from EB stress resultants is obtained as follows:

$$\begin{aligned}
 \delta U_E^{EB} &= \delta U_{E1}^{EB} + \delta U_{E2}^{EB} + \delta U_{E3}^{EB} \\
 &= \int_0^l \left\{ \bar{Q}_{11R} \left( A^* \frac{dw_o}{dz} \delta \frac{dw_o}{dz} + I_x^* \frac{d\varphi_x}{dz} \delta \frac{d\varphi_x}{dz} + I_y^* \frac{d\varphi_y}{dz} \delta \frac{d\varphi_y}{dz} + I_\omega^* \frac{d\theta}{dz} \delta \frac{d\theta}{dz} \right) + \bar{Q}_{66R} I_t^* \theta \delta \theta \right. \\
 &\quad + 2 \bar{Q}_{16R} \left[ E_{15} \left( \theta \delta \frac{dw_o}{dz} + \frac{dw_o}{dz} \delta \theta \right) + E_{25} \left( \theta \delta \frac{d\varphi_x}{dz} + \frac{d\varphi_x}{dz} \delta \theta \right) \right. \\
 &\quad \left. \left. - E_{35} \left( \theta \delta \frac{d\varphi_y}{dz} + \frac{d\varphi_y}{dz} \delta \theta \right) + E_{45} \left( \theta \delta \frac{d\theta}{dz} + \frac{d\theta}{dz} \delta \theta \right) \right] \right\} dz
 \end{aligned} \tag{4.16}$$

The virtual elastic strain energy arising from SD stress resultants can be rewritten from Eq. (3.48) in terms of displacements as:

$$\begin{aligned} \delta U_E^{SD} = \int_0^l \bar{Q}_{66R} \left[ \frac{A^*}{K_x} e_{zx}^{SD} \delta e_{zx}^{SD} + \frac{A^*}{K_y} e_{zy}^{SD} \delta e_{zy}^{SD} + \frac{I_t^*}{K_\omega} \theta^{SD} \delta \theta^{SD} + \frac{A^*}{K_{xy}} \left( e_{zx}^{SD} \delta e_{zy}^{SD} + e_{zy}^{SD} \delta e_{zx}^{SD} \right) \right. \\ \left. + \frac{\sqrt{A^* I_t^*}}{K_{x\omega}} \left( e_{zx}^{SD} \delta \theta^{SD} + \theta^{SD} \delta e_{zx}^{SD} \right) + \frac{\sqrt{A^* I_t^*}}{K_{y\omega}} \left( e_{zy}^{SD} \delta \theta^{SD} + \theta^{SD} \delta e_{zy}^{SD} \right) \right] dz \end{aligned} \quad (4.17)$$

Furthermore, the standrad geometric potential from Eq. (4.10) can be written as follows

$$\delta U_G = \delta U_{G1} + \delta U_{G2} + \delta U_{G3} \quad (4.18)$$

where:

$$\delta U_{G1} = \int_V {}^0 S_{ij} \delta \eta_{ij} dV, \quad \delta U_{G2} = \int_V {}^0 S_{ij} \delta \tilde{e}_{ij} dV, \quad \delta U_{G3} = - \int_{A_\sigma} {}^0 t_i \delta \tilde{u}_i dA_\sigma \quad (4.19)$$

By applying Eq. (3.21) the follwing can be obtained:

$$\begin{aligned} \delta U_{G1} = \int_V \left( {}^0 \sigma_z \delta \eta_z + {}^0 \tau_{zx} \delta \eta_{zx} + {}^0 \tau_{zy} \delta \eta_{zy} \right) dV \\ = \int_0^l \int_A \left\{ {}^0 \sigma_z \left( \frac{dw_o}{dz} + y \frac{d\varphi_x}{dz} - x \frac{d\varphi_y}{dz} + \Omega \frac{d\theta}{dz} \right) \delta \left( \frac{dw_o}{dz} + y \frac{d\varphi_x}{dz} - x \frac{d\varphi_y}{dz} + \Omega \frac{d\theta}{dz} \right) \right. \\ + {}^0 \sigma_z \left[ \frac{du_s}{dz} - (y - y_s) \frac{d\varphi_z}{dz} \right] \delta \left[ \frac{du_s}{dz} - (y - y_s) \frac{d\varphi_z}{dz} \right] \\ + {}^0 \sigma_z \left[ \frac{dv_s}{dz} + (x - x_s) \frac{d\varphi_z}{dz} \right] \delta \left[ \frac{dv_s}{dz} + (x - x_s) \frac{d\varphi_z}{dz} \right] \\ + {}^0 \tau_{zx} \left( \frac{dw_o}{dz} + y \frac{d\varphi_x}{dz} - x \frac{d\varphi_y}{dz} + \Omega \frac{d\theta}{dz} \right) \delta \left( -\varphi_y + \frac{\partial \Omega}{\partial x} \theta \right) + {}^0 \tau_{zx} \left[ \frac{dv_s}{dz} + (x - x_s) \frac{d\varphi_z}{dz} \right] \delta \varphi_z \\ + {}^0 \tau_{zx} \left( -\varphi_y + \frac{\partial \Omega}{\partial x} \theta \right) \delta \left( \frac{dw_o}{dz} + y \frac{d\varphi_x}{dz} - x \frac{d\varphi_y}{dz} + \Omega \frac{d\theta}{dz} \right) + {}^0 \tau_{zx} \varphi_z \delta \left[ \frac{dv_s}{dz} + (x - x_s) \frac{d\varphi_z}{dz} \right] \\ + {}^0 \tau_{zy} \left( \frac{dw_o}{dz} + y \frac{d\varphi_x}{dz} - x \frac{d\varphi_y}{dz} + \Omega \frac{d\theta}{dz} \right) \delta \left( \varphi_x + \frac{\partial \Omega}{\partial y} \theta \right) - {}^0 \tau_{zy} \left[ \frac{du_s}{dz} - (y - y_s) \frac{d\varphi_z}{dz} \right] \delta \varphi_z \\ + {}^0 \tau_{zy} \left( \varphi_x + \frac{\partial \Omega}{\partial y} \theta \right) \delta \left( \frac{dw_o}{dz} + y \frac{d\varphi_x}{dz} - x \frac{d\varphi_y}{dz} + \Omega \frac{d\theta}{dz} \right) \\ \left. - {}^0 \tau_{zx} \varphi_z \delta \left[ \frac{du_s}{dz} - (y - y_s) \frac{d\varphi_z}{dz} \right] \right\} dA dz \end{aligned} \quad (4.20)$$

and by ignoring the higer-order terms:

$$\begin{aligned}
 \delta U_{G1} = & \int_0^l \left\{ \frac{1}{2} \int_A {}^0\sigma_z [(x-x_s)^2 + (y-y_s)^2] dA \delta \left( \frac{d\varphi_z}{dz} \right)^2 + \int_A {}^0\sigma_z \Omega dA \delta \left( \frac{dw_o}{dz} \frac{d\theta}{dz} \right) \right. \\
 & + \int_A {}^0\sigma_z y dA \left[ \delta \left( \frac{dw_o}{dz} \frac{d\varphi_x}{dz} \right) - \delta \left( \frac{du_s}{dz} \frac{d\varphi_z}{dz} \right) \right] + \int_A {}^0\sigma_z x dA \left[ \delta \left( \frac{dv_s}{dz} \frac{d\varphi_z}{dz} \right) - \delta \left( \frac{dw_o}{dz} \frac{d\varphi_y}{dz} \right) \right] \\
 & + \frac{1}{2} \int_A {}^0\sigma_z dA \left[ \delta \left( \frac{dw_o}{dz} \right)^2 + \delta \left( \frac{du_s}{dz} \right)^2 + \delta \left( \frac{dv_s}{dz} \right)^2 + 2y_s \delta \left( \frac{du_s}{dz} \frac{d\varphi_z}{dz} \right) - 2x_s \delta \left( \frac{dv_s}{dz} \frac{d\varphi_z}{dz} \right) \right] \\
 & + \int_A {}^0\tau_{zx} dA \left[ \delta \left( \frac{dv_s}{dz} \varphi_z \right) - \delta \left( \frac{dw_o}{dz} \varphi_y \right) \right] + \int_A {}^0\tau_{zy} dA \left[ \delta \left( \frac{dw_o}{dz} \varphi_x \right) - \delta \left( \frac{du_s}{dz} \varphi_z \right) \right] \\
 & + \int_A [{}^0\tau_{zx} (x-x_s) + {}^0\tau_{zy} (y-y_s)] dA \delta \left( \varphi_z \frac{d\varphi_z}{dz} \right) + \int_A {}^0\tau_{zx} x dA \delta \left( \varphi_y \frac{d\varphi_y}{dz} \right) \\
 & \left. + \int_A {}^0\tau_{zy} y dA \delta \left( \varphi_x \frac{d\varphi_x}{dz} \right) - \int_A {}^0\tau_{zx} y dA \delta \left( \varphi_y \frac{d\varphi_x}{dz} \right) - \int_A {}^0\tau_{zy} x dA \delta \left( \varphi_x \frac{d\varphi_y}{dz} \right) \right\} dz
 \end{aligned} \tag{4.21}$$

If the stress resultants from Eq. (3.24) are included in the Eq. (4.21) the following is obtained:

$$\begin{aligned}
 \delta U_{G1} = & \int_0^l \left\{ {}^0F_x \left[ \delta \left( \frac{dv_s}{dz} \varphi_z \right) - \delta \left( \frac{dw_o}{dz} \varphi_y \right) \right] + {}^0F_y \left[ \delta \left( \frac{dw_o}{dz} \varphi_x \right) - \delta \left( \frac{du_s}{dz} \varphi_z \right) \right] \right. \\
 & + \frac{{}^0F_z}{2} \left[ \delta \left( \frac{dw_o}{dz} \right)^2 + \delta \left( \frac{du_s}{dz} \right)^2 + \delta \left( \frac{dv_s}{dz} \right)^2 + 2y_s \delta \left( \frac{du_s}{dz} \frac{d\varphi_z}{dz} \right) - 2x_s \delta \left( \frac{dv_s}{dz} \frac{d\varphi_z}{dz} \right) \right] \\
 & + {}^0M_x \left[ \delta \left( \frac{dw_o}{dz} \frac{d\varphi_x}{dz} \right) - \delta \left( \frac{du_s}{dz} \frac{d\varphi_z}{dz} \right) \right] + {}^0M_y \left[ \delta \left( \frac{dw_o}{dz} \frac{d\varphi_y}{dz} \right) - \delta \left( \frac{dv_s}{dz} \frac{d\varphi_z}{dz} \right) \right] \\
 & + \frac{{}^0\bar{K}}{2} \delta \left( \frac{d\varphi_z}{dz} \right)^2 + {}^0M_\omega \delta \left( \frac{dw_o}{dz} \frac{d\theta}{dz} \right) \left. \right\} dz \\
 & + \int_V [{}^0\tau_{zx} (x-x_s) + {}^0\tau_{zy} (y-y_s)] \delta \left( \varphi_z \frac{d\varphi_z}{dz} \right) dV + \int_V {}^0\tau_{zx} x \delta \left( \varphi_y \frac{d\varphi_y}{dz} \right) dV \\
 & + \int_V {}^0\tau_{zy} y \delta \left( \varphi_x \frac{d\varphi_x}{dz} \right) dV - \int_V {}^0\tau_{zx} y \delta \left( \varphi_y \frac{d\varphi_x}{dz} \right) dV - \int_V {}^0\tau_{zy} x \delta \left( \varphi_x \frac{d\varphi_y}{dz} \right) dV
 \end{aligned} \tag{4.22}$$

By applying Eq. (3.22) in the Eq. (4.19) the following can be obtained:

$$\begin{aligned}
 \delta U_{G2} &= \int_V \left( {}^0\sigma_z \delta \tilde{\varepsilon}_z + {}^0\tau_{zx} \delta \tilde{\varepsilon}_{zx} + {}^0\tau_{zy} \delta \tilde{\varepsilon}_{zy} \right) dV \\
 &= \frac{1}{2} \int_0^l \int_A \left\{ {}^0\sigma_z \delta \left[ (x-x_s) \frac{d}{dz} (\varphi_x \varphi_z) + (y-y_s) \frac{d}{dz} (\varphi_y \varphi_z) \right] \right. \\
 &\quad + {}^0\tau_{zx} \delta \left[ \varphi_z \varphi_x - 2x\varphi_y \frac{d\varphi_y}{dz} - 2(x-x_s)\varphi_z \frac{d\varphi_z}{dz} + y \frac{d}{dz} (\varphi_x \varphi_y) \right] \\
 &\quad \left. + {}^0\tau_{zy} \delta \left[ \varphi_z \varphi_y - 2y\varphi_x \frac{d\varphi_x}{dz} - 2(y-y_s)\varphi_z \frac{d\varphi_z}{dz} + x \frac{d}{dz} (\varphi_x \varphi_y) \right] \right\} dA dz \\
 &= \frac{1}{2} \int_0^l \left[ ({}^0M_x - {}^0F_z y_s) \delta \frac{d}{dz} (\varphi_y \varphi_z) - ({}^0M_y + {}^0F_z x_s) \delta \frac{d}{dz} (\varphi_x \varphi_z) \right. \\
 &\quad \left. + {}^0F_x \delta (\varphi_z \varphi_x) + {}^0F_y \delta (\varphi_z \varphi_y) \right] dz + \frac{1}{2} \int_V ({}^0\tau_{zx} y + {}^0\tau_{zy} x) \delta \frac{d}{dz} (\varphi_x \varphi_y) dV \\
 &\quad - \int_V [{}^0\tau_{zx} (x-x_s) + {}^0\tau_{zy} (y-y_s)] \delta \left( \varphi_z \frac{d\varphi_z}{dz} \right) dV \\
 &\quad - \int_V {}^0\tau_{zx} x \delta \left( \varphi_y \frac{d\varphi_y}{dz} \right) dV - \int_V {}^0\tau_{zy} y \delta \left( \varphi_x \frac{d\varphi_x}{dz} \right) dV
 \end{aligned} \tag{4.23}$$

If the Eq. (4.22) and (4.23) are added together, the following is obtained:

$$\begin{aligned}
 \delta U_{G1} + \delta U_{G2} &= \frac{1}{2} \int_0^l \left\{ {}^0F_z \left[ \delta \left( \frac{dw_o}{dz} \right)^2 + \delta \left( \frac{du_s}{dz} \right)^2 + \delta \left( \frac{dv_s}{dz} \right)^2 \right] \right. \\
 &\quad + ({}^0M_x - {}^0F_z y_s) \left[ \delta \frac{d}{dz} (\varphi_y \varphi_z) - 2\delta \left( \frac{du_s}{dz} \frac{d\varphi_z}{dz} \right) \right] + 2{}^0M_x \delta \left( \frac{dw_o}{dz} \frac{d\varphi_x}{dz} \right) \\
 &\quad - ({}^0M_y + {}^0F_z x_s) \left[ \delta \frac{d}{dz} (\varphi_x \varphi_z) + 2\delta \left( \frac{dv_s}{dz} \frac{d\varphi_z}{dz} \right) \right] + 2{}^0M_y \delta \left( \frac{dw_o}{dz} \frac{d\varphi_y}{dz} \right) \\
 &\quad + {}^0F_x \left[ \delta (\varphi_z \varphi_x) + 2\delta \left( \frac{dv_s}{dz} \varphi_z \right) - 2\delta \left( \frac{dw_o}{dz} \varphi_y \right) \right] + 2{}^0M_\omega \delta \left( \frac{dw_o}{dz} \frac{d\theta}{dz} \right) \\
 &\quad \left. + {}^0F_y \left[ \delta (\varphi_z \varphi_y) + 2\delta \left( \frac{dw_o}{dz} \varphi_x \right) - 2\delta \left( \frac{du_s}{dz} \varphi_z \right) \right] + {}^0\bar{K} \delta \left( \frac{d\varphi_z}{dz} \right)^2 \right\} dz \\
 &\quad + \frac{1}{2} \int_0^l \int_A ({}^0\tau_{zy} x - {}^0\tau_{zx} y) dA \left[ \delta \left( \varphi_y \frac{d\varphi_x}{dz} \right) - \delta \left( \varphi_x \frac{d\varphi_y}{dz} \right) \right] dz
 \end{aligned} \tag{4.24}$$

From [63] it can be seen that:

$$\int_A ({}^0\tau_{zy} x - {}^0\tau_{zx} y) dA = {}^0M_z - {}^0F_x y_s + {}^0F_y x_s \tag{4.25}$$

and by combining Eqs. (4.24) and (4.25) the following can be obtained:

$$\begin{aligned}
 \delta U_{G1} + \delta U_{G2} = & \frac{1}{2} \int_0^l \left\{ {}^0F_z \left[ \delta \left( \frac{dw_o}{dz} \right)^2 + \delta \left( \frac{du_s}{dz} \right)^2 + \delta \left( \frac{dv_s}{dz} \right)^2 \right] \right. \\
 & + ({}^0M_x - {}^0F_z y_s) \left[ \delta \frac{d}{dz} (\varphi_y \varphi_z) - 2\delta \left( \frac{du_s}{dz} \frac{d\varphi_z}{dz} \right) \right] + 2 {}^0M_x \delta \left( \frac{dw_o}{dz} \frac{d\varphi_x}{dz} \right) \\
 & - ({}^0M_y + {}^0F_z x_s) \left[ \delta \frac{d}{dz} (\varphi_x \varphi_z) + 2\delta \left( \frac{dv_s}{dz} \frac{d\varphi_z}{dz} \right) \right] + 2 {}^0M_y \delta \left( \frac{dw_o}{dz} \frac{d\varphi_y}{dz} \right) \\
 & + {}^0F_x \left[ \delta (\varphi_z \varphi_x) + 2\delta \left( \frac{dv_s}{dz} \varphi_z \right) - 2\delta \left( \frac{dw_o}{dz} \varphi_y \right) \right] + 2 {}^0M_\omega \delta \left( \frac{dw_o}{dz} \frac{d\theta}{dz} \right) \\
 & + {}^0M_z \left[ \delta \left( \varphi_y \frac{d\varphi_x}{dz} \right) - \delta \left( \varphi_x \frac{d\varphi_y}{dz} \right) \right] \\
 & + ({}^0F_y x_s - {}^0F_x y_s) \left[ \delta \left( \varphi_y \frac{d\varphi_x}{dz} \right) - \delta \left( \varphi_x \frac{d\varphi_y}{dz} \right) \right] \\
 & \left. + {}^0F_y \left[ \delta (\varphi_z \varphi_y) + 2\delta \left( \frac{dw_o}{dz} \varphi_x \right) - 2\delta \left( \frac{du_s}{dz} \varphi_z \right) \right] + {}^0\bar{K} \delta \left( \frac{d\varphi_z}{dz} \right)^2 \right\} dz
 \end{aligned} \tag{4.26}$$

If the axial force  ${}^0F_z$  is acting in the centroid of the cross-section, and if forces  ${}^0F_x$  and  ${}^0F_y$  are acting in the shear center of the cross-section the following is valid:

$$\begin{aligned}
 \delta U_{G3} = & - \int_{A_\sigma} ({}^0t_z \delta \tilde{w} + {}^0t_x \delta \tilde{u} + {}^0t_y \delta \tilde{v}) dA_\sigma = -\delta \int_{A_\sigma} ({}^0t_z \tilde{w} + {}^0t_x \tilde{u} + {}^0t_y \tilde{v}) dA_\sigma \\
 = & -\delta \left\{ \int_A [{}^0F_z \delta(x, y) \tilde{w} + {}^0F_x \delta(x - x_s, y - y_s) \tilde{u} + {}^0F_y \delta(x - x_s, y - y_s) \tilde{v}] dA \right\}_0^l
 \end{aligned} \tag{4.27}$$

Where  $\delta(x, y)$  and  $\delta(x - x_s, y - y_s)$  are the Dirac delta functions. On the basis of the Eq. (3.22) the solutions of the Dirac delta function are:

$$\begin{aligned}
 \delta(x, y) \tilde{w} = & -\frac{1}{2} (x_s \varphi_x \varphi_z + y_s \varphi_y \varphi_z) \\
 \delta(x - x_s, y - y_s) \tilde{u} = & \frac{1}{2} [-x_s \varphi_y^2 + y_s \varphi_x \varphi_y] \\
 \delta(x - x_s, y - y_s) \tilde{v} = & \frac{1}{2} [x_s \varphi_x \varphi_y - y_s \varphi_x^2]
 \end{aligned} \tag{4.28}$$

and by combining the Eqs. (4.27) and (4.28) it can be obtained:

$$\delta U_{G3} = \frac{1}{2} \left\{ {}^0F_z \delta(x_s \varphi_x \varphi_z + y_s \varphi_y \varphi_z) + {}^0F_x \delta(x_s \varphi_y^2 - y_s \varphi_x \varphi_y) - {}^0F_y \delta(x_s \varphi_x \varphi_y - y_s \varphi_x^2) \right\}_0^l \tag{4.29}$$

If the forces  ${}^0F_z$ ,  ${}^0F_x$ , and  ${}^0F_y$  are constant along the beam element length  $l$ , then Eq. (4.29)



can be written as follows:

$$\delta U_{G3} = \frac{1}{2} \int_0^l \left\{ {}^0F_z \delta \frac{d}{dz} (x_s \varphi_x \varphi_z + y_s \varphi_y \varphi_z) + {}^0F_x \delta \frac{d}{dz} (x_s \varphi_y^2 - y_s \varphi_x \varphi_y) - {}^0F_y \delta \frac{d}{dz} (x_s \varphi_x \varphi_y - y_s \varphi_x^2) \right\} dz \quad (4.30)$$

If the beam finite element from Fig. 4.1 is loaded only in the nodes A and B, then the standard geometric potential is calculated by combing the Eqs. (4.26) and (4.30):

$$\begin{aligned} \delta U_G &= \delta U_{G1} + \delta U_{G2} + \delta U_{G3} = \\ & \frac{1}{2} \int_0^l \left\{ {}^0F_z \left[ \delta \left( \frac{dw_o}{dz} \right)^2 + \delta \left( \frac{du_s}{dz} \right)^2 + \delta \left( \frac{dv_s}{dz} \right)^2 - 2x_s \delta \left( \frac{dv_s}{dz} \frac{d\varphi_z}{dz} \right) + 2y_s \delta \left( \frac{du_s}{dz} \frac{d\varphi_z}{dz} \right) \right] \right. \\ & + {}^0F_x \left[ \delta \left( \varphi_z \varphi_x \right) + 2\delta \left( \frac{dv_s}{dz} \varphi_z \right) - 2\delta \left( \frac{dw_o}{dz} \varphi_y \right) + 2x_s \delta \left( \varphi_y \frac{d\varphi_y}{dz} \right) - 2y_s \delta \left( \varphi_y \frac{d\varphi_x}{dz} \right) \right] \\ & + {}^0F_y \left[ \delta \left( \varphi_z \varphi_y \right) - 2\delta \left( \frac{du_s}{dz} \varphi_z \right) + 2\delta \left( \frac{dw_o}{dz} \varphi_x \right) - 2x_s \delta \left( \varphi_x \frac{d\varphi_y}{dz} \right) + 2y_s \delta \left( \varphi_x \frac{d\varphi_x}{dz} \right) \right] \\ & + {}^0M_x \left[ \delta \left( \varphi_z \frac{d\varphi_y}{dz} \right) + \delta \left( \varphi_y \frac{d\varphi_z}{dz} \right) - 2\delta \left( \frac{du_s}{dz} \frac{d\varphi_z}{dz} \right) + 2\delta \left( \frac{dw_o}{dz} \frac{d\varphi_x}{dz} \right) \right] \\ & - {}^0M_y \left[ \delta \left( \varphi_z \frac{d\varphi_x}{dz} \right) + \delta \left( \varphi_x \frac{d\varphi_z}{dz} \right) + 2\delta \left( \frac{dv_s}{dz} \frac{d\varphi_z}{dz} \right) - 2\delta \left( \frac{dw_o}{dz} \frac{d\varphi_y}{dz} \right) \right] \\ & \left. + {}^0M_z \left[ \delta \left( \varphi_y \frac{d\varphi_x}{dz} \right) - \delta \left( \varphi_x \frac{d\varphi_y}{dz} \right) \right] + {}^0\bar{K} \delta \left( \frac{d\varphi_z}{dz} \right)^2 + 2{}^0M_\omega \delta \left( \frac{dw_o}{dz} \frac{d\theta}{dz} \right) \right\} dz \quad (4.31) \end{aligned}$$

### 4.3 Updated Lagrangian (UL) formulation

In Fig. 4.2, incremental displacements of a thin-walled beam finite element are depicted. Here,  $C_0$  represents the initial or undeformed configuration,  $C_1$  represents the last known deformed configuration, and  $C_2$  represents the first upcoming unknown configuration. The Cartesian coordinate system  $(Z, X, Y)$  represents the global coordinate system, while  $(z, x, y)$  represents the local coordinate system of the finite element. The upper left index on the local axes defines the configuration of the finite element.

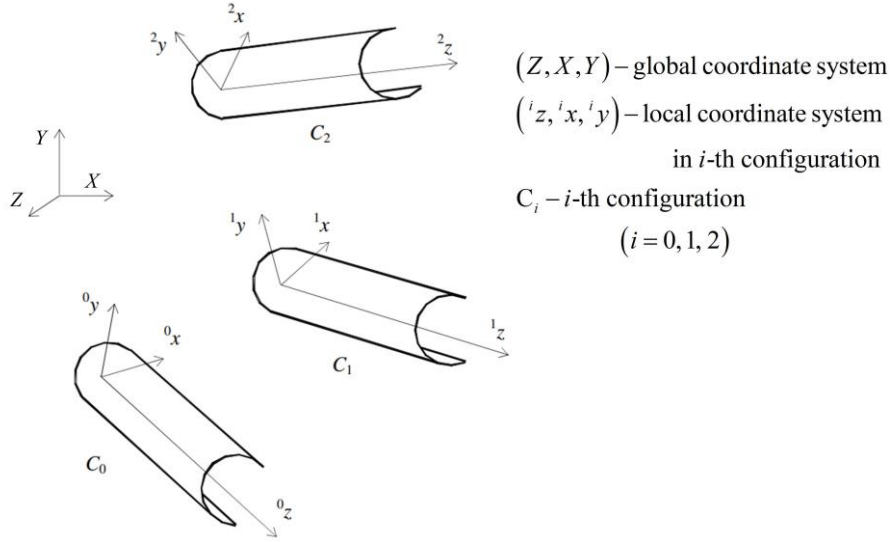


Fig. 4.2 Incremental displacements of the beam finite element

The principle of virtual work for the configuration  $C_2$  can be stated as follows:

$$\int_{^2V} {}^2\tau_{ij} \delta_2 e_{ij} \, dV = \delta_2^2 W \quad (4.32)$$

where  $\tau_{ij}$  represents the Cauchy (Euler) stress tensor,  $e_{ij}$  represents the Almansi strain tensor, and  $\delta W$  represents the virtual work done by external forces:

$$\delta_2^2 W = \int_{^2A_\sigma} {}^2t_i \delta(u_i + \tilde{u}_i) \, dA_\sigma + \int_{^2V} {}^2f_i \delta(u_i + \tilde{u}_i) \, dV \quad (4.33)$$

In Eq. (4.33)  $t_i$  represents surface or contact forces,  $f_i$  represents volumetric forces, and  $u_i$  and  $\tilde{u}_i$  represent the linear and nonlinear displacement components from Eq. (3.4). In Eqs. (4.32) and (4.33), the upper left index denotes the configuration in which the respective quantity appears. The absence of such an index indicates an incremental value. The lower left index represents the reference configuration for the given quantity. If both left indices are equal, the lower index can be omitted, for example,  ${}^2\tau_{ij} = {}^2\tau_{ij}$ . Assuming further that there are no volumetric forces acting on the finite element, the Eq. (4.33) reduces to:

$$\delta_2^2 W = \int_{^2A_\sigma} {}^2t_i \delta(u_i + \tilde{u}_i) \, dA_\sigma \quad (4.34)$$

Since all the values in Eq. (4.34) are defined with respect to the unknown configuration  $C_2$ , according to the Updated Lagrangian formulation, it is necessary to express them in terms of the last known configuration  $C_1$ . This is done as follows:

$$\int_{^2V} {}^2\tau_{ij} \delta_2 e_{ij} \, {}^2dV = \int_{^1V} {}^2S_{ij} \delta_1 \varepsilon_{ij} \, {}^1dV \quad (4.35)$$

where  $S_{ij}$  represents the second-order Piola-Kirchhoff stress tensor and  $\varepsilon_{ij}$  represents the Green-Lagrange strain tensor. On the other hand, since:

$${}^2t_i \, {}^2dA_\sigma = {}^2t_i \, {}^1dA_\sigma \quad (4.36)$$

by substituting Eqs. (4.35), (4.36) and (4.37) back into Eq. (4.32), the following is obtained:

$$\int_{^1V} {}^2S_{ij} \delta_1 \varepsilon_{ij} \, {}^1dV = \int_{^1A_\sigma} {}^2t_i \delta(u_i + \tilde{u}_i) \, {}^1dA_\sigma \quad (4.37)$$

Eq. (4.37) represents the equilibrium equations of the finite element in configuration  $C_2$ , with all quantities defined with respect to configuration  $C_1$ .

Furthermore, in incremental analysis, the tensor  $S_{ij}$  can be expressed as:

$${}^2S_{ij} = {}^1\tau_{ij} + {}^1S_{ij} = {}^1S_{ij} + {}^1S_{ij} \quad (4.38)$$

While according to Eq. (3.16):

$$\delta_1 \varepsilon_{ij} = \delta_1 e_{ij} + \delta_1 \eta_{ij} + \delta_1 \tilde{e}_{ij} \quad (4.39)$$

By substituting Eqs. (4.38) and (4.39) back to Eq. (4.37), the following is obtained:

$$\int_{^1V} {}^2S_{ij} (\delta_1 e_{ij} + \delta_1 \eta_{ij} + \delta_1 \tilde{e}_{ij}) \, {}^1dV = \int_{^1A_\sigma} {}^2t_i \delta(u_i + \tilde{u}_i) \, {}^1dA_\sigma \quad (4.40)$$

or, by the further arrangement:

$$\begin{aligned} \int_{^1V} {}^1S_{ij} \delta_1 \varepsilon_{ij} \, {}^1dV + \int_{^1V} {}^1S_{ij} \delta_1 \eta_{ij} \, {}^1dV + \int_{^1V} {}^1S_{ij} \delta_1 \tilde{e}_{ij} \, {}^1dV - \int_{^1A_\sigma} {}^2t_i \delta \tilde{u}_i \, {}^1dA_\sigma = \\ = \int_{^1A_\sigma} {}^2t_i \delta u_i \, {}^1dA_\sigma - \int_{^1V} {}^1S_{ij} \delta_1 e_{ij} \, {}^1dV \end{aligned} \quad (4.41)$$

Furthermore, the incremental constitutive equations can be expressed as follows:

$${}^1S_{ij} = {}^1C_{ijkl} \, {}^1\varepsilon_{kl} \quad (4.42)$$

where  $C_{ijkl}$  is the tensor of elastic constants [35], and it can be assumed that:

$$\int_{^1A_\sigma} {}^2t_i \delta \tilde{u}_i \, {}^1dA_\sigma = \int_{^1A_\sigma} ({}^1t_i + {}^1t_i) \delta \tilde{u}_i \, {}^1dA_\sigma \approx \int_{^1A_\sigma} {}^1t_i \delta \tilde{u}_i \, {}^1dA_\sigma \quad (4.43)$$

Then, according to Eq. (4.41) it follows that:

$$\begin{aligned}
 \int_{1V} {}_1C_{ijkl} \delta_1 \varepsilon_{kl} \delta_1 \varepsilon_{ij} \, dV + \int_{1V} {}_1S_{ij} \delta_1 \eta_{ij} \, dV + \int_{1V} {}_1S_{ij} \delta_1 \tilde{e}_{ij} \, dV - \int_{1A_\sigma} {}_1t_i \delta \tilde{u}_i \, dA_\sigma = \\
 = \int_{1A_\sigma} {}_2t_i \delta u_i \, dA_\sigma - \int_{1V} {}_1S_{ij} \delta_1 e_{ij} \, dV
 \end{aligned} \quad (4.44)$$

The Eq. (4.44) represents the tensor form of the incremental equilibrium equations of the finite element during the incremental displacement from configuration  $C_1$  to configuration  $C_2$ , formulated according to the Updated Lagrangian approach. However, since the Eq. (4.44) cannot be directly solved due to its nonlinearity in the incremental displacement, an approximate solution can be sought by introducing the following assumption:

$$\delta_1 \varepsilon_{ij} \approx \delta_1 e_{ij} \quad \rightarrow \quad {}_1S_{ij} \approx {}_1C_{ijkl} e_{kl} \quad (4.45)$$

which, ultimately, yields:

$$\begin{aligned}
 \int_{1V} {}_1C_{ijkl} e_{kl} \delta_1 e_{ij} \, dV + \int_{1V} {}_1S_{ij} \delta_1 \eta_{ij} \, dV + \int_{1V} {}_1S_{ij} \delta_1 \tilde{e}_{ij} \, dV - \int_{1A_\sigma} {}_1t_i \delta \tilde{u}_i \, dA_\sigma = \\
 = \delta_1^2 W - \delta_1^1 W
 \end{aligned} \quad (4.46)$$

where, for the finite element shown in Fig. 4.1:

$$\begin{aligned}
 \delta_1^2 W &= \int_{1A_\sigma} {}_2t_i \delta u_i \, dA_\sigma = (\delta \mathbf{u}^e)^T \mathbf{f}^e \\
 \delta_1^1 W &= \int_{1V} {}_1S_{ij} \delta_1 e_{ij} \, dV = (\delta \mathbf{u}^e)^T \mathbf{f}^e
 \end{aligned} \quad (4.47)$$

The Eq. (4.46) represents the linearized incremental equilibrium equations of the finite element formulated according to the Updated Lagrangian approach. If the Eq. (4.9) is rewritten as follows:

$$\delta U_E + \delta U_G = \delta W \quad (4.48)$$

Then, by comparing the Eq. (4.46) and (4.48) it can be concluded that both equations have the same left-hand side, with the only difference being the configuration with respect to which the values are defined. To define left hand-side of Eq. (4.48) in the configuration of the Eq. (4.46), the standard geometric potential needs to be rewritten as follows:

$$\begin{aligned}
 \delta^1 U_G = & \\
 & \frac{1}{2} \int_0^l \left\{ {}^1 F_z \left[ \delta \left( \frac{dw_o}{dz} \right)^2 + \delta \left( \frac{du_s}{dz} \right)^2 + \delta \left( \frac{dv_s}{dz} \right)^2 - 2x_s \delta \left( \frac{dv_s}{dz} \frac{d\varphi_z}{dz} \right) + 2y_s \delta \left( \frac{du_s}{dz} \frac{d\varphi_z}{dz} \right) \right] \right. \\
 & + {}^1 F_x \left[ \delta (\varphi_z \varphi_x) + 2 \delta \left( \frac{dv_s}{dz} \varphi_z \right) - 2 \delta \left( \frac{dw_o}{dz} \varphi_y \right) + 2x_s \delta \left( \varphi_y \frac{d\varphi_y}{dz} \right) - 2y_s \delta \left( \varphi_y \frac{d\varphi_x}{dz} \right) \right] \\
 & + {}^1 F_y \left[ \delta (\varphi_z \varphi_y) - 2 \delta \left( \frac{du_s}{dz} \varphi_z \right) + 2 \delta \left( \frac{dw_o}{dz} \varphi_x \right) - 2x_s \delta \left( \varphi_x \frac{d\varphi_y}{dz} \right) + 2y_s \delta \left( \varphi_x \frac{d\varphi_x}{dz} \right) \right] \\
 & + {}^1 M_x \left[ \delta \left( \varphi_z \frac{d\varphi_y}{dz} \right) + \delta \left( \varphi_y \frac{d\varphi_z}{dz} \right) - 2 \delta \left( \frac{du_s}{dz} \frac{d\varphi_z}{dz} \right) + 2 \delta \left( \frac{dw_o}{dz} \frac{d\varphi_x}{dz} \right) \right] \\
 & - {}^1 M_y \left[ \delta \left( \varphi_z \frac{d\varphi_x}{dz} \right) + \delta \left( \varphi_x \frac{d\varphi_z}{dz} \right) + 2 \delta \left( \frac{dv_s}{dz} \frac{d\varphi_z}{dz} \right) - 2 \delta \left( \frac{dw_o}{dz} \frac{d\varphi_y}{dz} \right) \right] \\
 & \left. + {}^1 M_z \left[ \delta \left( \varphi_y \frac{d\varphi_x}{dz} \right) - \delta \left( \varphi_x \frac{d\varphi_y}{dz} \right) \right] + {}^1 \bar{K} \delta \left( \frac{d\varphi_z}{dz} \right)^2 + 2 {}^1 M_\omega \delta \left( \frac{dw_o}{dz} \frac{d\theta}{dz} \right) \right\} dz
 \end{aligned} \tag{4.49}$$

then the the final solution of Eq. (4.46) can be expressed as follows:

$$\delta U_E + \delta^1 U_G = (\delta \mathbf{u}^e)^T ({}^2 \mathbf{f}^e - {}^1 \mathbf{f}^e) \tag{4.50}$$

In Eq. (4.50), the first part, in matrix formulation, yields the elastic or linear stiffness matrix  $\mathbf{k}_E^e$  of the finite element and is given by Eq. (4.11), while the second term yields the geometric or nonlinear stiffness matrix  $\mathbf{k}_G^e$  of the finite element and is given by the above Eq. (4.49).

#### 4.4 Hermite shape functions

In order to avoid shear locking, the shape functions for the rotations due to bending and torsion and the shape functions for the translations due to bending and torsion need to be connected. In order to achieve this, special Hermite shape functions will be used. To obtain these Hermite shape functions first interpolations for translations and twist rotation needs to be adopted with the following expression:

$$\begin{aligned}
 w_o &= \alpha_1 + \alpha_2 z, & u_s &= \alpha_3 + \alpha_4 z + \alpha_5 z^2 + \alpha_6 z^3, \\
 v_s &= \alpha_7 + \alpha_8 z + \alpha_9 z^2 + \alpha_{10} z^3, & \varphi_z &= \alpha_{11} + \alpha_{12} z + \alpha_{13} z^2 + \alpha_{14} z^3
 \end{aligned} \tag{4.51}$$

where  $\alpha_1$  through  $\alpha_{14}$  are the constants of integration. Due to sake of simplicity, if the shear stress increments are taken from Eq. (3.51) without coupling terms and by applying the Eq. (3.11), the following is obtained:

$${}^1F_x = \frac{\bar{Q}_{66R} A^*}{K_x} \left( \frac{dv_s}{dz} - \varphi_y \right), \quad {}^1F_y = \frac{\bar{Q}_{66R} A^*}{K_y} \left( \frac{dv_s}{dz} + \varphi_x \right), \quad {}^1T_\omega = \frac{\bar{Q}_{66R} I_t^*}{K_\omega} \left( \frac{d\varphi_z}{dz} + \theta \right) \quad (4.52)$$

Also the following expressions are valid:

$$\begin{aligned} {}^1M_x &= \bar{Q}_{11R} I_x^* \frac{d\varphi_x}{dz}, \quad {}^1M_y = \bar{Q}_{11R} I_y^* \frac{d\varphi_y}{dz}, \quad {}^1M_\omega = \bar{Q}_{11R} I_\omega^* \frac{d\theta}{dz} \\ {}^1F_y &= \frac{d^1M_x}{dz}, \quad {}^1F_x = -\frac{d^1M_y}{dz}, \quad {}^1T_\omega = \frac{d^1M_\omega}{dz} \\ \frac{d^2 {}^1F_y}{dz^2} &= 0, \quad \frac{d^2 {}^1F_x}{dz^2} = 0, \quad \frac{d^2 {}^1T_\omega}{dz^2} = 0 \end{aligned} \quad (4.53)$$

If the expression for the incremental force  ${}^1F_y$  from Eq. (4.52) is differentiated with respect to variable  $z$ , the following is obtained:

$$\frac{K_y}{\bar{Q}_{66R} A^*} \frac{d^1F_y}{dz} = \frac{d^2v_s}{dz^2} + \frac{d\varphi_x}{dz} \quad (4.54)$$

and if Eq. (4.53) is applied to Eq. (4.54):

$$\frac{K_y}{\bar{Q}_{66R} A^*} \frac{d^1F_y}{dz} = \frac{d^2v_s}{dz^2} + \frac{{}^1M_x}{\bar{Q}_{11R} I_x^*} \quad (4.55)$$

Now, by taking a further derivative of Eq. (4.55) with respect to the variable  $z$ , the following can be obtained:

$$\frac{K_y}{\bar{Q}_{66R} A^*} \frac{d^2 {}^1F_y}{dz^2} = \frac{d^3v_s}{dz^3} + \frac{1}{\bar{Q}_{11R} I_x^*} \frac{d^1M_x}{dz} \quad (4.56)$$

and lastly, by applying expressions from Eq. (4.53) it can be obtained that:

$${}^1F_y = -\bar{Q}_{11R} I_x^* \frac{d^3v_s}{dz^3} \quad (4.57)$$

From Eq. (4.51), the derivatives of vertical displacement  $v_s$  follow as:

$$v_s = \alpha_7 + \alpha_8 z + \alpha_9 z^2 + \alpha_{10} z^3, \quad \frac{dv_s}{dz} = \alpha_8 + 2\alpha_9 z + 3\alpha_{10} z^2, \quad \frac{d^3v_s}{dz^3} = 6\alpha_{10} \quad (4.58)$$

Finally by applying Eqs. (4.52), (4.57) and (4.58), the expression for  $\varphi_x$  can be obtained as:

$$\varphi_x = -\alpha_8 - 2\alpha_9 z - 3\alpha_{10} \left( z^2 + 2K_y \frac{\bar{Q}_{11R} I_x^*}{\bar{Q}_{66R} A^*} \right) \quad (4.59)$$

By taking the similar procedure, as to obtain  $\varphi_x$ , the expressions for  $\varphi_y$  and  $\theta$  can be obtained as:

$$\begin{aligned}\varphi_y &= \alpha_4 + 2\alpha_5 z + 3\alpha_6 \left( z^2 + 2K_x \frac{\bar{Q}_{11R} I_y^*}{\bar{Q}_{66R} A^*} \right) \\ \theta &= -\alpha_{12} - 2\alpha_{13} z - 3\alpha_{14} \left( z^2 + 2K_\omega \frac{\bar{Q}_{11R} I_\omega^*}{\bar{Q}_{66R} I_t^*} \right)\end{aligned}\quad (4.60)$$

If the expression for vertical displacement from Eq. (4.51) and the rotation around  $x$  axis from Eq. (4.59) is written in tensor notation, it can be seen that:

$$v_S = \mathbf{a}_{v_S} \boldsymbol{\alpha}_{v_S}, \quad \varphi_x = \mathbf{a}_{\varphi_x} \boldsymbol{\alpha}_{v_S} \quad (4.61)$$

where:

$$\begin{aligned}\mathbf{a}_{v_S} &= \{1 \quad z \quad z^2 \quad z^3\}, \quad \mathbf{a}_{\varphi_x} = \{0 \quad -1 \quad -2z \quad -3z^2 - \psi_y\}, \\ \boldsymbol{\alpha}_{v_S}^T &= \{\alpha_7 \quad \alpha_8 \quad \alpha_9 \quad \alpha_{10}\}, \quad \psi_y = 6K_y \frac{\bar{Q}_{11R} I_x^*}{\bar{Q}_{66R} A^*}\end{aligned}\quad (4.62)$$

By applying the boundary conditions for the A and B node of the finite element, it can be seen that:

$$\begin{aligned}z=0 &\rightarrow v_S = \alpha_7 = v_{SA}, \quad \varphi_x = -\alpha_8 - \alpha_{10} \psi_y = \varphi_{xA} \\ z=l &\rightarrow v_S = \alpha_7 + \alpha_8 l + \alpha_9 l^2 + \alpha_{10} l^3 = v_{SB}, \\ \varphi_x &= -\alpha_8 - 2\alpha_9 l - 3\alpha_{10} l^2 - \alpha_{10} \psi_y = \varphi_{xB}\end{aligned}\quad (4.63)$$

Where the vector of vertical displacements  $\mathbf{u}_v$  take the following form:

$$\mathbf{u}_v = \begin{Bmatrix} v_{SA} \\ \varphi_{xA} \\ v_{SB} \\ \varphi_{xB} \end{Bmatrix} = \begin{bmatrix} 1 & 0 & 0 & 0 \\ 0 & -1 & 0 & -\psi_y \\ 1 & l & l^2 & l^3 \\ 0 & -1 & -2l & -3l^2 - \psi_y \end{bmatrix} \begin{Bmatrix} \alpha_7 \\ \alpha_8 \\ \alpha_9 \\ \alpha_{10} \end{Bmatrix} = \mathbf{A} \boldsymbol{\alpha}_{v_S} \quad (4.64)$$

The vector of the constants of integrations can be derived from Eq. (4.64) as:

$$\boldsymbol{\alpha}_{v_S} = \mathbf{A}^{-1} \mathbf{u}_v \quad (4.65)$$

and by combining Eqs. (4.61) and (4.65), the following can be obtained:

$$v_S = \mathbf{a}_{v_S} \mathbf{A}^{-1} \mathbf{u}_v = \mathbf{N}_v \mathbf{u}_v, \quad \varphi_x = \mathbf{a}_{\varphi_x} \mathbf{A}^{-1} \mathbf{u}_v = \mathbf{N}_{\varphi_x} \mathbf{u}_v \quad (4.66)$$

where:

$$\mathbf{N}_v = \mathbf{a}_{v_S} \mathbf{A}^{-1}, \quad \mathbf{N}_{\varphi_x} = \mathbf{a}_{\varphi_x} \mathbf{A}^{-1} \quad (4.67)$$

If the derivatives of the respective shape function vector is needed the following procedure is employed:

$$\frac{d\mathbf{N}_v}{dz} = \mathbf{B}_v = \frac{d\mathbf{a}_{v_S}}{dz} \mathbf{A}^{-1}, \quad \frac{d\mathbf{N}_{\varphi_x}}{dz} = \mathbf{B}_{\varphi_x} = \frac{d\mathbf{a}_{\varphi_x}}{dz} \mathbf{A}^{-1} \quad (4.68)$$

By applying the similar procedure, as to obtain Eqs. (4.61)-(4.67), the interpolations for the displacements and twist rotations take the following form:

- axial displacement:

$$w_O = \mathbf{N}_w \mathbf{u}_w, \quad \frac{dw_O}{dz} = \frac{d\mathbf{N}_w}{dz} \mathbf{u}_w, \quad \mathbf{u}_w^T = \{w_A \quad w_B\} \quad (4.69)$$

$$\mathbf{N}_w = [1 - \zeta \quad \zeta], \quad \mathbf{B}_w = \frac{d\mathbf{N}_w}{dz} = \begin{bmatrix} -\frac{1}{l} & \frac{1}{l} \end{bmatrix}$$

- bending in the  $(z, y)$  plane:

$$v_S = \mathbf{N}_v \mathbf{u}_v, \quad \varphi_x = \mathbf{N}_{\varphi_x} \mathbf{u}_v, \quad \frac{dv_S}{dz} = \frac{d\mathbf{N}_v}{dz} \mathbf{u}_v, \quad \frac{d\varphi_x}{dz} = \frac{d\mathbf{N}_{\varphi_x}}{dz} \mathbf{u}_v$$

$$\mathbf{u}_v^T = \{v_{SA} \quad \varphi_{xA} \quad v_{SB} \quad \varphi_{xB}\}$$

$$\mathbf{N}_v = \begin{bmatrix} \frac{(\zeta - 1)(\phi_y + \zeta - 2\zeta^2)}{\phi_y} & \frac{l(\zeta - 1)(1 + \phi_y - 2\zeta)\zeta}{2\phi_y} \\ \frac{\zeta(\phi_y + 3\zeta - 2\zeta^2 - 1)}{\phi_y} & -\frac{l(\zeta - 1)(\phi_y + 2\zeta - 1)\zeta}{2\phi_y} \end{bmatrix}$$

$$\mathbf{B}_v = \frac{d\mathbf{N}_v}{dz} = \begin{bmatrix} \frac{1 - \phi_y - 6\zeta + 6\zeta^2}{l\phi_y} & \frac{-1 - \phi_y + 6\zeta + 2\zeta\phi_y - 6\zeta^2}{2\phi_y} \\ \frac{-1 + \phi_y + 6\zeta - 6\zeta^2}{l\phi_y} & \frac{-1 + \phi_y + 6\zeta - 2\zeta\phi_y - 6\zeta^2}{2\phi_y} \end{bmatrix} \quad (4.70)$$

$$\mathbf{N}_{\varphi_x} = \begin{bmatrix} -\frac{6\zeta(\zeta - 1)}{l\phi_y} & -\frac{(\zeta - 1)(\phi_y - 3\zeta)}{\phi_y} & \frac{6\zeta(\zeta - 1)}{l\phi_y} & \frac{\zeta(\phi_y + 3\zeta - 3)}{\phi_y} \end{bmatrix}$$

$$\mathbf{B}_{\varphi_x} = \frac{d\mathbf{N}_{\varphi_x}}{dz} = \begin{bmatrix} \frac{6 - 12\zeta}{l^2\phi_y} & \frac{-3 - \phi_y + 6\zeta}{l\phi_y} & \frac{12\zeta - 6}{l^2\phi_y} & \frac{-3 + \phi_y + 6\zeta}{l\phi_y} \end{bmatrix}$$

- bending in the  $(z, x)$  plane:



$$\begin{aligned}
 u_S &= \mathbf{N}_u \mathbf{u}_u, \quad \varphi_y = \mathbf{N}_{\varphi_y} \mathbf{u}_u, \quad \frac{du_S}{dz} = \frac{d\mathbf{N}_u}{dz} \mathbf{u}_u, \quad \frac{d\varphi_y}{dz} = \frac{d\mathbf{N}_{\varphi_y}}{dz} \mathbf{u}_u \\
 \mathbf{u}_u^T &= \{u_{SA} \quad \varphi_{yA} \quad u_{SB} \quad \varphi_{yB}\} \\
 \mathbf{N}_u &= \begin{bmatrix} -\frac{(\zeta-1)(\phi_x + \zeta - 2\zeta^2)}{\phi_x} & -\frac{l(\zeta-1)(1+\phi_x - 2\zeta)\zeta}{2\phi_x} \\ \frac{\zeta(\phi_x + 3\zeta - 2\zeta^2 - 1)}{\phi_x} & \frac{l(\zeta-1)(\phi_x + 2\zeta - 1)\zeta}{2\phi_x} \end{bmatrix} \\
 \mathbf{B}_u &= \frac{d\mathbf{N}_u}{dz} = \begin{bmatrix} \frac{1-\phi_x - 6\zeta + 6\zeta^2}{l\phi_x} & \frac{1+\phi_x - 6\zeta - 2\zeta\phi_x + 6\zeta^2}{2\phi_x} \\ \frac{-1+\phi_x + 6\zeta - 6\zeta^2}{l\phi_x} & \frac{1-\phi_x - 6\zeta + 2\zeta\phi_x + 6\zeta^2}{2\phi_x} \end{bmatrix} \\
 \mathbf{N}_{\varphi_y} &= \begin{bmatrix} \frac{6\zeta(\zeta-1)}{l\phi_x} & -\frac{(\zeta-1)(\phi_x - 3\zeta)}{\phi_x} & -\frac{6\zeta(\zeta-1)}{l\phi_x} & \frac{\zeta(\phi_x + 3\zeta - 3)}{\phi_x} \end{bmatrix} \\
 \mathbf{B}_{\varphi_y} &= \frac{d\mathbf{N}_{\varphi_y}}{dz} = \begin{bmatrix} \frac{12\zeta - 6}{l^2\phi_x} & \frac{-3 - \phi_x + 6\zeta}{l\phi_x} & \frac{6 - 12\zeta}{l^2\phi_x} & \frac{-3 + \phi_x + 6\zeta}{l\phi_x} \end{bmatrix}
 \end{aligned} \tag{4.71}$$

• torsion:

$$\begin{aligned}
 \varphi_z &= \mathbf{N}_{\varphi_z} \mathbf{u}_{\varphi_z}, \quad \theta = \mathbf{N}_{\theta} \mathbf{u}_{\varphi_z}, \quad \frac{d\varphi_z}{dz} = \frac{d\mathbf{N}_{\varphi_z}}{dz} \mathbf{u}_{\varphi_z}, \quad \frac{d\theta}{dz} = \frac{d\mathbf{N}_{\theta}}{dz} \mathbf{u}_{\varphi_z} \\
 \mathbf{u}_{\varphi_z}^T &= \{\varphi_{zA} \quad \theta_A \quad \varphi_{zB} \quad \theta_B\} \\
 \mathbf{N}_{\varphi_z} &= \begin{bmatrix} -\frac{(\zeta-1)(\phi_\omega + \zeta - 2\zeta^2)}{\phi_\omega} & \frac{l(\zeta-1)(1+\phi_\omega - 2\zeta)\zeta}{2\phi_\omega} \\ \frac{\zeta(\phi_\omega + 3\zeta - 2\zeta^2 - 1)}{\phi_\omega} & -\frac{l(\zeta-1)(\phi_\omega + 2\zeta - 1)\zeta}{2\phi_\omega} \end{bmatrix} \\
 \mathbf{B}_{\varphi_z} &= \frac{d\mathbf{N}_{\varphi_z}}{dz} = \begin{bmatrix} \frac{1-\phi_\omega - 6\zeta + 6\zeta^2}{l\phi_\omega} & \frac{-1-\phi_\omega + 6\zeta + 2\zeta\phi_\omega - 6\zeta^2}{2\phi_\omega} \\ \frac{-1+\phi_\omega + 6\zeta - 6\zeta^2}{l\phi_\omega} & \frac{-1+\phi_\omega + 6\zeta - 2\zeta\phi_\omega - 6\zeta^2}{2\phi_\omega} \end{bmatrix} \\
 \mathbf{N}_{\theta} &= \begin{bmatrix} -\frac{6\zeta(\zeta-1)}{l\phi_\omega} & -\frac{(\zeta-1)(\phi_\omega - 3\zeta)}{\phi_\omega} & \frac{6\zeta(\zeta-1)}{l\phi_\omega} & \frac{\zeta(\phi_\omega + 3\zeta - 3)}{\phi_\omega} \end{bmatrix} \\
 \mathbf{B}_{\theta} &= \frac{d\mathbf{N}_{\theta}}{dz} = \begin{bmatrix} \frac{6 - 12\zeta}{l^2\phi_\omega} & \frac{-3 - \phi_\omega + 6\zeta}{l\phi_\omega} & \frac{12\zeta - 6}{l^2\phi_\omega} & \frac{-3 + \phi_\omega + 6\zeta}{l\phi_\omega} \end{bmatrix}
 \end{aligned} \tag{4.72}$$

where:

$$\zeta = \frac{z}{l}, \quad \phi_y = 1 + \frac{12}{l^2} \frac{K_y \bar{Q}_{11R} I_x^*}{\bar{Q}_{66R} A^*}, \quad \phi_x = 1 + \frac{12}{l^2} \frac{K_x \bar{Q}_{11R} I_y^*}{\bar{Q}_{66R} A^*}, \quad \phi_\omega = 1 + \frac{12}{l^2} \frac{K_\omega \bar{Q}_{11R} I_\omega^*}{\bar{Q}_{66R} I_t^*} \quad (4.73)$$

As previously stated, the elastic stiffness matrix of a finite element is derived from the first term of the Eq. (4.50), i.e.

$$\delta U_E^{EB} + \delta U_E^{SD} + \delta U_E^{COL} + \delta U_E^{COR} = (\delta \mathbf{u}^e)^T \mathbf{k}_E^e \mathbf{u}^e \quad (4.74)$$

The geometric stiffness matrix is derived from the second term of the Eq. (4.50):

$$\delta^1 U_G = (\delta \mathbf{u}^e)^T \mathbf{k}_G^e \mathbf{u}^e \quad (4.75)$$

Since the beam finite element shown in Fig. 4.1 has 14 degrees of freedom, the dimensions of the elastic and the geometric stiffness matrix from Eqs. (4.74) and (4.75) will be 14×14. The elements of these matrices can be obtained by decomposing the total deformation of the finite element into those due to: axial loading, bending in the (z, y) plane, bending in the (z, x) plane and torsion, for which the interpolations are given in Eqs. (4.69)-(4.72).

For example, if the particular integral form Eq. (4.15) is solved, the following procedure is applied:

$$\begin{aligned} 2 \int_0^l \bar{Q}_{16R} E_{25} \theta \delta \frac{d\varphi_x}{dz} dz &= 2 \int_0^l \bar{Q}_{16R} E_{25} \delta \frac{d\varphi_x}{dz} \theta dz = \\ &= (\delta \mathbf{u}_v)^T \left[ 2 \int_0^l \bar{Q}_{16R} E_{25} (\mathbf{B}_{\varphi_x})^T \mathbf{N}_\theta dz \right] \mathbf{u}_{\varphi_z} \end{aligned} \quad (4.76)$$

and after integration, the following expression is derived:

$$(\delta \mathbf{u}_v)^T \left[ 2 \int_0^l \bar{Q}_{16R} E_{25} (\mathbf{B}_{\varphi_x})^T \mathbf{N}_\theta dz \right] \mathbf{u}_{\varphi_z} = (\delta \mathbf{u}_v)^T (\mathbf{k}_{B\varphi_x N_\theta}^e) \mathbf{u}_{\varphi_z} \quad (4.77)$$

where matrix  $\mathbf{k}_{B\varphi_x N_\theta}^e$  take the following form:

$$\mathbf{k}_{B\varphi_x N\theta}^e = 2\bar{Q}_{16R} E_{25} \begin{bmatrix} 0 & \frac{1}{l\phi_y} & 0 & -\frac{1}{l\phi_y} \\ -\frac{1}{l\phi_\omega} & \frac{1}{2}\left(-1 - \frac{1}{\phi_y} + \frac{1}{\phi_\omega}\right) & \frac{1}{l\phi_\omega} & \frac{1}{2}\left(-1 + \frac{1}{\phi_y} + \frac{1}{\phi_\omega}\right) \\ 0 & -\frac{1}{l\phi_y} & 0 & \frac{1}{l\phi_y} \\ \frac{1}{l\phi_\omega} & \frac{1}{2}\left(1 - \frac{1}{\phi_y} - \frac{1}{\phi_\omega}\right) & -\frac{1}{l\phi_\omega} & \frac{1}{2}\left(1 + \frac{1}{\phi_y} - \frac{1}{\phi_\omega}\right) \end{bmatrix} \quad (4.78)$$

It is important to note that the virtual displacements are defining the rows of the stiffness matrix, while the real displacements are defining the columns of the stiffness matrix. With that in hand, if the  $\mathbf{k}_{B\varphi_x N\theta}^e$  is added to the corresponding stiffness matrix, it would be responsible for change of the following elements of the stiffness matrix:

$$\mathbf{k}_E^e = \begin{array}{c} \vdots \\ \text{Row 3} \\ \vdots \\ \text{Row 5} \\ \vdots \\ \text{Row 10} \\ \vdots \\ \text{Row 12} \\ \vdots \end{array} \begin{bmatrix} \cdots & \text{Column 4} & \cdots & \text{Column 7} & \cdots & \text{Column 11} & \cdots & \text{Column 14} \\ \vdots & \vdots & \vdots & \vdots & \vdots & \vdots & \vdots & \vdots \\ \mathbf{k}_{E\ 3,4}^e + \mathbf{k}_{B\varphi_x N\theta\ 1,1}^e & \mathbf{k}_{E\ 3,7}^e + \mathbf{k}_{B\varphi_x N\theta\ 1,2}^e & \mathbf{k}_{E\ 3,11}^e + \mathbf{k}_{B\varphi_x N\theta\ 1,3}^e & \mathbf{k}_{E\ 3,14}^e + \mathbf{k}_{B\varphi_x N\theta\ 1,4}^e & & & & \\ \vdots & \vdots & \vdots & \vdots & & & & \\ \mathbf{k}_{E\ 5,4}^e + \mathbf{k}_{B\varphi_x N\theta\ 2,1}^e & \mathbf{k}_{E\ 5,7}^e + \mathbf{k}_{B\varphi_x N\theta\ 2,2}^e & \mathbf{k}_{E\ 5,11}^e + \mathbf{k}_{B\varphi_x N\theta\ 2,3}^e & \mathbf{k}_{E\ 5,14}^e + \mathbf{k}_{B\varphi_x N\theta\ 2,4}^e & & & & \\ \vdots & \vdots & \vdots & \vdots & & & & \\ \mathbf{k}_{E\ 10,4}^e + \mathbf{k}_{B\varphi_x N\theta\ 3,1}^e & \mathbf{k}_{E\ 10,7}^e + \mathbf{k}_{B\varphi_x N\theta\ 3,2}^e & \mathbf{k}_{E\ 10,11}^e + \mathbf{k}_{B\varphi_x N\theta\ 3,3}^e & \mathbf{k}_{E\ 10,14}^e + \mathbf{k}_{B\varphi_x N\theta\ 3,4}^e & & & & \\ \vdots & \vdots & \vdots & \vdots & & & & \\ \mathbf{k}_{E\ 12,4}^e + \mathbf{k}_{B\varphi_x N\theta\ 4,1}^e & \mathbf{k}_{E\ 12,7}^e + \mathbf{k}_{B\varphi_x N\theta\ 4,2}^e & \mathbf{k}_{E\ 12,11}^e + \mathbf{k}_{B\varphi_x N\theta\ 4,3}^e & \mathbf{k}_{E\ 12,14}^e + \mathbf{k}_{B\varphi_x N\theta\ 4,4}^e & & & & \\ \vdots & \vdots & \vdots & \vdots & & & & \end{bmatrix} \quad (4.79)$$

With solving all the integrals from Eq. (4.74), by following the procedure shown in Eqs. (4.76)-(4.79), and by adding them to the corresponding place in elastic stiffness matrix, the final element elastic stiffness matrix is defined. To obtain the geometric stiffness matrix of the element, the incremental beam-stress resultants at the  $z$ -cross section defined with reference to those at the element nodes should be introduced, i.e.

$$\begin{aligned}
 {}^1F_z &= -{}^1F_{zA} = {}^1F_{zB}, & {}^1F_x &= -{}^1F_{xA} = {}^1F_{xB} = -\frac{1}{l}({}^1M_{yA} + {}^1M_{yB}) \\
 {}^1F_y &= -{}^1F_{yA} = {}^1F_{yB} = \frac{1}{l}({}^1M_{xA} + {}^1M_{xB}) \\
 {}^1M_x &= -{}^1M_{xA} - {}^1F_{yA} z = -{}^1M_{xA} \left(1 - \frac{z}{l}\right) + {}^1M_{xB} \frac{z}{l} \\
 {}^1M_y &= -{}^1M_{yA} + {}^1F_{xA} z = -{}^1M_{yA} \left(1 - \frac{z}{l}\right) + {}^1M_{yB} \frac{z}{l} \\
 {}^1M_z &= -{}^1M_{zA} = {}^1M_{zB}, & {}^1M_\omega &= -{}^1M_{\omega A} = {}^1M_{\omega B} \\
 {}^1\bar{K} &= ({}^1F_z \alpha_z + {}^1M_x \alpha_x + {}^1M_y \alpha_y + {}^1M_\omega \alpha_\omega) = \\
 &= {}^1F_{zB} \alpha_z + \left[ -{}^1M_{xA} \left(1 - \frac{z}{l}\right) + {}^1M_{xB} \frac{z}{l} \right] \alpha_x + \left[ -{}^1M_{yA} \left(1 - \frac{z}{l}\right) + {}^1M_{yB} \frac{z}{l} \right] \alpha_y + {}^1M_{\omega B} \alpha_\omega
 \end{aligned} \tag{4.80}$$

After employing Eq. (4.80) in Eq. (4.75), and by solving all the integrals, following the same procedure as in Eqs. (4.76)-(4.79), and by adding them to the corresponding place in geometric stiffness matrix, the final element geometric stiffness matrix is derived.

#### 4.5 Finite element equation

Equation for the equilibrium of the  $e$ -th finite element, for the incremental displacement from configuration  $C_1$  to configuration  $C_2$ , with all quantities defined with respect to configuration  $C_1$  in accordance with the UL formulation, is given by:

$$(\delta_1 \mathbf{u}^e)^T ({}^1\mathbf{k}_E^e + {}^1\mathbf{k}_G^e)_1 \mathbf{u}^e = (\delta_1 \mathbf{u}^e)^T ({}^2\mathbf{f}^e + {}^1\mathbf{f}^e) \tag{4.81}$$

or if written in matrix form:

$${}^1\mathbf{k}_T^e \mathbf{u}^e = {}^1\mathbf{f}^e \tag{4.82}$$

where  $\mathbf{k}_T^e$  is the tangent stiffness matrix of the  $e$ -th finite element:

$${}^1\mathbf{k}_T^e = {}^1\mathbf{k}_E^e + {}^1\mathbf{k}_G^e \tag{4.83}$$

while  $\mathbf{f}^e$  represents the corresponding vector of incremental nodal loads:

$${}^1\mathbf{f}^e = {}^2\mathbf{f}^e + {}^1\mathbf{f}^e \tag{4.84}$$

Once the vector  $\mathbf{u}^e$  is available, one can obtain from Eq. (4.81) the following:

$${}^2\mathbf{f}^e = {}^1\mathbf{f}^e + ({}^1\mathbf{k}_E^e + {}^1\mathbf{k}_G^e)_1 \mathbf{u}^e \tag{4.85}$$

in which the vector  ${}^2\mathbf{f}^e$  contains the force components acting on the element at  $C_2$ , but which

are stated in the direction of the element axes at  $C_1$ . To obtain the nodal force vector which contains components acting on and stated in  $C_2$ , a force recovery procedure based on the conventional approach [42] is adopted, i.e.

$${}^2\mathbf{f}^e = {}^2\mathbf{T}^e {}^1\mathbf{f}^e \quad (4.86)$$

where  ${}^2\mathbf{T}^e$  is the incremental transformation matrix for relating the axes of the  $e$ -th beam element in  $C_1$  and  $C_2$ , respectively. In this work, the procedure for developing such a matrix is based on the concept of semitangential rotations [4] and is reported in [64,67].

After performing the standard assembling procedure, the overall incremental equilibrium equations for the structure can be obtained as:

$$\left( {}^1\mathbf{K}_E + {}^1\mathbf{K}_G \right) \mathbf{U} = {}^2\mathbf{P} - {}^1\mathbf{P}, \quad {}^1\mathbf{K}_E = \sum_e \left( {}^1\mathbf{t}^e \right)^T {}^1\mathbf{k}_E^e {}^1\mathbf{t}^e, \quad {}^1\mathbf{K}_G = \sum_e \left( {}^1\mathbf{t}^e \right)^T {}^1\mathbf{k}_G^e {}^1\mathbf{t}^e \quad (4.87)$$

where  ${}^1\mathbf{K}_E$  and  ${}^1\mathbf{K}_G$  denote the incremental elastic and geometric stiffness matrices of the structure, respectively,  $\mathbf{U}$  is the incremental displacement vector,  ${}^1\mathbf{P}$  and  ${}^2\mathbf{P}$  denote the vectors of external loads applied on the structure at  $C_1$  and  $C_2$ , respectively, while the matrix  ${}^1\mathbf{t}^e$  transforms the  $e$ -th beam element from the corresponding local coordinate system  $({}^1z, {}^1x, {}^1y)$  in  $C_1$  configuration to the global coordinate system  $(Z, X, Y)$ .

When the linearised stability analysis is sufficient, which provides no message concerning pre- and post-buckling response of a structure, an eigenvalue approach can be appealing. In such a case,  $C_1$  is assumed to be an undeformed stressed configuration of the structure,  $C_2$  is a buckled configuration. During the buckling deformation from  $C_1$  to  $C_2$ , and the external loads are assumed to remain unchanged. Thus, the buckling (critical) load  $\mathbf{P}_{cr}$  can be represented as a multiplication of a reference load  $\hat{\mathbf{P}}$  by a proportional parameter  $\Lambda$ , i.e.  $\mathbf{P}_{cr} = {}^2\mathbf{P} = {}^1\mathbf{P} = \Lambda \hat{\mathbf{P}}$ . Accordingly, the incremental geometric stiffness matrix  $\mathbf{K}_G$  can be linearized as  $\mathbf{K}_G = \Lambda \hat{\mathbf{K}}_G$ , where  $\hat{\mathbf{K}}_G \neq \hat{\mathbf{K}}_G(\mathbf{U})$ , and one can derive from Eq. (4.87) the following eigenvalue problem:

$$\left( \mathbf{K}_E + \Lambda \hat{\mathbf{K}}_G \right) \mathbf{U} = \mathbf{0} \quad (4.88)$$

where the eigenvalue  $\Lambda$  and eigenvector  $\mathbf{U}$  denote a buckling load parameter and corresponding buckling deformation, respectively. For the sake of completeness, readers interested in further details about this procedure can refer to the work [63], conducted by the candidate's mentor.

## 5 COMPUTER PROGRAMS CCSC AND THINWALL V18

---

The computer program CCSC was developed based on the numerical algorithm presented in Chapter 3. Similarly, the computer program THINWALL, originally developed by the candidate's mentor in [63], was updated using the numerical algorithm presented in Chapter 4, resulting in a revised version called THINWALL V18.

The program CCSC, an acronym for the *Composite Cross-Section Calculation*, was created by the author to implement the procedure outlined in Chapter 3. In the following subchapter, a description of this program will be provided.

The most significant difference in THINWALL V18 compared to its previous versions lies in the updates made to the Elastic and Geometric stiffness matrices, which are now based on Eqs. (4.74) and (4.75) respectively. Additionally, new shape functions described in Eqs. (4.69) to (4.72) have been applied. THINWALL V18 relies on the finite element method and is programmed in Fortran. It consists of a main program and several subroutines, all operating in double precision mode. For more detailed information about this program, readers are encouraged to refer to the candidate's mentor work [63]. In the following subchapter, only a brief description of the computer program THINWALL V18 will be provided.

Furthermore, this section will include numerical examples to demonstrate the accuracy and reliability of the aforementioned programs.

### 5.1 CCSC program description

The purpose of developing the CCSC program is to calculate the properties of composite cross-sections, which are required as input for the THINWALL V18 computer program. The main components of the CCSC program are the numerical algorithms presented in Chapter 3. Additionally, a flowchart depicting the program's structure can be found in Fig. 5.1.

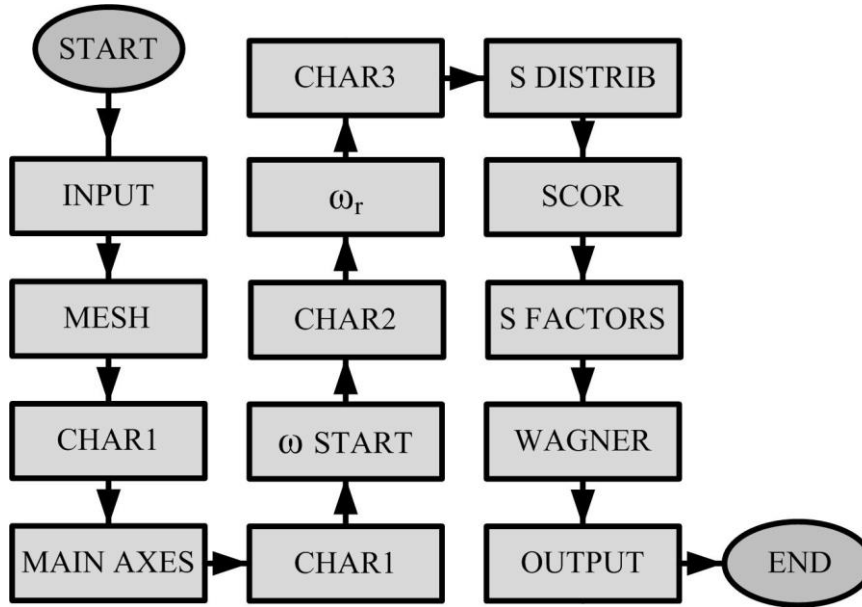


Fig. 5.1 Flowchart of the CCSC program

From Fig. 5.1, it is evident that the CCSC program consists of 13 different subroutines in addition to the main program. CCSC is a straightforward program that runs linearly from START to END without iterations. The program begins by reading input parameters through the subroutine INPUT. The input file is a txt file containing the following information:

- the first line specifies the number of branches in the cross-section.
- For each branch, the start and end points, start and end branch thickness, and the number of divisions or elements in the branch need to be provided.
- After defining the branches of the cross-section, the number of layers need to be specified for the first branch.
- For each layer of the first branch, the program requires information about the material properties, including  $E_1$ ,  $E_2$ ,  $G_{12}$ ,  $\nu_{12}$ , ply angle ( $\theta$ ), and the relative ply thickness (a multiplier used to calculate the layer thickness based on the actual thickness of the branch).
- The previous two points need to be repeated for the each following branch of the cross-section.

Examples of input files for U and I profiles can be found in Fig. 5.2.

The subroutine MESH generates the mesh based on the input parameters and calculates the reduced stiffness, referent moduli and composite thickness components as defined in the Eqs. (2.32), (3.25), (3.80), (3.85), (3.102), (3.104), (3.109) and (3.111). It should be noted that the initial cross-section axes position is determined by the point with coordinates (0, 0).

The subroutine CHAR1 calculates various cross-section properties, including  $A^*$ ,  $\hat{S}_x^*$ ,  $\hat{S}_y^*$ ,  $\hat{I}_x^*$ ,  $\hat{I}_y^*$ ,  $\hat{I}_{xy}^*$  and  $I_t^*$  based on the Eqs. (3.79), (3.84) and (3.101).

In the MAIN AXES subroutine, the position of the material-weighted centroid is first calculated by the Eq. (3.78). Then, the entire cross-section is translated to the centroid position based on the Eq. (3.81). Using the parallel axis theorem, Eq. (3.89),  $\tilde{I}_x^*$ ,  $\tilde{I}_y^*$  and  $\tilde{I}_{xy}^*$  are computed. The position of the main axes is determined by the Eq. (3.83), and the cross-section is rotated accordingly, Eq. (3.87).

						5							
						0.0	0.0	5.0	0.0	1.0	1.0	100000.0	
						5.0	0.0	10.0	0.0	1.0	1.0	100000.0	
						5.0	0.0	5.0	10.0	1.0	1.0	100000.0	
						5.0	10.0	0.0	10.0	1.0	1.0	100000.0	
						5.0	10.0	10.0	10.0	1.0	1.0	100000.0	
						8							
						144.0e5		9.65e5		4.14e5	0.3	15	0.125
						144.0e5		9.65e5		4.14e5	0.3	-15	0.125
						144.0e5		9.65e5		4.14e5	0.3	15	0.125
						144.0e5		9.65e5		4.14e5	0.3	-15	0.125
3						144.0e5		9.65e5		4.14e5	0.3	-15	0.125
0.0	0.0					144.0e5		9.65e5		4.14e5	0.3	-15	0.125
20.0	0.0	20.0	0.0	1.0	1.0	100000.0		100000.0					
20.0	40.0	0.0	40.0	1.0	1.0	100000.0		100000.0					
8						144.0e5		9.65e5		4.14e5	0.3	15	0.125
140.0e5						8							
140.0e5	3.5e5					144.0e5		9.65e5		4.14e5	0.3	15	0.125
140.0e5	3.5e5	2.1e5	0.25	15	0.125	144.0e5		9.65e5		4.14e5	0.3	-15	0.125
140.0e5	3.5e5	2.1e5	0.25	15	0.125	144.0e5		9.65e5		4.14e5	0.3	15	0.125
140.0e5	3.5e5	2.1e5	0.25	-15	0.125	144.0e5		9.65e5		4.14e5	0.3	-15	0.125
140.0e5	3.5e5	2.1e5	0.25	-15	0.125	144.0e5		9.65e5		4.14e5	0.3	15	0.125
140.0e5	3.5e5	2.1e5	0.25	15	0.125	144.0e5		9.65e5		4.14e5	0.3	-15	0.125
140.0e5	3.5e5	2.1e5	0.25	-15	0.125	144.0e5		9.65e5		4.14e5	0.3	15	0.125
140.0e5	3.5e5	2.1e5	0.25	15	0.125	144.0e5		9.65e5		4.14e5	0.3	-15	0.125
8						144.0e5		9.65e5		4.14e5	0.3	15	0.125
140.0e5	3.5e5	2.1e5	0.25	0	0.125	8							
140.0e5	3.5e5	2.1e5	0.25	0	0.125	144.0e5		9.65e5		4.14e5	0.3	15	0.125
140.0e5	3.5e5	2.1e5	0.25	0	0.125	144.0e5		9.65e5		4.14e5	0.3	-15	0.125
140.0e5	3.5e5	2.1e5	0.25	0	0.125	144.0e5		9.65e5		4.14e5	0.3	15	0.125
140.0e5	3.5e5	2.1e5	0.25	0	0.125	144.0e5		9.65e5		4.14e5	0.3	-15	0.125
140.0e5	3.5e5	2.1e5	0.25	0	0.125	144.0e5		9.65e5		4.14e5	0.3	15	0.125
140.0e5	3.5e5	2.1e5	0.25	0	0.125	144.0e5		9.65e5		4.14e5	0.3	-15	0.125
140.0e5	3.5e5	2.1e5	0.25	0	0.125	144.0e5		9.65e5		4.14e5	0.3	15	0.125
8						144.0e5		9.65e5		4.14e5	0.3	15	0.125
140.0e5	3.5e5	2.1e5	0.25	15	0.125	8							
140.0e5	3.5e5	2.1e5	0.25	-15	0.125	144.0e5		9.65e5		4.14e5	0.3	15	0.125
140.0e5	3.5e5	2.1e5	0.25	15	0.125	144.0e5		9.65e5		4.14e5	0.3	-15	0.125
140.0e5	3.5e5	2.1e5	0.25	-15	0.125	144.0e5		9.65e5		4.14e5	0.3	15	0.125
140.0e5	3.5e5	2.1e5	0.25	-15	0.125	144.0e5		9.65e5		4.14e5	0.3	-15	0.125
140.0e5	3.5e5	2.1e5	0.25	15	0.125	144.0e5		9.65e5		4.14e5	0.3	15	0.125
140.0e5	3.5e5	2.1e5	0.25	-15	0.125	144.0e5		9.65e5		4.14e5	0.3	15	0.125
140.0e5	3.5e5	2.1e5	0.25	15	0.125	144.0e5		9.65e5		4.14e5	0.3	-15	0.125
140.0e5	3.5e5	2.1e5	0.25	15	0.125	144.0e5		9.65e5		4.14e5	0.3	15	0.125
						8							
						144.0e5		9.65e5		4.14e5	0.3	15	0.125
						144.0e5		9.65e5		4.14e5	0.3	-15	0.125
						144.0e5		9.65e5		4.14e5	0.3	15	0.125
						144.0e5		9.65e5		4.14e5	0.3	-15	0.125
						144.0e5		9.65e5		4.14e5	0.3	15	0.125
						144.0e5		9.65e5		4.14e5	0.3	-15	0.125
						144.0e5		9.65e5		4.14e5	0.3	15	0.125
						144.0e5		9.65e5		4.14e5	0.3	-15	0.125
						144.0e5		9.65e5		4.14e5	0.3	15	0.125
						144.0e5		9.65e5		4.14e5	0.3	-15	0.125
						144.0e5		9.65e5		4.14e5	0.3	15	0.125
						144.0e5		9.65e5		4.14e5	0.3	-15	0.125
						144.0e5		9.65e5		4.14e5	0.3	15	0.125
						144.0e5		9.65e5		4.14e5	0.3	-15	0.125

(a) (b)  
 Fig. 5.2 Examples of the txt input files for: (a) U profile, (b) I profile

After the MAIN AXES subroutine, the CHAR1 subroutine is executed again to calculate the



cross-section properties  $I_x^*$  and  $I_y^*$ . It also verifies if the properties  $S_x^*$ ,  $S_y^*$  and  $I_{xy}^*$  are equal to zero.

The  $\omega$  START subroutine calculates the warping function for the entire cross-section, considering the pole set at the centroid of the cross-section and the starting point defined by the first point specified in the input file, Eq. (3.94). The coordinates of the starting point are adjusted based on the translation and rotation of the cross-section.

The CHAR2 subroutine calculates the properties  $S_\omega^*$ ,  $I_{x\omega}^*$  and  $I_{y\omega}^*$  by the Eqs. (3.96) and (3.98) and determines the position of the material-weighted shear center by the Eq. (3.95).

The  $\omega_r$  subroutine calculates the principal warping function for the entire cross-section, Eq. (3.97).

The CHAR3 subroutine determines the warping constant  $I_\omega^*$ , by the Eq. (3.99).

In the S DISTRIB subroutine, the distributions of  $S_x^*$ ,  $S_y^*$  and  $S_\omega^*$  are calculated for the entire cross-section, Eq. (3.105).

The SCOR subroutine carries out the correction procedure, if necessary, as depicted in Fig. 3.11.

In the subsequent S FACTORS and WAGNER subroutines, all the shear factors and Wagner coefficients are computed, Eqs. (3.49), (3.52), (3.64), (3.66), (3.71) and Eq. (3.73).

Lastly, in the OUTPUT subroutine, a file containing all the output information required for the THINWALL V18 program is generated.

## 5.2 THINWALL V18 brief program description

The THINWALL V18 program has been developed for the analysis of stability in thin-walled structures, both linear and nonlinear. Its purpose is to perform the discretization of structures using the thin-walled beam finite element, which is detailed in Fig. 4.1.

Linear stability analysis, known as bifurcation stability, is based on the assumption that the relationship between internal forces in the structure is qualitatively the same for each level of external loading. This relationship is described by Eq. (4.88).

Nonlinear stability analysis is conducted by solving the problem defined by Eq. (4.87). For this purpose, an incremental-iterative procedure with automatic adjustment of load increments (generalised displacement control method), as described in the work [63], is employed. To perform nonlinear stability analysis, disturbances need to be introduced into the ideal systems

(structures) considered in bifurcation stability. These disturbances initiate the corresponding deformation patterns and allow tracking of these patterns during the loading of the structure. Within each increment, iterations are repeated until the convergence condition is met or until the maximum allowable number of iterations within an increment is reached to prevent infinite iteration. The process of deformation continues until the level of external loading falls below the maximum allowable value or until the maximum allowable number of increments is reached. The interesting reader is advised to inform more about this program in candidate's mentor work [63]. Some brief information will be provided about subroutines of the program THINWALL V18 shown in the Fig. 5.3.

The subroutine INPUT reads the input file, which defines the following parameters:

- Geometry of the structure
- Type of analysis
- Geometry and characteristics of the finite elements
- Boundary conditions and external loads

The subprogram TRANMAT0 generates transformation matrices for the finite element configuration  $C_0$ , or the components of the vector  ${}^0\mathbf{z}_s$ ,  ${}^0\mathbf{x}_s$ , and  ${}^0\mathbf{y}_s$ .

The subroutine PREF, based on the initial values of external loads from the input file, constructs the reference load vector  $\hat{\mathbf{P}}$ .

The subroutine INITIAL initializes the initial values of all necessary parameters for:

- the structure
- each node of the structure
- each finite element

The subroutine ELMAT constructs the stiffness matrices of all finite elements, transforms them into the global coordinate system, and then subroutine EMATKON assembles them into the elastic stiffness matrix of the structure.

Similarly, the subroutine GMAT constructs the geometric stiffness matrices of the finite elements and transforms them into the global coordinate system. Subsequently, the subroutine GMATKON assembles them into the geometric stiffness matrix of the structure, to which corrective stiffness matrices are optionally added by calling the subroutine KORMAT.

In the case of bifurcation stability, the subroutine EIVALUE condenses the elastic and geometric stiffness matrices of the structure, forms the eigenvalue problem, calculates and outputs the eigenvalues and eigenvectors, with the previously obtained eigenvector expanded by adding

zero displacements.

The subroutine EXTMAT constructs the external stiffness matrices of the finite elements for the force recovery phase.

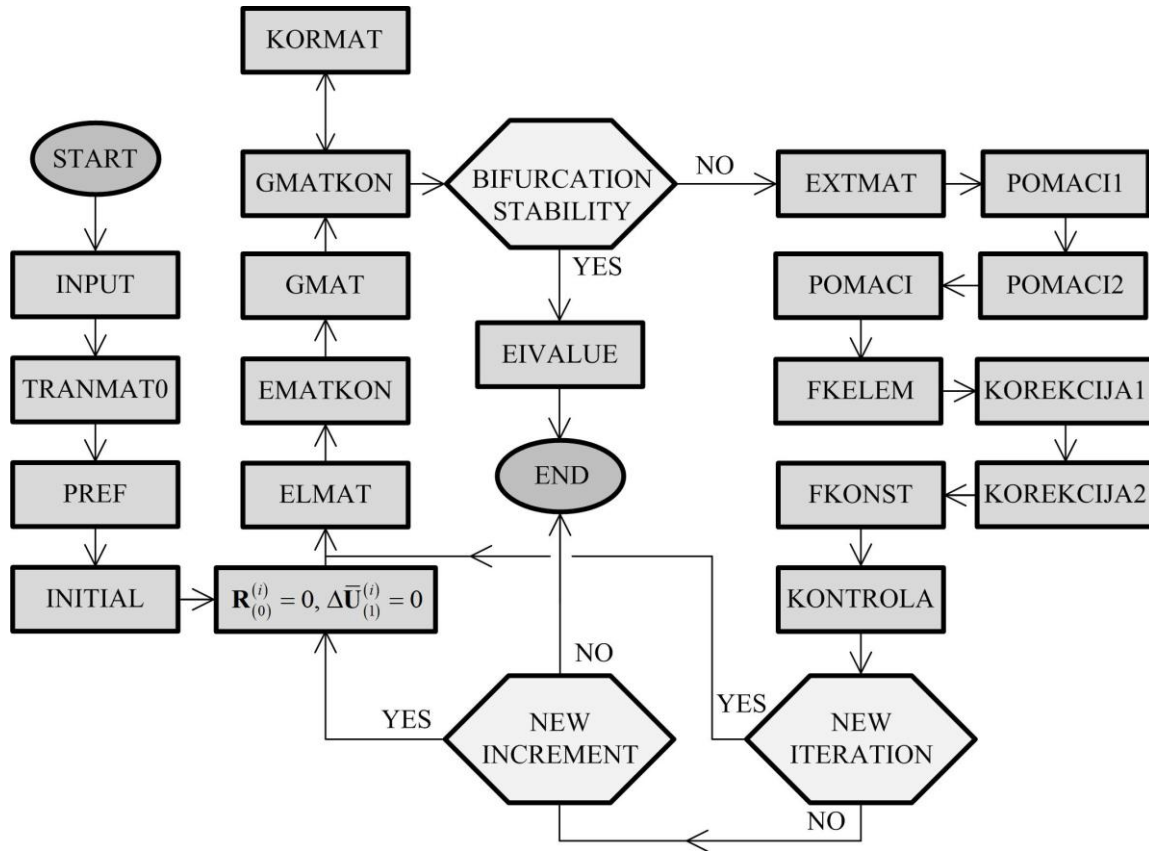


Fig. 5.3 Flowchart of the THINWALL V18 program

The subroutine POMACI1 condenses the tangent stiffness matrix of the structure and determines the incremental nodal displacement vector of the structure, while the subroutine POMACI2 condenses the unbalanced load vector and determines the incremental nodal displacement vector of the structure.

The subroutine POMACI determines the total incremental nodal displacement vector of the structure, as well as the incremental nodal displacement vectors of the finite elements in the local coordinate system.

For each finite element, the subroutine FKELEM determines the nodal force vector based on its incremental nodal displacement vector.

The subroutine KOREKCIJA1 corrects the coordinates of the structure nodes and the position of the reference axes of the nodes, while the subroutine KOREKCIJA2 corrects the geometry of the finite elements and constructs the transformation matrices of the finite elements for the next iteration.

The subroutine FKONST transforms the nodal force vectors of the finite elements and constructs the internal force vector of the structure.

Then, the subroutine KONTROLA calculates the unbalanced load vector and the specific work of the unbalanced load. If the specific work is greater than the allowed energy criterion tolerance defined by the input parameter, the program proceeds to a new iteration. If the specific work is smaller than the allowed energy criterion tolerance, the program proceeds to a new increment.

### 5.3 Numerical examples

The nonlinear stability analysis was performed using the generalised displacement control method [74], which served as an incremental-iterative procedure. It was necessary to introduce a small perturbation load. The updating of nodal coordinates and orientations of the cross-section axes for each beam element was carried out at the end of each loading step [63]. Iteration was stopped using an energy criterion with a tolerance value of  $10^{-6}$ .

To analyze the significance of shear effects on the stability behavior of the structure under consideration, a comparison of four beam models was conducted. The first model completely ignored shear deformability effects and was labeled 'SR' in the presented results. The second model included shear deformation couplings as presented in this paper and was labeled 'SD'. The third model, previously introduced by the authors in [66] and labeled 'SD1', neglected the off-diagonal members in Eq. (3.50) and introduced the shear deformation coupling effects through the virtual incremental strain energy. The last model entirely disregarded shear coupling effects and was denoted as 'SD2' in the given diagrams and tables. In all the examples, except example 1, the assumption that  $\sigma_s = 0$  was considered, corresponding to Eq. (2.30). It was assumed that all the plies had the same thickness<sup>1</sup>.

---

<sup>1</sup> Part of the work described in this section was published by the author of the thesis and his collaborators in peer-reviewed scientific papers ([7] and [8]), which were produced and published as part of the obligations foreseen in the curriculum of the doctoral study of the Faculty of Engineering of the University of Rijeka, Croatia, hence this section is based, partly directly derived and cited from this work.

### 5.3.1 Example 1

In the first example, the effects of anisotropy and laminate stacking sequence on the locations of the material-weighted centroid and shear center are investigated. This investigation is conducted by considering a thin-walled composite beam with an open section. The structural material used possesses the following properties:  $E_1 = 140$  GPa,  $E_2 = 3.5$  GPa,  $G_{12} = 2.1$  GPa,  $\nu_{12} = 0.25$ . Two cross-section shapes are considered and depicted in Fig. 5.4. It should be noted that the same thickness is maintained for all cross-section branches. A comparison is made between the results obtained and the work conducted by Lee [36].

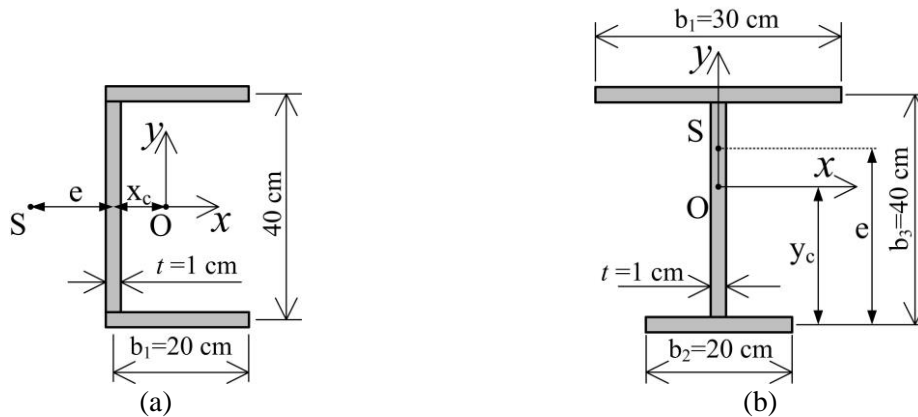


Fig. 5.4 Example 1 cross-section geometry: (a) monosymmetric U profile, (b) monosymmetric I profile

The positions of the material-weighted centroid and shear center for the monosymmetric U profile shown in Fig. 5.4 (a) are presented in Fig. 5.5. The fiber angle is varied in two ways. Firstly, an angle-ply laminate with the stacking sequence  $[\theta/-\theta]_{2S}$  is used for the flanges of the U profile, while a unidirectional laminate with the stacking sequence  $[0^\circ]_8$  is employed for the web. Secondly, a unidirectional laminate  $[0^\circ]_8$  is utilized for the flanges, while an angle-ply laminate  $[\theta/-\theta]_{2S}$  is employed for the web. In this example, separate tables for cross-section properties will not be provided due to the variations in the cross-section. However, the data pertaining to the material-weighted centroid and material-weighted shear center can be found in the figures presented.

Both simplification cases from Chapter 2 are also taken into consideration. The first assumption assumes  $\varepsilon_s = 0$ , which corresponds to Eq. (2.27). This assumption can be achieved by restricting the cross-section from deforming in the contour direction. The second assumption is that  $\sigma_s = 0$ , corresponding to Eq. (2.30). It should be noted that the results in [36] only consider the first assumption.

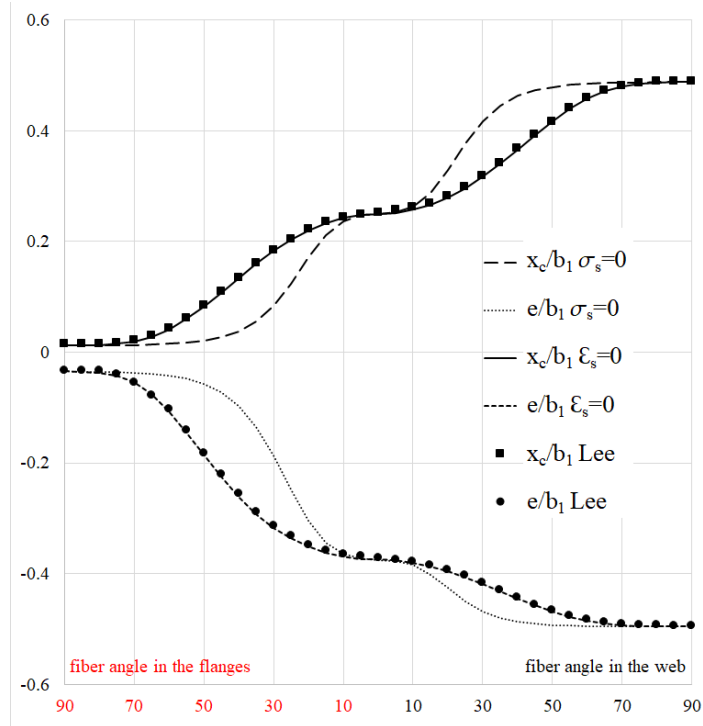


Fig. 5.5 Positions of material-weighted centroid and shear centre for the monosymmetric U profile with respect to fiber angle change in the flanges and the web

By observing Fig. 5.5, it becomes apparent that the results obtained through the comparable assumption align with the findings presented in [36]. The classical isotropic solution corresponds to a fiber angle of  $0^\circ$ . As the fiber angle is altered in the web, the material-weighted centroid shifts closer to the center of the flanges, while the shear center moves farther away. This indicates an increase in the distance between the centroid and the shear center. Conversely, when the fiber angle is changed in the flange, both the center of gravity and the shear center move towards the web, which is in contrast to the previous case.

Table 5.1 Example 1 U profile cross-section properties.

$A^*$ ( $\text{cm}^2$ )	$I_{x\text{max}}^*$ ( $\text{cm}^4$ )	$I_{y\text{max}}^*$ ( $\text{cm}^4$ )	$I_t^*$ ( $\text{cm}^4$ )	$I_{\omega\text{max}}^*$ ( $\text{cm}^4$ )	$\bar{Q}_{11R\text{max}}$ (GPa)	$\bar{Q}_{66R\text{max}}$ (GPa)
80	31486	3557	26.67	1069270	140	6.31967
$K_{x\text{max}}$	$K_{y\text{max}}$	$K_{\omega\text{max}}$	$K_{y\omega\text{max}}$	$\alpha_{z\text{max}}$ ( $\text{cm}^2$ )	$\alpha_{y\text{max}}$ (cm)	
7.2267	6.3476	0.003253	7.0793	815.362	47.226	

Cross-section properties are not independent of the material variations. Variations of the material-weighted cross-section properties for the monosymmetric U profile with respect to fiber angle change in the flanges and the web can be observed in the Fig. 5.6. The properties presented in the Fig. 5.6 are divided by their maximum values shown in the Table 5.1. It should

be noted that values presented in the Table 5.1 and Fig. 5.6 are calculated according to assumption that  $\sigma_s = 0$ , corresponding to constitutive equation given in Eq. (2.30).

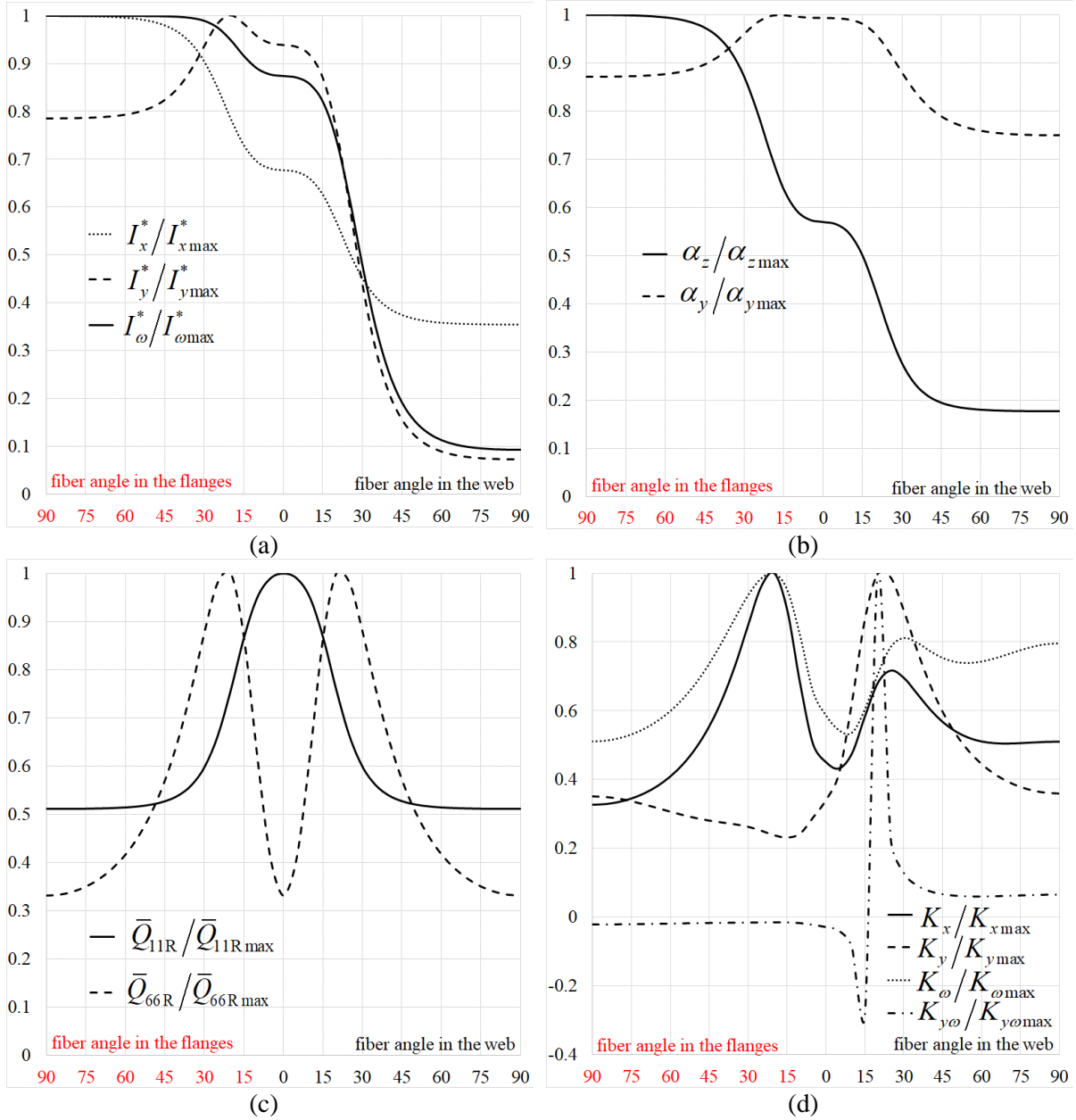


Fig. 5.6 Various U profile cross-section properties with respect to fiber angle change in the flanges and the web: (a)  $I_x^*$ ,  $I_y^*$  and  $I_\omega^*$ , (b)  $\alpha_z$  and  $\alpha_y$ , (c)  $\bar{Q}_{11R}$  and  $\bar{Q}_{66R}$ , (d)  $K_x$ ,  $K_y$ ,  $K_\omega$  and  $K_{y\omega}$

Fig. 5.7 depicts the positions of the material-weighted centroid and shear center for the monosymmetric I profile shown in Fig. 5.4 (b). The fiber angle is varied in the top and bottom flanges following the same principle as in the previous variation. In the first case, the bottom flange of the I profile is composed of an angle-ply laminate with the stacking sequence  $[\theta/-\theta]_{2S}$ , while the web and top flange consist of a unidirectional laminate with the stacking sequence  $[0^\circ]_8$ . In the second case, a unidirectional laminate is used in the bottom flange and the

web  $[0^\circ]_8$ , while the top flange is constructed with an angle-ply laminate  $[\theta/-\theta]_{2s}$ .

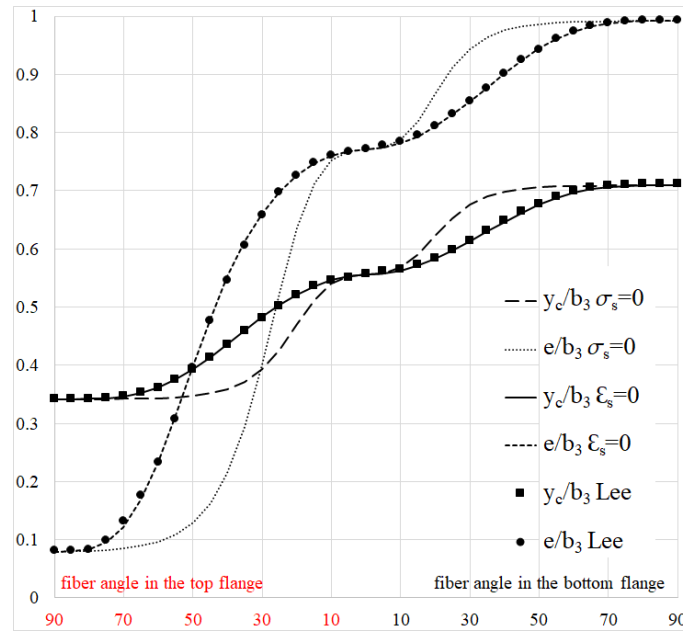


Fig. 5.7 Positions of material-weighted centroid and shear centre for the monosymmetric I profile with respect to fiber angle change in the top and the bottom flange

Table 5.2 Example 1 I profile cross-section properties with respect to fiber angle change in the top and bottom flange.

$A^*$ (cm <sup>2</sup> )	$I_{x\max}^*$ (cm <sup>4</sup> )	$I_{y\max}^*$ (cm <sup>4</sup> )	$I_t^*$ (cm <sup>4</sup> )	$I_{\omega\max}^*$ (cm <sup>4</sup> )	$\bar{Q}_{11R\max}$ (GPa)	$\bar{Q}_{66R\max}$ (GPa)
90	24893	2920	30	834845	140	4.913116
$K_x\max$	$K_y\max$	$K_\omega\max$	$ K_{x\omega} _{\max}$	$\alpha_z\max$ (cm <sup>2</sup> )	$ \alpha_x _{\max}$ (cm)	
2.1538	5.5071	0.002259	0.46387	383.382	30.221	

Similar to the previous analysis, the results obtained through the comparable assumption align with the findings presented in [36]. Furthermore, as the fiber angle is varied in the bottom flange, the centroid exhibits a slight upward movement, and the shear center approaches the top flange. When the fiber angle is varied in the top flange, the centroid gradually moves downward, while the shear center rapidly approaches the bottom flange. As a result, the centroid and shear center coincide near  $\theta = 50^\circ$  or  $\theta = 30^\circ$ , depending on the  $\epsilon_s$  or  $\sigma_s$  assumption. This indicates that bending-torsion can be decoupled for certain laminate stacking sequences, even in monosymmetric sections.



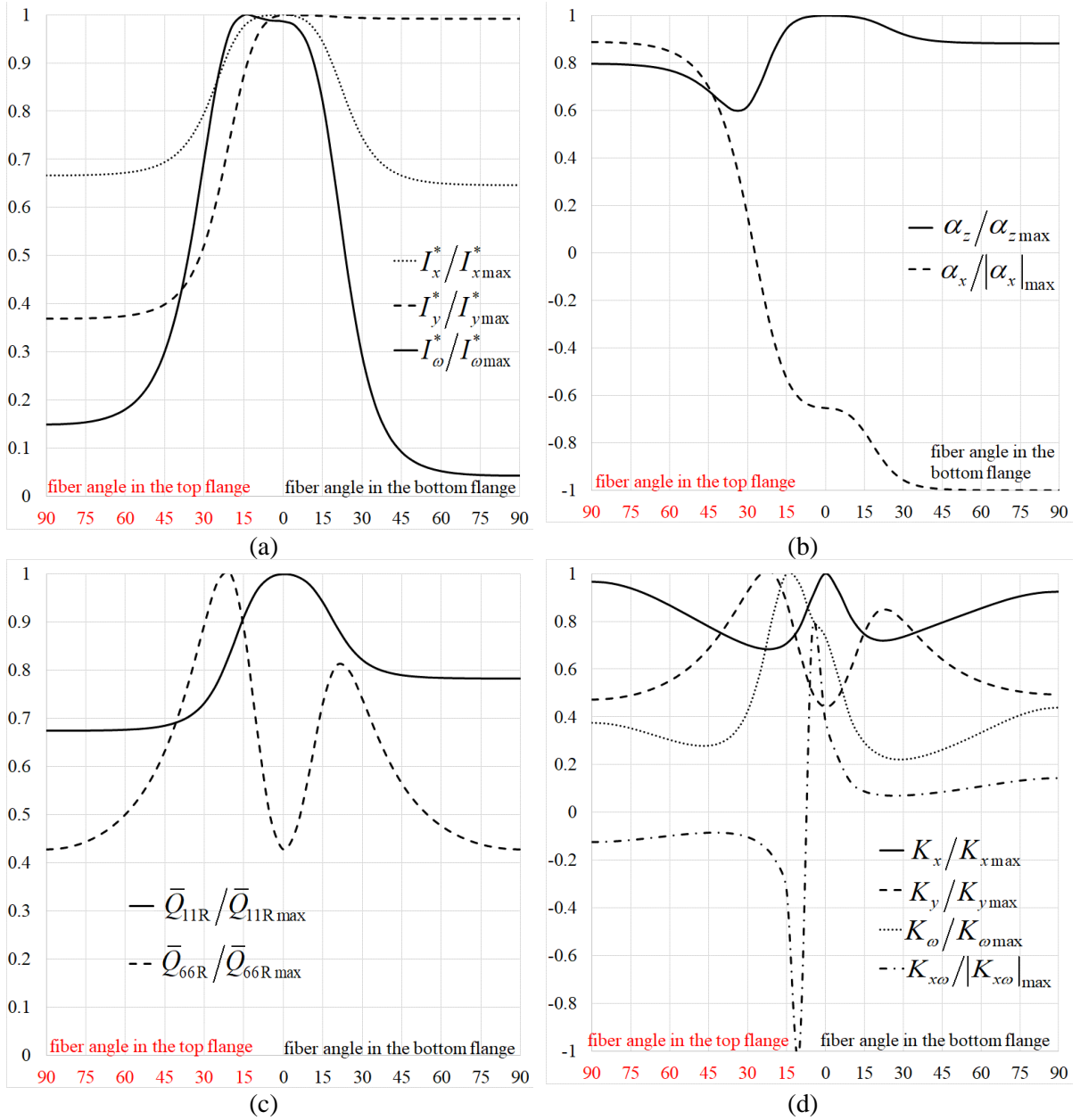


Fig. 5.8 Various I profile cross-section properties with respect to fiber angle change in the top and bottom flange: (a)  $I_x^*$ ,  $I_y^*$  and  $I_\omega^*$ , (b)  $\alpha_z$  and  $\alpha_x$ , (c)  $\bar{Q}_{11R}$  and  $\bar{Q}_{66R}$ , (d)  $K_x$ ,  $K_y$ ,  $K_\omega$  and  $K_{x\omega}$

Variations of the material-weighted cross-section properties for the monosymmetric I profile with respect to fiber angle change in the top and the bottom flange can be observed in the Fig. 5.8. The properties presented in the Fig. 5.8 are divided by their maximum values shown in the Table 5.2. It should be noted that values presented in the Table 5.2 and Fig. 5.8 are calculated according to assumption that  $\sigma_s = 0$ , corresponding to constitutive equation given in Eq. (2.30).

Table 5.3 Example 1 I profile cross-section properties with respect to fiber angle change in the flanges and the web.

$A^*$ (cm <sup>2</sup> )	$I_{x\max}^*$ (cm <sup>4</sup> )	$I_{y\max}^*$ (cm <sup>4</sup> )	$I_t^*$ (cm <sup>4</sup> )	$I_{\omega\max}^*$ (cm <sup>4</sup> )	$\bar{Q}_{11R\max}$ (GPa)	$\bar{Q}_{66R\max}$ (GPa)
90	34152	5147	30	1452567	140	6.788527
$K_x\max$	$K_y\max$	$K_{\omega\max}$	$K_{x\omega\max}$	$\alpha_z\max$ (cm <sup>2</sup> )	$ \alpha_x _{\max}$ (cm)	
6.009	7.5277	0.004646	0.505254	484.763	20.613	

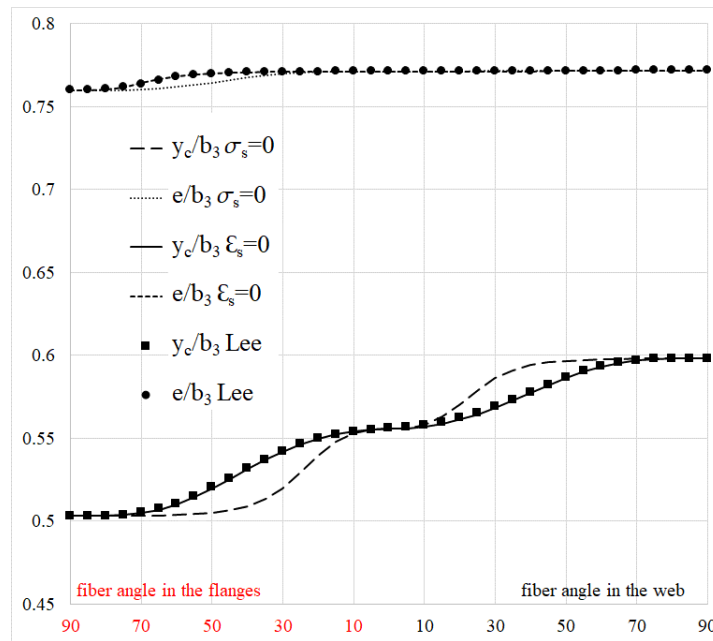


Fig. 5.9 Positions of material-weighted centroid and shear centre for the monosymmetric I profile with respect to fiber angle change in the flanges and the web

The positions of the material-weighted centroid and shear center for the monosymmetric I profile shown in Fig. 5.4 (b) are illustrated in Fig. 5.9. The fiber angle is varied in the flanges and the web following the same principle as in Fig. 5.5. It is evident that the results obtained through the comparable assumption align with the findings presented in [36]. Moreover, the location of the shear center remains nearly unchanged regardless of variations in the fiber angle, while the position of the centroid exhibits slight variations as the fiber angle is altered.

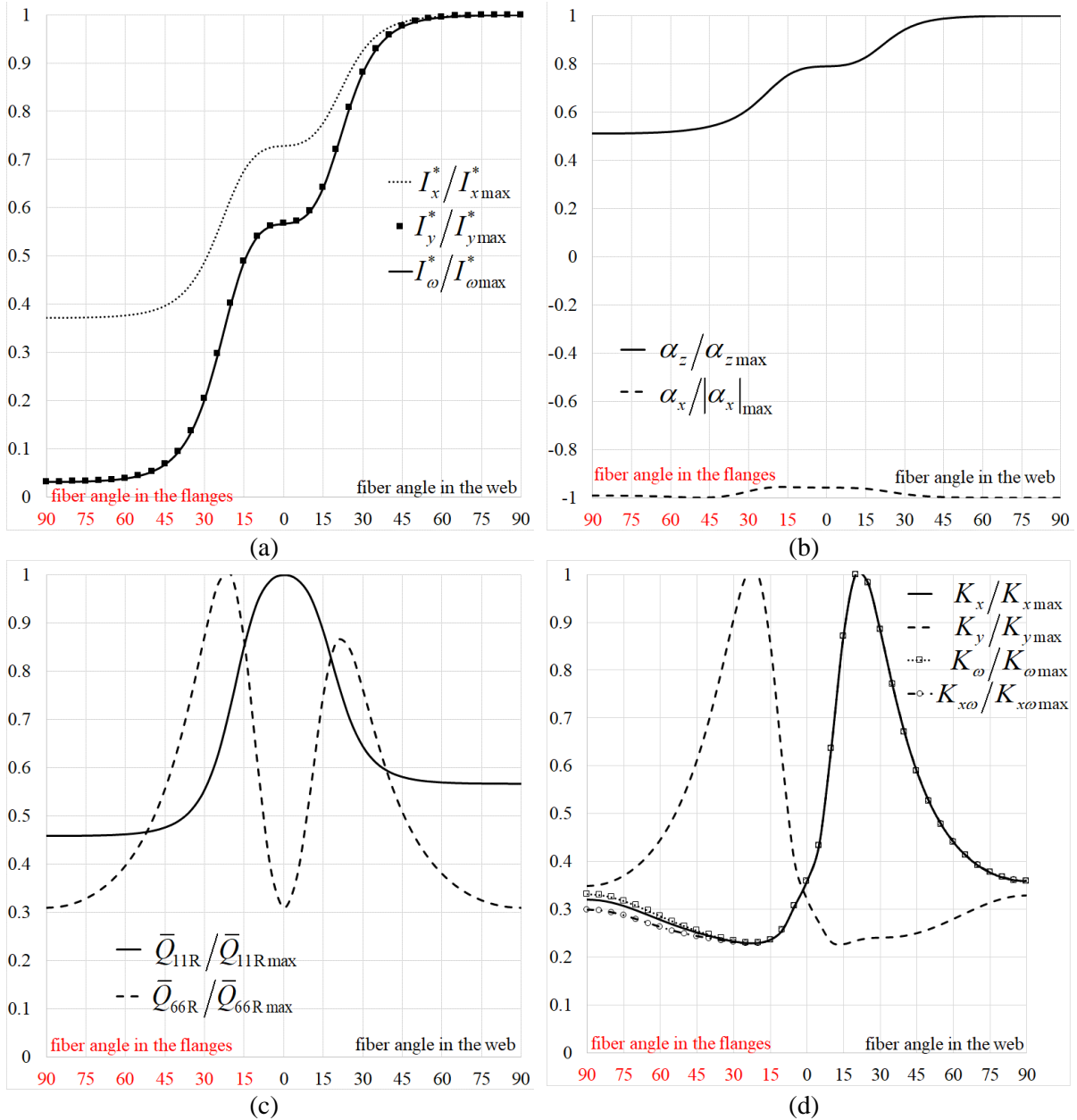


Fig. 5.10 Various I profile cross-section properties with respect to fiber angle change in the flanges and the web: (a)  $I_x^*$ ,  $I_y^*$  and  $I_\omega^*$ , (b)  $\alpha_z$  and  $\alpha_x$ , (c)  $\bar{Q}_{11R}$  and  $\bar{Q}_{66R}$ , (d)  $K_x$ ,  $K_y$ ,  $K_\omega$  and  $K_{x\omega}$

Variations of the material-weighted cross-section properties for the monosymmetric I profile with respect to fiber angle change in the top and the bottom flange can be observed in the Fig. 5.10. The properties presented in the Fig. 5.10 are divided by their maximum values shown in the Table 5.3. It should be noted that values presented in the Table 5.3 and Fig. 5.10 are calculated according to assumption that  $\sigma_s = 0$ , corresponding to constitute equation given in Eq. (2.30).

### 5.3.2 Example 2

In the second example, the behavior of a cantilever beam (CF), simply supported beam (SS), and clamped-clamped beam (CC) under an axial force at the centroid is considered. The cross-section under analysis is depicted in Fig. 5.4 (b), with dimensions of  $b_1=b_3=5$  cm and  $b_2=3$ cm. The cross-section properties are listed in Table 5.4. Both the flanges and the web consist of 16 layers, with each layer having a thickness of 0.013 cm, resulting in a branch thickness of  $t = 0.208$  cm. The laminate is composed of the stacking sequence  $[\theta/-\theta]_{8S}$ .

Table 5.4 Example 2 cross-section properties.

$A^*$ (cm <sup>2</sup> )	$I_x^*$ (cm <sup>4</sup> )	$I_y^*$ (cm <sup>4</sup> )	$I_t^*$ (cm <sup>4</sup> )	$I_\omega^*$ (cm <sup>4</sup> )	$y_s$ (cm)	$\bar{Q}_{11R}$ (GPa)	$\bar{Q}_{66R}$ (GPa)
2.704	12.173	2.638	0.0389	9.649	1.225	varies	varies
$K_x$	$K_y$	$K_\omega$	$K_{x\omega}$				
1.9421	2.8678	0.00409	0.2353				

The structural material employed in this analysis is glass-epoxy, which possesses the following properties:  $E_1 = 53.78$  GPa,  $E_2 = 17.93$  GPa,  $G_{12} = 8.96$  GPa,  $\nu_{12} = 0.25$ . The length of the beam is denoted as  $L$ . The critical buckling loads obtained from the present model are compared with those of Vo and Lee [72].

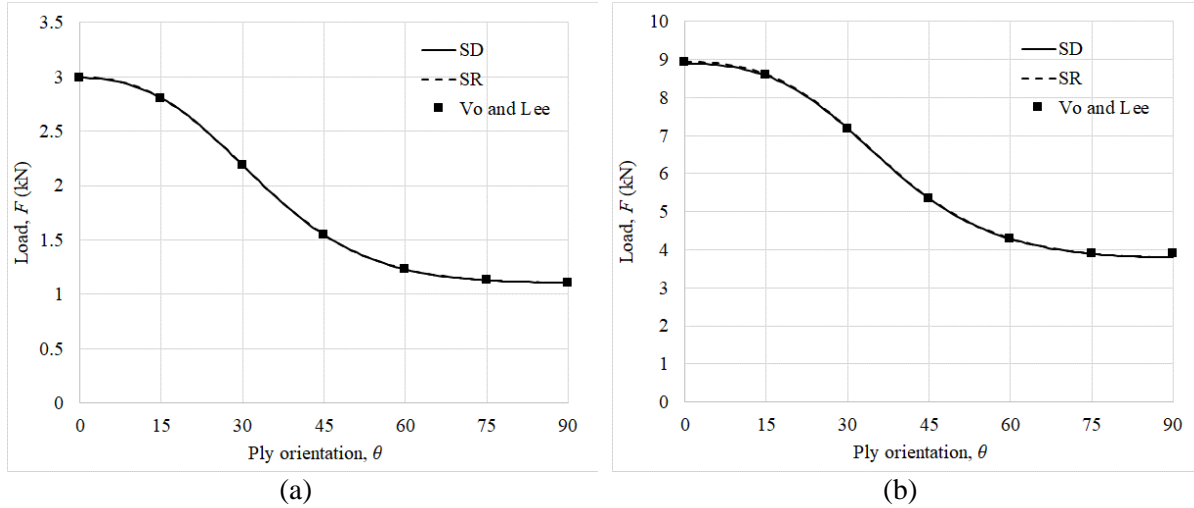


Fig. 5.11 Buckling load vs. ply orientation ( $\theta$ ) for  $L=100$  cm and: (a) CF, (b) SS

Fig. 5.11 presents the critical buckling load for different ply orientations under CF and SS boundary conditions. The results exhibit good agreement with [72], although there is minimal difference observed between the SD and SR models.

In Fig. 5.12 to Fig. 5.14, the critical buckling load for various beam lengths is shown for three boundary conditions and two ply angles. It can be observed that the SR model exhibits significant differences from the SD model in the case of a CC beam when the  $L/b_3$  ratio is below

7. Additionally, for an SS beam with a ratio below 5, a noticeable difference between the SR and SD models can be seen. However, the CF beam model shows negligible differences between the SR and SD models.

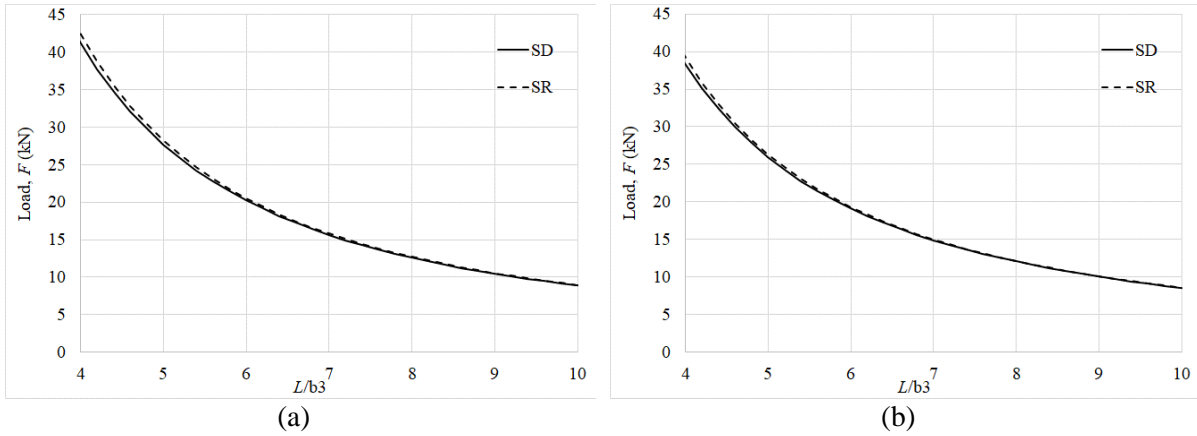


Fig. 5.12 Buckling load vs. beam length for CF beam and: (a)  $\theta=0^\circ$ , (b)  $\theta=15^\circ$

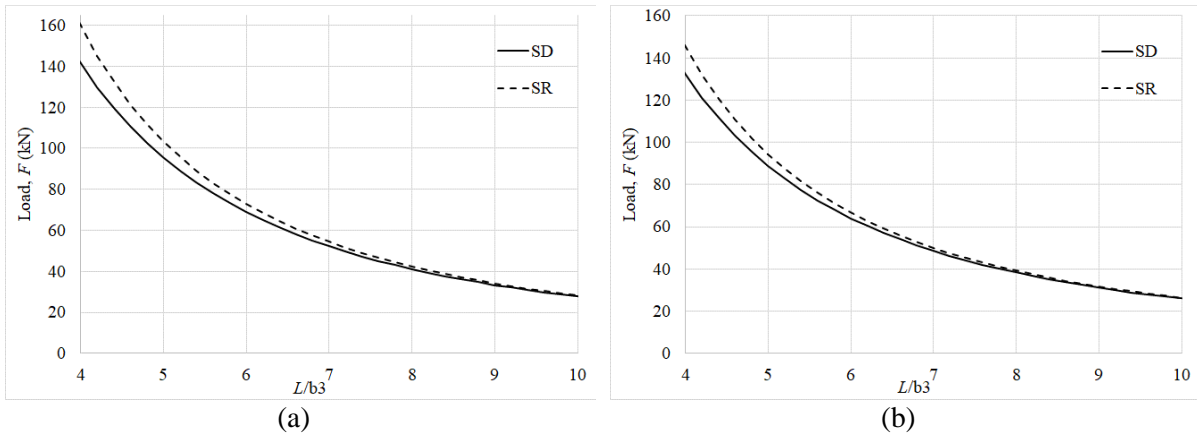


Fig. 5.13 Buckling load vs. beam length for SS beam and: (a)  $\theta=0^\circ$ , (b)  $\theta=15^\circ$

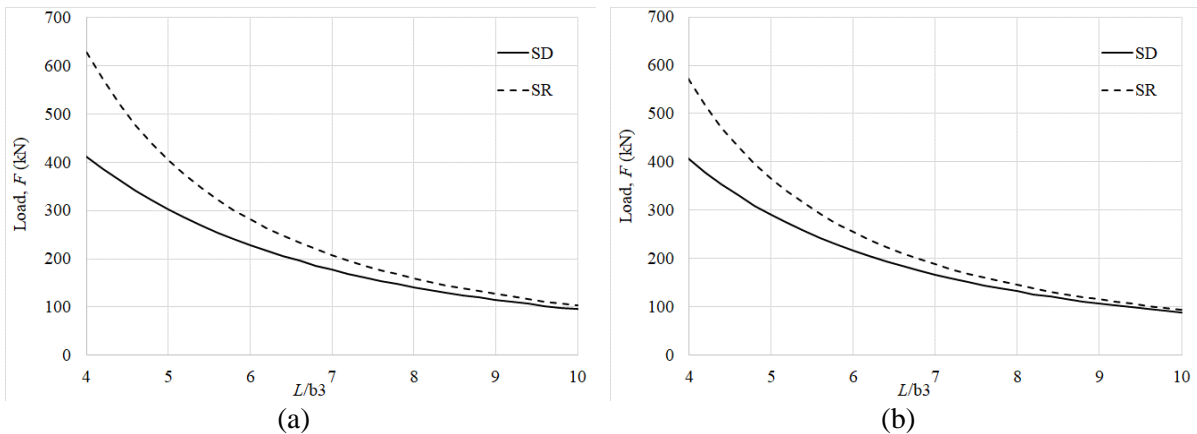


Fig. 5.14 Buckling load vs. beam length for CC beam and: (a)  $\theta=0^\circ$ , (b)  $\theta=15^\circ$

## 5.3.3 Example 3

In Fig. 5.15 (a), a simply supported column subjected to an axial force  $F$  is depicted. The column adopts a mono-symmetric cross-section from Fig. 5.15 (b), with properties listed in Table 5.5. Two stacking sequences,  $[0^\circ/0^\circ]_s$  and  $[0^\circ/90^\circ]_s$ , are assumed for the cross-section. The structural material employed in this analysis is graphite-epoxy (AS4/3501), which possesses the following properties:  $E_1 = 144$  GPa,  $E_2 = 9.65$  GPa,  $G_{12} = 4.14$  GPa,  $\nu_{12} = 0.3$ .

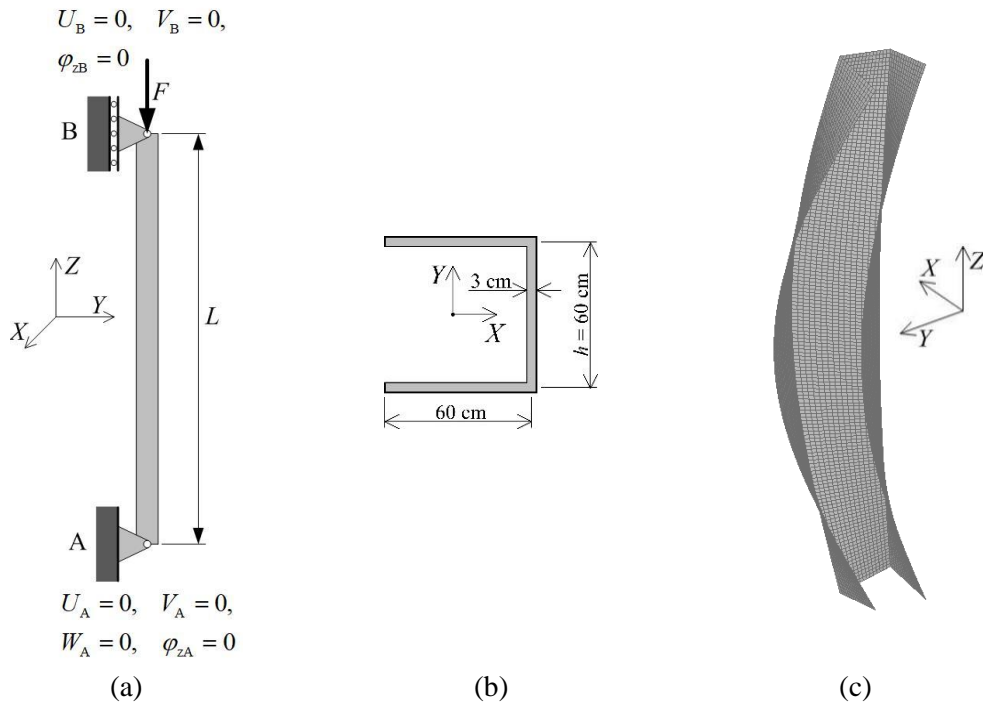


Fig. 5.15 Simply supported column: (a) geometry, (b) cross-section, (c) torsional-flexural buckling mode

Table 5.5 Example 3 cross-section properties

	$A^*$ (cm <sup>2</sup> )	$I_x^*$ ( $\times 10^3$ cm <sup>4</sup> )	$I_y^*$ ( $\times 10^3$ cm <sup>4</sup> )	$I_t^*$ (cm <sup>4</sup> )	$I_\omega^*$ ( $\times 10^6$ cm <sup>4</sup> )	$x_s$ (cm)	$\bar{Q}_{11R}$ (GPa)	$\bar{Q}_{66R}$ (GPa)
$[0^\circ/0^\circ]_s$	540	378.270	216.135	1620	139.657	45.675	144	4.14
$[0^\circ/90^\circ]_s$	540	378.447	216.224	1620	140.284	45.648	76.825	4.14
	$K_x$	$K_y$	$K_\omega$	$K_{y\omega}$				
$[0^\circ/0^\circ]_s$	1.9476	3.3768	0.0043	-0.2441				
$[0^\circ/90^\circ]_s$	1.9460	3.3622	0.0043	-0.2412				

The torsional-flexural mode depicted in Fig. 5.15 (c) corresponds to the lowest buckling load. This mode is analyzed using five different mesh configurations, each consisting of two, four, eight, sixteen, and thirty-two beam elements.

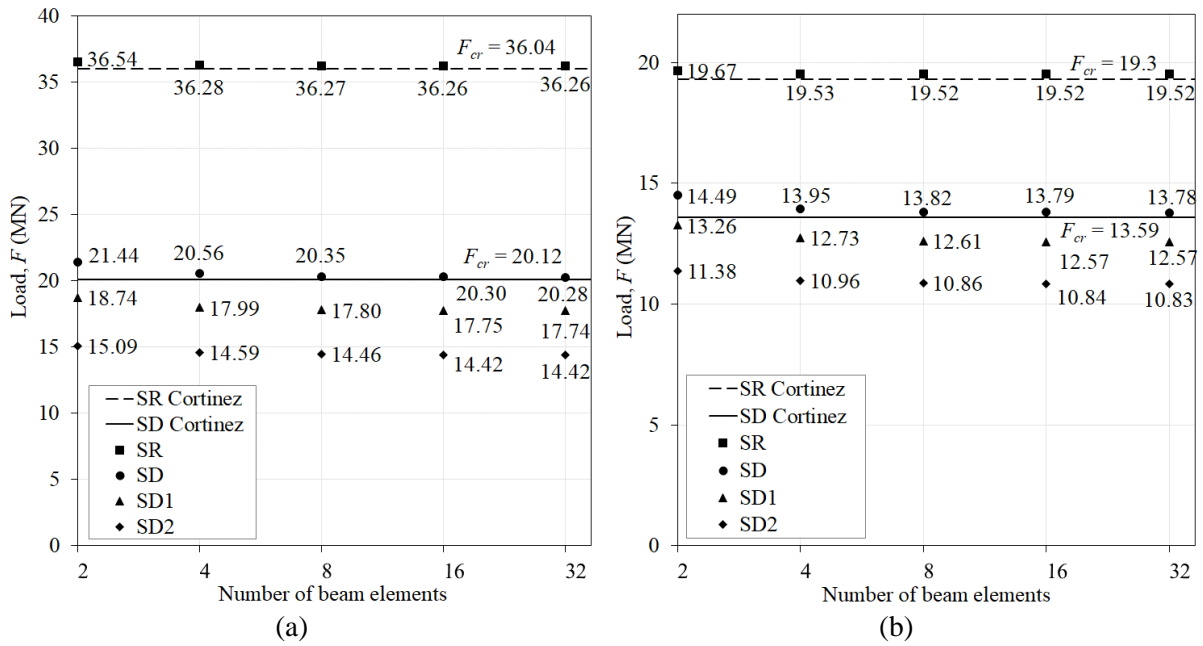


Fig. 5.16 Buckling load convergence for SS column,  $L = 400$  cm: (a)  $[0^\circ/0^\circ]_s$ , (b)  $[0^\circ/90^\circ]_s$

The obtained results are presented in Fig. 5.16 and compared with the analytical solution provided by Cortinez in [22]. It can be observed that none of the shear deformable models experience shear locking, and the results obtained from the SD model closely align with the analytical solution. On the other hand, the results obtained from the SD1 and SD2 models underestimate the buckling strength of the column.

Additionally, the shear deformability leads to a reduction of 44% and 29% in the buckling strength when compared to the shear rigid model for the stacking sequences  $[0^\circ/0^\circ]_s$  and  $[0^\circ/90^\circ]_s$ , respectively.

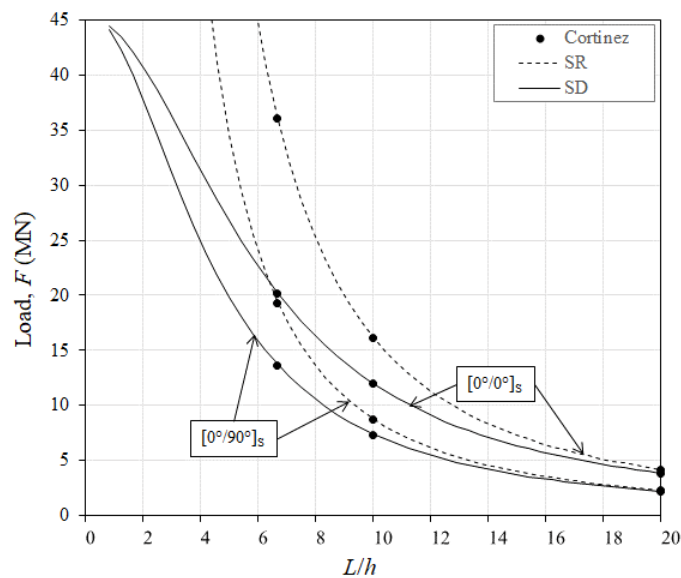


Fig. 5.17 Buckling load vs. column length for SS column

Fig. 5.17 displays the variations in the buckling load value as a function of the column slenderness ratio. It is observed that the difference in results obtained between the SR and SD models decreases as the slenderness ratio increases.

### 5.3.4 Example 4

In Fig. 5.18 (a), a cantilever column subjected to an axial force  $F$  is depicted. The column adopts a mono-symmetric cross-section from Fig. 5.18 (b), with the properties provided in Table 5.6. The structural material utilized for the column is graphite-epoxy (AS4/3501), which possesses the following properties:  $E_1 = 144$  GPa,  $E_2 = 9.65$  GPa,  $G_{12} = 4.14$  GPa,  $\nu_{12} = 0.3$ . Each wall of the cross-section has the same thickness and is composed of a single AS4/3501 ply. The ply orientations are indicated in Fig. 5.18 (b).

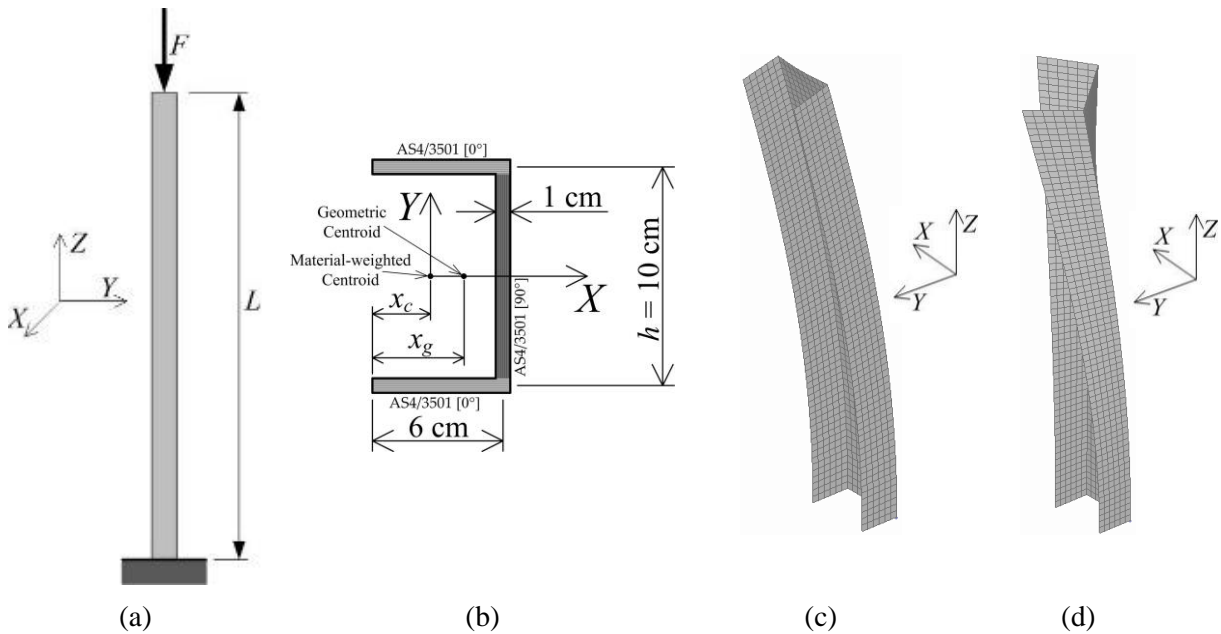


Fig. 5.18 Cantilever column: (a) geometry, (b) cross-section, (c) flexural buckling mode, (d) torsional-flexural buckling mode

Table 5.6 Example 4 cross-section properties.

$A^*$ (cm <sup>2</sup> )	$I_x^*$ (cm <sup>4</sup> )	$I_y^*$ (cm <sup>4</sup> )	$I_t^*$ (cm <sup>4</sup> )	$I_\omega^*$ (cm <sup>4</sup> )	$x_c$ (cm)	$x_g$ (cm)	$x_s$ (cm)
22	532.343	72.525	7.333	1718.819	3.159	4.364	5.767
$\bar{Q}_{11R}$ (GPa)	$\bar{Q}_{66R}$ (GPa)	$K_x$	$K_y$	$K_\omega$	$K_{y\omega}$		
82.932	4.14	2.1504	2.3969	0.0217	-0.4999		



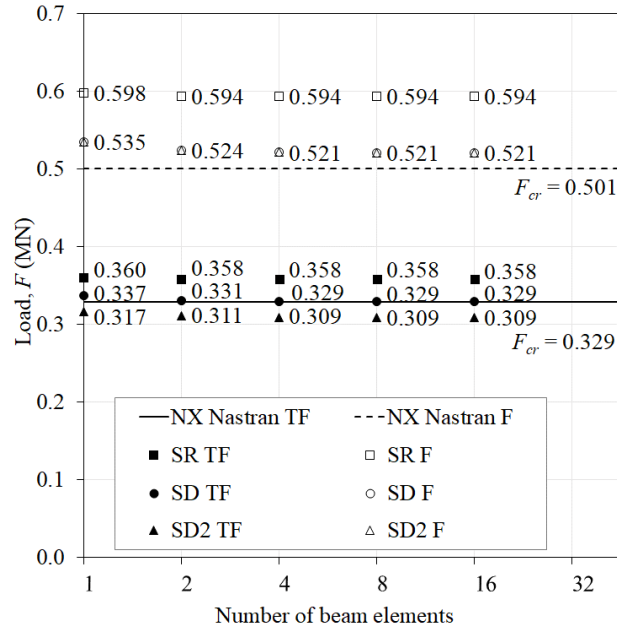


Fig. 5.19 Buckling load convergence for the CF column,  $L=50$  cm

The force  $F$  is applied at the geometric centroid of the cross-section. Since the neutral axis passes through the material-weighted centroid, the force acting through the geometric centroid behaves as an off-axis load.

The torsional-flexural (TF) mode is identified as the lowest buckling load, as depicted in Fig. 5.18 (d). The second buckling mode is the flexural (F) mode, shown in Fig. 5.18 (c). Both modes are analyzed using five different mesh configurations, consisting of one, two, four, eight, and sixteen beam elements.

The obtained results are presented in Fig. 5.19 and are compared with the laminate shell results from NX Nastran.

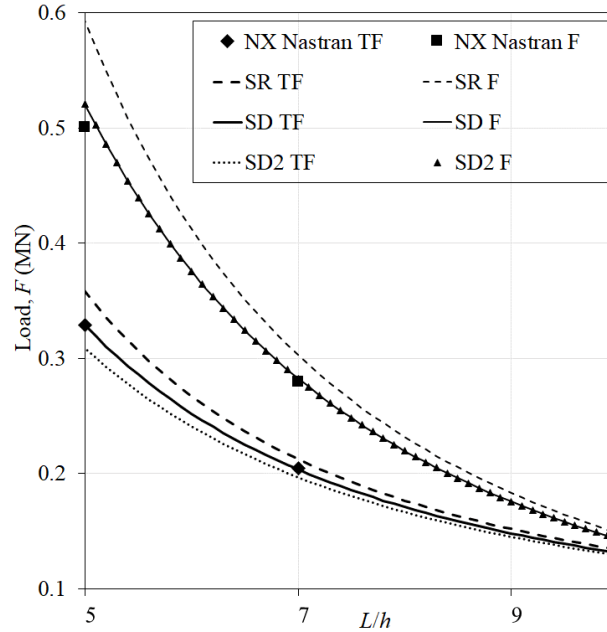


Fig. 5.20 Buckling load vs. column length for the CF column

It is observed that shear locking does not occur in any of the shear deformable models, and the results obtained from the SD model closely approach the shell solution. However, the results obtained from the SD2 model underestimate the column buckling strength in the TF mode, indicating that ignoring shear coupling effects provides a conservative estimate for construction purposes.

Since the beam model assumes a rigid cross-section and cannot capture cross-section distortion, some differences between the beam model and the shell model are expected, particularly for higher loads and shorter beams where cross-section distortion significantly impacts the critical load. This can be seen in the results of the F mode.

Furthermore, the buckling strength reductions due to shear deformability are 8% and 12% for the TF and F modes, respectively, when compared to the shear rigid model. The inclusion of shear coupling effects leads to a 6% increase in the buckling strength for the TF mode, while there is no influence of shear couplings for the F mode.

Fig. 5.20 illustrates the variations in the buckling load value as a function of the column slenderness ratio. It is evident that the differences between the results obtained from the SR and SD beam models decrease as the slenderness ratio increases.

## 5.3.5 Example 5

A cantilever column with a length of  $L = 50$  cm is being analyzed in this example. The column is subjected to an axial force  $F$ , as shown in Fig. 5.21 (a). The cross-section shape being analyzed is depicted in Fig. 5.21 (b) with the properties listed in Table 5.7. The structural material utilized for the column is graphite-epoxy (AS4/3501), which possesses the following properties:  $E_1 = 144$  GPa,  $E_2 = 9.65$  GPa,  $G_{12} = 4.14$  GPa,  $\nu_{12} = 0.3$ .

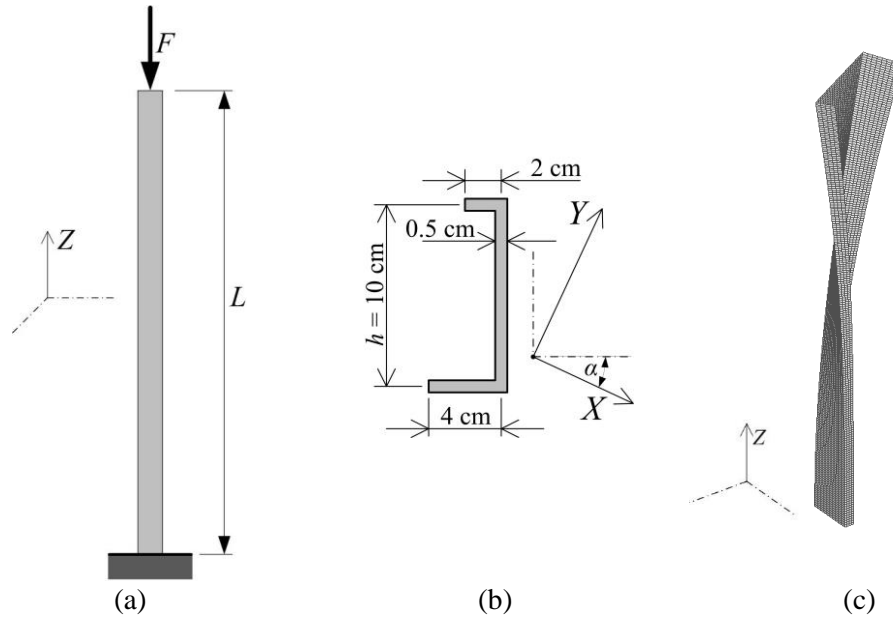


Fig. 5.21 Cantilever column: (a) geometry, (b) cross-section, (c) torsional-flexural buckling mode

Table 5.7 Example 5 cross-section properties.

$A^*$ (cm <sup>2</sup> )	$I_x^*$ (cm <sup>4</sup> )	$I_y^*$ (cm <sup>4</sup> )	$I_t^*$ (cm <sup>4</sup> )	$I_\omega^*$ (cm <sup>4</sup> )	$x_s$ (cm)	$y_s$ (cm)	$\alpha$ (°)
8	114.935	7.648	0.667	73.348	1.586	-2.473	6.395
$\bar{Q}_{11R}$ (GPa)	$\bar{Q}_{66R}$ (GPa)	$K_x$	$K_y$	$K_\omega$	$K_{xy}$	$K_{x\omega}$	$K_{y\omega}$
varies	varies	5.0081	1.7419	0.01634	-22.2823	-3.696	-1.9182

The asymmetric channel profile under analysis exhibits buckling in a torsional-flexural mode, as shown in Fig. 5.21 (c). The cross-section's branches are constructed using a symmetric and balanced laminate with a  $[\theta/-\theta]_{2s}$  stacking sequence, where all plies have uniform thickness. Fig. 5.22 illustrates the relationship between the buckling load and the ply orientation angle  $\theta$ . It can be observed that the column achieves its maximum buckling strength when the ply angle is approximately  $15^\circ$ .

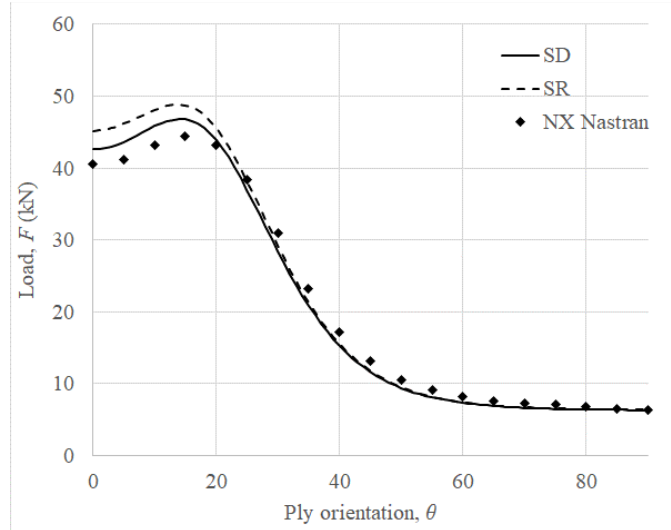


Fig. 5.22 Buckling load vs. ply orientation ( $\theta$ ) for the CF column

To perform the nonlinear stability analysis, a small perturbation force with an intensity of  $0.001F$  is applied in the  $X$ -direction. Fig. 5.23 displays the convergence study for the nonlinear analysis conducted using four different mesh configurations, comprising one, two, four, and eight beam elements. The results shown in Fig. 5.23 are normalized by the critical buckling force obtained from the laminate shell solution using NX Nastran software. The critical buckling force for a ply orientation of  $\theta = 0^\circ$  is  $F_{cr} = 40.5$  kN, while for a ply orientation of  $\theta = 15^\circ$ , it is  $F_{cr} = 44.5$  kN. It is evident that the SD model accurately predicts the buckling behavior across all the mesh configurations employed, while the SR model overestimates the buckling strength by approximately 10%.

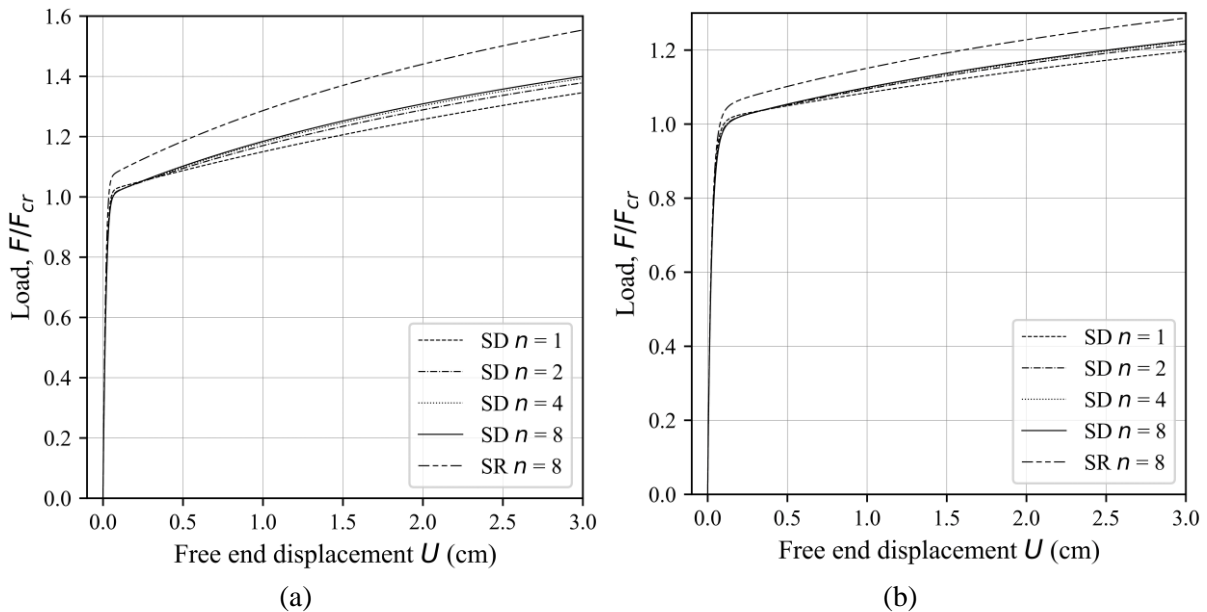


Fig. 5.23 Convergence analysis for the CF column: (a)  $\theta=0^\circ$ , (b)  $\theta=15^\circ$

## 5.3.6 Example 6

In Fig. 5.24 (a), a cantilever beam is depicted, subjected to a lateral force  $F$  applied at the free end in the  $Y$ -direction. The force is applied through the shear centre of the asymmetric cross-section, as shown in Fig. 5.24 (b).

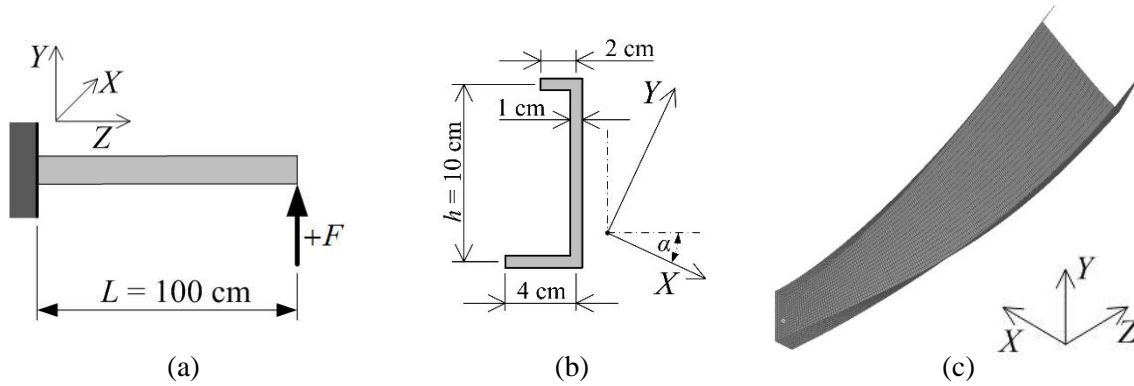


Fig. 5.24 Cantilever beam: (a) geometry, (b) cross-section, (c) lateral-torsional buckling mode

Table 5.8 Example 6 cross-section properties.

	$A^*$ (cm <sup>2</sup> )	$I_x^*$ (cm <sup>4</sup> )	$I_y^*$ (cm <sup>4</sup> )	$I_t^*$ (cm <sup>4</sup> )	$I_\omega^*$ (cm <sup>4</sup> )	$x_s$ (cm)	$y_s$ (cm)	$\alpha$ (°)
$[0^\circ/0^\circ]_s$	16	230.248	15.918	5.333	160.765	1.582	-2.351	6.402
$[0^\circ/90^\circ]_s$	16	230.579	16.462	5.333	172.694	1.578	-2.253	6.409
	$\bar{Q}_{11R}$ (GPa)	$\bar{Q}_{66R}$ (GPa)	$K_x$	$K_y$	$K_\omega$	$K_{xy}$	$K_{x\omega}$	$K_{y\omega}$
$[0^\circ/0^\circ]_s$	144	4.14	4.5809	1.7228	0.0547	-23.1153	-4.0434	-2.4496
$[0^\circ/90^\circ]_s$	76.825	4.14	4.2175	1.7099	0.0474	-24.4762	-2.5619	-1.9877

In Table 5.8, the cross-section properties for the asymmetric beam are provided. The beam is made of graphite-epoxy (AS4/3501) material, which has the following properties:  $E_1 = 144$  GPa,  $E_2 = 9.65$  GPa,  $G_{12} = 4.14$  GPa,  $\nu_{12} = 0.3$ . The lateral-torsional buckling mode, as shown in Fig. 5.24 (c), is analyzed for two stacking sequences:  $[0^\circ/0^\circ]_s$  and  $[0^\circ/90^\circ]_s$ . The analysis is performed using four different mesh configurations, consisting of two, four, eight, and sixteen beam elements. It should be noted that due to the asymmetry of the cross-section, there may be a difference in the buckling load for the positive and negative directions of the applied force [20]. The results obtained from the eigenvalue approach for both force directions are presented in Fig. 5.25, along with the results obtained from NX Nastran's laminate shell model.

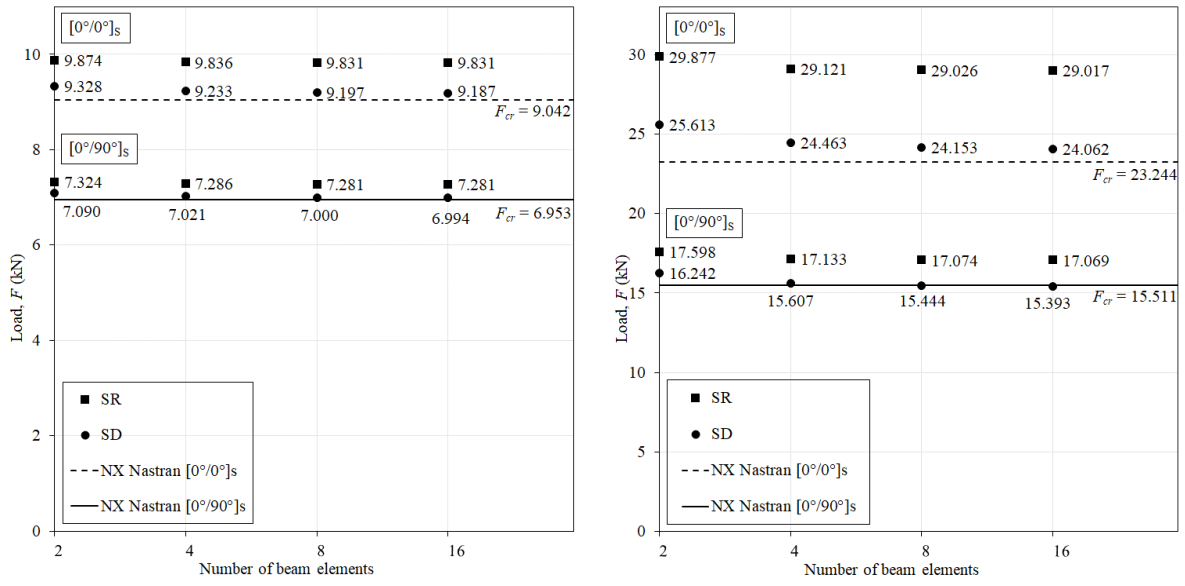


Fig. 5.25 Buckling load convergence for the CF beam: (a) +F, (b) -F

It is observed that for the positive force direction, the shear deformability results in a reduction of 7% and 4% in the buckling strength for the stacking sequences  $[0^\circ/0^\circ]_s$  and  $[0^\circ/90^\circ]_s$ , respectively. On the other hand, for the negative force direction, the reduction in buckling strength is 17% and 10% for the same stacking sequences.

To conduct the nonlinear stability analysis, a small perturbation force with an intensity of  $0.001F$  is applied in the X-direction at the free end of the beam, acting through the shear centre.

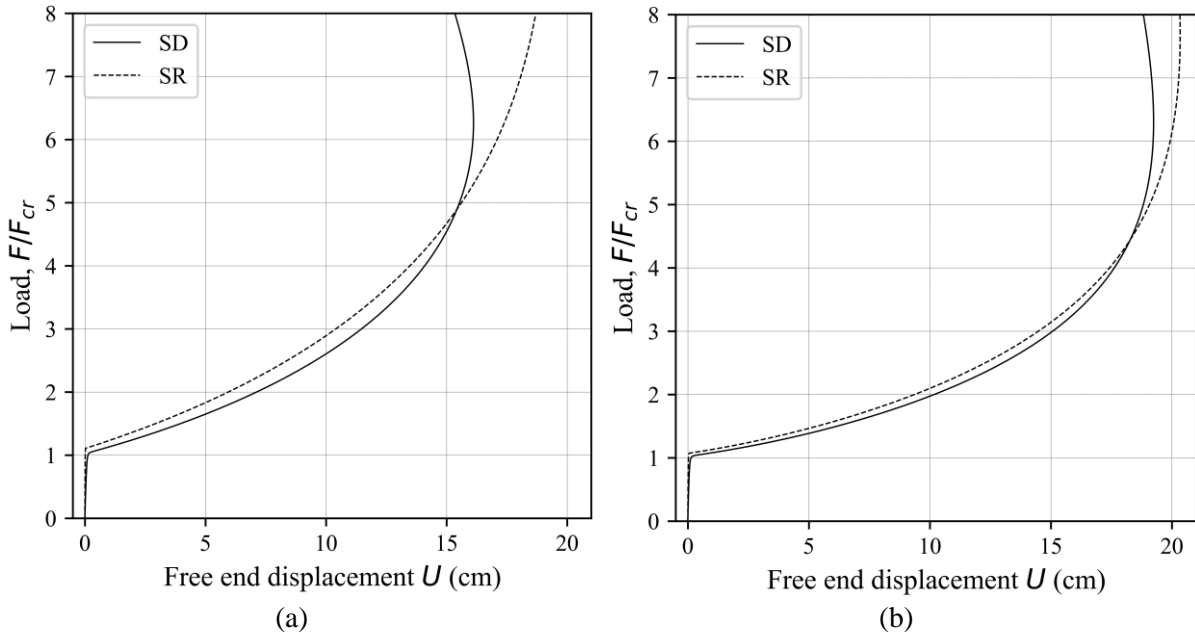


Fig. 5.26 Buckling load for the +F vs. free end displacement in the X-direction: (a)  $[0^\circ/0^\circ]_s$ , (b)  $[0^\circ/90^\circ]_s$

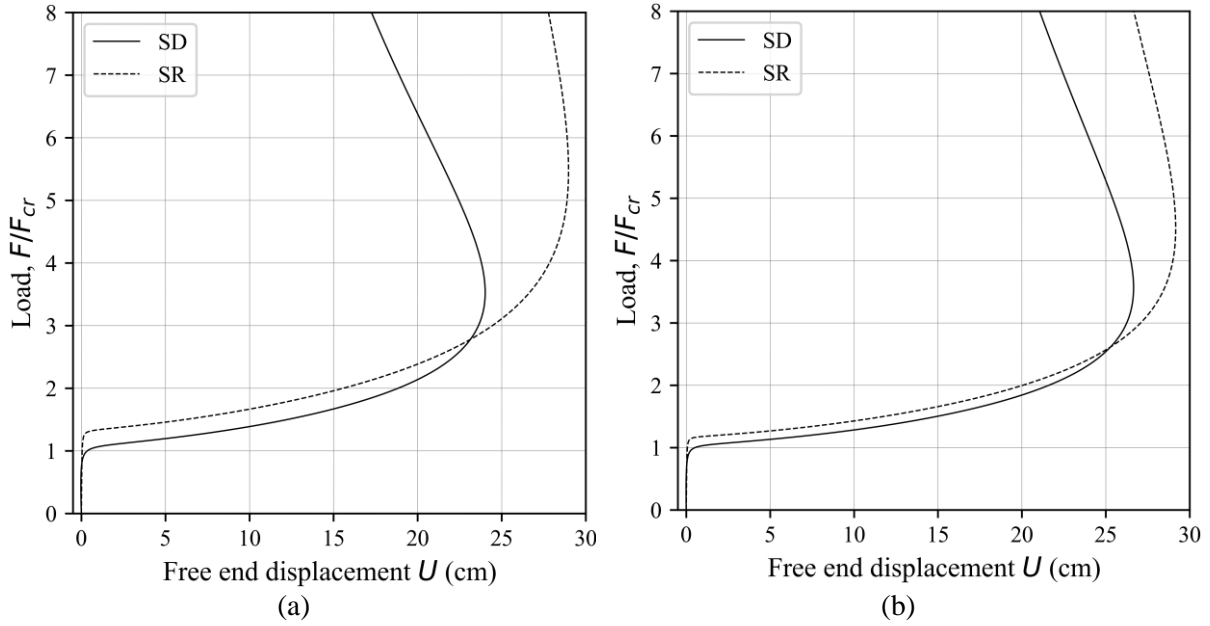


Fig. 5.27 Buckling load for the  $-F$  vs. free end displacement in the  $X$ -direction: (a)  $[0^\circ/0^\circ]_s$ , (b)  $[0^\circ/90^\circ]_s$

The load-deflection curves for both stacking sequences and force directions, obtained using sixteen beam elements, are presented in Fig. 5.26 and Fig. 5.27. Additionally, the convergence study is depicted in Fig. 5.28.

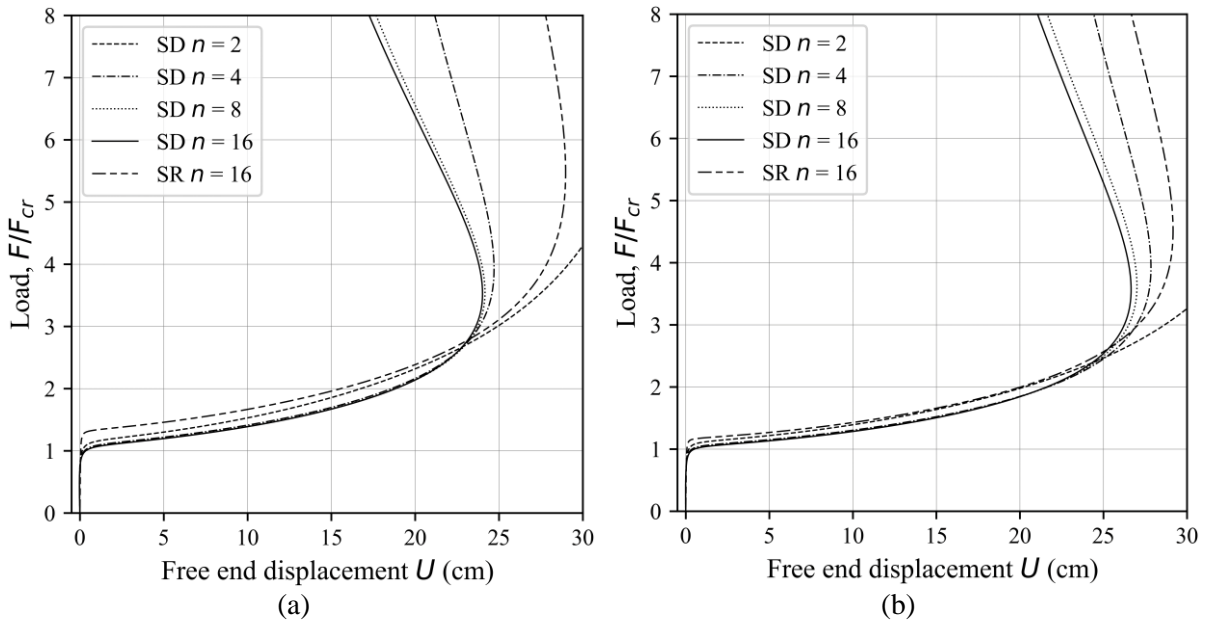


Fig. 5.28 Buckling load convergence for the  $-F$  vs. free end displacement in the  $X$ -direction: (a)  $[0^\circ/0^\circ]_s$ , (b)  $[0^\circ/90^\circ]_s$

In all the figures, the buckling load values  $F_{cr}$  are taken from Fig. 5.25, which were obtained using the shell model. It can be observed that all the mesh models accurately identify the buckling load, and significant differences occur only in the post-buckling range above  $F > 3 F_{cr}$  and  $F > 2.5 F_{cr}$ , respectively.

## 5.3.7 Example 7

Fig. 5.29 (a) presents an L-frame structure subjected to a load  $F$  in the  $Y$ -direction, acting through the centroid of the cross-section at the free end. The beam length is  $L = 100$  cm. The cross-section is a mono-symmetric U-profile with properties provided in Table 5.9 for the stacking sequences  $[0^\circ/0^\circ]_s$  and  $[0^\circ/90^\circ]_s$ , respectively. The structural material used in this analysis is graphite-epoxy (AS4/3501), which possesses the following properties:  $E_1 = 144$  GPa,  $E_2 = 9.65$  GPa,  $G_{12} = 4.14$  GPa,  $\nu_{12} = 0.3$ .

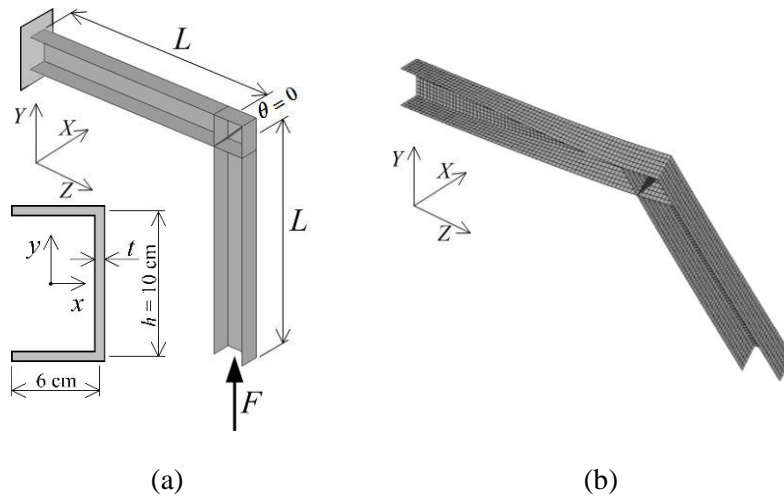


Fig. 5.29 L-frame: (a) geometry, (b) lateral-torsional buckling mode.

Table 5.9 Example 7 and Example 8 cross-section properties.

	$A^*$ (cm <sup>2</sup> )	$I_x^*$ (cm <sup>4</sup> )	$I_y^*$ (cm <sup>4</sup> )	$I_t^*$ (cm <sup>4</sup> )	$I_\omega^*$ (cm <sup>4</sup> )	$x_s$ (cm)	$\bar{Q}_{11R}$ (GPa)	$\bar{Q}_{66R}$ (GPa)
$[0^\circ/0^\circ]_s$	22	384.333	85.924	7.333	1521.472	3.970	144	4.14
$[0^\circ/90^\circ]_s$	22	384.989	86.471	7.333	1546.574	3.961	76.825	4.14
	$K_x$	$K_y$	$K_\omega$	$K_{y\omega}$				
$[0^\circ/0^\circ]_s$	2.7267	2.3635	0.0248	-0.6490				
$[0^\circ/90^\circ]_s$	2.6923	2.3325	0.0240	-0.6160				

Assuming full warping restraint at the frame corner, the lateral-torsional buckling mode depicted in Fig. 5.29 (b) is analyzed using four different mesh configurations: one, two, four, and eight beam elements per frame member. The eigenvalue approach is employed to obtain the results, which are presented in Fig. 5.30. These results are compared with those obtained from the NX Nastran's laminate shell model.



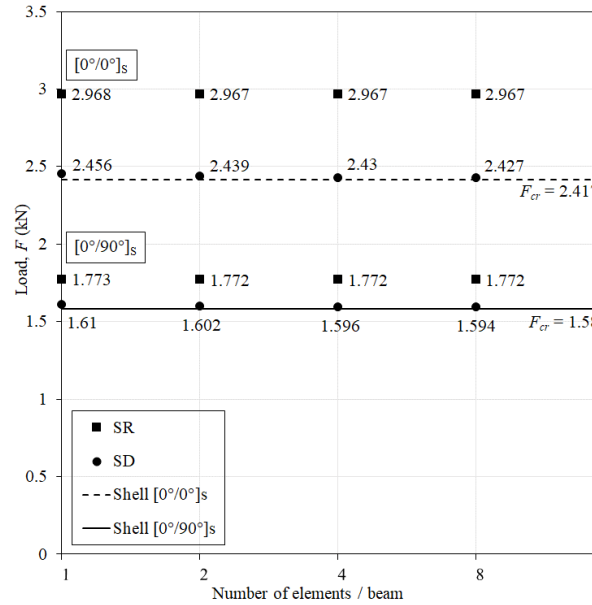


Fig. 5.30 Buckling load convergence for the L-frame

To conduct the nonlinear stability analysis, a small perturbation force with an intensity of  $0.001F$  is introduced in the  $X$ -direction. In all the figures, the buckling load values  $F_{cr}$  are taken from Fig. 5.30, which were obtained using the shell model. The obtained results for the  $[0^\circ/0^\circ]_s$  stacking sequence are shown in Fig. 5.31, while the results for the  $[0^\circ/90^\circ]_s$  stacking sequence are presented in Fig. 5.32.

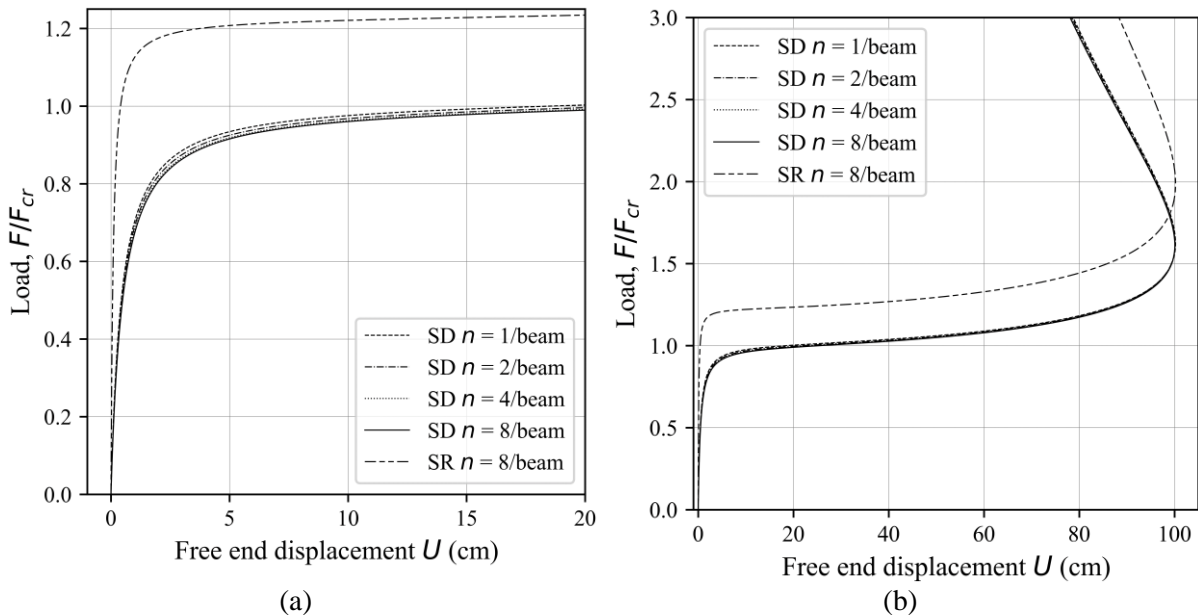


Fig. 5.31 Buckling load convergence vs. free end displacement in the  $X$ -direction for the  $[0^\circ/0^\circ]_s$  stacking sequence: (a) prebuckling response, (b) postbuckling response

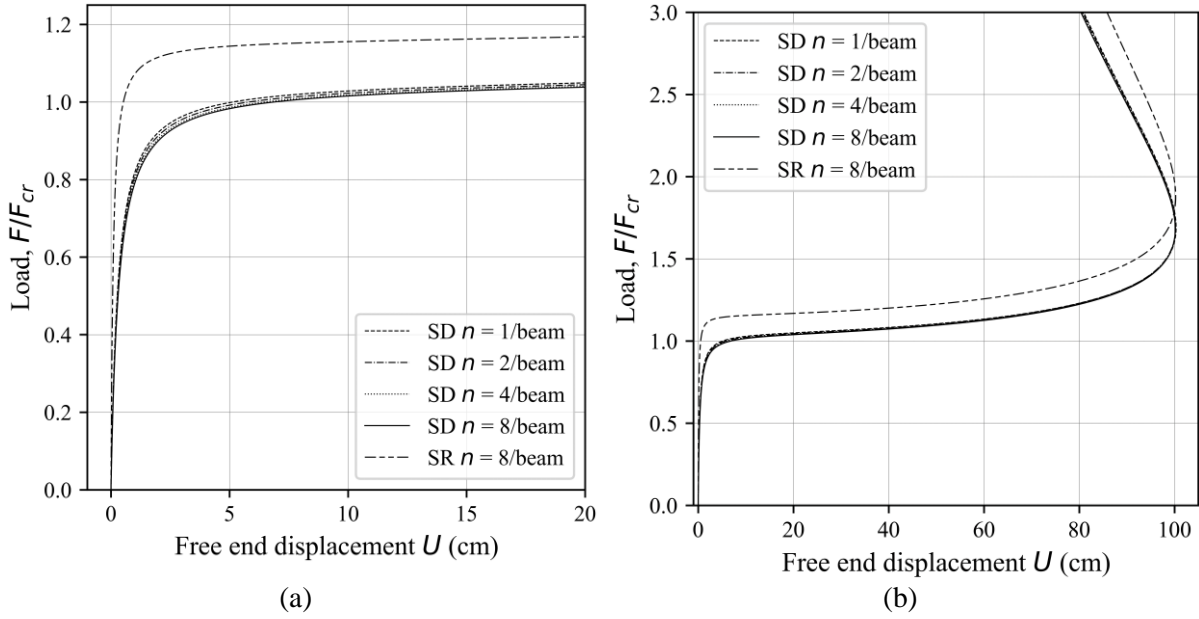


Fig. 5.32 Buckling load convergence vs. free end displacement in the X-direction for the  $[0^\circ/90^\circ]_s$  stacking sequence: (a) prebuckling response, (b) postbuckling response

As observed, the SD model accurately identifies the buckling state across all the mesh configurations used, while the SR model overestimates the buckling strength by a significant margin.

### 5.3.8 Example 8

In this case, an L-frame structure is considered, where a load  $F$  is applied in the negative Z-direction through the shear center of the cross-section at the free end, Fig. 5.33. The cross-section used is a mono-symmetric U-profile, as shown in Fig. 5.29 (a), and its properties are provided in Table 5.9 under  $[0^\circ/0^\circ]_s$  row. The structural material employed is graphite-epoxy (AS4/3501), with the following properties:  $E_1 = 144$  GPa,  $E_2 = 9.65$  GPa,  $G_{12} = 4.14$  GPa,  $\nu_{12} = 0.3$ . The cross-section branches of the L-frame are composed of an angle-ply laminate with the stacking sequence  $[\theta/-\theta]_{2s}$ . The specific values of  $\bar{Q}_{11R}$  and  $\bar{Q}_{66R}$  depend on the angle  $\theta$  but are not listed in Table 5.9 for this particular example.

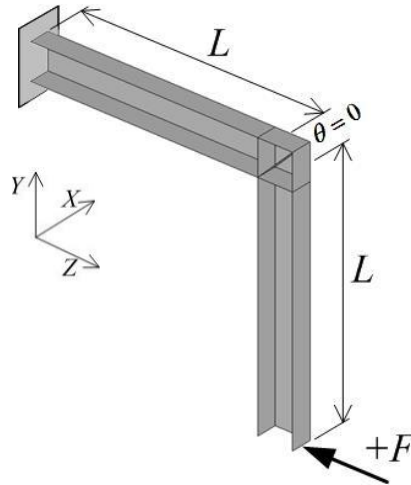


Fig. 5.33 L-frame with lateral force

In this analysis of the L-frame structure, where full warping restraint is assumed at the frame corner, the results obtained by the eigenvalue approach are shown in Fig. 5.34. These results are compared with those obtained from the NX Nastran's laminate shell model.

Fig. 5.34 illustrates the relationship between the buckling load and the ply orientation  $\theta$  for two different force directions:  $+F$  acting in the negative Z-direction and  $-F$  acting in the positive Z-direction. In the eigenvalue analysis, eight beam elements per frame member are used.

The results obtained from the SD beam model show good agreement with the shell model, indicating accurate prediction of the buckling strength. It can be observed that the structure exhibits the highest buckling strength when the ply angle is near  $10^\circ$ . Notably, the difference between the SR and SD models is only significant for ply angles  $\theta < 15^\circ$ .

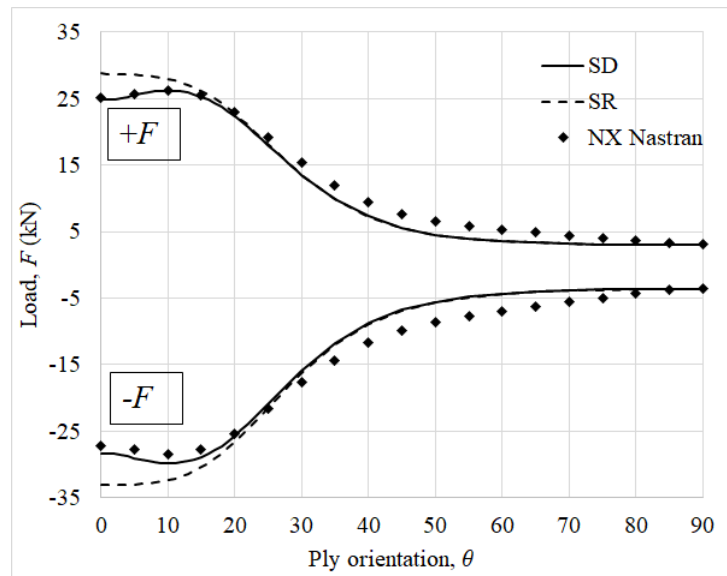


Fig. 5.34 Buckling load of the L-frame vs. ply orientation ( $\theta$ ) for the  $+F$  and  $-F$

To perform the nonlinear stability analysis, a small perturbation force of intensity  $0.001F$ ,

acting in the  $X$ -direction is introduced, and obtained results are shown in Fig. 5.35 to Fig. 5.40, for the various angles ( $\theta$ ) and for both  $F$  directions. The results shown in these figures are normalized by the critical buckling force obtained from the laminate shell solution using NX Nastro software. The critical buckling force for a ply orientation of  $\theta = 10^\circ$  is  $F_{cr} = 26.3$  kN for the  $+F$ , and  $F_{cr} = 28.5$  kN for the  $-F$ . For a ply orientation of  $\theta = 15^\circ$ , the critical buckling force for the  $+F$  is  $F_{cr} = 25.5$  kN, and for the  $-F$  is  $F_{cr} = 27.8$  kN. While, for a ply orientation of  $\theta = 20^\circ$ , the critical buckling force for the  $+F$  is  $F_{cr} = 22.9$  kN, and for the  $-F$  is  $F_{cr} = 25.3$  kN.

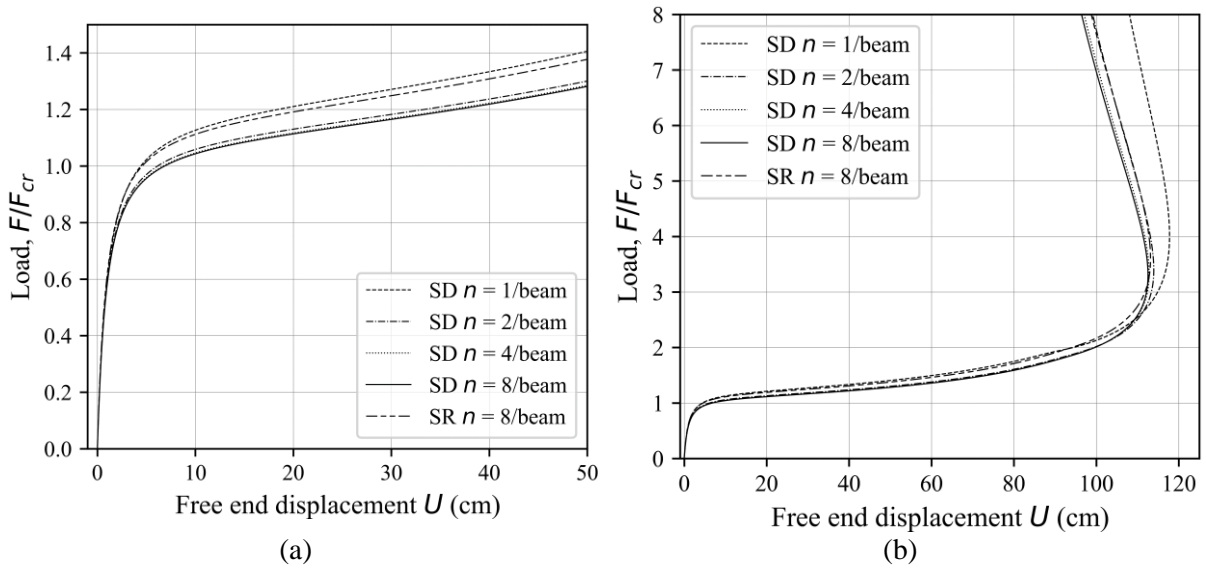


Fig. 5.35 Buckling load convergence vs. free end displacement in the  $X$ -direction for the  $+F$  and  $\theta=10^\circ$ : (a) pre-buckling response, (b) postbuckling response

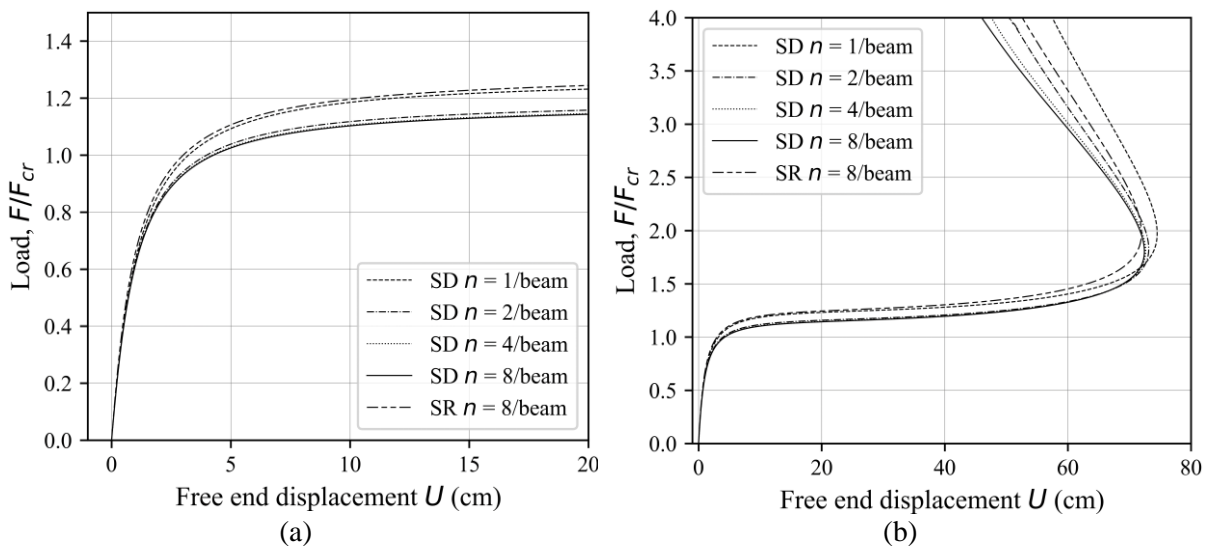


Fig. 5.36 Buckling load convergence vs. free end displacement in the  $X$ -direction for the  $-F$  and  $\theta=10^\circ$ : (a) pre-buckling response, (b) postbuckling response

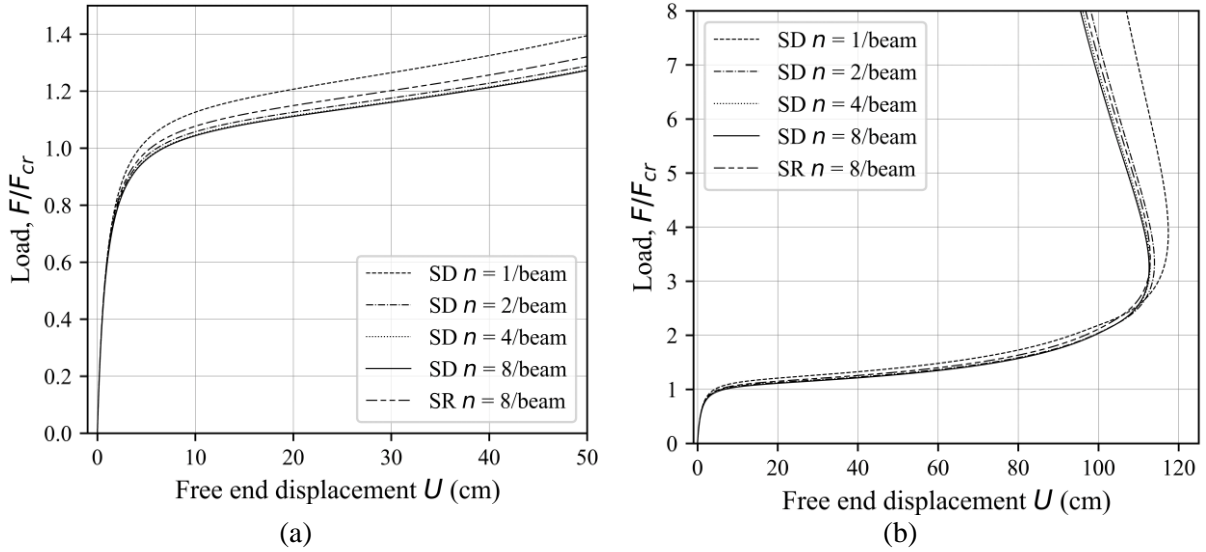


Fig. 5.37 Buckling load convergence vs. free end displacement in the X-direction for the  $+F$  and  $\theta=15^\circ$ : (a) pre-buckling response, (b) postbuckling response

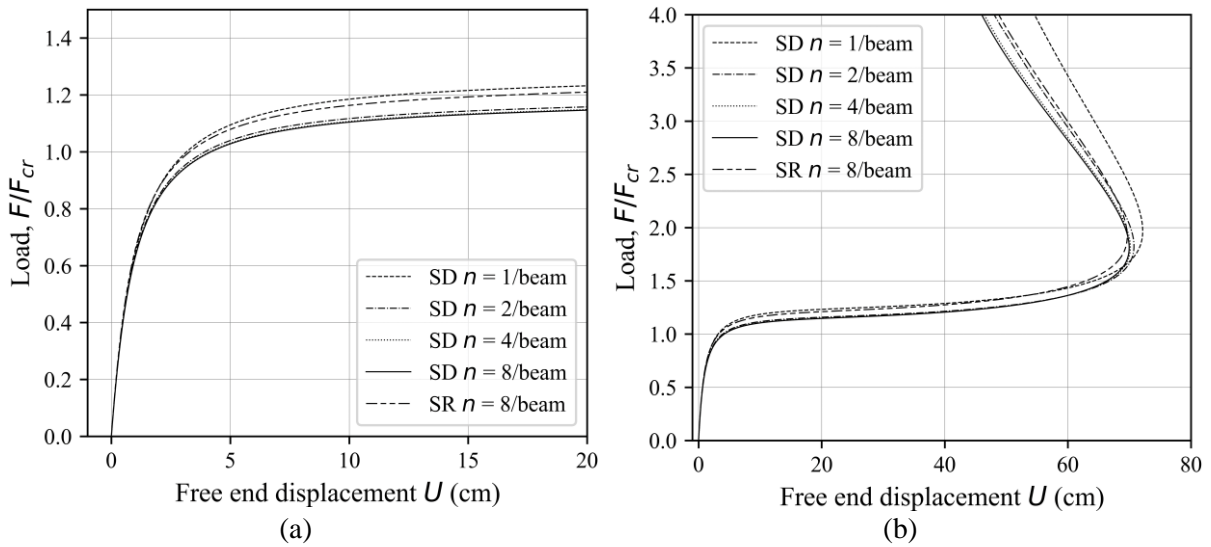


Fig. 5.38 Buckling load convergence vs. free end displacement in the X-direction for the  $-F$  and  $\theta=15^\circ$ : (a) pre-buckling response, (b) postbuckling response

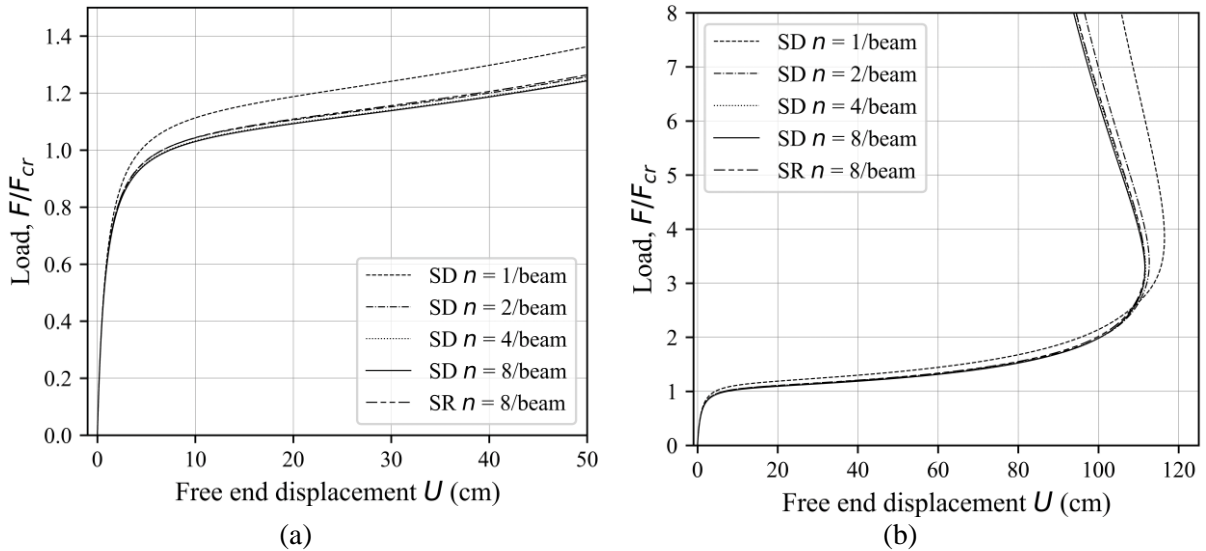


Fig. 5.39 Buckling load convergence vs. free end displacement in the  $X$ -direction for the  $+F$  and  $\theta=20^\circ$ : (a) pre-buckling response, (b) postbuckling response

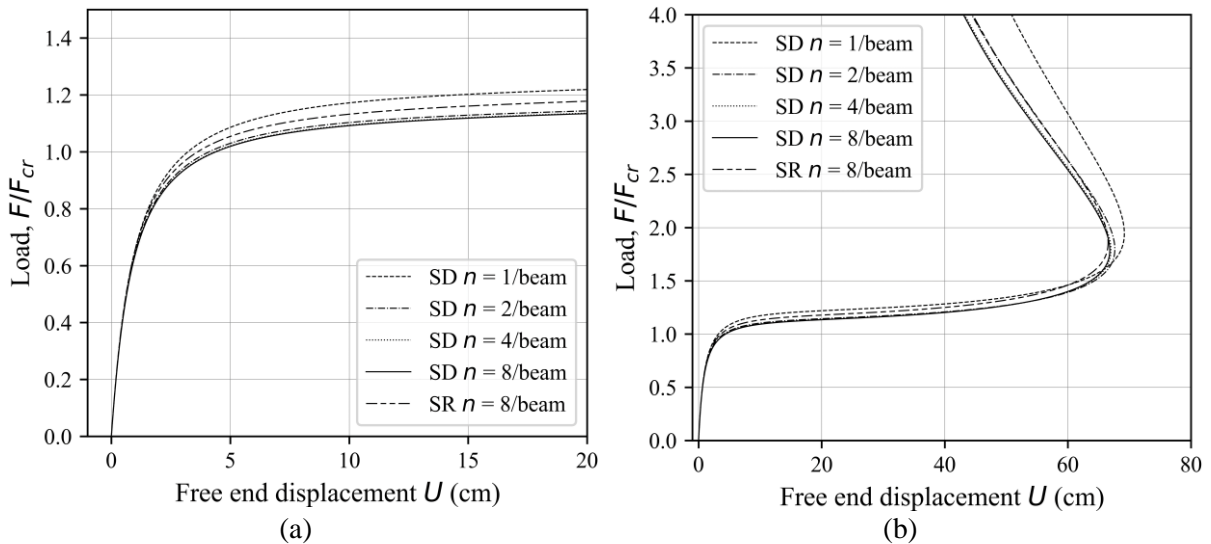


Fig. 5.40 Buckling load convergence vs. free end displacement in the  $X$ -direction for the  $-F$  and  $\theta=20^\circ$ : (a) pre-buckling response, (b) postbuckling response

The results clearly demonstrate that SD model accurately identifies the buckling state across all the mesh configurations employed. In contrast, SR model tends to significantly overestimate the buckling strength.

### 5.3.9 Example 9

The structural configuration depicted in Fig. 5.41 (a) represents a one-storey, one-bay space frame with fixed bases. The frame is subjected to vertical forces of equal intensity, denoted as  $F$ . The structural material employed for this analysis is graphite-epoxy (AS4/3501), characterized by the following properties:  $E_1 = 144$  GPa,  $E_2 = 9.65$  GPa,  $G_{12} = 4.14$  GPa,  $\nu_{12} = 0.3$ .

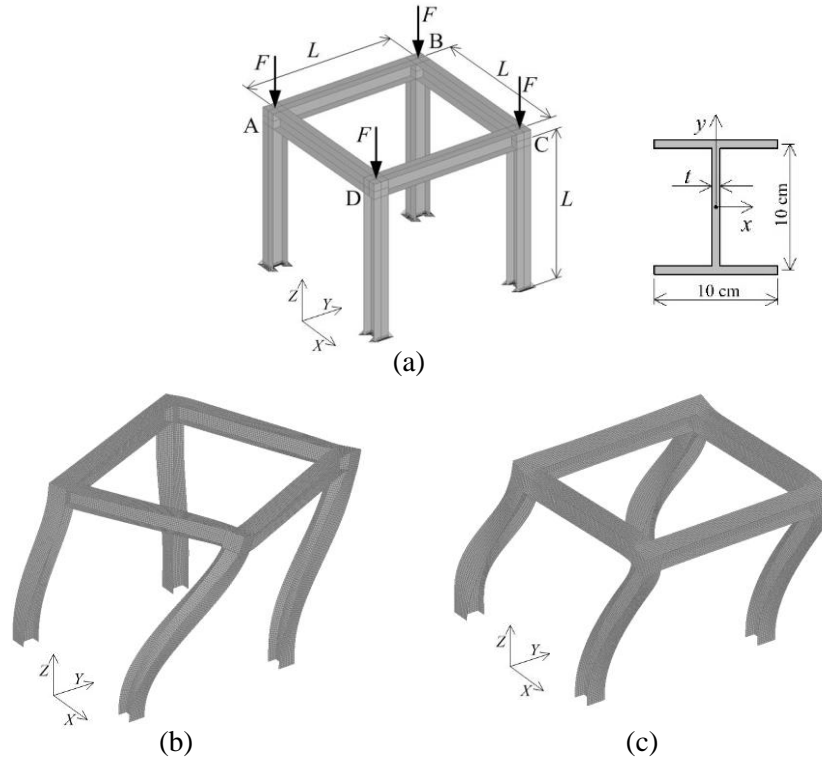


Fig. 5.41 Space frame: (a) geometry, (b) twist-sway mode, (c) sway mode

The cross-section properties for the columns and beams can be found in Table 5.10. Each column and beam in the space frame has a length of  $L = 100$  cm. Full warping restraint is assumed at all the upper frame joints. Two buckling modes are analyzed: the twist-sway buckling mode, depicted in Fig. 5.41 (b), and the sway buckling mode, depicted in Fig. 5.41 (c). To investigate these modes, five different mesh configurations are used, with each configuration consisting of one, two, four, eight, and sixteen beam elements per frame member.

Table 5.10 Example 9 and Example 10 cross-section properties.

	$A^*$ (cm <sup>2</sup> )	$I_x^*$ (cm <sup>4</sup> )	$I_y^*$ (cm <sup>4</sup> )	$I_t^*$ (cm <sup>4</sup> )	$I_\omega^*$ (cm <sup>4</sup> )	$\bar{Q}_{11R}$ (GPa)	$\bar{Q}_{66R}$ (GPa)
<i>t</i> = 1 cm							
[0°/0°] <sub>s</sub>	30	585	167.5	10	4187.5	144	4.14
[0° <sub>4</sub> /90°] <sub>s</sub>	30	585.367	167.684	10	4192.088	117.13	4.14
[0° <sub>2</sub> /90°] <sub>s</sub>	30	585.669	167.834	10	4195.859	99.217	4.14
[0° <sub>2</sub> /90° <sub>2</sub> /0°] <sub>s</sub>	30	585.476	167.738	10	4193.454	90.26	4.14
[0°/90°] <sub>s</sub>	30	586.093	168.046	10	4201.162	76.825	4.14
<i>t</i> = 1.5 cm							
[0°/0°] <sub>s</sub>	45	880.625	252.812	33.75	6320.313	144	4.14
[0° <sub>4</sub> /90°] <sub>s</sub>	45	881.864	253.432	33.75	6335.797	117.13	4.14
[0° <sub>2</sub> /90°] <sub>s</sub>	45	882.882	253.941	33.75	6348.523	99.217	4.14
[0° <sub>2</sub> /90° <sub>2</sub> /0°] <sub>s</sub>	45	882.233	253.616	33.75	6340.407	90.26	4.14
[0°/90°] <sub>s</sub>	45	884.314	254.657	33.75	6366.423	76.825	4.14
<i>t</i> = 2 cm							
[0°/0°] <sub>s</sub>	60	1180	340	80	8500	144	4.14
[0° <sub>4</sub> /90°] <sub>s</sub>	60	1182.936	341.468	80	8536.705	117.13	4.14
[0° <sub>2</sub> /90°] <sub>s</sub>	60	1185.350	342.675	80	8566.869	99.217	4.14
[0° <sub>2</sub> /90° <sub>2</sub> /0°] <sub>s</sub>	60	1183.811	341.905	80	8547.631	90.26	4.14
[0°/90°] <sub>s</sub>	60	1188.744	344.372	80	8609.299	76.825	4.14
	$K_x$	$K_y$	$K_\omega$				
<i>t</i> = 1 cm							
[0°/0°] <sub>s</sub>	1.7821	3.3604	0.0238				
[0° <sub>4</sub> /90°] <sub>s</sub>	1.7782	3.3561	0.0237				
[0° <sub>2</sub> /90°] <sub>s</sub>	1.775	3.3527	0.0237				
[0° <sub>2</sub> /90° <sub>2</sub> /0°] <sub>s</sub>	1.7771	3.3549	0.0237				
[0°/90°] <sub>s</sub>	1.7706	3.3478	0.0236				
<i>t</i> = 1.5 cm							
[0°/0°] <sub>s</sub>	1.7602	3.3366	0.0528				
[0° <sub>4</sub> /90°] <sub>s</sub>	1.7516	3.3272	0.0525				
[0° <sub>2</sub> /90°] <sub>s</sub>	1.7446	3.3195	0.0523				
[0° <sub>2</sub> /90° <sub>2</sub> /0°] <sub>s</sub>	1.7490	3.3244	0.0525				
[0°/90°] <sub>s</sub>	1.7348	3.3088	0.052				
<i>t</i> = 2 cm							
[0°/0°] <sub>s</sub>	1.7301	3.3036	0.0923				
[0° <sub>4</sub> /90°] <sub>s</sub>	1.7153	3.2873	0.0915				
[0° <sub>2</sub> /90°] <sub>s</sub>	1.7032	3.2739	0.0908				
[0° <sub>2</sub> /90° <sub>2</sub> /0°] <sub>s</sub>	1.7109	3.2824	0.0912				
[0°/90°] <sub>s</sub>	1.6865	3.2552	0.0899				



Table 5.11 Critical buckling load convergence for the twist-sway mode (MN).

Number of elements per beam	SR	SD					$F_{cr}$	
		1	2	4	8	16		
$[0^\circ/0^\circ]_s$	$t = 1$ cm	2.549	1.515	1.499	1.479	1.474	1.473	1.416
	$t = 1.5$ cm	3.846	2.289	2.265	2.235	2.228	2.226	2.105
	$t = 2$ cm	5.169	3.084	3.052	3.012	3.001	2.999	2.827
$[0^\circ_4/90^\circ]_s$	$t = 1$ cm	2.076	1.331	1.319	1.301	1.297	1.296	1.267
	$t = 1.5$ cm	3.135	2.015	1.996	1.970	1.963	1.961	1.908
	$t = 2$ cm	4.221	2.720	2.694	2.659	2.650	2.648	2.569
$[0^\circ_2/90^\circ]_s$	$t = 1$ cm	1.760	1.193	1.183	1.167	1.163	1.162	1.154
	$t = 1.5$ cm	2.661	1.808	1.792	1.768	1.763	1.761	1.737
	$t = 2$ cm	3.588	2.444	2.422	2.391	2.383	2.381	2.341
$[0^\circ_2/90^\circ_2/0^\circ]_s$	$t = 1$ cm	1.6	1.117	1.107	1.093	1.089	1.089	1.094
	$t = 1.5$ cm	2.418	1.691	1.676	1.655	1.649	1.648	1.644
	$t = 2$ cm	3.258	2.283	2.264	2.234	2.227	2.226	2.214
$[0^\circ/90^\circ]_s$	$t = 1$ cm	1.364	0.997	0.989	0.976	0.974	0.973	0.985
	$t = 1.5$ cm	2.066	1.513	1.501	1.482	1.477	1.476	1.484
	$t = 2$ cm	2.791	2.049	2.033	2.007	2.001	2	2.005

Table 5.12 Critical buckling load convergence for the sway mode (MN).

Number of elements per beam	SR	SD					$F_{cr}$	
		1	2	4	8	16		
$[0^\circ/0^\circ]_s$	$t = 1$ cm	3.868	1.715	1.691	1.67	1.665	1.663	1.632
	$t = 1.5$ cm	5.828	2.589	2.553	2.521	2.513	2.511	2.497
	$t = 2$ cm	7.818	3.483	3.435	3.392	3.381	3.379	3.383
$[0^\circ_4/90^\circ]_s$	$t = 1$ cm	3.149	1.547	1.527	1.508	1.503	1.502	1.499
	$t = 1.5$ cm	4.748	2.339	2.309	2.279	2.272	2.27	2.275
	$t = 2$ cm	6.379	3.152	3.111	3.072	3.062	3.059	3.084
$[0^\circ_2/90^\circ]_s$	$t = 1$ cm	2.669	1.417	1.4	1.381	1.377	1.376	1.384
	$t = 1.5$ cm	4.028	2.143	2.118	2.09	2.083	2.081	2.098
	$t = 2$ cm	5.417	2.892	2.857	2.82	2.811	2.809	2.844
$[0^\circ_2/90^\circ_2/0^\circ]_s$	$t = 1$ cm	2.427	1.343	1.327	1.309	1.305	1.304	1.321
	$t = 1.5$ cm	3.661	2.030	2.006	1.980	1.973	1.971	1.994
	$t = 2$ cm	4.920	2.736	2.704	2.668	2.660	2.657	2.696
$[0^\circ/90^\circ]_s$	$t = 1$ cm	2.068	1.224	1.21	1.194	1.190	1.189	1.21
	$t = 1.5$ cm	3.125	1.854	1.833	1.809	1.803	1.802	1.832
	$t = 2$ cm	4.210	2.506	2.478	2.445	2.437	2.435	2.484

The results of the eigenvalue approach for the twist-sway and sway buckling modes, along with the results from the NX Nastran's laminate shell model, are presented in Table 5.11 and Table 5.12, respectively. It is evident that the SR beam model significantly overestimates the buckling strength for all the considered cases.

For the nonlinear stability analysis, to obtain twist-sway buckling mode a small perturbation force with an intensity of  $0.001F$  is applied in the  $X$ -direction at corner A of the space frame. Additionally, to obtain sway buckling mode, two small perturbation forces, each with an intensity of  $0.001F$ , are applied in the  $X$ -direction at corners A and B. The results obtained from this analysis are plotted in Fig. 5.42.

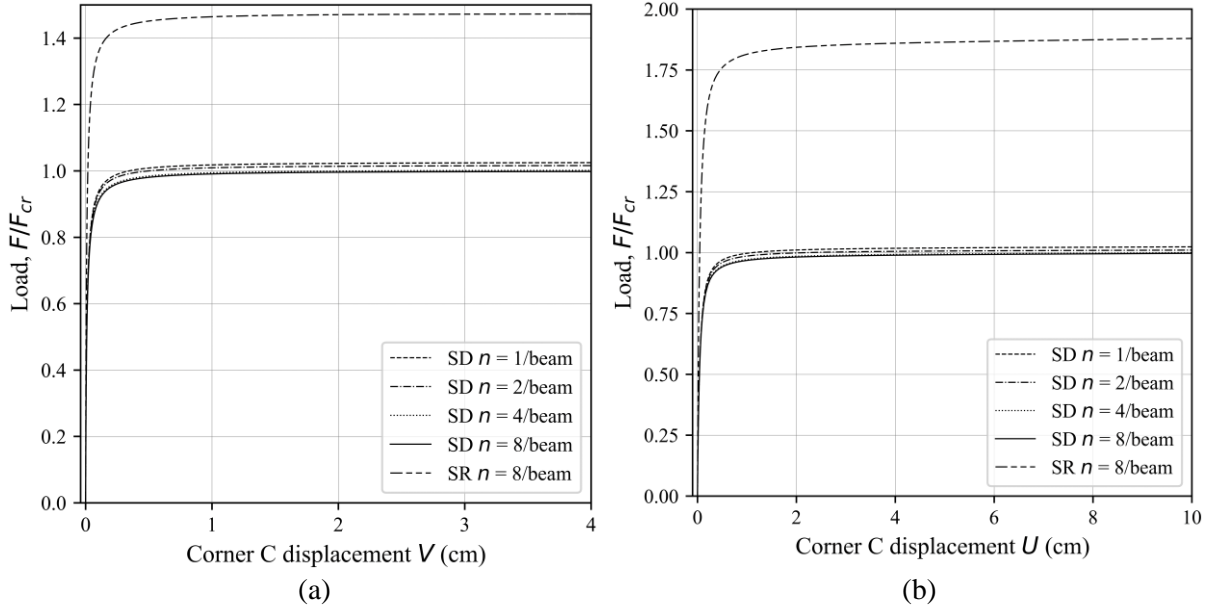


Fig. 5.42 Space frame, lateral deflection of corner C for the  $[0^{\circ}_2/90^{\circ}_2/0^{\circ}]_S$  stacking sequence,  $t = 1$  cm, in: (a) Y-direction, twist-sway mode, (b) X-direction, sway mode

As observed, all the SD meshes accurately capture the buckling behavior without experiencing shear locking. However, the SR beam model significantly overestimates the buckling stage, with an overestimation of over 40% for the twist-sway buckling mode and approximately 80% for the sway buckling mode.

### 5.3.10 Example 10

In Fig. 5.43 (a), a three-storey one-bay space frame with fixed bases is depicted. The frame is subjected to vertical forces of intensity  $F$ . The structural material used for the frame is graphite-epoxy (AS4/3501) with the following properties:  $E_1 = 144$  GPa,  $E_2 = 9.65$  GPa,  $G_{12} = 4.14$  GPa,  $\nu_{12} = 0.3$ .

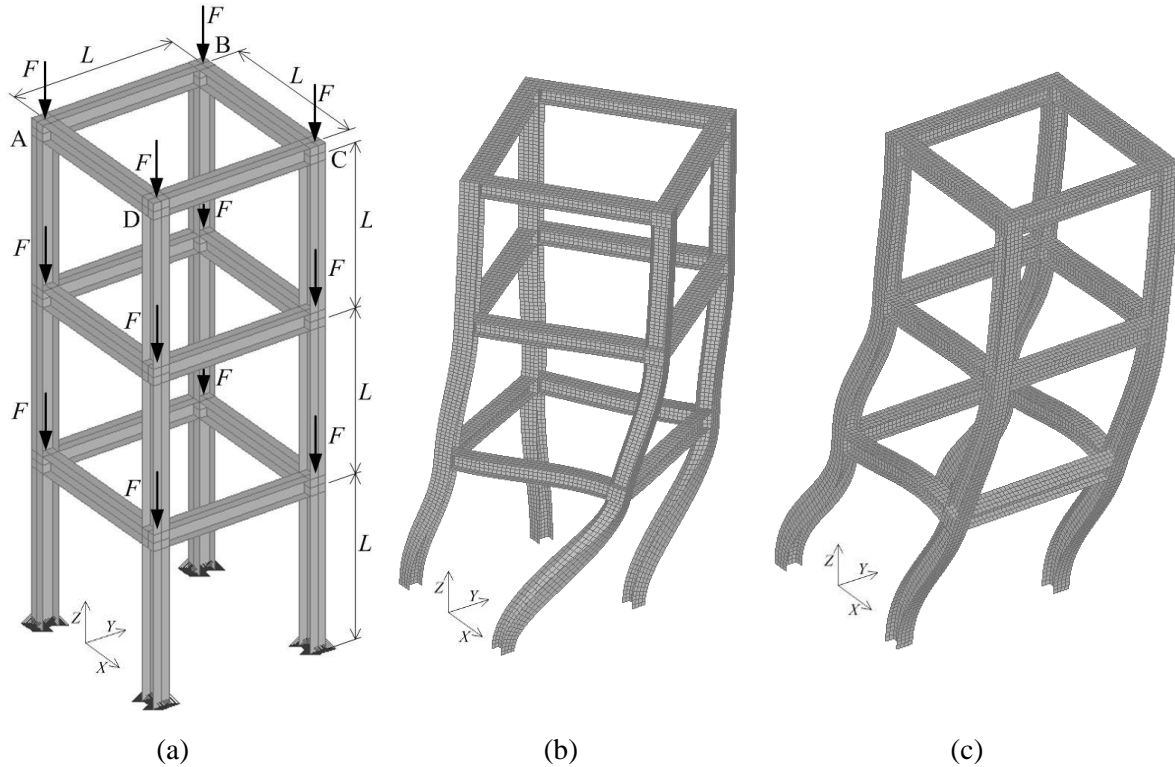


Fig. 5.43 Three storey one bay space frame: (a) geometry, (b) twist-sway mode, (c) sway mode

Analysed cross-section shape is I profile from Fig. 5.41 (a), while the cross-section properties can be found in Table 5.10 under  $[0^\circ/0^\circ]_S$  row. The cross-section branches are composed of an angle-ply laminate with the stacking sequence  $[\theta/-\theta]_{2S}$ , where the values of  $\bar{Q}_{11R}$  and  $\bar{Q}_{66R}$  vary depending on the angle  $\theta$  and they are not listed in Table 5.10 for this example.

Each column and beam in the frame has a length of  $L = 100$  cm, and each cross-section branch is 1 cm thick. Full warping restraint is assumed in all the frame joints. The analysis considers both the twist-sway buckling mode and the sway buckling mode, using four different mesh configurations consisting of one, two, four, and six beam elements per frame member.

Fig. 5.44 and Fig. 5.45 illustrate the relationship between the buckling load and the ply orientation  $\theta$  for the twist-sway and sway buckling modes, respectively. The eigenvalue analysis is conducted using six beam elements per frame member. The results obtained from the SD beam model are in good agreement with the shell model, indicating that the structure's buckling strength is highest when the ply angle is near  $15^\circ$ . The discrepancy between the SR and SD models is noticeable for ply angles  $\theta < 30^\circ$ .

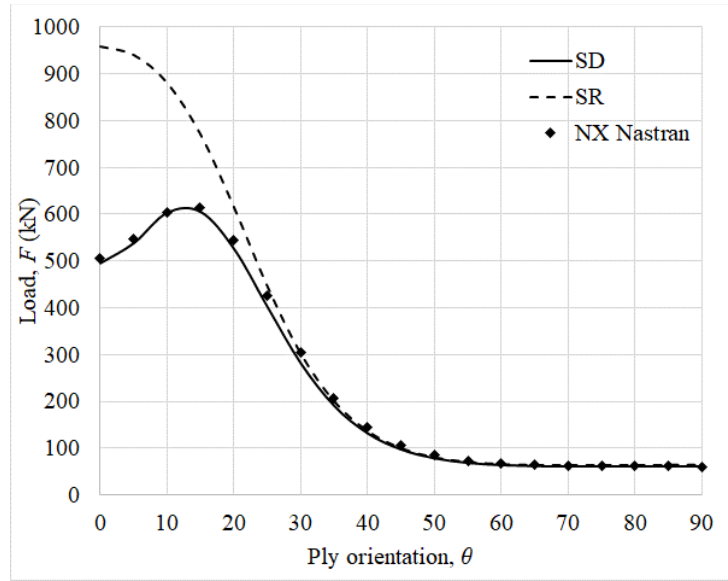


Fig. 5.44 Three-storey one-bay space frame, buckling load vs ply orientation for twist-sway buckling mode

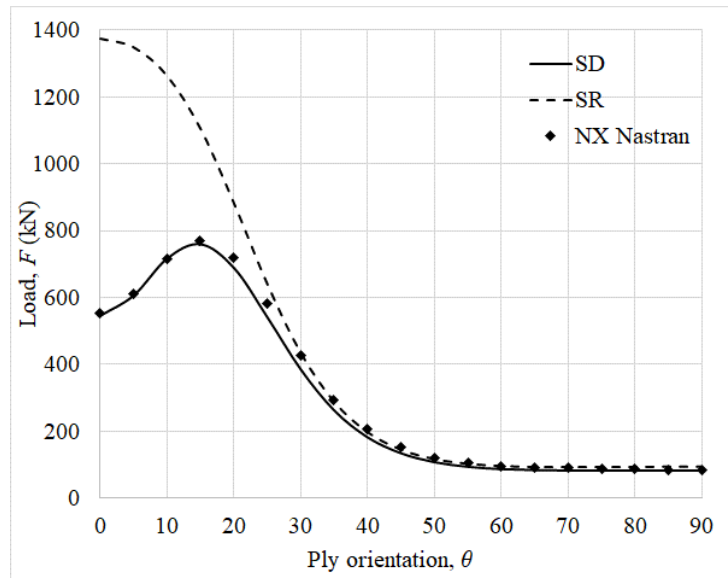


Fig. 5.45 Three-storey one-bay space frame, buckling load vs ply orientation for sway buckling mode

To perform the nonlinear stability analysis, two cases of applied perturbation forces are considered. In the first case, to obtain the twist-sway buckling mode, three perturbation forces are applied in the  $X$ -direction: one in each corner beneath corner A and one at corner A. Additionally, three perturbation forces are applied in the  $Y$  direction: one in each corner beneath corner D and one at corner D. In the second case, to obtain the sway buckling mode, six perturbation forces are applied. These forces are applied in all the corners beneath corners A and B, as well as at corners A and B. All the perturbation forces have an intensity of  $0.001F$ .

The results obtained from these analyses are plotted in Fig. 5.46 for the twist-sway buckling

mode and Fig. 5.47 for the sway buckling mode. The results shown in these figures are normalized by the critical buckling force obtained from the laminate shell solution using NX Nastran software. The critical buckling force for a twist-sway buckling mode and ply orientation of  $\theta = 0^\circ$  is  $F_{cr} = 506.6$  kN, for a ply orientation of  $\theta = 15^\circ$  is  $F_{cr} = 613.7$  kN, for a ply orientation of  $\theta = 30^\circ$  is  $F_{cr} = 303.4$  kN, while for a ply orientation of  $\theta = 90^\circ$  is  $F_{cr} = 60.5$  kN.

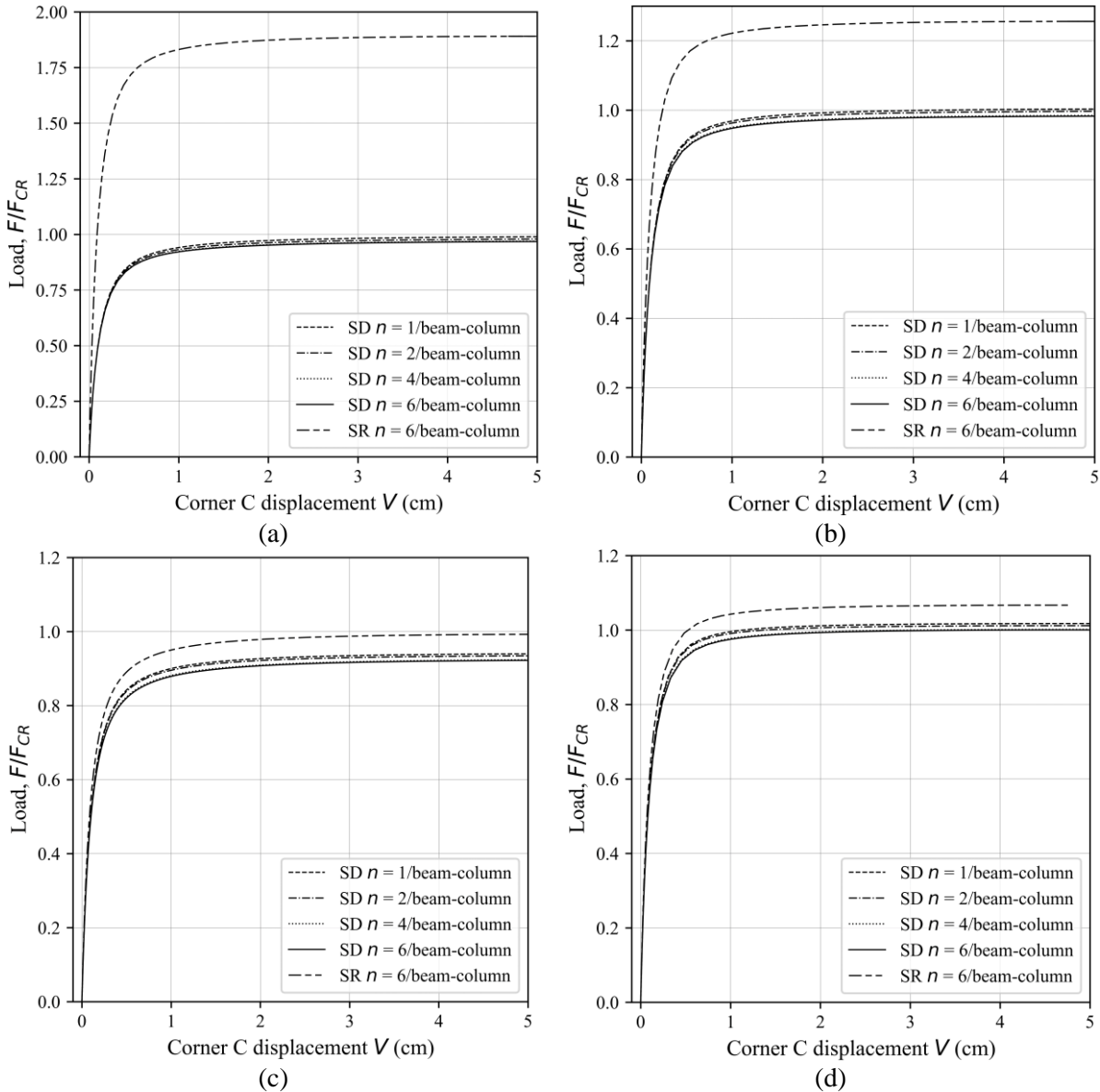


Fig. 5.46 Three-storey one-bay space frame, twist-sway buckling mode – lateral deflection of corner C in Y-direction: (a)  $\theta=0^\circ$ , (b)  $\theta=15^\circ$ , (c)  $\theta=30^\circ$ , (d)  $\theta= 90^\circ$

The critical buckling force for a sway buckling mode and ply orientation of  $\theta = 0^\circ$  is  $F_{cr} = 554.6$  kN, for a ply orientation of  $\theta = 15^\circ$  is  $F_{cr} = 771.3$  kN, for a ply orientation of  $\theta = 30^\circ$  is  $F_{cr} = 424.7$  kN, while for a ply orientation of  $\theta = 90^\circ$  is  $F_{cr} = 83.2$  kN.

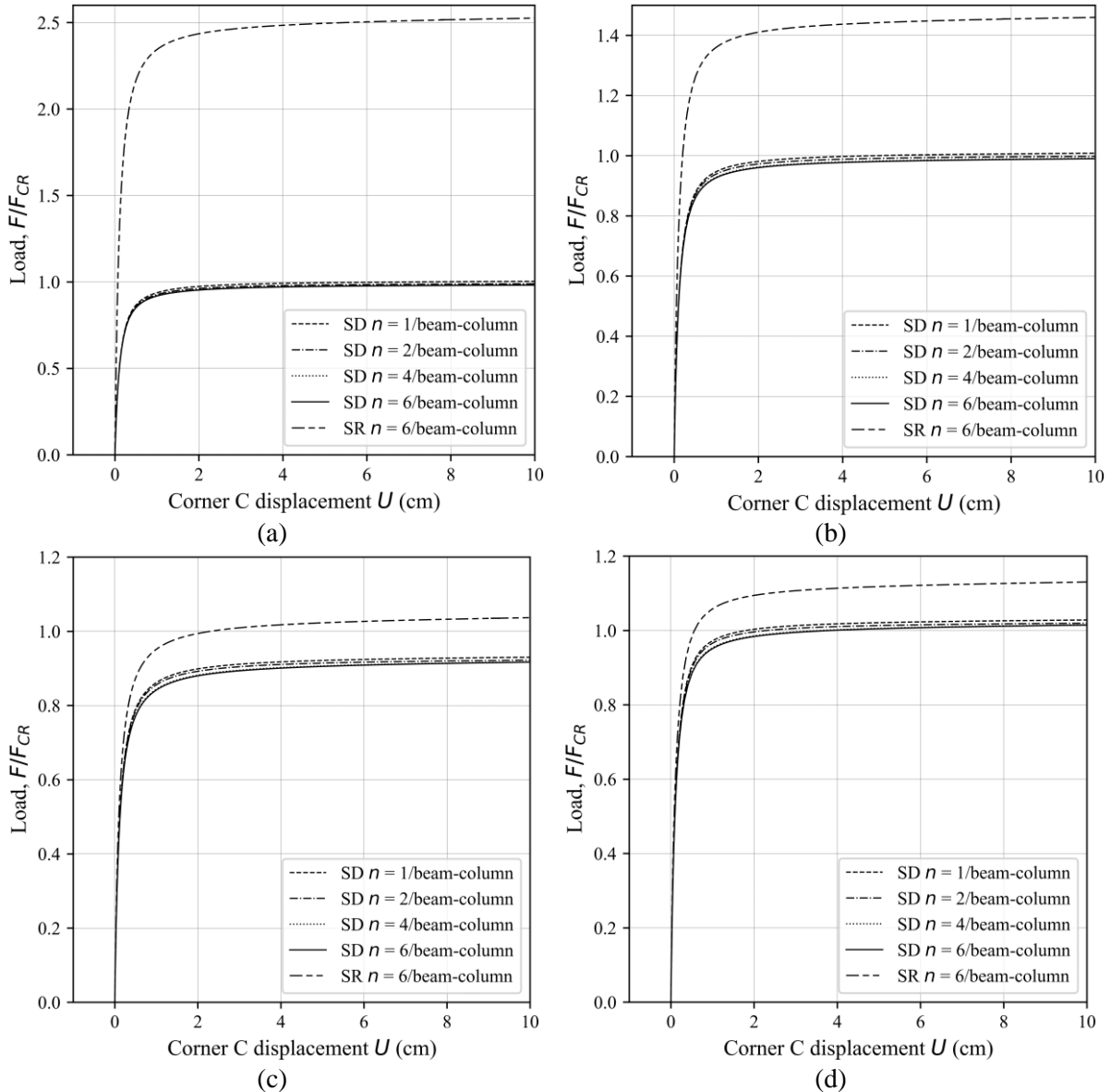


Fig. 5.47 Three-storey one-bay space frame, sway buckling mode – lateral deflection of corner C in X-direction: (a)  $\theta=0^\circ$ , (b)  $\theta=15^\circ$ , (c)  $\theta=30^\circ$ , (d)  $\theta=90^\circ$

From the presented cases, it is clear that neglecting the shear deformation effects leads to significant errors, with the critical buckling load being underestimated by up to 2.5 times in certain cases.



## 6 CONCLUSION

---

This doctoral thesis delves into the realm of finite element analysis to investigate the stability of thin-walled composite beam structures. The research employs the shear deformable bending theory, specifically the adapted Timoshenko bending theory, along with the adapted Vlasov torsion theory with restrained warping. These theories, in conjunction with the refined shear correction factors, enable the derivation of a beam finite element with fourteen degrees of freedom. A noteworthy aspect of this model is its capability to analyze asymmetric thin-walled cross-sections, accounting for the intricate coupling between shear deformations resulting from bending and torsion.

To introduce geometric nonlinearity, a nonlinear displacement field is incorporated into the cross-section, taking into account the influence of large rotations under the assumption of small deformations. It is also assumed that the cross-section maintains its undeformable nature within its plane, while the shear deformation of the mean surface is assumed to be zero. The equilibrium equations of the beam finite element are established through the application of the principle of virtual work.

This model proves applicable to open thin-walled cross-sections, accommodating various boundary conditions and allowing for different warping modeling. Additionally, it can analyze different types of laminate stacking, albeit exclusively for symmetric and balanced laminates.

The stability analyses conducted in this research encompass both linearized and nonlinear approaches. In the linearized stability analysis, the problem is transformed into a matrix eigenvalue problem, with the resulting eigenvalues representing critical loads and the corresponding eigenvectors representing buckling modes. The nonlinear behavior is described using an incremental-iterative procedure, specifically the generalized displacement method, while an updated Lagrangian formulation is employed to depict the incremental process. To facilitate force recovery, a conventional approach based on semitangential rotations is utilized. In the nonlinear analysis, a perturbation is introduced to initiate the deformation mode at which the structure loses stability.

The scientific contribution of this work manifests in the development of an original numerical model based on the finite element method. This model serves as an enhancement to an existing computer program developed at the Department of Technical Mechanics, Faculty of Engineering, University of Rijeka. The enhanced computer programs, CCSC and THINWALL



V18, have been thoroughly verified against test cases, and the obtained results have been compared with those available in the literature and obtained through the utilization of shell and solid models. Remarkably, the results indicate that the presented beam element experiences no shear locking phenomenon.

The CCSC and THINWALL V18 computer programs stand as a significant contribution to the technical sciences, offering a reliable tool for describing and analyzing the geometrically nonlinear behavior of composite beams including the effects of the shear deformations. Notably, the influence of shear deformations holds particular significance for shorter beams, particularly those with clamped and boundary conditions featuring restrained warping, which are commonly encountered in civil and mechanical engineering structures. Compared to commercial software relying on shell and solid finite element models, which often face memory limitations and prolonged computation times, THINWALL V18 enables more efficient and expedited analysis of the studied problems.

Nevertheless, further work is necessary to extend the algorithm's capabilities to encompass closed profiles, thick-walled and solid profiles. Moreover, there are plans to enhance the numerical model to facilitate the analysis of asymmetric and unbalanced laminates, as well as Functionally Graded materials. Additionally, the author aims to incorporate one of the well-known models for cross-sectional deformation, such as CUF (*Carrera Unified Formulation*) or GBT (*Generalized Beam Theory*), in order to enable deformation analysis of the cross-section within the cross-sectional plane.

## Bibliography

---

- [1] S. Adany, B.W. Schafer, Buckling mode decomposition of single-branched open cross-section members via finite strip method: Derivation, *Thin Walled Struct.* 44 (2006).
- [2] S. Adany, B.W. Schafer, A full modal decomposition of thin-walled, single-branched open cross-section members via the constrained finite strip method, *J. Constr. Steel Res.* 64 (2008).
- [3] I. Alfirević, *Linearna analiza konstrukcija*, Fakultet strojarstva i brodogradnje Sveučilišta u Zagrebu, 1999.
- [4] J.H. Argyris, P.C. Dunne, G. Malejannakis, D.W. Scharpf, On large displacement-small strain analysis of flexibly connected thin-walled beam-type structures, *Comput. Methods Appl. Mech. Eng.* 15 (1978) 99–135.
- [5] S.Y. Back, K.M. Will, A shear-flexible element with warping for thin-walled open beams, *Int. J. Numer. Methods Eng.* 43 (1998) 1173–1191.
- [6] C.E. Bakis, L.C. Bank, V.L. Brown, E. Cosenza, J.F. Davalos, J.J. Lesko, A. Machida, S.H. Rizkalla, T.C. Triantafillou, Fiber-Reinforced Polymer Composites for Construction - State-of-the-Art Review, *J. Compos. Constr.* 6 (2003) 369–383.
- [7] D. Banić, G. Turkalj, S. Kvaternik Simonetti, D. Lanc, Numerical model for a geometrically nonlinear analysis of beams with composite cross-sections, *J. Compos. Sci.* (2022) 377–394.
- [8] D. Banić, G. Turkalj, D. Lanc, Stability analysis of shear deformable cross-ply laminated composite beam-type structures, *Compos. Struct.* 303 (2023) 116270.
- [9] R. Bebiano, D. Camotim, R. Gonçalves, GBTUL 2.0 – A second-generation code for the GBT-based buckling and vibration analysis of thin-walled members, *Thin-Walled Struct.* 124 (2018) 235–257.
- [10] R. Bebiano, D. Camotim, N. Silvestre, Dynamic analysis of thin-walled members using Generalised Beam Theory (GBT), *Thin-Walled Struct.* 72 (2013) 188–205.
- [11] J. Brnić, *Mehanika i elementi konstrukcija*, Školska knjiga, Zagreb, 1993.
- [12] E.H. Brown, C.J. Burgoyne, Nonuniform elastic torsion and flexure of members with asymmetric cross-section, *Int. J. Mechanical Sci.* (1994) 39–48.
- [13] C.J. Burgoyne, E.H. Brown, T. Street, Nonuniform elastic torsion, 36 (1994) 23–38.
- [14] D. Camotim, C. Basaglia, N. Silvestre, GBT buckling analysis of thin-walled steel frames: A state-of-the-art report, *Thin-Walled Struct.* 48 (2010) 726–743.

- [15] J.E.B. Cardoso, N.M.B. Benedito, A.J.J. Valido, Finite element analysis of thin-walled composite laminated beams with geometrically nonlinear behavior including warping deformation, *Thin-Walled Struct.* 47 (2009) 1363–1372.
- [16] E. Carrera, M. Filippi, P.K. Mahato, A. Pagani, Accurate static response of single- and multi-cell laminated box beams, *Compos. Struct.* 136 (2016) 372–383.
- [17] E. Carrera, G. Giunta, Refined beam theories based on a unified formulation, *Int. J. Appl. Mech.* 2 (2010) 117–143.
- [18] E. Carrera, G. Giunta, P. Nali, M. Petrolo, Refined beam elements with arbitrary cross-section geometries, *Comput. Struct.* 88 (2010) 283–293.
- [19] A. Catapano, G. Giunta, S. Belouettar, E. Carrera, Static analysis of laminated beams via a unified formulation, *Compos. Struct.* 94 (2011) 75–83.
- [20] W.-F. Chen, T. Atsuta, *Theory of Beam Columns*, J. Ross Publishing, New York, 2008.
- [21] R.M. Christensen, *Mechanics of Composite Materials*, Dover Publications Inc, Mineola, 2005.
- [22] V.H. Cortínez, M.T. Piovan, Vibration and buckling of composite thin-walled beams with shear deformability, *J. Sound Vib.* 258 (2002) 701–723.
- [23] I.M. Daniel, O. Ishai, *Engineering Mechanics of Composite Materials*, Oxford University Press, New York, 2006.
- [24] Y.M. Ghugal, R.P. Shimpi, A Review of Refined Shear Deformation Theories for Isotropic and Anisotropic Laminated Beams, *J. Reinf. Plast. Compos.* 20 (2001) 255–272.
- [25] A. Gjelsvik, *The theory of thin walled bars*, Wiley, New York, 1981.
- [26] R. Gonçalves, P.B. Dinis, D. Camotim, GBT formulation to analyse the first-order and buckling behaviour of thin-walled members with arbitrary cross-sections, *Thin-Walled Struct.* 47 (2009) 583–600.
- [27] P.R. Heyliger, J.N. Reddy, A higher order beam finite element for bending and vibration problems, *J. Sound Vib.* 126 (1988) 309–326.
- [28] D.H. Hodges, *Nonlinear Composite Beam Theory*, American Institute of Aeronautics and Astronautics, Reston, 2006.
- [29] R.M. Jones, *Mechanics of Composite Materials*, 2nd ed., Taylor & Francis, Virginia, 1999.
- [30] N. Il Kim, M.Y. Kim, Exact dynamic/static stiffness matrices of non-symmetric thin-walled beams considering coupled shear deformation effects, *Thin-Walled Struct.* 43

- (2005) 701–734.
- [31] N. Il Kim, B.J. Lee, M.Y. Kim, Exact element static stiffness matrices of shear deformable thin-walled beam-columns, *Thin-Walled Struct.* 42 (2004) 1231–1256.
- [32] L.P. Kollár, G.S. Springer, *Mechanics of Composite Structures*, First edti, Cambridge University Press, New York, USA, 2003.
- [33] D. Lanc, G. Turkalj, T.P. Vo, J. Brnić, Nonlinear buckling behaviours of thin-walled functionally graded open section beams, *Compos. Struct.* 152 (2016) 829–839.
- [34] D. Lanc, T.P. Vo, G. Turkalj, J. Lee, Buckling analysis of thin-walled functionally graded sandwich box beams, *Thin Walled Struct.* 86 (2015) 148–156.
- [35] L.D. Landau, E.M. Lifshitz, *Theory of elasticity*, Pergamon Press, Oxford, 1986.
- [36] J. Lee, Center of gravity and shear center of thin-walled open-section composite beams, *Compos. Struct.* 52 (2001) 255–260.
- [37] J. Lee, Lateral buckling analysis of thin-walled laminated composite beams with monosymmetric sections, *Eng. Struct.* 28 (2006) 1997–2009.
- [38] J. Lee, S.E. Kim, Flexural-torsional buckling of thin-walled I-section composites, *Comput. Struct.* 79 (2001) 987–995.
- [39] J. Lee, S.E. Kim, Lateral buckling analysis of thin-walled laminated channel-section beams, *Compos. Struct.* 56 (2002) 391–399.
- [40] J. Lee, S.E. Kim, Free vibration of thin-walled composite beams with I-shaped cross-sections, *Compos. Struct.* 55 (2002) 205–215.
- [41] J. Lee, S.E. Kim, K. Hong, Lateral buckling of I-section composite beams, *Eng. Struct.* 24 (2002) 955–964.
- [42] W. McGuire, R.H. Gallagher, R.D. Ziemian, *Matrix Structural Analysis*, 2nd ed., John Wiley & Sons, New York, USA, 1999.
- [43] F. Minghini, N. Tullini, F. Laudiero, Locking-free finite elements for shear deformable orthotropic thin-walled beams, *Int. J. Numer. Meth. Engng.* (2007) 808–834.
- [44] F. Minghini, N. Tullini, F. Laudiero, Elastic buckling analysis of pultruded FRP portal frames having semi-rigid connections, *Eng. Struct.* 31 (2009) 292–299.
- [45] L.A.T. Mororó, A.M.C. de Melo, E. Parente Junior, Geometrically nonlinear analysis of thin-walled laminated composite beams, *Lat. Am. J. Solids Struct.* 12 (2015) 2094–2117.
- [46] S. Musat, B.I. Epureanu, Study of warping torsion of thin-walled beams with open cross-section using macro-elements, *Int. J. Numer. Methods Eng.* (1999) 853–868.
- [47] A. Pagani, M. Boscolo, J.R. Banerjee, E. Carrera, Exact dynamic stiffness elements

- based on one-dimensional higher-order theories for free vibration analysis of solid and thin-walled structures, *J. Sound Vib.* 332 (2013) 6104–6127.
- [48] A. Pagani, E. Carrera, Unified formulation of geometrically nonlinear refined beam theories, *Mech. Adv. Mater. Struct.* 25 (2018) 15–31.
- [49] A. Pagani, E. Carrera, A.J.M. Ferreira, Higher-order theories and radial basis functions applied to free vibration analysis of thin-walled beams, *Mech. Adv. Mater. Struct.* 23 (2016) 1080–1091.
- [50] W.D. Pilkey, *Analysis and design of elastic beams: computational methods*, Wiley, New York, USA, 2002.
- [51] J.N. Reddy, A simple higher-order theory for laminated composite plates, *J. Appl. Mech. Trans. ASME.* 51 (1984) 745–752.
- [52] J.N. Reddy, *Energy Principles and Variational Methods in Applied Mechanics, Theory Anal. Elastic Plates Shells.* (2002).
- [53] J.N. Reddy, Nonlocal theories for bending, buckling and vibration of beams, *Int. J. Eng. Sci.* 45 (2007) 288–307.
- [54] J.N. Reddy, Microstructure-dependent couple stress theories of functionally graded beams, *J. Mech. Phys. Solids.* 59 (2011) 2382–2399.
- [55] J.N. Reddy, J. Kim, A nonlinear modified couple stress-based third-order theory of functionally graded plates, *Compos. Struct.* 94 (2012) 1128–1143.
- [56] R. Schardt, Generalized beam theory—an adequate method for coupled stability problems, *Thin-Walled Struct.* 19 (1994) 161–180.
- [57] N. Silvestre, D. Camotim, Second-order generalised beam theory for arbitrary orthotropic materials, *Thin-Walled Struct.* 40 (2002) 791–820.
- [58] N. Silvestre, D. Camotim, First-order generalised beam theory for arbitrary orthotropic materials, *Thin-Walled Struct.* 40 (2002).
- [59] N. Silvestre, D. Camotim, Shear Deformable Generalized Beam Theory for the Analysis of Thin-Walled Composite Members, *J. Eng. Mech.* 139 (2013) 1010–1024.
- [60] V. Šimić, *Otpornost materijala II, Školska knjiga*, Zagreb, 1995.
- [61] M. Şimşek, H.H. Yurtcu, Analytical solutions for bending and buckling of functionally graded nanobeams based on the nonlocal Timoshenko beam theory, *Compos. Struct.* 97 (2013) 378–386.
- [62] H.T. Thai, A nonlocal beam theory for bending, buckling, and vibration of nanobeams, *Int. J. Eng. Sci.* 52 (2012) 56–64.

- [63] G. Turkalj, Nelinearna analiza stabilnosti tankostijenih grednih struktura, Doctoral dissertation, (2000).
- [64] G. Turkalj, J. Brnic, S. Kravanja, A beam model for large displacement analysis of flexibly connected thin-walled beam-type structures, *Thin-Walled Struct.* 49 (2011) 1007–1016.
- [65] G. Turkalj, J. Brnic, D. Lanc, S. Kravanja, Updated Lagrangian formulation for nonlinear stability analysis of thin-walled frames with semi-rigid connections, *Int. J. Struct. Stab. Dyn.* 12 (2012) 1250013, 1–23.
- [66] G. Turkalj, D. Lanc, D. Banić, J. Brnić, T.P. Vo, A shear-deformable beam model for stability analysis of orthotropic composite semi-rigid frames, *Compos. Struct.* 189 (2018) 648–660.
- [67] G. Turkalj, D. Lanc, I. Pesic, A beam formulation for large displacement analysis of composite frames with semi-rigid connections, *Compos. Struct.* 134 (2015) 237–246.
- [68] V. V. Vasiliev, E. V. Morozov, *Advanced Mechanics of Composite Materials and Structural Elements*, Third edit, Elsevier, Amsterdam, Netherlands, 2013.
- [69] V.Z. Vlasov, *Thin-Walled Elastic Bars*, 2nd editio, Fizmatgiz, Moscow, 1959.
- [70] T.P. Vo, J. Lee, Geometrically nonlinear analysis of thin-walled open-section composite beams, *Comput. Struct.* 88 (2010) 347–356.
- [71] T.P. Vo, J. Lee, Free vibration of axially loaded thin-walled composite Timoshenko beams, *Arch. Appl. Mech.* 81 (2011) 1165–1180.
- [72] T.P. Vo, J. Lee, Geometrical nonlinear analysis of thin-walled composite beams using finite element method based on first order shear deformation theory, *Arch. Appl. Mech.* 81 (2011) 419–435.
- [73] T.P. Vo, J. Lee, K. Lee, On triply coupled vibrations of axially loaded thin-walled composite beams, *Comput. Struct.* 88 (2010) 144–153.
- [74] Y. Yang, S. Kuo, *Theory and Analysis of Nonlinear Framed Structures*, (1994).
- [75] X.L. Zhao, L. Zhang, State-of-the-art review on FRP strengthened steel structures, *Eng. Struct.* 29 (2007) 1808–1823.

## List of symbols and abbreviations

### List of symbols

symbol	description
$A$	The arbitrary point
$A$	The surface of the cross-section [m <sup>2</sup> ]
$A_\sigma$	The area over a surface forces are acting [m <sup>2</sup> ]
$A_{ij}$	Tensor connecting shear stress resultants with the shear strains [m <sup>2</sup> ]
$A^*$	The modulus-weighted cross-sectional area [m <sup>2</sup> ]
$\mathbf{a}_{v_S}, \mathbf{a}_{\varphi_x}$	The vector of the corresponding variables
$\boldsymbol{\alpha}_{v_S}$	The vector of the corresponding constants of the integrations
$\mathbf{A}$	The matrix needed to derive Hermite shape functions
$\widehat{\mathbf{A}}_{11}, \widehat{\mathbf{B}}_{11}, \widehat{\mathbf{D}}_{11}, \widehat{\mathbf{E}}_{11}$	The $\bar{Q}_{11R}$ modulus-weighted various thickness integrals over the cross-section branch laminate ([m], [m <sup>2</sup> ], [m <sup>3</sup> ], [m <sup>4</sup> ])
$\widehat{\mathbf{A}}_{16}, \widehat{\mathbf{B}}_{16}, \widehat{\mathbf{D}}_{16}$	The $\bar{Q}_{16R}$ modulus-weighted various thickness integrals over the cross-section branch laminate ([m], [m <sup>2</sup> ], [m <sup>3</sup> ])
$\widehat{\mathbf{A}}_{66}, \widehat{\mathbf{D}}_{66}$	The $\bar{Q}_{66R}$ modulus-weighted various thickness integrals over the cross-section branch laminate ([m], [m <sup>3</sup> ])
$\mathbf{B}_w, \mathbf{B}_v, \mathbf{B}_{\varphi_x}, \mathbf{B}_u, \mathbf{B}_{\varphi_y}, \mathbf{B}_{\varphi_z}, \mathbf{B}_\theta$	The derivations of the various shape functions
$C$	The constant of the integration
$C_{ij}$ or $C_{ijkl}$	Stiffness matrix or the tensor of elastic components [Pa]
$C_0, C_1, C_2$	The starting, the last known and the unknown configuration
$\mathbf{Q}^{\text{CO}}$	The coupling relation matrix between the stress resultants and the strains
$d, \partial, \delta, \delta$	Derivative, partial derivative, the variational operator and the Dirac delta function, respectively
$e_{ij}, \eta_{ij}, \tilde{e}_{ij}$	Cauchy strain tensor, nonlinear strain tensor obtained from the linear rigid body displacements and linear strain tensor obtained from the nonlinear rigid body displacements, respectively ([-], [-], [-])
$e_z, e_{zs}$	Axial strain and contour shear strain components of the Cauchy strain tensor, respectively ([-], [-])
$e_{zx}, e_{zy}$	Shear strain components of the Cauchy strain tensor in global reference system ([-], [-])
$e_{zx}^{\text{SD}}, e_{zy}^{\text{SD}}, \theta^{\text{SD}}$	Shear strain components of the Cauchy strain tensor due to the shear deformability ([-], [-], [-])
$E$	Elastic or Young's modulus [Pa]
$E_{15}, E_{25}, E_{35}, E_{45}$	The modulus-weighted coupling stiffnesses used to relate the couplings between normal stress resultants and the St. Venant's torsional moment ([m <sup>3</sup> ], [m <sup>4</sup> ], [m <sup>4</sup> ], [m <sup>5</sup> ])
$\mathbf{Q}^{\text{EB}}$	The relation matrix between the normal stress resultants and the normal strains plus the St. Venant's terms
$F_z$	Axial force applied at the modulus-weighted centroid [N]

$F_x, F_y$	Shear forces applied at the modulus-weighted shear centre in the $x$ and $y$ directions, respectively ([N], [N])
$\mathbf{f}^e, \mathbf{f}_i^e$	The force vector and the nodal force vector for the $e$ -th beam finite element, respectively
$G$	Shear modulus [Pa]
$\bar{h}_R, \bar{\bar{h}}_R$	Distance from the modulus-weighted centroid to the reference point R along the thickness coordinate $n$ and along the contour coordinate $s$ , respectively ([m], [m])
$I_x, I_y, I_\omega$	The second area moments around $x$ and $y$ axes and the warping constant, respectively ([m <sup>4</sup> ], [m <sup>4</sup> ], [m <sup>6</sup> ])
$I_x^*, I_y^*, I_{xy}^*$	The modulus-weighted second area moments around $x$ and $y$ axes and the modulus-weighted product of inertia ([m <sup>4</sup> ], [m <sup>4</sup> ], [m <sup>4</sup> ])
$I_{x\omega}^*, I_{y\omega}^*, I_\omega^*$	The modulus-weighted second sectorial moments around $x$ and $y$ axes and the modulus-weighted warping constant, respectively ([m <sup>5</sup> ], [m <sup>5</sup> ], [m <sup>6</sup> ])
$I_t^*$	The modulus-weighted torsional constant [m <sup>4</sup> ]
$\bar{K}$	Wagner's coefficient [Nm <sup>2</sup> ]
$k_{ij}, K_{ij}$	The shear correction factors depending on the stress resultants with strain relation direction ([-], [-])
$k_{61} - k_{84}, K_{61} - K_{84}$	The coupling shear correction factors depending on the stress resultants with strain relation direction ([-]-[-], [-]-[-])
$K_1, K_2, K_3, K_4$	The various simplifications ([m], [m], [m <sup>2</sup> ], [m])
$\mathbf{k}_E^e, \mathbf{k}_G^e, \mathbf{k}_T^e$	The elastic stiffness matrix, the geometric stiffness matrix and the tangent stiffness matrix, respectively
$\mathbf{K}_E, \mathbf{K}_G, \mathbf{U}, \mathbf{P}$	The elastic stiffness matrix of the structure, the geometric stiffness matrix of the structure, the displacement vector of the structure, the vector of the external loads applied to the structure
$\hat{\mathbf{K}}_G$	The linearized geometric stiffness matrix of the structure
$l$	The length of the beam element [m]
$l_j$	The length of the $j$ -th division in the $i$ -th rectangle [m]
$M_x, M_y$	Bending moments applied at the modulus-weighted centroid around $x$ and $y$ axes, respectively ([Nm], [Nm])
$M_z$	Torsional moment applied at the modulus-weighted shear centre [Nm]
$M_\omega$	Bimoment [Nm <sup>2</sup> ]
$n_k, n_{k-1}$	The thickness coordinates of the $k$ -th ply, upper and lower point along the thickness coordinate $n$ , respectively ([m], [m])
$N$	The number of plies in the cross-section branch
$\mathbf{N}_w, \mathbf{N}_v, \mathbf{N}_{\varphi_x}, \mathbf{N}_u, \mathbf{N}_{\varphi_y}, \mathbf{N}_{\varphi_z}$	The various shape functions
$\mathbf{N}_\theta$	
$O$	Modulus-weighted cross-section centroid
$O_\omega$	The starting point of the contour coordinate $s$ or the sector null point
$\mathbf{P}_{cr}$	The buckling load
$\hat{\mathbf{P}}$	The reference load
$Q_{ij}$	Reduced stiffnesses [Pa]
$\hat{Q}_{ij}$	Transformed reduced stiffnesses [Pa]
$\bar{Q}_{11}, \bar{Q}_{16}, \bar{Q}_{66}$	Transformed reduced stiffnesses for the case when $\sigma_s = 0$ ([Pa], [Pa], [Pa])



$\bar{Q}_{11k}, \bar{Q}_{16k}, \bar{Q}_{66k}$	Transformed reduced stiffnesses for the case when $\sigma_s = 0$ and for the $k$ -th lamina of the laminate ([Pa], [Pa], [Pa])
$\bar{Q}_{11R}, \bar{Q}_{16R}, \bar{Q}_{66R}$	The reference transformed reduced stiffnesses ([Pa], [Pa], [Pa])
$r, q$	Distance from the modulus-weighted shear center to the reference point R along the thickness coordinate $n$ and along the contour coordinate $s$ , respectively ([m], [m])
R	The reference point
R1	The number of the rectangles (branches) present in the cross-section [-]
R2	The number of divisions within the $i$ -th rectangle [-]
$s, n$	Contour and thickness coordinate in a cross-section plane ([m], [m])
S	Modulus-weighted cross-section shear center
$S_{x1}, S_{y1}, S_{\omega 1}$	The first area moments around $x$ and $y$ axes and the first sectorial moment, all for the part of the cross-section cut off, respectively ([m <sup>3</sup> ], [m <sup>3</sup> ], [m <sup>4</sup> ])
$S_{x1}^*, S_{y1}^*, S_{\omega 1}^*$	The modulus-weighted first area moments around $x$ and $y$ axes and the modulus-weighted first sectorial moment, all for the part of the cross-section cut off, respectively ([m <sup>3</sup> ], [m <sup>3</sup> ], [m <sup>4</sup> ])
$S_{x0}^*, S_{y0}^*, S_{\omega 0}^*$	The modulus-weighted first area moments around $x$ and $y$ axes and the modulus-weighted first sectorial moment calculated for the each reference point R, respectively. Results of each generate the distribution of the desired property along the whole cross-section ([m <sup>3</sup> ], [m <sup>3</sup> ], [m <sup>4</sup> ])
$S_x^*, S_y^*, S_{\omega}^*$	The modulus-weighted first area moments around $x$ and $y$ axes and the modulus-weighted first sectorial moment, respectively ([m <sup>3</sup> ], [m <sup>3</sup> ], [m <sup>4</sup> ])
$S_{ij}$	In the 2 <sup>nd</sup> chapter: Compliance matrix [Pa <sup>-1</sup> ]. In the 4 <sup>th</sup> chapter: the second Piola-Kirchhoff stress tensor [Pa].
<b>Q</b> <sup>SD</sup>	The relation matrix between the shear stress resultants and the shear strains due to the shear deformability
$t, t_k$	Thickness of the cross-section branch and the thickness of the $k$ -th lamina, respectively ([m], [m])
$t_i$	The surface forces [Pa]
$T_{SV}, T_{\omega}, T_{\sigma}$	St. Venant torsional moment, torsional moment due to restrained warping and additional torsional moment due to Wagner's effect, respectively ([Nm], [Nm], [Nm])
$\mathbf{T}_{\sigma}, \mathbf{T}_{\epsilon}$	Stress and strain transformation matrices for a plane stress assumption ([-],[ -])
${}^2_1\mathbf{T}^e$	The incremental transformation matrix
$\mathbf{u}^e, \mathbf{u}_i^e$	The displacement vector and the nodal displacement vector for the $e$ -th beam finite element, respectively
$\delta U, \delta W$	The virtual elastic strain energy and the virtual work of external forces, respectively
$U_E, U_G, \Pi$	The elastic strain energy, the standard geometric potential and the total potential, respectively ([J], [J], [J])
$U_E^{EB}, U_E^{SD}, U_E^{COL}, U_E^{COR}$	The elastic strain energy arising from: EB stress resultants, SD stress resultants and the coupling terms, respectively ([J], [J], [J], [J])
$w, u, v$ or $u_i$	Linear rigid body displacements along $z, x$ and $y$ axes, respectively ([m], [m], [m])
$w_0, u_s, v_s$	Rigid body displacements along $z, x$ and $y$ axes, respectively, where displacement along $z$ axis is measured from the modulus-weighted centroid, while other ones are measured from the modulus-weighted shear centre ([m], [m], [m])
$\tilde{w}, \tilde{u}, \tilde{v}$ or $\tilde{u}_i$	Nonlinear rigid body displacements along $z, x$ and $y$ axes, respectively ([m], [m], [m])
$W, U, V$	Total rigid body displacements along $z, x$ and $y$ axes, respectively ([m], [m], [m])
$x_s, y_s$	Modulus-weighted shear center coordinates along $x$ and $y$ axes, respectively, measured from the modulus-weighted cross-section centroid ([m], [m])
$\hat{x}, \hat{y}$	The system of the reference axes for the cross-section ([m], [m])
$\tilde{x}, \tilde{y}$	The system of the centroid axes for the cross-section ([m], [m])

$x, y$	The cross-section principal axes ([m], [m])
$x_R, y_R$	The position coordinates of the reference point R ([m], [m])
$\hat{x}_0, \hat{y}_0$	The modulus-weighted centroid position ([m], [m])
${}^0_z, {}^0_x, {}^0_y$	The local coordinate system in $C_0$ configuration
${}^1_z, {}^1_x, {}^1_y$	The local coordinate system in $C_1$ configuration
$Z, X, Y$	The global coordinate system
$\alpha$ or $\alpha_i$	In the 3 <sup>rd</sup> chapter: Angular position of the $i$ -th cross-section rectangle in the system of principal axes ([rad] or [°]). In the 4 <sup>th</sup> chapter: the constants of integration used in Hermite shape functions
$\hat{\alpha}$ or $\hat{\alpha}_i$	Angular position of the $i$ -th cross-section rectangle in the system of reference axes ([rad] or [°])
$\alpha_z, \alpha_x, \alpha_y, \alpha_\omega$	The subcoefficients resulting from the Wagner's coefficient $\bar{K}$ ([m <sup>2</sup> ], [m], [m], [-])
$\gamma_{12}, \gamma_{13}, \gamma_{23}$	Shear strain components [-]
$\Delta \bar{\omega}, \Delta \bar{\omega}$	The contour warping and the thickness warping change, respectively ([m <sup>2</sup> ], [m <sup>2</sup> ])
$\varepsilon_j$	Strain components [-]
$\varepsilon_1, \varepsilon_2, \varepsilon_3$	Normal strain components [-]
$\varepsilon_{ij}$	Green-Lagrange strain tensor [-]
$\eta_s, \xi_s$	Rigid body displacement in the contour $s$ and thickness $n$ direction, respectively ([m], [m])
$\theta_i$	Fiber angle orientation ([rad] or [°])
$\theta$	Warping parameter ([rad/m] or [°/m])
$[\theta_1/\dots/\theta_k/\dots/\theta_N]$	The general laminate inscription
$[\theta_1/\dots/\theta_{N/2}]_S$	The inscription for the symmetric laminate
$\Lambda$	The proportional parameter
$\nu$	Poisson's ratio [-]
$\sigma_i$	Stress components [Pa]
$\sigma_1, \sigma_2, \sigma_3$	Normal stress components [Pa]
$\sigma_z, \varepsilon_z$	Axial stress and strain ([Pa], [-])
$\sigma_s, \varepsilon_s$	Contour normal stress and strain ([Pa], [-])
$\sigma_{zk}, \tau_{zsk}$	Axial stress and contour shear stress for the $k$ -th lamina of the laminate ([Pa], [Pa])
$\sigma_{zR}$	The reference normal stress [Pa]
$\tau_{12}, \tau_{13}, \tau_{23}$	Shear stress components [Pa]
$\tau_{zs}, \gamma_{zs}$	Contour shear stress and strain ([Pa], [-])
$\tau_{zs}^{SV}, e_{zs}^{SV}$	Shear stress and Cauchy shear strain due to the St. Venant torsional moment along the contour coordinate $s$ , respectively ([Pa], [-])
$\tau_{zs}^{SD}, e_{zs}^{SD}$	Shear stress and the contour shear strain component of the Cauchy strain tensor due to the shear deformability, respectively ([Pa], [-])
$\tau_{zsR}^{SD}$	The reference contour shear stress due to the shear deformability [Pa]
$\varphi_z, \varphi_x, \varphi_y$	Rigid body rotations around $z, x$ and $y$ axes, respectively ([rad] or [°], [rad] or [°], [rad] or [°])
$\chi$	The principal axes angle ([rad] or [°])
$\Psi$	St. Venant stress function [N/m]
$\omega, \Omega$	The warping function and the primary warping function, respectively ([m <sup>2</sup> ], [m <sup>2</sup> ])

$\omega_R, \Omega_R$       The sectorial coordinate and the principal sectorial coordinate of the reference point R, respectively ( $[m^2]$ ,  $[m^2]$ )

## List of abbreviations

<b>abbreviation</b>	<b>description</b>
CC	Beam/column clamped at both ends
CF	Clamped-free end
cFSM	Constrained finite strip method
CO	Coupling relations
CUF	Carrera unified formulation
EB	Euler-Bernoulli relations
F	Flexural buckling mode
FEM	Finite element method
GBT	General beam theory
SD	Shear deformable or Shear deformable relations
SR	Shear rigid
SS	simply supported beam/column at both ends
TF	Torsional-flexural buckling mode
UL	Updated Lagrangian
1D	One dimensional
2D	Two dimensional

## List of figures

---

Fig. 2.1 Unbonded view of fiber-reinforced composite laminate.....	9
Fig. 2.2 Stresses in an elemental volume.....	11
Fig. 2.3 Unidirectionally reinforced lamina.....	13
Fig. 2.4 Lamina of an arbitrary orientation.....	14
Fig. 3.1 Thin-walled beam with open cross-section: (a) full geometry, (b) middle surface with rigid-body displacements.....	18
Fig. 3.2 Rigid-body displacements of a thin-walled cross-section.....	20
Fig. 3.3 Deformation of the composite thin-walled beam cut off.....	21
Fig. 3.4 Stress resultants of the cross-section.....	23
Fig. 3.5 Cross-section example.....	26
Fig. 3.6 Stresses and strains of the composite thin-walled beam cut off.....	28
Fig. 3.7 Open thin-walled composite cross-section: (a) real geometry, (b) approximated geometry.....	38
Fig. 3.8 Geometry of N-layered i-th rectangle.....	38
Fig. 3.9 Arbitrary rectangle geometry: (a) general coordinates, (b) contour warping function, (c) thickness warping function.....	39
Fig. 3.10 Node transformation.....	41
Fig. 3.11 Various distributions over the cross-section contour (left: distribution without correction, right: distribution with correction): (a) $S_x^*$ , (b) $S_y^*$ , (c) $S_\omega^*$ .....	47
Fig. 4.1 Thin-walled beam finite element: nodal displacements and nodal forces.....	54
Fig. 4.2 Incremental displacements of the beam finite element.....	63
Fig. 5.1 Flowchart of the CCSC program.....	76
Fig. 5.2 Examples of the txt input files for: (a) U profile, (b) I profile.....	77
Fig. 5.3 Flowchart of the THINWALL V18 program.....	80
Fig. 5.4 Example 1 cross-section geometry: (a) monosymmetric U profile, (b) monosymmetric I profile.....	82
Fig. 5.5 Positions of material-weighted centroid and shear centre for the monosymmetric U profile with respect to fiber angle change in the flanges and the web.....	83
Fig. 5.6 Various U profile cross-section properties with respect to fiber angle change in the flanges and the web: (a) $I_x^*$ , $I_y^*$ and $I_\omega^*$ , (b) $\alpha_z$ and $\alpha_y$ , (c) $\bar{Q}_{11R}$ and $\bar{Q}_{66R}$ , (d) $K_x$ , $K_y$ , $K_\omega$ and $K_{y\omega}$ .....	84

Fig. 5.7 Positions of material-weighted centroid and shear centre for the monosymmetric I profile with respect to fiber angle change in the top and the bottom flange ..... 85

Fig. 5.8 Various I profile cross-section properties with respect to fiber angle change in the top and bottom flange:  
 (a)  $I_x^*$ ,  $I_y^*$  and  $I_\omega^*$ , (b)  $\alpha_z$  and  $\alpha_x$ , (c)  $\bar{Q}_{11R}$  and  $\bar{Q}_{66R}$ , (d)  $K_x$ ,  $K_y$ ,  $K_\omega$  and  $K_{x\omega}$  ..... 86

Fig. 5.9 Positions of material-weighted centroid and shear centre for the monosymmetric I profile with respect to fiber angle change in the flanges and the web..... 87

Fig. 5.10 Various I profile cross-section properties with respect to fiber angle change in the flanges and the web:  
 (a)  $I_x^*$ ,  $I_y^*$  and  $I_\omega^*$ , (b)  $\alpha_z$  and  $\alpha_x$ , (c)  $\bar{Q}_{11R}$  and  $\bar{Q}_{66R}$ , (d)  $K_x$ ,  $K_y$ ,  $K_\omega$  and  $K_{x\omega}$  ..... 88

Fig. 5.11 Buckling load vs. ply orientation ( $\theta$ ) for  $L=100$  cm and: (a) CF, (b) SS..... 89

Fig. 5.12 Buckling load vs. beam length for CF beam and: (a)  $\theta=0^\circ$ , (b)  $\theta=15^\circ$ ..... 90

Fig. 5.13 Buckling load vs. beam length for SS beam and: (a)  $\theta=0^\circ$ , (b)  $\theta=15^\circ$ ..... 90

Fig. 5.14 Buckling load vs. beam length for CC beam and: (a)  $\theta=0^\circ$ , (b)  $\theta=15^\circ$ ..... 90

Fig. 5.15 Simply supported column: (a) geometry, (b) cross-section, (c) torsional-flexural buckling mode..... 91

Fig. 5.16 Buckling load convergence for SS column,  $L = 400$  cm: (a)  $[0^\circ/0^\circ]_s$ , (b)  $[0^\circ/90^\circ]_s$ ..... 92

Fig. 5.17 Buckling load vs. column length for SS column..... 92

Fig. 5.18 Cantilever column: (a) geometry, (b) cross-section, (c) flexural buckling mode,(d) torsional-flexural buckling mode..... 93

Fig. 5.19 Buckling load convergence for the CF column,  $L=50$  cm ..... 94

Fig. 5.20 Buckling load vs. column length for the CF column..... 95

Fig. 5.21 Cantilever column: (a) geometry, (b) cross-section, (c) torsional-flexural buckling mode..... 96

Fig. 5.22 Buckling load vs. ply orientation ( $\theta$ ) for the CF column ..... 97

Fig. 5.23 Convergence analysis for the CF column: (a)  $\theta=0^\circ$ , (b)  $\theta=15^\circ$  ..... 97

Fig. 5.24 Cantilever beam: (a) geometry, (b) cross-section, (b) lateral-torsional buckling mode ..... 98

Fig. 5.25 Buckling load convergence for the CF beam: (a)  $+F$ , (b)  $-F$ ..... 99

Fig. 5.26 Buckling load for the  $+F$  vs. free end displacement in the X-direction: (a)  $[0^\circ/0^\circ]_s$ , (b)  $[0^\circ/90^\circ]_s$  ..... 99

Fig. 5.27 Buckling load for the  $-F$  vs. free end displacement in the X-direction: (a)  $[0^\circ/0^\circ]_s$ , (b)  $[0^\circ/90^\circ]_s$ ... 100

Fig. 5.28 Buckling load convergence for the  $-F$  vs. free end displacement in the X-direction: (a)  $[0^\circ/0^\circ]_s$ , (b)  $[0^\circ/90^\circ]_s$ ..... 100

Fig. 5.29 L-frame: (a) geometry, (b) lateral-torsional buckling mode. .... 101

Fig. 5.30 Buckling load convergence for the L-frame..... 102

Fig. 5.31 Buckling load convergence vs. free end displacement in the X-direction for the  $[0^\circ/0^\circ]_S$  stacking sequence: (a) prebuckling response, (b) postbuckling response ..... 102

Fig. 5.32 Buckling load convergence vs. free end displacement in the X-direction for the  $[0^\circ/90^\circ]_S$  stacking sequence: (a) prebuckling response, (b) postbuckling response ..... 103

Fig. 5.33 L-frame with lateral force..... 104

Fig. 5.34 Buckling load of the L-frame vs. ply orientation ( $\theta$ ) for the  $+F$  and  $-F$ ..... 104

Fig. 5.35 Buckling load convergence vs. free end displacement in the X-direction for the  $+F$  and  $\theta=10^\circ$ : (a) prebuckling response, (b) postbuckling response..... 105

Fig. 5.36 Buckling load convergence vs. free end displacement in the X-direction for the  $-F$  and  $\theta=10^\circ$ : (a) prebuckling response, (b) postbuckling response..... 105

Fig. 5.37 Buckling load convergence vs. free end displacement in the X-direction for the  $+F$  and  $\theta=15^\circ$ : (a) prebuckling response, (b) postbuckling response..... 106

Fig. 5.38 Buckling load convergence vs. free end displacement in the X-direction for the  $-F$  and  $\theta=15^\circ$ : (a) prebuckling response, (b) postbuckling response..... 106

Fig. 5.39 Buckling load convergence vs. free end displacement in the X-direction for the  $+F$  and  $\theta=20^\circ$ : (a) prebuckling response, (b) postbuckling response..... 107

Fig. 5.40 Buckling load convergence vs. free end displacement in the X-direction for the  $-F$  and  $\theta=20^\circ$ : (a) prebuckling response, (b) postbuckling response..... 107

Fig. 5.41 Space frame: (a) geometry, (b) twist-sway mode, (c) sway mode..... 108

Fig. 5.42 Space frame, lateral deflection of corner C for the  $[0^\circ_2/90^\circ_2/0^\circ]_S$  stacking sequence,  $t = 1$  cm, in: (a) Y-direction, twist-sway mode, (b) X-direction, sway mode..... 111

Fig. 5.43 Three storey one bay space frame: (a) geometry, (b) twist-sway mode, (c) sway mode..... 112

Fig. 5.44 Three-storey one-bay space frame, buckling load vs ply orientation for twist-sway buckling mode... 113

Fig. 5.45 Three-storey one-bay space frame, buckling load vs ply orientation for sway buckling mode ..... 113

Fig. 5.46 Three-storey one-bay space frame, twist-sway buckling mode – lateral deflection of corner C in Y-direction: (a)  $\theta=0^\circ$ , (b)  $\theta=15^\circ$ , (c)  $\theta=30^\circ$ , (d)  $\theta= 90^\circ$  ..... 114

Fig. 5.47 Three-storey one-bay space frame, sway buckling mode – lateral deflection of corner C in X-direction: (a)  $\theta=0^\circ$ , (b)  $\theta=15^\circ$ , (c)  $\theta=30^\circ$ , (d)  $\theta= 90^\circ$  ..... 115

## List of tables

---

<i>Table 5.1 Example 1 U profile cross-section properties. ....</i>	<i>83</i>
<i>Table 5.2 Example 1 I profile cross-section properties with respect to fiber angle change in the top and bottom flange. ....</i>	<i>85</i>
<i>Table 5.3 Example 1 I profile cross-section properties with respect to fiber angle change in the flanges and the web. ....</i>	<i>87</i>
<i>Table 5.4 Example 2 cross-section properties. ....</i>	<i>89</i>
<i>Table 5.5 Example 3 cross-section properties. ....</i>	<i>91</i>
<i>Table 5.6 Example 4 cross-section properties. ....</i>	<i>93</i>
<i>Table 5.7 Example 5 cross-section properties. ....</i>	<i>96</i>
<i>Table 5.8 Example 6 cross-section properties. ....</i>	<i>98</i>
<i>Table 5.9 Example 7 and Example 8 cross-section properties. ....</i>	<i>101</i>
<i>Table 5.10 Example 9 and Example 10 cross-section properties. ....</i>	<i>109</i>
<i>Table 5.11 Critical buckling load convergence for the twist-sway mode (MN). ....</i>	<i>110</i>
<i>Table 5.12 Critical buckling load convergence for the sway mode (MN). ....</i>	<i>110</i>



## Curriculum vitae

---

Damjan Banić, born on January 23, 1988, in Rijeka, is the second son of a seven-member family, with his father Donat and mother Kristina. He completed his primary and secondary education in Rijeka. Damjan earned a Bachelor's degree in Mechanical Engineering and a Master's degree in Mechanical Engineering from the Faculty of Engineering at the University of Rijeka, where he received high honors, graduating *summa cum laude* in both programs. He successfully completed his studies in 2012.

From 2013 to 2015, Damjan worked at Vertex B.S., specializing in ship documentation and the creation of 3D models for various ship systems. In 2014, he embarked on a postgraduate doctoral program in Computational Mechanics at the Faculty of Engineering, University of Rijeka. During 2015-2017, he served as a research associate on the project "Career Development of Young Researchers," funded by the Croatian Science Foundation. Since 2017, Damjan has been working as an Assistant at the Department of Technical Mechanics.

Throughout his academic journey, Damjan demonstrated exceptional academic performance, achieving outstanding results in his doctoral program exams and publishing eight research papers in renowned scientific journals, six of which are indexed in bibliographic databases such as CC, SCI, and/or SCI-Exp. Additionally, he actively participated in five international scientific conferences.

In 2017, Damjan had the opportunity to broaden his horizons as part of the Erasmus+ project, spending four months at the Department of Civil, Chemical, Environmental, and Materials Engineering at the University of Bologna. Beyond his academic pursuits, Damjan has cultivated a passion for ballroom dancing and choral singing, engaging in these activities for many years.

## List of published works

---

### Journal papers:

1. Banić, D., Turkalj, G., Lanc, D., Stability analysis of shear deformable cross-ply laminated composite beam-type structures, *Composite structures*, 303 (2023), 116270, 20, doi: 10.1016/j.compstruct.2022.116270.
2. Banić, D., Turkalj, G., Kvaternik Simonetti, S., Lanc, D., Numerical model for a geometrically nonlinear analysis of beams with composite cross-sections, *Journal of Composites Science*, 6 (2022), 12, 377, 18, doi: 10.3390/jcs6120377.
3. Banić, D., Bacciocchi, M., Tornabene, F., Ferreira, A., Influence of Winkler-Pasternak Foundation on the Vibrational Behavior of Plates and Shells Reinforced by Agglomerated Carbon Nanotubes, *Applied Sciences-Basel*, 7 (2017), 12, 1228, 55, doi: 10.3390/app7121228.
4. Banić, D., Turkalj, G., Brnić, J., Finite element stress analysis of elastic beams under non-uniform torsion, *Transactions of FAMENA*, 40 (2016), 2, 71-82, doi: 10.21278/TOF.40206.
5. Banić, D., Lanc, D., Kvaternik, S., Creep analysis of elastic beams under constant torque, *Machines. Technologies. Materials*, XI (2017), 5, 229-232.
6. Kvaternik Simonetti, S., Turkalj, G., Banić, D., Lanc, D., Bimetallic Thin-Walled Box Beam Thermal Buckling Response, *Materials*, 15 (2022), 21, 7357, 13, doi: 10.3390/ma15217537.
7. Turkalj, G., Lanc, D., Banić, D., Brnić, J., Vo, T.P.: A shear-deformable beam model for stability analysis of orthotropic composite semi-rigid frames, *Composite structures*, 189 (2018), 648-660, doi: 10.1016/j.compstruct.2018.01.105.
8. Kvaternik, S., Turkalj, G., Banić, D., Finite element analysis of torsional-flexural behaviour of thin-walled frame considering joint warping conditions, *Trans & Motauto World*, II (2017), 5, 181-183.

### Conference papers:

1. Banić, D., Turkalj, G., Lanc, D., Kvaternik Simonetti, S., *Shear deformable beam model for stability analysis of beam-type structures with composite thin-walled cross sections*, Proceedings of the Fourteenth International Conference on Computational Structures Technology, 3 (2022), Montpellier, France, doi: 10.4203/ccc.3.15.3.
2. Banić, D., Turkalj, G., Kvaternik Simonetti, S., Lanc, D., *Stability analysis of beam-type structures with composite cross-section considering coupled shear deformation effects*, Proceedings of the conference ICCSE2, 2nd International Conference on Computations for Science and Engineering 2022, Rimini, Italy.
3. Banić, D., Turkalj, G., Lanc, D., Kvaternik Simonetti, S., *Stability analysis of composite beam-type structures including shear deformation effects*, ICCSM 7th International congress of Croatian society of mechanics: book of abstracts, 10th ICCSM 2022, Pula, Croatia.

4. Banić, D., Turkalj, G., Kvaternik, S., Lanc, D., *Shear deformable beam model for stability analysis of beam type structures with composite cross sections*, 5th International Conference on Mechanics of Composites Book of Abstracts, MECHCOMP 2019, Lisbon, Portugal.
5. Banić, D., Turkalj, G., Lanc, D.: *Large displacement analysis of laminated composite frames considering shear deformation effects*, Proceedings of the 4th International Conference on Mechanics of Composites MECHCOMP2018, Madrid, Spain, July 9-12, 2018, 7-7.
6. Kvaternik Simonetti, S., Lanc, D., Turkalj, G., Banić, D., *Beam model for thermal buckling of thin-walled functionally graded box-beam*, Proceedings of the Fourteenth International Conference on Computational Structures Technology, 3 (2022), Montpellier, France, doi: 10.4203/coc.3.15.1.
7. Kvaternik Simonetti, S., Lanc, D., Turkalj, G., Banić, D., *Thermal buckling analysis of thin-walled functionally graded closed section beams*, Proceedings of the conference ICCSE2, 2nd International Conference on Computations for Science and Engineering 2022, Rimini, Italija
8. Kvaternik Simonetti, S., Lanc, D., Turkalj, G., Banić, D., *Thermal buckling analysis of thin-walled FG closed section beams*, ICCSM 7th International congress of Croatian society of mechanics: book of abstracts, 10th ICCSM 2022, Pula, Croatia.
9. Turkalj, G., Banić, D., Lanc, D., *Numerical stability analysis of composite beam-type structures considering coupled shear deformation effects*, ICCS25 25th International Conference on Composite Structures, Porto, Portugal.
10. Lanc, D., Turkalj, G., Banić, D., Kvaternik Simonetti, S., *FE model for global buckling analysis of composite beams*, ICCS25 25th International Conference on Composite Structures, Porto, Portugal.
11. Kvaternik Simonetti, S., Lanc, D., Turkalj, G., Banić, D., *Beam model for thermal buckling analysis of thin-walled functionally graded open section beams*, 5th International Conference on Mechanics of Composites Book of Abstracts, MECHCOMP 2019, Lisbon, Portugal.
12. Turkalj, G., Lanc, D., Banić, D., Kvaternik, S.: *Finite element analysis of thin-walled functionally graded open section beams exposed to thermal loading*, Proceedings of the 4th International Conference on Mechanics of Composites MECHCOMP2018, Madrid, Spain, July 9-12, 2018, 33-33.
13. Turkalj, G., Lanc, D., Banić, D., Brnić, J.: *A shear-flexible beam model for large displacement analysis of composite beam-type structures*, Proceedings of the 3rd International Conference on Mechanics of Composites MECHCOMP3, Bologna, Italy, July 4-7, 2017, 18-19.
14. Turkalj, G., Lanc, D., Brnić, J., Banić, D., *Numerical simulation of instability behaviour of composite semi-rigid frames using a shear flexible thin-walled beam element*, Proceedings of the 2th International Conference on Mechanics of Composites MECHCOMP2, Bologna, Italy, 2016, 120-120.